ADAPTIVE RELIABILITY ANALYSIS OF EXCAVATION PROBLEMS

A Dissertation

by

JUN KYUNG PARK

Submitted to the Office of Graduate Studies of
Texas A&M University
in partial fulfillment of the requirements for the degree of

DOCTOR OF PHILOSOPHY

August 2011

Major Subject: Civil Engineering

Adaptive Reliability Analysis of Excavation Problems

ADAPTIVE RELIABILITY ANALYSIS OF EXCAVATION PROBLEMS

A Dissertation

by

JUN KYUNG PARK

Submitted to the Office of Graduate Studies of
Texas A&M University
in partial fulfillment of the requirements for the degree of

DOCTOR OF PHILOSOPHY

Approved by:

Co-Chairs of Committee,	Giovanna Biscontin
	Paolo Gardoni
Committee Members,	Jean-Louis Briaud
	Thomas E. Wehrly
Head of Department,	John Niedzwecki

August 2011

Major Subject: Civil Engineering

ABSTRACT

Adaptive Reliability Analysis of Excavation Problems. (August 2011)

Jun Kyung Park, B.S.; M.S., Korea University, Seoul, Korea

Co-Chairs of Advisory Committee: Dr. Giovanna Biscontin
Dr. Paolo Gardoni

Excavation activities like open cutting and tunneling work may cause ground movements. Many of these activities are performed in urban areas where many structures and facilities already exist. These activities are close enough to affect adjacent structures. It is therefore important to understand how the ground movements due to excavations influence nearby structures.

The goal of the proposed research is to investigate and develop analytical methods for addressing uncertainty during observation-based, adaptive design of deep excavation and tunneling projects. Computational procedures based on a Bayesian probabilistic framework are developed for comparative analysis between observed and predicted soil and structure response during construction phases. This analysis couples the adaptive design capabilities of the observational method with updated reliability indices, to be used in risk-based design decisions.

A probabilistic framework is developed to predict three-dimensional deformation profiles due to supported excavations using a semi-empirical approach. The key advantage of this approach for practicing engineers is that an already common semi-empirical chart can be used together with a few additional simple calculations to better

evaluate three-dimensional displacement profiles. A reliability analysis framework is also developed to assess the fragility of excavation-induced infrastructure system damage for multiple serviceability limit states.

Finally, a reliability analysis of a shallow circular tunnel driven by a pressurized shield in a frictional and cohesive soil is developed to consider the inherent uncertainty in the input parameters and the proposed model. The ultimate limit state for the face stability is considered in the analysis. The probability of failure that exceeding a specified applied pressure at the tunnel face is estimated. Sensitivity and importance measures are computed to identify the key parameters and random variables in the model.

DEDICATION

To my parents:

Kwanghee Park and Geumyeon Kim

To my parents-in-law:

Panjoong Kim and Youngsoon Koh

My two sons:

Daniel Minho Park and Dylan Kyungho Park

And my wife:

Kangmi Kim

ACKNOWLEDGEMENTS

I would like to express my sincere gratitude to Dr. Giovanna Biscontin and Dr. Paolo Gardoni for their guidance and support throughout the course of this research. I am deeply impressed with their knowledge, ideas, care, encouragement, valuable suggestion, challenges and philosophy of life. I also want to extend my thanks to Dr. Jean-Louis Briaud and Dr. Thomas E. Wehrly for their time, suggestions and critical reviews of this dissertation.

Thanks also go to my friends and colleagues and the department faculty and staff for making my time at Texas A&M University a wonderful experience.

I am greatly indebted to the Graduate Studies Abroad Program Scholarship (Korea Science and Engineering Foundation Grant funded by the Korea government (MOST) (No. D00346)) and the Eisenhower Graduate Fellowship (United States Department of Transportation, Federal Highway Administration) which sponsored this research and provided the financial support for my research studies.

Last, but not least, I would like to express my deep gratitude to my parents and parents-in-law for their unconditional love and support. Of all people, I am most grateful to my wife, Kangmi, and my two sons for their patience, encouragement and love.

TABLE OF CONTENTS

Page

Page

Page

LIST OF FIGURES

Page

Page

Page

Page

LIST OF TABLES

Page

Page

Page

1. INTRODUCTION

1.1 Background

Excavation activities like open cutting and tunneling work may cause ground movements. Many of these activities are performed in urban areas where many structures and facilities already exist. These activities are close enough to affect adjacent structures. It is therefore important to understand how the ground movements due to excavations influence nearby structures. This mechanism can be explained in the following figure for each type of different excavation.

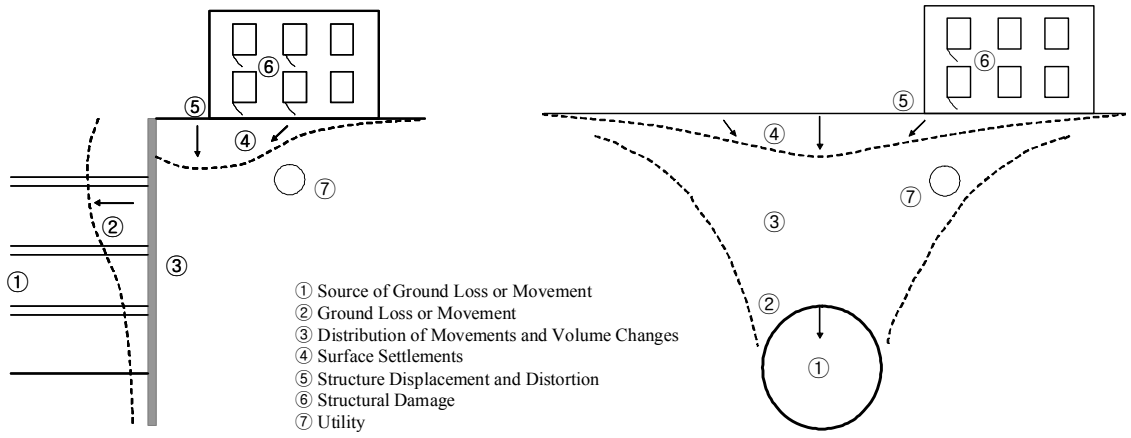

(a) Supported excavation (b) Tunnel excavation

Figure 1.1 Ground movements and building damages due to excavation (Modified from Cording 1985)

This dissertation follows the style of the *Journal of Geotechnical and Geoenvironmental Engineering.*

Construction of supported excavation systems inevitably causes horizontal wall deflections and ground movements including surface settlement as shown in Figure 1.1(a). A major concern with deep excavation projects is the potentially large ground deformations in and around the excavation, which might cause damage to the adjacent buildings and utilities. The observational method (Peck 1969) of design in geotechnical engineering is a valuable tool for addressing soil and structural uncertainties during subsurface construction projects. In the observational method, project design and construction sequences are evaluated and revised as necessary based on comparisons between observed and predicted responses. Traditionally, several empirical and semi-empirical methods have been used to estimate the excavation-induced maximum wall deflection (Mana and Clough 1981; Hashash and Whittle 1996; Kung et al. 2007) and the surface settlement profile (Mana and Clough 1981; Hashash and Whittle 1996; Kung et al. 2007). It is, however, not practical to incorporate all possible factors in a simplified empirical and semi-empirical model for excavation-induced wall and ground deformations. Additionally, past works have suffered from important limitations; some of them are related to the difficulties of implementing an automated inverse analysis technique during execution of the geotechnical works.

In terms of tunneling-induced ground movements, the relationship between surface settlements which affect adjacent structures and tunnel depth is neither simple nor linear. In reality, ground movements due to tunnel excavation depend on a number of factors including geological and geotechnical conditions, tunnel geometry and depth, excavation methods, and the quality of workmanship. It is however clear that a shallow

tunnel tends to have a greater effect on surface structures than a deep one. In weaker ground conditions, the failure zone may propagate towards the ground ahead of the tunnel face. A good appreciation of the probability of failure at the tunnel face is essential, both from the standpoint of providing a safe working environment and of evaluating the probability for large settlements to occur, given that ground movement at the face accounts for the majority of tunneling induced surface settlements. Analytical and limit based methods have been developed (Atkinson and Potts 1977; Davis et al. 1980; Leca and Dormieux 1990) to calculate the optimum supporting pressure, which avoids face collapse (active failure) and surface 'blow-out' (passive failure). A reasonable agreement was found between the theoretical upper bound estimates and the measured face pressures at failure from centrifuge tests in frictional soil (Leca and Dormieux 1990). However, general solutions that consider the strength characteristics of normally consolidated (NC) clays and the influence of seepage forces have not been reported.

Furthermore, supported excavation and tunneling projects related to urban redevelopment and infrastructure improvement are often governed by serviceability-based criteria, rather than failure prevention. However, recent applications of reliability concepts toward excavation system design have mainly focused on assessing the stability of the structure itself (Schweiger and Peschl 2005; Xu and Low 2006; Goh et al. 2008).

The goal of the proposed research is to investigate and develop analytical methods for addressing uncertainty during observation-based, adaptive design of deep excavation and tunneling projects. Computational procedures based on a Bayesian

probabilistic framework are developed for comparative analysis between observed and predicted soil and structure response during construction phases. This analysis will couple the adaptive design capabilities of the observational method with updated reliability indices, to be used in risk-based design decisions.

1.2 Research Objectives

The main goal of this study is to develop analytical methods to assess the reliability and account for the uncertainties during deep excavation and tunneling projects. In particular, the following objectives are addressed:

Objective 1: Develop a probabilistic framework for estimating soil properties and deformations for supported excavation

Develop a Bayesian probabilistic framework to assess soil properties and better predict excavation-induced deformations using field information data. Probabilistic models to provide an accurate and unbiased model will be developed to account for the underlying uncertainties.

Objective 2: Develop reliability assessment technique considering both stability and serviceability performance

Combine a system reliability analysis technique with the finite element method to assess both stability and serviceability performance of braced excavation wall systems in probabilistic terms.

Objective 3: Assess fragility estimates for the staged excavation systems

Develop an adaptive reliability analysis framework based on a semi-empirical method to assess the fragility of infrastructure adjacent to deep excavations for multiple serviceability criteria.

Objective 4: Validate probabilistic model and reliability estimates using case histories

Validate all newly developed probabilistic frameworks with measurements of field deformation data for several supported excavation sites.

Objective 5: Develop upper bound solution for tunnel face stability

Develop a general upper bound solution for the pressurized shield tunnel face stability that combines both the depth-dependence of the effective cohesion (c') of normally consolidated (NC) clays and the influence of seepage into the shallow circular tunnel.

Objective 6: Assess fragility estimates for tunnel face stability

Develop a probabilistic stability analysis for tunnel face stability and a reliability analysis framework to assess the probability that specified threshold design stability criteria are exceeded.

1.3 Organization of Dissertation

The dissertation is composed of the eight sections, each containing a journal paper.

In Section 2, a probabilistic methodology is developed to estimate soil properties and model uncertainty to better predict deformations during supported excavations. A Bayesian approach is used to assess the unknown soil properties by updating pertinent prior information based on field measurement data. The proposed method provides up-to-date predictions that reflect all sources of available information, and properly account for of the underlying uncertainty. The title of the corresponding paper is "Estimating Soil Properties and Deformations during Staged Excavations — I. A Bayesian Approach" and submitted to the *Computers and Geotechnics*.

In Section 3, the application of a newly developed Bayesian probabilistic method to estimate the soil properties and predict the deformations in two supported excavation case histories is presented. The two well documented case histories are the Lurie Research Center excavation project in Evanston, Illinois and the Caobao subway excavation project in Shanghai. The title of the corresponding paper is "Estimating Soil Properties and Deformations during Staged Excavations — II. Application to Case Histories" and submitted to the *Computers and Geotechnics*.

In Section 4, a Bayesian framework is proposed to predict the ground movements using a semi-empirical approach and to update the predictions in the later stages of excavation based on recorded deformation measurements. The predictions are probabilistic and account for the relevant uncertainties. As an application, the proposed framework is used to predict the three-dimensional deformation shapes at four incremental excavation stages of an actual supported excavation project. The developed approach can be used for the design of optimal revisions of supported excavation

systems based on simple calculations rather than complex finite element analysis. The corresponding paper titled "A Bayesian Framework to Predict Deformations During Supported Excavations Using a Semi-empirical Approach" is currently under preparation for submission.

In Section 5, an approach to conduct a probabilistic assessment of infrastructure damage including buildings, bridges, and utility pipelines due to excavation works in a complex urban area. A Bayesian framework based on a semi-empirical method developed in Section 4 is used to update the predictions of ground movements in the later stages of excavation based on the field measurements. The system fragility of infrastructure adjacent to excavation works is computed by Monte Carlo Simulation (MCS) employing the component fragility of each infrastructure and the identified correlation coefficients. An example is presented to show how the system reliability for multiple serviceability limit states can be assessed. Sensitivity and importance measures are also computed to identify the key components, unknown parameters and random variables in the model for an optimal design of the excavation works. The corresponding paper titled "Reliability Analysis of Infrastructure Adjacent to Deep Excavations" is currently under preparation for submission.

In Section 6, a system reliability analysis technique with the finite element method to assess both stability and serviceability performance of braced excavation wall systems in probabilistic terms is developed. The title of the corresponding paper is "Reliability assessment of excavation systems considering both stability and serviceability performance" and was published in the *Georisk*, 1(3).

In Section 7, a general upper bound solution for the pressurized shield tunnel face stability that combines both the depth-dependence of the effective cohesion (c') of normally consolidated (NC) clays and the influence of seepage into the shallow circular tunnel is developed. The reliability analysis framework to assess the probability that specified threshold design stability criteria are exceeded is developed. The corresponding paper titled "Reliability Analysis of Tunnel Face Stability Considering Seepage and Strength Increase with Depth" is currently under preparation for submission.

Finally, in Section 8, the conclusions are included.

2. ESTIMATING SOIL PROPERTIES AND DEFORMATIONS DURING STAGED EXCAVATIONS — I. A BAYESIAN APPROACH

Numerical simulation of staged construction in excavation problems is generally used to estimate the induced ground deformations. During construction it is desirable to obtain accurate estimates of anticipated ground deformations especially in later construction stages when the excavation is deeper. This section presents a Bayesian probabilistic framework to assess soil properties and model uncertainty to better predict excavation-induced deformations both in the horizontal and vertical directions. A Bayesian updating is used to assess the unknown soil properties based on field measurement data and pertinent prior information. The proposed approach properly accounts for the prevailing uncertainties, including model, measurement errors, and statistical uncertainty. The potential correlations between deformations at different depths are accounted for in the likelihood function, which is needed in the Bayesian approach, using unknown model parameters. The posterior statistics of the unknown soil properties and model parameters are computed using an adaptive Markov Chain Monte Carlo (MCMC) simulation method. Markov chains are generated with the likelihood formulation of the probabilistic model based on initial points and a prior distribution until a convergence criterion is met. As an illustration of the proposed approach, the soil properties and deformations during an example supported excavation project are estimated.

2.1 Introduction

Construction of supported excavation systems inevitably causes horizontal wall deflections and ground movements including surface settlements. The observational method (Schweiger and Peschl 2005; Xu and Low 2006; Goh et al. 2008) has been used to address the uncertainties associated with design and construction of geotechnical projects. In the observational method, project design and construction sequences are evaluated and revised as necessary based on comparisons between observed and predicted responses.

Once soil properties are estimated, the induced ground movements due to the excavation are typically predicted by empirical/semi-empirical methods or numerical simulations. Several empirical/semi-empirical methods have been used to estimate the excavation-induced maximum wall deflection (Peck 1969) and surface settlement profile (Mana and Clough 1981; Hashash and Whittle 1996). It is, however, not possible to incorporate all influential factors, such as excavation width/depth, strut spacing, wall stiffness/preloading, adjacent surcharge, soil stiffness, and groundwater, in a simplified empirical/semi-empirical model for excavation-induced wall and ground deformations. More recently, numerical simulations have become more common since they can be more accurate and they can better capture the effect of the main influential factors. Finno and Calvello (Clough and O'Rourke 1990; Hsieh and Ou 1998) developed an automated inverse method to evaluate soil properties based on field measurements from previous excavation stages for a finite element analysis of a deep excavation. This procedure allows engineers to revise predictions of soil response and determine the

influence of individual constitutive parameters based on an optimization technique that uses a weighted least-square objective function.

Although the observational method has been successfully implemented in actual geotechnical engineering projects, it still has limitations. The observational method (1) cannot objectively account for engineering judgment and experience, and information from previous excavations, (2) might be biased because of the bias inherent in the calculations, and (3) is deterministic and does not capture the underlying uncertainties. Because of the last two limitations, the observational method cannot be used to assess probabilities of failure and for a reliability-based design.

A field engineer would benefit from having a prediction method that (1) properly account for all sources of information, objective and subjective, (2) can provide unbiased predictions of deflections and settlements of excavation system, and (3) incorporates the underlying uncertainty, and provides credible intervals around these predictions to assess the confidence the field engineer should have in the predictions. Such method would allow for the assessment of the probability of failure of supported excavations and for a reliability-based design.

This section addresses these needs by developing a Bayesian framework to assess soil properties accounting for the available sources of information and the underlying uncertainties. The soil properties are updated after each excavation stage. The updated properties are then used to develop new and more accurate predictions of the excavation-induced horizontal deformations and surface settlements in the subsequent stages until the end of the excavation project. The posterior statistics of the unknown properties and

additional model parameters are computed using the DRAM (Delayed Rejection Adaptive Metropolis) method, which is an adaptive Markov Chain Monte Carlo (MCMC) simulation technique that combines the Delayed Rejection (DR) method and the Adaptive Metropolis (AM) method.

This section is composed of five subsections. Following this introduction, we discuss the formulation of the probabilistic framework and the Bayesian model updating. Next, we introduce the MCMC method to calculate the posterior statistics of the unknown properties and model parameters. Finally, as an application, the proposed framework is used to assess the moduli of elasticity of multiple soil layers for an example excavation, using both horizontal displacement and surface settlement data at different locations for four incremental excavation stages.

2.2 Probabilistic Model Formulation

A probabilistic model to predict the deformation of the soil for the kth excavation stage at the ith location, D_{ki}, at a depth/location, z_i, can be written as

$$D_{ki}(z_i) = \hat{d}_{ki}(\boldsymbol{\theta}; z_i) + \sigma\varepsilon_{ki}, \quad k = 1,\ldots,m, \quad i = 1,\ldots,(n_V + n_H) \tag{2.1}$$

where $\hat{d}_{ki}$ = the mean of the deformation estimate, $\boldsymbol{\theta} = (\theta_1,\ldots,\theta_n)$ = a set of unknown model parameters, $\sigma\varepsilon_{ki}$ = the model error, σ = the unknown standard deviation of the model error, ε_{ki} = a random variable with zero mean and unit variance, n_V = the number of points where the surface settlement is predicted, and n_H = the number of points where

the horizontal displacement is predicted. The correlation coefficients between ε_{ki} and ε_{kj} of any two horizontal displacements, ρ_H, any two surface settlements, ρ_V, and an horizontal displacement and a surface settlement, ρ_{VH}, all within the same excavation stage k, are additional unknown model parameters. Therefore, the correlation matrix for the kth excavation stage with $(n_V + n_H)$ prediction points can be written as

$$\mathbf{R} = \left(\begin{array}{c|c} \mathbf{R}_V & \mathbf{R}_{VH} \\ \hline \mathbf{R}_{HV} & \mathbf{R}_H \end{array} \right)_{(n_V+n_H)\times(n_V+n_H)} \tag{2.2}$$

where

$$\mathbf{R}_V = \begin{pmatrix} 1 & \cdots & \rho_V & \cdots & \rho_V \\ & \ddots & \vdots & & \vdots \\ & & 1 & \cdots & \rho_V \\ & \text{sym.} & & \ddots & \vdots \\ & & & & 1 \end{pmatrix}_{n_V \times n_V} \qquad \mathbf{R}_H = \begin{pmatrix} 1 & \cdots & \rho_H & \cdots & \rho_H \\ & \ddots & \vdots & & \vdots \\ & & 1 & \cdots & \rho_H \\ & \text{sym.} & & \ddots & \vdots \\ & & & & 1 \end{pmatrix}_{n_H \times n_H}$$

$$\mathbf{R}_{VH} = \begin{pmatrix} \rho_{VH} & \cdots & \rho_{VH} & \cdots & \rho_{VH} \\ & \ddots & \vdots & & \vdots \\ & & \rho_{VH} & \cdots & \rho_{VH} \\ & \text{sym.} & & \ddots & \vdots \\ & & & & \rho_{VH} \end{pmatrix}_{n_V \times n_H} \tag{2.3}$$

The covariance matrix of the model errors, $\boldsymbol{\Sigma}$, can be written as $\boldsymbol{\Sigma} = \mathbf{SRS}$, where $\mathbf{S}$ = the diagonal matrix of standard deviations σ. Finally, $\boldsymbol{\Theta} = (\boldsymbol{\theta}, \boldsymbol{\Sigma})$ denotes the set of all unknown parameters in Eq. (2.1). Note that for given z_i, $\boldsymbol{\theta}$ and σ, $\text{Var}[D_{ki}(z_i)] = \sigma^2$ is the variance of the model. In assessing the probabilistic model, three assumptions are made: (a) the model variance σ^2 is independent of z_i

(homoskedasticity assumption), (b) ε_{ki} follows the normal distribution (normality assumption), and (c) ε_{ki} and ε_{qj} at two different excavation stages ($k \neq q$) are uncorrelated. These assumptions are verified by using diagnostic plots (Rao and Toutenburg 1999) of the data or the residuals versus the model predictions.

2.3 Uncertainties in Model Assessment and Predictions

Uncertainties are present in formulating, assessing and using a model for prediction purposes (Gardoni et al. 2002). Uncertainties can be classified as aleatory (which are not reducible and arise from the inherent randomness) and epistemic (which are reducible and arise from the limited available data and knowledge). In our model formulation, aleatory uncertainty is present both in the soil/structural properties and in the error term ε_{ki}. The epistemic uncertainties can be eliminated by using improved models, increasing the number of data and introducing advanced measurements devices or procedures. This uncertainty is present in the model parameters $\boldsymbol{\Theta}$ and partly in the error term ε_{ki}. Next, following Gardoni et al. (2002), we describe three specific types of epistemic uncertainties.

2.3.1 Model inexactness

This type of uncertainty arises when approximations are introduced in the estimation of the deformations. It has two essential components: error in the form of the model (e.g., finite size of the finite element mesh) and missing variables (i.e., the estimate is

calculated by only a subset of the variables that influence the quantity of interest). The error due to the inexact model form and the effect of the missing variables are captured by the error term $\sigma\varepsilon_{ki}$. The model inexactness has both an aleatory and an epistemic component.

2.3.2 Measurement error

This uncertainty arises from errors inherent in the measurement of the deformations during the excavation process. For example, the measured values could be inexact due to human errors in following a measurement procedure or accuracy errors of the device(s) used. In theory, the statistics of the measurement errors can be obtained through calibration of the measurement procedure. The mean values of these errors represent biases in the measurements (systematic error), whereas their variances represent the inherent uncertainties.

In our formulation, the model parameters $\boldsymbol{\Theta}$ are assessed or updated after each excavation stage by use of the measurements $\hat{\mathbf{D}}_k = (\hat{D}_{k1}, \ldots, \hat{D}_{k\,(n_V+n_H)})$ of the corresponding predicted variables at different locations $\hat{\mathbf{z}} = (\hat{z}_1, \ldots, \hat{z}_{(n_V+n_H)})$. These measured values, however, could be inexact due to errors in the measurements. To model these errors, we let $\mathbf{D}_k = \hat{\mathbf{D}}_k + \mathbf{e}_{\mathbf{D}k}$ and $\mathbf{z} = \hat{\mathbf{z}} + \mathbf{e}_{\mathbf{z}}$ be the true deformation and location values for the kth excavation stage, where $\hat{\mathbf{D}}_k$ and $\hat{\mathbf{z}}$ are the measured values, and $\mathbf{e}_{\mathbf{D}k}$ and $\mathbf{e}_{\mathbf{z}}$ are the respective measurement errors. In most cases, the random variables $\mathbf{e}_{\mathbf{D}k}$ and $\mathbf{e}_{\mathbf{z}}$ can be assumed to be statistically independent and normally

distributed. The uncertainty arising from measurement errors is epistemic, and can be reduced by using more accurate measurement devices or procedures.

2.3.3 Statistical uncertainty

Statistical uncertainty is due to the sparseness of the data and can be reduced by gathering more data. If additional data cannot be collected, then one must properly account for the effects of this uncertainty in all predictions and interpretations of the results. In particular, the accuracy of a statistical inference depends on the observation sample size. The smaller is the sample size, the larger is the uncertainty in the estimated values of the parameters.

2.4 Bayesian Model Updating

The proposed probabilistic approach uses a Bayesian formulation to incorporate all types of available information, including mathematical models, field measurements, and subjective engineering experience and judgment. In the Bayesian approach, the likelihood function is used to update the prior distribution of a vector of unknown parameters $\boldsymbol{\Theta}$ using the following rule (Gardoni et al. 2002):

$$p\left(\boldsymbol{\Theta}\middle|\mathbf{D}_k\right) = \kappa\, L\left(\boldsymbol{\Theta}\middle|\mathbf{D}_k\right) p\left(\boldsymbol{\Theta}\right) \tag{2.4}$$

where $p(\boldsymbol{\Theta}\,|\,\mathbf{D}_k)$ = the posterior distribution of $\boldsymbol{\Theta}$ that incorporates all the information from the prior distribution and the likelihood function, $L(\boldsymbol{\Theta}\,|\,\mathbf{D}_k)$ = the likelihood function representing the objective information on $\boldsymbol{\Theta}$ contained in a set of the

measurement data $\mathbf{D}_k$, $p(\boldsymbol{\Theta}) =$ the prior distribution reflecting our state of knowledge about $\boldsymbol{\Theta}$ before the measurement data is available, and $\kappa = [\int L(\boldsymbol{\Theta} \mid \mathbf{D}_k)\, p(\boldsymbol{\Theta}) d\boldsymbol{\Theta}]^{-1} =$ the normalizing factor.

One significant virtue of the Bayesian framework is that updating a model can be repeated when new observations become available. For staged excavation projects, this feature allows updating the estimates of $\boldsymbol{\Theta}$ as new deformation data from subsequent excavations stages become available. For example, if an initial set of measurement data, $\mathbf{D}_1$, is available after the first excavation stage, then application of the Bayes' formula gives

$$p\left(\boldsymbol{\Theta} \middle| \mathbf{D}_1\right) \propto p\left(\boldsymbol{\Theta}\right) L\left(\boldsymbol{\Theta} \middle| \mathbf{D}_1\right) \tag{2.5}$$

If a second sample of measurements, $\mathbf{D}_2$, becomes available, we can update $p(\boldsymbol{\Theta} \mid \mathbf{D}_1)$ to account for the new information as

$$p\left(\boldsymbol{\Theta} \middle| \mathbf{D}_1, \mathbf{D}_2\right) \propto p\left(\boldsymbol{\Theta}\right) L\left(\boldsymbol{\Theta} \middle| \mathbf{D}_1\right) L\left(\boldsymbol{\Theta} \middle| \mathbf{D}_2\right) \propto p\left(\boldsymbol{\Theta} \middle| \mathbf{D}_1\right) L\left(\boldsymbol{\Theta} \middle| \mathbf{D}_2\right) \tag{2.6}$$

Eqs. (2.5) and (2.6) are applications of Eq. (2.4) where the posterior distribution in Eq. (2.4) now plays the role of the prior distribution in Eq. (2.6). In writing Eq. (2.6) we assumed that $\mathbf{D}_2$ and $\mathbf{D}_1$ are statistically independent sets of deformation measurements. Given m sets of independent deformation measurements, the posterior distribution can be updated after each new set of measurement data become available. That is, the likelihood associated with the kth sample is combined with the posterior

distribution of $\boldsymbol{\Theta}$ that accounts for the information content of the previous $(k-1)$ samples. Mathematically, we can write

$$p\left(\boldsymbol{\Theta}\middle|\mathbf{D}_1,\ldots,\mathbf{D}_k\right) \propto p\left(\boldsymbol{\Theta}\middle|\mathbf{D}_1,\ldots,\mathbf{D}_{k-1}\right) L\left(\boldsymbol{\Theta}\middle|\mathbf{D}_k\right) \qquad k=2,\ldots,m \tag{2.7}$$

where $p(\boldsymbol{\Theta}\,|\,\mathbf{D}_1)$ is given as in Eq. (2.5). Eq. (2.7) can be used to repeatedly update our current knowledge about $\boldsymbol{\Theta}$, as the new set of measurement data become available.

2.4.1 Objective information – likelihood functions

The objective information is entered through the likelihood function, $L(\boldsymbol{\Theta}\,|\,\mathbf{D}_k)$. The likelihood function describes the probability of a set of measurement data $\mathbf{D}_k$ for given values of the model parameters $\boldsymbol{\Theta}$. Here, we start by considering the case of exact measurements. The effect of measurement error is then incorporated in an approximate manner. Using Eq. (2.1) we can define $\mathbf{r}_k(\boldsymbol{\theta}) = [r_{k1}(\boldsymbol{\theta}),\ldots,r_{k(n_V+n_H)}(\boldsymbol{\theta})]$ where $r_{ki}(\boldsymbol{\theta}) = [D_{ki}(z_i) - \hat{d}_{ki}(\boldsymbol{\theta};z_i)]$. The likelihood function can then be written as

$$L\left(\boldsymbol{\Theta}\middle|\mathbf{D}_k\right) \propto P\left\{\bigcap_{i=1}^{(n_V+n_H)}\left[\sigma\varepsilon_{ki} = r_{ki}\left(\boldsymbol{\theta}\right)\right]\right\} \tag{2.8}$$

Using the transformation rule (Ang and Tang 2007),

$$
\begin{aligned}
&P\left\{\bigcap_{i=1}^{(n_V+n_H)}\left[\sigma\varepsilon_{ki}=r_{ki}\left(\boldsymbol{\theta}\right)\right]\right\}=\left|\frac{\partial(\varepsilon_{k1},\ldots,\varepsilon_{k(n_V+n_H)})}{\partial(D_{k1},\ldots,D_{k(n_V+n_H)})}\right|f_{\mathbf{E}}\left[\frac{\mathbf{r}_k\left(\boldsymbol{\theta}\right)}{\sigma}\right]\\
&=\left|J_{\boldsymbol{\varepsilon}k,\mathbf{D}k}\right|\times f_{\mathbf{E}}\left[\frac{\mathbf{r}_k\left(\boldsymbol{\theta}\right)}{\sigma}\right]=\left|J_{\mathbf{D}k,\boldsymbol{\varepsilon}k}\right|^{-1}\times f_{\mathbf{E}}\left[\frac{\mathbf{r}_k\left(\boldsymbol{\theta}\right)}{\sigma}\right]\\
&=\left|J_{\mathbf{D}k,\boldsymbol{\varepsilon}k}\right|^{-1}\times\left(2\pi\right)^{-(n_V+n_H)/2}\left|\mathbf{R}\right|^{-1/2}\exp\left\{-\frac{1}{2}\left[\frac{\mathbf{r}_k\left(\boldsymbol{\theta}\right)}{\sigma}\right]^T\mathbf{R}^{-1}\left[\frac{\mathbf{r}_k\left(\boldsymbol{\theta}\right)}{\sigma}\right]\right\}\\
&=\sigma^{-(n_V+n_H)}\left(2\pi\right)^{-(n_V+n_H)/2}\left|\mathbf{R}\right|^{-1/2}\exp\left\{-\frac{1}{2}\left[\frac{\mathbf{r}_k\left(\boldsymbol{\theta}\right)}{\sigma}\right]^T\mathbf{R}^{-1}\left[\frac{\mathbf{r}_k\left(\boldsymbol{\theta}\right)}{\sigma}\right]\right\}
\end{aligned}
\tag{2.9}
$$

where $f_{\mathbf{E}}[\cdot]=$ the joint probability density function (PDF) of $\sigma\varepsilon_{ki}$ for $i=1,\ldots,n_V+n_H$, $n_V+n_H=$ the sample size, $|\cdot|=$ the determinant, $[\cdot]^T=$ the transpose, and $J_{\cdot,\cdot}=$ the Jacobian defined as

$$
J_{\mathbf{D}k,\boldsymbol{\varepsilon}k}=\begin{bmatrix}\frac{\partial D_{k1}}{\partial\varepsilon_{k1}} & \cdots & \frac{\partial D_{k1}}{\partial\varepsilon_{k(n_V+n_H)}}\\ \vdots & \ddots & \vdots\\ \frac{\partial D_{k(n_V+n_H)}}{\partial\varepsilon_{k1}} & \cdots & \frac{\partial D_{k(n_V+n_H)}}{\partial\varepsilon_{k(n_V+n_H)}}\end{bmatrix}\qquad \left|J_{\mathbf{D}k,\boldsymbol{\varepsilon}k}\right|=\sigma^{(n_V+n_H)} \tag{2.10}
$$

Finally, the likelihood function can be written as

$$
L\left(\boldsymbol{\Theta}\middle|\mathbf{D}_k\right)\propto\sigma^{-(n_V+n_H)}\left(2\pi\right)^{-(n_V+n_H)/2}\left|\mathbf{R}\right|^{-1/2}\exp\left[-\frac{1}{2\sigma^2}\mathbf{r}_k^T\left(\boldsymbol{\theta}\right)\mathbf{R}^{-1}\mathbf{r}_k\left(\boldsymbol{\theta}\right)\right] \tag{2.11}
$$

2.4.2 Subjective information – prior distributions

The prior distribution $p(\boldsymbol{\Theta})$ should be constructed using the knowledge available before the observations used to construct the likelihood function are made. If there is no

existing information, a noninformative prior should be used reflecting that nothing or little is known a priori. Assuming that $\boldsymbol{\theta}$ and $\boldsymbol{\Sigma}$ are approximately independent, the prior distribution can be written as

$$p(\boldsymbol{\Theta}) \approx p(\boldsymbol{\theta})\, p(\boldsymbol{\Sigma}) \tag{2.12}$$

Gardoni et al. (2002) have shown that the noninformative prior for $\boldsymbol{\Sigma}$ can be written as

$$p(\boldsymbol{\Sigma}) \propto \left|\mathbf{R}\right|^{-\left[(n_V+n_H)+1\right]/2} \prod_{i=1}^{(n_V+n_H)} \frac{1}{\sigma_i} \tag{2.13}$$

Furthermore, when the model is linear in $\boldsymbol{\theta}$, a uniform prior can be used as the noninformative prior for $p(\boldsymbol{\theta})$ so that $p(\boldsymbol{\Theta}) \approx p(\boldsymbol{\Sigma})$ (Box and Tiao 1992). However, when a probabilistic model is a nonlinear function of $\boldsymbol{\theta}$, a uniform distribution might not be noninformative. In this case, an approximate noninformative prior can be developed using Jeffreys' rule (Jeffreys 1961). According to Jeffreys' rule, an approximate noninformative prior distribution of $\boldsymbol{\theta}$ is proportional to the positive square root of the determinant of the information matrix, $\mathbf{I}(\boldsymbol{\theta})$.

The information matrix is the expected value of the negative of the Hessian (the matrix of the second partial derivatives) of the natural logarithm of the likelihood function with respect to $\boldsymbol{\theta}$. Hence, the Jeffreys' approximate noninformative prior for $\boldsymbol{\theta}$ can be written as

$$p(\boldsymbol{\theta}) \propto \left|\mathbf{I}(\boldsymbol{\theta})\right|^{1/2} = \left| E_{\mathbf{D}_k|\boldsymbol{\theta}}\left[-\frac{\partial^2 \log L\left(\boldsymbol{\Theta}\middle|\mathbf{D}_k\right)}{\partial\boldsymbol{\theta}\partial\boldsymbol{\theta}^T} \right] \right|^{1/2}$$

$$= \left| \int_{(n_V+n_H)} \cdots \int -\frac{\partial^2 \log L\left(\boldsymbol{\Theta}\middle|\mathbf{D}_k\right)}{\partial\boldsymbol{\theta}\partial\boldsymbol{\theta}^T} \cdot f_{\mathbf{D}_k|\boldsymbol{\theta}}\left(\mathbf{D}_k\middle|\boldsymbol{\theta}\right) d\mathbf{D}_k \right|^{1/2} \tag{2.14}$$

$$= \left| \int_{(n_V+n_H)} \cdots \int \frac{\partial^2 \left[\frac{1}{2\sigma^2} \mathbf{r}_k^T(\boldsymbol{\theta}) \mathbf{R}^{-1} \mathbf{r}_k(\boldsymbol{\theta}) \right]}{\partial\boldsymbol{\theta}\partial\boldsymbol{\theta}^T} \cdot f_{\mathbf{D}_k|\boldsymbol{\theta}}\left(\mathbf{D}_k\middle|\boldsymbol{\theta}\right) d\mathbf{D}_k \right|^{1/2}$$

where $E_{\mathbf{D}_k|\boldsymbol{\theta}}[\cdot] =$ the conditional expected value.

2.4.3 Posterior distributions

The prior distribution, $p(\boldsymbol{\Theta})$, is updated into the posterior distribution, $p(\boldsymbol{\Theta} \mid \mathbf{D}_k)$, using the Bayes' theorem in Eq. (2.4). This updating combines the objective information in $L(\boldsymbol{\Theta} \mid \mathbf{D}_k)$ with the prior information in $p(\boldsymbol{\Theta})$ creating a compromise between the two sets of information. As the sample size increases, this compromise is gradually governed by the observed data. Obtaining the posterior distribution required integrating the Bayesian kernel, $L(\boldsymbol{\Theta} \mid \mathbf{D}_k) p(\boldsymbol{\Theta})$, over the range of $\boldsymbol{\Theta}$. This integration is typically not possible in closed form and standard integral approximations perform poorly. We discuss alternative solution strategies in a later subsection.

2.5 Accounting for Measurement Errors

Following Gardoni et al. (2002), measurement errors can be accounted for by modifying the likelihood function as described next. In formulating the new likelihood function, each vector of measurement errors $\mathbf{e}_{\mathbf{D}k}$ and $\mathbf{e}_{\mathbf{z}}$ can be assumed to be jointly normally

distributed with zero means (i.e., the instrumentation has been corrected for any systematic error) and known covariance matrixes $\mathbf{\Sigma}_{\mathbf{D}k}$ and $\mathbf{\Sigma}_{\mathbf{z}}$, respectively. Accounting for the measurement errors, Eq. (2.1) can be rewritten as

$$\hat{\mathbf{D}}_k + \mathbf{e}_{\mathbf{D}k} = \hat{\mathbf{d}}_k\left(\boldsymbol{\theta}; \hat{\mathbf{z}} + \mathbf{e}_{\mathbf{z}}\right) + \sigma\boldsymbol{\varepsilon}_k \tag{2.15}$$

Defining $\hat{\mathbf{r}}_k(\boldsymbol{\theta}; \mathbf{e}_{\mathbf{z}}) = [\hat{r}_{k1}(\boldsymbol{\theta}; \mathbf{e}_{\mathbf{z}}), \ldots, \hat{r}_{k(n_V + n_H)}(\boldsymbol{\theta}; \mathbf{e}_{\mathbf{z}})] = \hat{\mathbf{D}}_k - \hat{\mathbf{d}}_k(\boldsymbol{\theta}; \hat{\mathbf{z}} + \mathbf{e}_{\mathbf{z}})$, Eq (2.15) can be rewritten as $\sigma\boldsymbol{\varepsilon}_k - \mathbf{e}_{\mathbf{D}k} = \hat{\mathbf{r}}_k(\boldsymbol{\theta}; \mathbf{e}_{\mathbf{z}})$. However, the computation of the likelihood function is more difficult than in the case without measurement errors, because $\hat{\mathbf{r}}_k(\boldsymbol{\theta}; \mathbf{e}_{\mathbf{z}})$ is a nonlinear function of the random variables $\mathbf{e}_{\mathbf{z}}$. We can use a first-order approximation to express $\hat{\mathbf{r}}_k(\boldsymbol{\theta}; \mathbf{e}_{\mathbf{z}})$ as a linear function of $\mathbf{e}_{\mathbf{z}}$ under the assumption that the errors $\mathbf{e}_{\mathbf{z}}$ are small in relation to the measurements $\hat{\mathbf{z}}$. Using a Maclaurin series expansion around $\mathbf{e}_{\mathbf{z}} = \mathbf{0}$, we have

$$\hat{\mathbf{r}}_k\left(\boldsymbol{\theta}; \mathbf{e}_{\mathbf{z}}\right) \cong \hat{\mathbf{D}}_k - \hat{\mathbf{d}}_k\left(\boldsymbol{\theta}; \hat{\mathbf{z}}\right) - J_{\hat{\mathbf{r}},\hat{\mathbf{z}}} \cdot \mathbf{e}_{\mathbf{z}} = \hat{\mathbf{r}}_k\left(\boldsymbol{\theta}\right) - J_{\hat{\mathbf{r}},\hat{\mathbf{z}}} \cdot \mathbf{e}_{\mathbf{z}} \tag{2.16}$$

where $\hat{\mathbf{r}}_k(\boldsymbol{\theta}) = \hat{\mathbf{D}}_k - \hat{\mathbf{d}}_k(\boldsymbol{\theta}; \hat{\mathbf{z}})$.

Eq. (2.15) can now be rewritten as $\sigma\boldsymbol{\varepsilon}_k - \mathbf{e}_{\mathbf{D}k} + J_{\hat{\mathbf{r}},\hat{\mathbf{z}}} \cdot \mathbf{e}_{\mathbf{z}} = \hat{\mathbf{r}}_k(\boldsymbol{\theta})$. The left-hand side of this expression is a vector of jointly normal random variables with zero mean and covariance matrix $\hat{\mathbf{\Sigma}} = \mathbf{\Sigma} + \mathbf{\Sigma}_{\mathbf{D}k} + J_{\hat{\mathbf{r}},\hat{\mathbf{z}}}\mathbf{\Sigma}_{\mathbf{z}}J_{\hat{\mathbf{r}},\hat{\mathbf{z}}}^T$, where $\mathbf{\Sigma}_{\mathbf{D}k}$ = the covariance matrix for measurement device errors, $\mathbf{\Sigma}_{\mathbf{z}}$ = the covariance matrix for the misplacement of the measurement device for vertical locations. We can also write as $\hat{\mathbf{\Sigma}} = \hat{\mathbf{S}}\hat{\mathbf{R}}\hat{\mathbf{S}}$, where $\hat{\mathbf{R}}$ =

the revised correlation matrix, $\hat{\mathbf{S}} =$ the diagonal matrix of new standard deviations $\hat{\sigma}$, are written as

$$\hat{\mathbf{R}} = \left(\begin{array}{c|c} \hat{\mathbf{R}}_V & \hat{\mathbf{R}}_{VH} \\ \hline \hat{\mathbf{R}}_{HV} & \hat{\mathbf{R}}_H \end{array} \right)_{(n_V+n_H)\times(n_V+n_H)} \tag{2.17}$$

where

$$\hat{\mathbf{R}}_V = \begin{pmatrix} 1 & \cdots & \hat{\rho}_V & \cdots & \hat{\rho}_V \\ & \ddots & \vdots & & \vdots \\ & & 1 & \cdots & \hat{\rho}_V \\ & \text{sym.} & & \ddots & \vdots \\ & & & & 1 \end{pmatrix}_{n_V \times n_V} \quad \hat{\mathbf{R}}_H = \begin{pmatrix} 1 & \cdots & \hat{\rho}_H & \cdots & \hat{\rho}_H \\ & \ddots & \vdots & & \vdots \\ & & 1 & \cdots & \hat{\rho}_H \\ & \text{sym.} & & \ddots & \vdots \\ & & & & 1 \end{pmatrix}_{n_H \times n_H}$$

$$\hat{\mathbf{R}}_{VH} = \begin{pmatrix} \hat{\rho}_{VH} & \cdots & \hat{\rho}_{VH} & \cdots & \hat{\rho}_{VH} \\ & \ddots & \vdots & & \vdots \\ & & \hat{\rho}_{VH} & \cdots & \hat{\rho}_{VH} \\ & \text{sym.} & & \ddots & \vdots \\ & & & & \hat{\rho}_{VH} \end{pmatrix}_{n_V \times n_H} \tag{2.18}$$

The new correlation coefficients between ε_{ki} and ε_{kj} of any two horizontal displacements, $\hat{\rho}_H$, any two surface settlements, $\hat{\rho}_V$, and an horizontal displacement and a surface settlement, $\hat{\rho}_{VH}$, all within the same excavation stage k, are additional unknown model parameters. The likelihood function can then be rewritten as

$$L\left(\boldsymbol{\Theta} \middle| \hat{\mathbf{D}}_k\right) \propto P\left\{ \bigcap_{i=1}^{(n_V+n_H)} \left[\hat{\sigma}\varepsilon_{ki} = \hat{r}_{ki}\left(\boldsymbol{\theta}\right) \right] \right\} \tag{2.19}$$

Using the transformation rule (Ang and Tang 2007),

$$L\left(\boldsymbol{\Theta}\middle|\hat{\mathbf{D}}_k\right) \propto \sigma^{-(n_V+n_H)}\left(2\pi\right)^{-(n_V+n_H)/2}\left|\hat{\mathbf{R}}\right|^{-1/2}\exp\left\{-\frac{1}{2}\left[\frac{\hat{\mathbf{r}}_k\left(\boldsymbol{\theta}\right)}{\hat{\sigma}}\right]^T\hat{\mathbf{R}}^{-1}\left[\frac{\hat{\mathbf{r}}_k\left(\boldsymbol{\theta}\right)}{\hat{\sigma}}\right]\right\}$$
$$= \sigma^{-(n_V+n_H)}\left(2\pi\right)^{-(n_V+n_H)/2}\left|\hat{\mathbf{R}}\right|^{-1/2}\exp\left\{-\frac{1}{2\hat{\sigma}^2}\hat{\mathbf{r}}_k^T\left(\boldsymbol{\theta}\right)\hat{\mathbf{R}}^{-1}\hat{\mathbf{r}}_k\left(\boldsymbol{\theta}\right)\right\} \tag{2.20}$$

2.5.1 Measurement error of deformation data

Instruments for measuring deformation in the construction of supported excavation systems are installed to verify design assumptions and to effectively monitor ground response for the various construction activities. The vertical inclinometer is generally used to measure the excavation-induced horizontal deformations, and the optical surveying method of pre-installed surface marker is used for the surface settlements.

Vertical inclinometers are instruments used to measure relative horizontal displacements affecting the shape of a guide casing embedded in the ground or structure. Inclinometer probes usually measure displacement in two perpendicular planes to estimate both displacement magnitudes and directions. The guide casing is installed vertically for most applications in order to measure horizontal ground movements. The bottom end of the guide casing serves as a stable reference and must be embedded beyond the displacement zone. However, the inclinometer probe does not provide horizontal movement of the casing directly. The probe measures the tilt of the casing which is converted to a horizontal movement. In Figure 2.1(a), the deviation from vertical, i.e., the horizontal displacement, is determined as $l\sin\alpha$, where $\alpha =$ the angle of tilt measured by the inclinometer probe, and $l =$ the measurement interval (Dunnicliff 1988; Green and Mikkelsen 1988). The total horizontal displacement profile of the

casing can be obtained by summing the individual horizontal displacements from the bottom of the casing to the top, and this summation process is shown as $\Sigma(l_p \sin\alpha_p)$ in Figure 2.1(b).

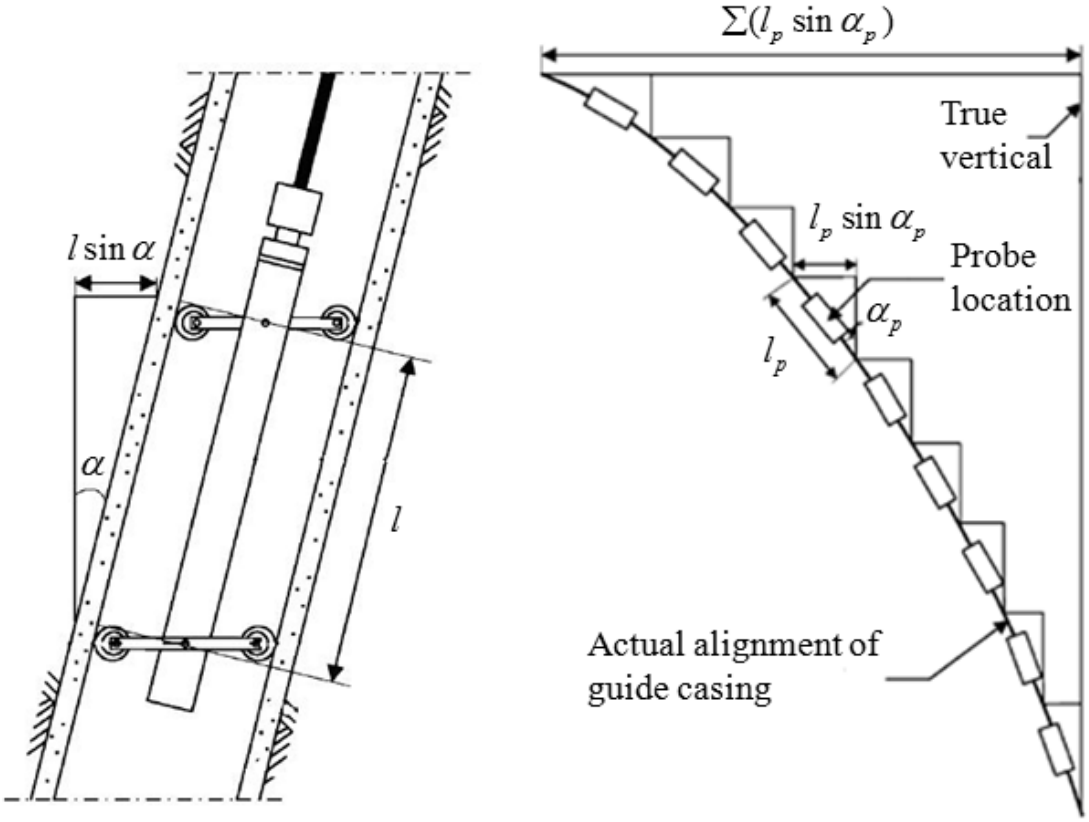

(a) Inclinometer configuration **(b) Illustration of inclinometer operation**

Figure 2.1 Schematic view of the inclinometer probe inserted in casing (Modified from Dunnicliff 1988)

The cumulative horizontal displacement profile provides a representation of the actual deformation pattern. The precision of inclinometer measurements depends on several factors, such as the design of the sensor and quality of the casing, probe, cable, and readout system. Even if all of these factors are addressed, there still can be errors in

the readings. Mikkelsen (2003) indicates that a random error, which is a form of aleatory uncertainty and irreducible, is typically no more than ±0.16 mm for a single reading interval and accumulates at a rate equal to the square root of the number of reading intervals over the entire casing. On the other hand, the systematic error, which is related to the epistemic uncertainty and is reducible, is about ±0.11 mm per reading under controlled laboratory conditions, and it accumulates arithmetically. Finally, the standard deviation of the total error for inclinometer measurements, $\sigma_{\mathbf{D}k}$, is defined as

$$\sigma_{\mathbf{D}k} = 0.16 \times \sqrt{n_H} + 0.11 \times n_H \tag{2.21}$$

where, n_H = the total number of reading intervals.

The measurement accuracy of the optical surveying method for the surface settlements is controlled by the choice and quality of surveying technique and by characteristics of reference datum and measuring points. Even though Finno (2007) summarized the accuracy is ±3.0 mm for the ground surface settlements with optical survey, it is assumed that the error from the ground surface settlement measurements with optical survey is same with that from the inclinometer measurements because detailed information for the quality of surveying technique is not usually available.

2.5.2 Structure of $\Sigma_{\mathbf{D}k}$

Measurement errors are not independent for both inclinometer and optical survey observations along a line. The value of the displacement – and the error associated with

it – is based on all the previously measured displacements. It is useful to express the covariance matrix for inclinometer measurements as

$$\boldsymbol{\Sigma}_{\mathbf{D}k} = \sigma^2_{\mathbf{D}k}\mathbf{E}_{\mathbf{x}} \tag{2.22}$$

where $\sigma^2_{\mathbf{D}k}$ = the scale factor which represent the measurement errors, and $\mathbf{E}_{\mathbf{x}}$ = the error structure of the instrument which depends on the apparatus itself. If the measurements are independent and have the same variance, $\mathbf{E}_{\mathbf{x}}$ will be an identity matrix. As discussed above, the inclinometer measures angle (α_p) representing the deviation from the vertical at fixed depth intervals, and these values are used to compute horizontal displacements. The value α_p is assumed to be small and the horizontal displacement (D_i) is computed as

$$D_i = \sum_{p=1}^{n_H} \sin\alpha_p \cdot l_p + B \approx \sum_{p=1}^{n_H} \alpha_p l_p + B \tag{2.23}$$

where, l_p = the length between two consecutive points of measurement, and B = an integration constant representing the horizontal movement of the initial point. Assuming that the value of B is exactly known, the $\boldsymbol{\Sigma}_{\mathbf{D}k}$ matrix for an inclinometer is

$$\begin{aligned}(\boldsymbol{\Sigma}_{\mathbf{D}k})_{tu} &= \operatorname{cov}\left[D_t, D_u\right] = \operatorname{cov}\left[\sum_{a=1}^{t}\alpha_a l_a, \sum_{b=1}^{u}\alpha_b l_b\right] = \sum_{a=1}^{t}\sum_{b=1}^{u}\operatorname{cov}\left(\alpha_a, \alpha_b\right) l_a l_b \\ &= \sigma^2_{\mathbf{D}k}\sum_{a=1}^{t}\sum_{b=1}^{u} l_a l_b \delta_{ab} = \sigma^2_{\mathbf{D}k}\sum_{a=1}^{\min(t,u)} l_a^2\end{aligned} \tag{2.24}$$

where δ_{ab} = the Kronecker delta. In this study, the $\sigma^2_{\mathbf{D}k}$ for both inclinometer and the surface settlements is assumed to be constant with a value of 25mm^2 for each 30 reading intervals based on Mikkelsen (2003).

2.5.3 Structure of $\boldsymbol{\Sigma}_{\mathbf{z}}$

Since the influence of the inclination of the alignment of the guide casing is negligible $(\sigma_\alpha \approx 0)$, only the effect of the misplacement of the inclinometer $(\boldsymbol{\Sigma}_{\mathbf{z}_0})$ is considered as summarized in Eq. (2.25).

$$
\begin{aligned}
\boldsymbol{\Sigma}_{\mathbf{z}} &= \boldsymbol{\Sigma}_{\alpha} + \boldsymbol{\Sigma}_{\mathbf{z}_0} \\
&= \sigma^2_{\alpha}\begin{pmatrix} z_1/z_{n_H} & \cdots & A & \cdots & A \\ & \ddots & \vdots & & \vdots \\ & & z_i/z_{n_H} & \cdots & A \\ & \text{sym.} & & \ddots & \vdots \\ & & & & z_{n_H}/z_{n_H} \end{pmatrix} + \sigma^2_{\mathbf{z}_0}\begin{pmatrix} 1 & \cdots & 1 & \cdots & 1 \\ & \ddots & \vdots & & \vdots \\ & & 1 & \cdots & 1 \\ & \text{sym.} & & \ddots & \vdots \\ & & & & 1 \end{pmatrix} \\
&\approx \sigma^2_{\mathbf{z}_0}\begin{pmatrix} 1 & \cdots & 1 & \cdots & 1 \\ & \ddots & \vdots & & \vdots \\ & & 1 & \cdots & 1 \\ & \text{sym.} & & \ddots & \vdots \\ & & & & 1 \end{pmatrix}
\end{aligned}
\tag{2.25}
$$

The constant A will depend on the stiffness of the guide casing. It will be 1 if it is rigid, and will be a constant less than 1 if it is not rigid. In this study, the $\sigma^2_{\mathbf{z}_0}$ is assumed to be as constant with value of 50mm^2 based on the literature for horizontal displacements and the surface settlements (Mikkelsen 2003).

2.6 Solution Strategies

Since the proposed model is nonlinear in the unknown parameters, a closed-form solution is not available. In this case, numerical solutions are the only option to compute the posterior statistics and the normalizing constant (Gelman et al. 2004). There are numerous simulation methods in Bayesian inference. Rejection sampling (Robert and Casella 2004) is a general method for simulating from an arbitrary posterior distribution, but it can be difficult to set up since it requires the construction of a suitable proposal density. Importance Sampling (IS) and Sampling Importance Resampling (SIR) (Rubin 1987) algorithms are also general-purpose methods, but they also require proposal densities that may be difficult to find for high-dimensional problems.

In this study, a Markov Chain Monte Carlo (MCMC) algorithm is used for computing the posterior statistics as described in the following subsection. MCMC algorithms are very attractive in that they are easy to set up and program and require relatively little prior input from the user. Markov chains are generated with the likelihood formulation of the probabilistic models based on the initial points and a prior distribution until a convergence criterion is met. Additional details about MCMC can be found in several references (Gilks et al. 1998; Gelman et al. 2004; Robert and Casella 2004).

2.6.1 Markov Chain Monte Carlo simulation – Metropolis-Hastings (MH) algorithm

MCMC methods are based on constructing a Markov chain of numerical samples representing the target distribution, so that each sample depends only on the previous value in the chain. In Bayesian data analysis, the posterior distribution in question is set as the stationary target distribution towards which the chain converges. The samples obtained from the simulation are representatives of the desired distribution.

With an MCMC algorithm, we are generating a chain of values $\boldsymbol{\Theta}_0,\ldots,\boldsymbol{\Theta}_{t-1},\boldsymbol{\Theta}_t,\boldsymbol{\Theta}_{t+1},\ldots,\boldsymbol{\Theta}_N$ in such a way that it can be used as a sample of the target posterior density. A MCMC simulation produces a sequence of values $\boldsymbol{\Theta}_t$ that depend on the values at the previous step $\boldsymbol{\Theta}_{t-1}$. The algorithm used in the simulation ensures that the chain takes values in the domain of the unknown parameters $\boldsymbol{\Theta}$ and that its limiting distribution is the posterior distribution $p(\boldsymbol{\Theta}\,|\,\mathbf{D}_k)$. The basic idea is that instead of computing the values $p(\boldsymbol{\Theta}\,|\,\mathbf{D}_k)$ we only compute the ratio of the posterior distribution at two distinct parameter values $p(\boldsymbol{\Theta}\,|\,\mathbf{D}_k)\,/\,p(\boldsymbol{\Theta}_t\,|\,\mathbf{D}_k)$. In terms of the Markov chain theory, when using the Metropolis-Hastings algorithm, we generate a Markov chain that has a transition kernel according to

$$p\left(\boldsymbol{\Theta},\boldsymbol{\Theta}_t\right)=q\left(\boldsymbol{\Theta},\boldsymbol{\Theta}_t\right)\chi\left(\boldsymbol{\Theta},\boldsymbol{\Theta}_t\right),\ \boldsymbol{\Theta}\neq\boldsymbol{\Theta}_t \tag{2.26}$$

where, q = the transition density, and χ = an acceptance probability. The density $q(\boldsymbol{\Theta}, \cdot)$, with $\boldsymbol{\Theta}$ being the current location of the chain, is called the proposal density. The chain is said to be reversible if we have

$$p\left(\boldsymbol{\Theta}\middle|\mathbf{D}_k\right)q\left(\boldsymbol{\Theta},\boldsymbol{\Theta}_t\right)\chi\left(\boldsymbol{\Theta},\boldsymbol{\Theta}_t\right) = p\left(\boldsymbol{\Theta}_t\middle|\mathbf{D}_k\right)q\left(\boldsymbol{\Theta}_t,\boldsymbol{\Theta}\right)\chi\left(\boldsymbol{\Theta}_t,\boldsymbol{\Theta}\right) \tag{2.27}$$

Reversibility is a sufficient condition for the density $p(\boldsymbol{\Theta} \mid \mathbf{D}_k)$ to be the stationary distribution of the chain,

$$\int p\left(\boldsymbol{\Theta}\middle|\mathbf{D}_k\right)p\left(\boldsymbol{\Theta},\boldsymbol{\Theta}_t\right)d\boldsymbol{\Theta} = p\left(\boldsymbol{\Theta}_t\middle|\mathbf{D}_k\right) \tag{2.28}$$

meaning that if the chain were to reach $p(\boldsymbol{\Theta} \mid \mathbf{D}_k)$, it would also follow this distribution for the rest of the simulation. This leads to the choice of the Metropolis-Hastings acceptance probability (χ) as

$$\chi\left(\boldsymbol{\Theta},\boldsymbol{\Theta}_t\right) = \min\left\{1, \frac{p\left(\boldsymbol{\Theta}_t\middle|\mathbf{D}_k\right)q\left(\boldsymbol{\Theta}_t,\boldsymbol{\Theta}\right)}{p\left(\boldsymbol{\Theta}\middle|\mathbf{D}_k\right)q\left(\boldsymbol{\Theta},\boldsymbol{\Theta}_t\right)}\right\} \tag{2.29}$$

We formulate a general Metropolis-Hastings algorithm in the following way:

(i) Start from an initial value $\boldsymbol{\Theta}_0$, and select a proposal distribution q.

(ii) At each step where the current value is $\boldsymbol{\Theta}_{t-1}$, propose a candidate for the new parameter $\boldsymbol{\Theta}_t$ from the distribution $q(\boldsymbol{\Theta}_{t-1}, \cdot)$.

(iii) If the proposed value $\boldsymbol{\Theta}_t$ is better than the previous value $\boldsymbol{\Theta}_{t-1}$ in the sense that $p(\boldsymbol{\Theta}_t \mid \mathbf{D}_k)q(\boldsymbol{\Theta}_t,\boldsymbol{\Theta}) > p(\boldsymbol{\Theta}_{t-1} \mid \mathbf{D}_k)q(\boldsymbol{\Theta},\boldsymbol{\Theta}_t)$, $\boldsymbol{\Theta}_t$ is accepted unconditionally.

(iv) If it is not better in the above sense, $\boldsymbol{\Theta}_t$ is accepted as the new value with a probability χ given by Eq. (2.29).

(v) If $\boldsymbol{\Theta}_t$ is not accepted, then the chain stays at the current value, that is, we set $\boldsymbol{\Theta}_t = \boldsymbol{\Theta}_{t-1}$.

(vi) Repeat the simulation from Step (ii) until enough values have been generated.

The proposal distribution from which we choose new values for the chain can be quite arbitrary, but choosing a distribution that most closely resembles the true target posterior distribution can accelerate the convergence of the values generated to the right distribution. The closer the proposal distribution (q) is to the actual target posterior, the better the chain mixes and the better a short sequence represents a random draw from the posterior. This is especially true in multidimensional cases and when there is a correlation between the components of the parameter vector. The algorithm is constructed in such a way that the target posterior distribution is the stationary distribution of the Markov chain. This means that the values generated will eventually follow the posterior distribution.

2.6.2 Delayed Rejection Adaptive Metropolis (DRAM) method

In the basic MCMC method based on Metropolis-Hastings, the problem is how to choose the proposal distribution so that the algorithm converges as quickly as possible. This normally requires a lot of manual tuning of the proposal.

When using a Gaussian proposal, the problem is to find a suitable covariance matrix for the proposal. In Adaptive Metropolis (AM) algorithms, the adaptive method simply adds one step to the simulation loop of the basic MCMC algorithm. Let us suppose that we are at step t in the algorithm and already have created chain $(\boldsymbol{\Theta}_0, \boldsymbol{\Theta}_1, \ldots, \boldsymbol{\Theta}_t)$. The proposal distribution is now at the current state $\boldsymbol{\Theta}_t$ and new covariance matrix $\boldsymbol{\Sigma}_{t+1}$.

$$\boldsymbol{\Sigma}_{t+1} = s \times \boldsymbol{\Sigma}\left(\boldsymbol{\Theta}_0, \ldots, \boldsymbol{\Theta}_t\right), \text{ when } t > t_0 \tag{2.30}$$

where $s =$ the constant scaling parameter that depends only on the dimension of the parameter space, $t_0 =$ the step at which the adaptation begins. When $t < t_0$, we can use a fixed initial covariance $\boldsymbol{\Sigma}_0$.

The Delayed Rejection (DR) algorithm is a modification of the standard Metropolis-Hastings algorithm that has been proved to improve the efficiency of MCMC estimators. The idea in DR is that in case of rejection in the acceptance step we propose another move instead of storing the old parameter values in the chain. The acceptance probability of this "second stage" acceptance step is chosen so that the reversibility conditions of the chain are preserved and thus the chain stays ergodic. The second stage move depends on the current position and on the point that has been rejected in the previous stage. The delayed rejection mechanism can be extended to any number of stages.

Delayed Rejection Adaptive Metropolis (DRAM) combines adaptation to the DR procedure. Here, after every AM step using an adapted covariance $\boldsymbol{\Sigma}_t$, DR is applied

upon rejection so that for stage ξ the proposal covariance $\boldsymbol{\Sigma} = \boldsymbol{\Sigma}_t^{\xi}$. The covariance at DR stage ξ can be computed simply by scaling the covariance produced by the AM step: $\boldsymbol{\Sigma}_t^{\xi} = s_{\xi} \times \boldsymbol{\Sigma}_t$, where $\xi = 1, \ldots, u$, and $u =$ the number of DR stages applied for every rejected point. The purpose of the algorithm is to guarantee that at least one of the proposals is chosen. Other second stage moves can be designed as well. The DRAM algorithm improves the efficiency compared to standard MCMC and AM approaches, especially when the initial point is badly chosen and the parameters are not well identifiable.

We adapted the Geweke's convergence diagnostic to decide when to terminate the MCMC simulations. Geweke (1992) proposed a convergence diagnostic for Markov chains based on a test for equality of the means of the initial and final part of a Markov chain (by default the first 10% and the last 50%). If the samples are drawn from the stationary distribution of the chain, the two means are equal and Geweke's statistic has an asymptotically standard normal distribution. The test statistic is a standard Z-score: the difference between the two sample means divided by its estimated standard error. We terminated the simulation when the Geweke's convergence diagnostic is sufficiently large, i.e., larger than 0.95.

2.7 Application

This subsection is devoted to a simplified deep excavation example project through which detailed step-by-step procedures are illustrated and proposed probabilistic framework is verified. The example consists of a two layer stratigraphy, with soil

modeled as an elasto-plastic Mohr-Coulomb material. "Measurements" values are generated by assigning fixed elastic properties to the soils and performing a deterministic numerical analysis. The proposed approach is then used to assess the moduli of the two soil layers, using both horizontal deformation and surface settlement data in multiple incremental excavation stages.

The soil stratigraphy and the finite element mesh for this example are shown in Figure 2.2. The entire mesh is fixed at the bottom and allowed to move vertically at both sides. The mesh behind the sheet pile wall is extended to a distance five times the excavation depth to eliminate the influence of the boundary condition on the model. The soils are modeled using 8-node biquadratic elements with reduced integration (CPE8R in ABAQUS (2003)), the sheet pile wall is represented by the 3-node quadratic beam element (B22), and the interfaces between the wall and soils are simulated by a small sliding contact pair. The tiebacks are modeled by 2-D truss elements (T2D2) with axial stiffness. In terms of materials, the soil layers are modeled using the Mohr-Coulomb model and the structural members using a linear-elastic model as summarized in Table 2.1.

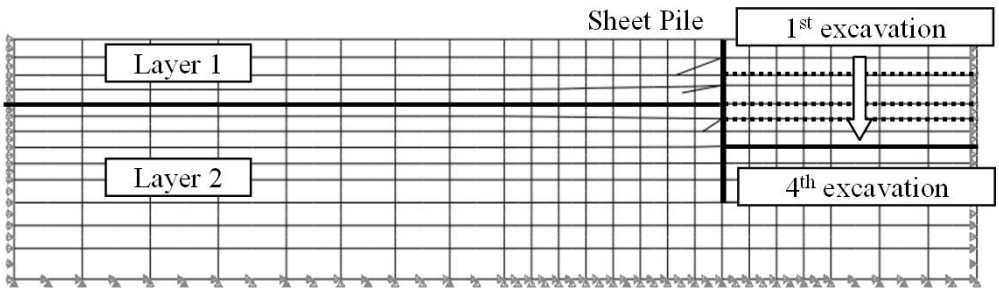

Figure 2.2 Finite element mesh for example case

Table 2.1 Material properties of example case

Types	γ_t(kN/m^3)	E(MPa)	ν	c(kPa)	ϕ(°)	ψ(°)
Sheet Pile	78 (0.4m thick)	8068	0.30	-	-	-
Strut 1	78	69.60	0.30	-	-	-
Strut 2	78	57.50	0.30	-	-	-
Strut 3	78	17.20	0.30	-	-	-
Layer 1	19	θ_{E1}	0.39	0	35	5
Layer 2	19	θ_{E2}	0.39	0	35	5

The elastic moduli of each layer are assumed to be unknown parameters (θ_{E1}, θ_{E2}) and estimated using the proposed probabilistic approach. Tables 2.2−2.5 show the posterior statistics of $\boldsymbol{\Theta}$ after each excavation stage. In the first excavation stage, a non-informative prior distribution is assumed according to Eqs. (2.13) and (2.14) . After each subsequent excavation state, the posterior statistics are obtained by updating the posterior statistics from the previous stage with the observation from the current stage. The proposed framework retrieves the unknown soil properties well from early excavation stages. Furthermore, the standard deviation of the unknown parameters $\boldsymbol{\Theta}$ gradually decreased as excavation steps increase. This indicated that the uncertainty can be reduced by the proposed probabilistic framework.

Table 2.2 Posterior statistics of the unknown parameters using prior information

	θ_{E1}	θ_{E2}	σ	ρ_V	ρ_H	ρ_{VH}
Mean	78.63	782.18	0.10	0.14	0.18	0.19
St. dev.	45.29	287.56	0.07	0.09	0.08	0.09
Correlation Coefficient						
θ_{E1}	1					
θ_{E2}	0.78	1				
σ	0.02	–0.05	1			
ρ_V	0.12	–0.09	–0.11	1		
ρ_H	0.06	–0.02	–0.13	–0.06	1	
ρ_{VH}	–0.11	0.09	0.08	0.04	0.08	1

Table 2.3 Posterior statistics of the unknown parameters after 1st stage

	θ_{E1}	θ_{E2}	σ	ρ_V	ρ_H	ρ_{VH}
Mean	78.76	784.16	0.08	0.18	0.13	0.12
St. dev.	36.49	251.47	0.06	0.09	0.06	0.08
Correlation Coefficient						
θ_{E1}	1					
θ_{E2}	0.82	1				
σ	0.06	–0.08	1			
ρ_V	0.12	0.11	0.09	1		
ρ_H	–0.16	0.09	–0.12	0.08	1	
ρ_{VH}	–0.03	0.08	0.03	0.09	–0.03	1

Table 2.4 Posterior statistics of the unknown parameters after 2nd stage

	θ_{E1}	θ_{E2}	σ	ρ_V	ρ_H	ρ_{VH}
Mean	78.89	788.56	0.08	0.12	0.17	0.18
St. dev.	28.64	214.76	0.04	0.08	0.06	0.07
Correlation Coefficient						
θ_{E1}	1					
θ_{E2}	0.78	1				
σ	–0.03	0.12	1			
ρ_V	0.18	0.09	–0.13	1		
ρ_H	0.16	0.10	–0.09	0.08	1	
ρ_{VH}	0.08	–0.08	0.08	–0.17	–0.06	1

Table 2.5 Posterior statistics of the unknown parameters after 3rd stage

	θ_{E1}	θ_{E2}	σ	ρ_V	ρ_H	ρ_{VH}
Mean	78.92	789.58	0.07	0.08	0.14	0.18
St. dev.	23.58	189.73	0.03	0.02	0.03	0.01
Correlation Coefficient						
θ_{E1}	1					
θ_{E2}	0.72	1				
σ	0.12	–0.09	1			
ρ_V	0.08	–0.02	0.12	1		
ρ_H	0.09	0.04	0.13	–0.09	1	
ρ_{VH}	–0.12	0.12	–0.04	–0.06	–0.08	1

Figure 2.3 shows the comparisons between the wall deflections based on the virtual measurements and the FEM results using the posterior means after each excavation stage. The width of the credible interval decreases as the excavation proceeds because more available information help reduce uncertainties.

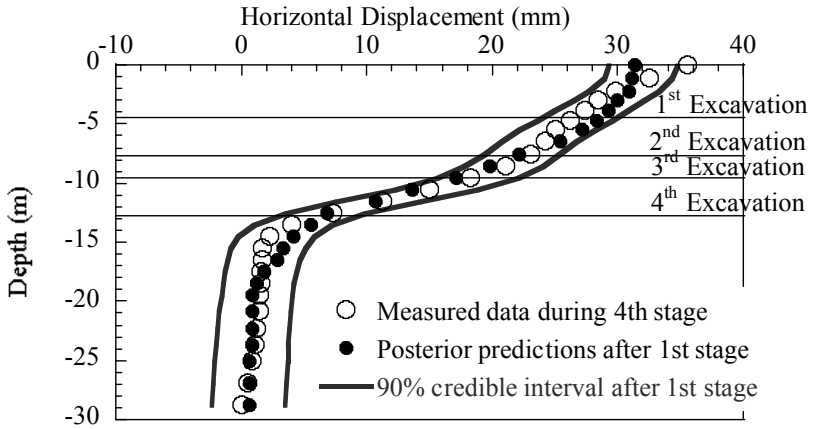

(a) Prediction after 1st stage

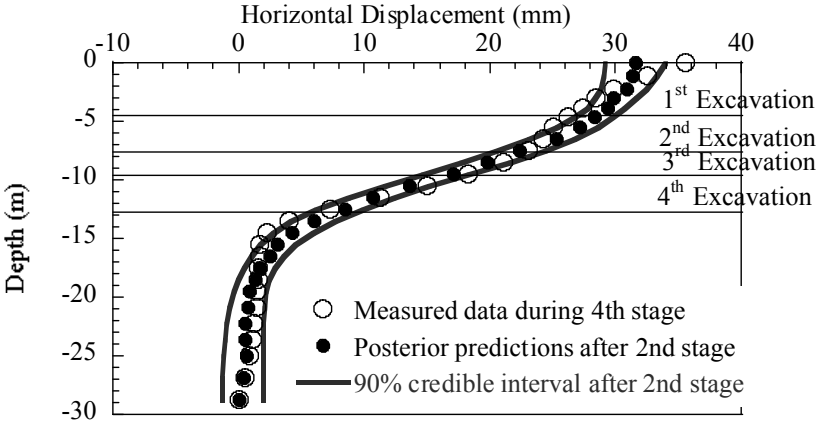

(b) Prediction after 2nd stage

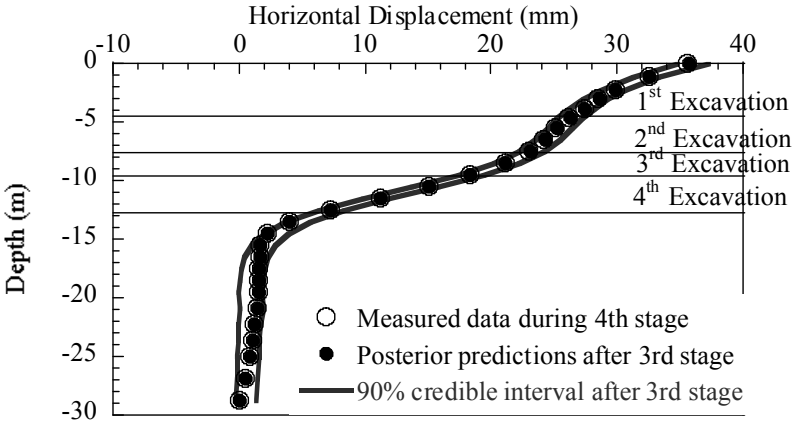

(c) Prediction after 3rd stage

Figure 2.3 Comparison of measured and predicted horizontal displacement based on posterior estimates without measurement error

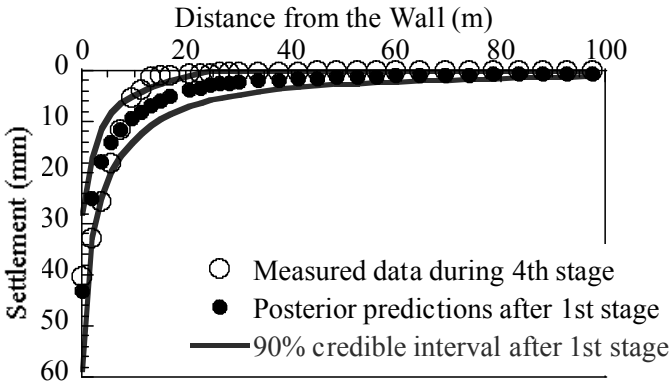

(a) Prediction after 1st stage

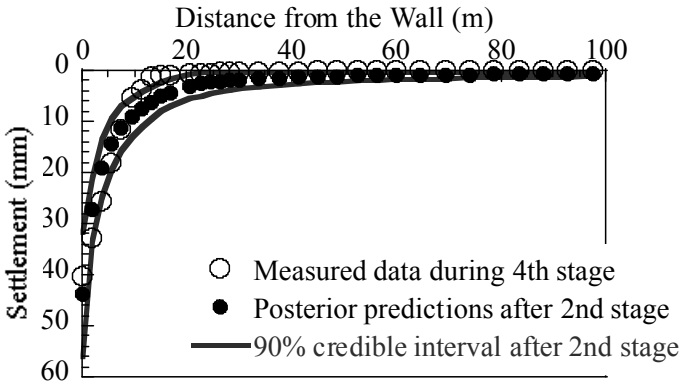

(b) Prediction after 2nd stage

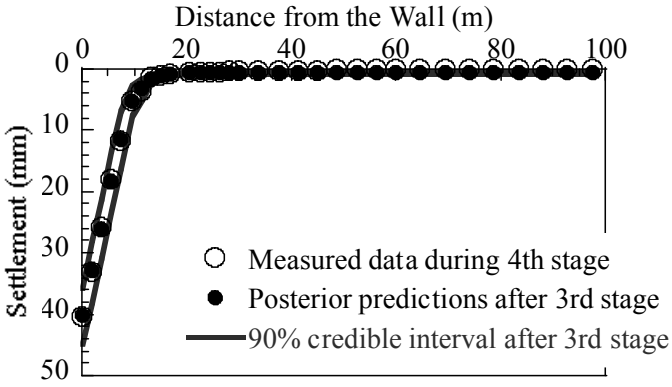

(c) Prediction after 3rd stage

Figure 2.4 Comparison of measured and predicted settlement based on posterior estimates without measurement error

Figure 2.4 shows the comparisons between the settlements based on the virtual measurements and the FEM results using the posterior means after each excavation stage. The predicted values capture accurately the overall settlement profile and the location of the maximum surface settlement.

The accuracy of the model fit can be assessed using the Mean Absolute Percent Error (*MAPE*) defined as

$$MAPE = \frac{1}{\left(n_V + n_H\right)}\left(\sum_{i=1}^{(n_V+n_H)} \frac{\left|D_{ki}\left(z_i\right) - \hat{d}_{ki}\left(\boldsymbol{\theta}; z_i\right)\right|}{D_{ki}\left(z_i\right)}\right)\times 100 \tag{2.31}$$

The *MAPE* indicates the average relative error and is an intuitive measure of the accuracy of model predictions. Table 2.6 lists the values of *MAPE* computed after each excavation stage. The small values of *MAPE* indicate that the proposed probabilistic models are accurate. The diagonal terms describe the quality of fit of the proposed probabilistic framework and show smaller values than the lower diagonal terms because the updated posterior estimates reflect both the information content of the old and the current excavation stage data in the probabilistic model. The lower diagonal terms represents how accurate the prediction is. As the excavation proceeds, more information is available and the accuracy increase means that the *MAPE* values decrease.

Figure 2.5 and Figure 2.6 show the comparisons of wall deflections and settlements based on the virtual measurements and the FEM results using the posterior means after each excavation stage when measurement errors are present. In this case, *MAPE* values are higher than in the previous case, without measurement error, as

summarized in Table 2.7 due to the effect of the additional error terms in the covariance matrix formulation.

Table 2.6 *MAPE* values for all excavation stages without measurement error

%	Stage 1	Stage 2	Stage 3	Stage 4
Stage 1	3.17			
Stage 2	15.24	2.66		
Stage 3	18.35	7.56	1.80	
Stage 4	22.95	13.46	0.91	0.75

Table 2.7 *MAPE* values for all excavation stages with measurement error

%	Stage 1	Stage 2	Stage 3	Stage 4
Stage 1	5.23			
Stage 2	18.67	4.56		
Stage 3	24.26	12.86	3.24	
Stage 4	26.68	21.07	2.38	1.37

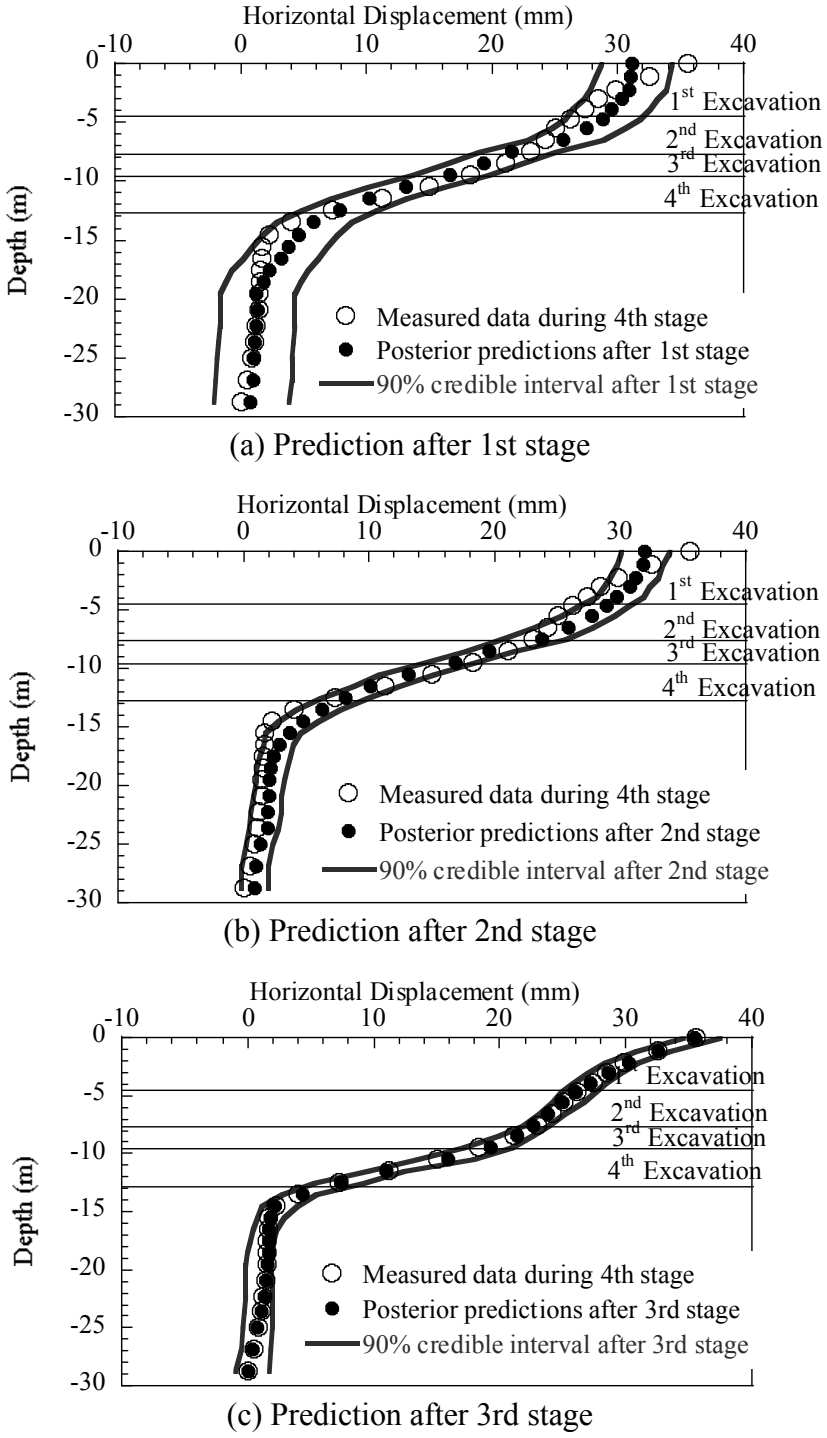

Figure 2.5 Comparison of measured and predicted horizontal displacement based on posterior estimates with measurement error

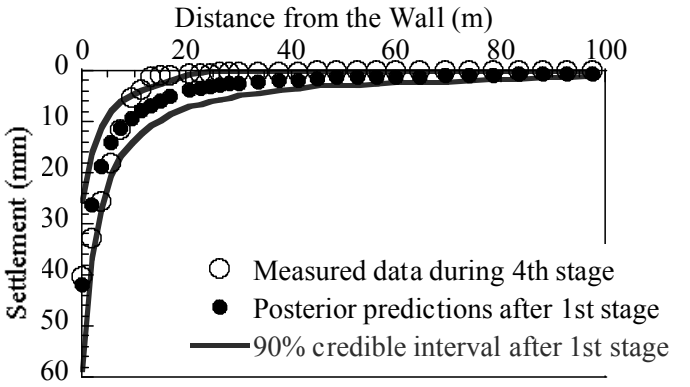

(a) Prediction after 1st stage

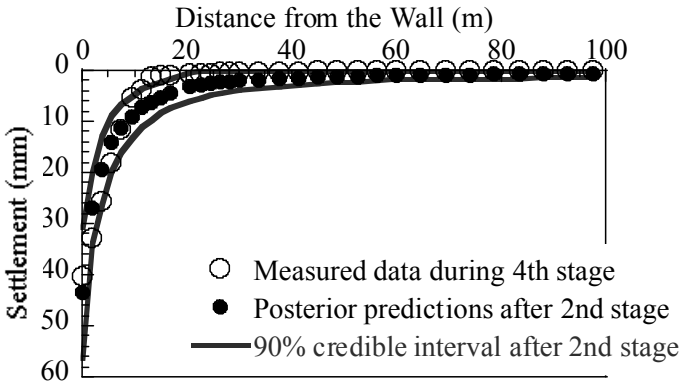

(b) Prediction after 2nd stage

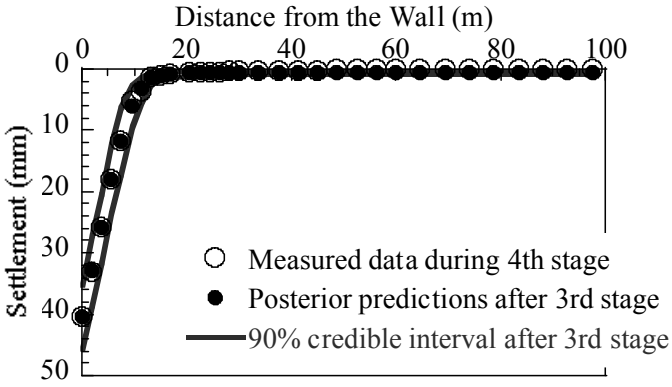

(c) Prediction after 3rd stage

Figure 2.6 Comparison of measured and predicted settlement based on posterior estimates with measurement error

2.8 Conclusions

A probabilistic methodology is developed to estimate soil properties and model uncertainty to better predict deformations during supported excavations. A Bayesian approach is used to assess the unknown soil properties by updating pertinent prior information based on field measurement data. The proposed method provides up-to-date predictions that reflect all sources of available information, and properly account for of the underlying uncertainty.

This section presents a numerical illustration of the proposed approach. In the example, the soils properties and the model parameters are updated after each excavation stage. The updated parameters are then used to develop new and more accurate predictions of the deformations in the subsequent excavation stages. This approach can be used for the design of optimal revisions for supported excavation systems. By applying the proposed Bayesian approach to the reliability-based design of geotechnical engineering projects, engineers can combine the advantages of the observational method with the advantages of probabilistic methods.

3. ESTIMATING SOIL PROPERTIES AND DEFORMATIONS DURING STAGED EXCAVATIONS — II. APPLICATION TO CASE HISTORIES

A general Bayesian probabilistic framework to assess soil properties and the model uncertainty to better predict excavation-induced deformations using field deformation data has been presented in the previous section. The proposed framework can be used to assess the unknown soil properties of multiple soil layers using deformation data at different locations and for multiple incremental excavation stages. This section describes an application of the developed method to two real case studies of staged excavation projects in Evanston, Illinois and Shanghai City, China. Horizontal displacements and settlement profiles measured in the field are used as input data to estimate the elastic modulus and other plasticity parameters using the developed Bayesian approach. The posterior statistics of the unknown soil properties and model parameters are computed using the Delayed Rejection (DR) method and the Adaptive Metropolis (AM) method.

3.1 Bayesian Probabilistic Framework

The observational method, formalized by Peck (1969) and recently further refined by Hashash et al. (2003), Calvello and Finno (2004), Finno and Calvello (2005), Chua and Goh (2005), Hashash and Finno (2008) and Hsiao et al. (2008), provides a motivation for employing adaptive design in geotechnical projects, including deep excavations.

Monitoring and continuously evaluating observed vs. predicted response during construction are the basic tenets of the observational method. Although the method has been successfully implemented in actual geotechnical engineering projects, the feedback and revision concept can also be developed through a probabilistic analysis framework.

A general Bayesian probabilistic framework to assess and refine soil properties for staged excavation problems was presented in a companion paper (Park et al. 2010a). The data or engineering judgment employed during initial design can be quantitatively updated based on additional information, such as support system responses or additional soil tests as they become available.

As a demonstration of the applicability of the proposed procedure, the process of estimating soil properties and model parameters from field measurements obtained during the excavation is illustrated herein using previously published examples. The first case illustrates the application of the developed methodology to the Lurie Research Center excavation project in Evanston, Illinois (Finno and Roboski 2005). The second example is an application of the developed approach to the Caobao Subway excavation project in Shanghai, China (Shao and Macari 2008).

The proposed Bayesian probabilistic approach is implemented through a MATLAB-based application program designed as a general purpose Bayesian probabilistic tool for the solution of inverse problems. The flow chart shown in Figure 3.1 illustrates the calculation procedure in the program as applied to deep excavations. The updating of soil properties and model parameters for the finite element analysis is carried out using the Delayed Rejection Adaptive Metropolis (DRAM) method as

described in the previous section. This procedure allows engineers to revise soil response predictions and determine the influence of individual constitutive parameters and model parameters. The feedback reduces the total uncertainty inherent in excavation projects due to soil variability, modeling methods, and construction procedures.

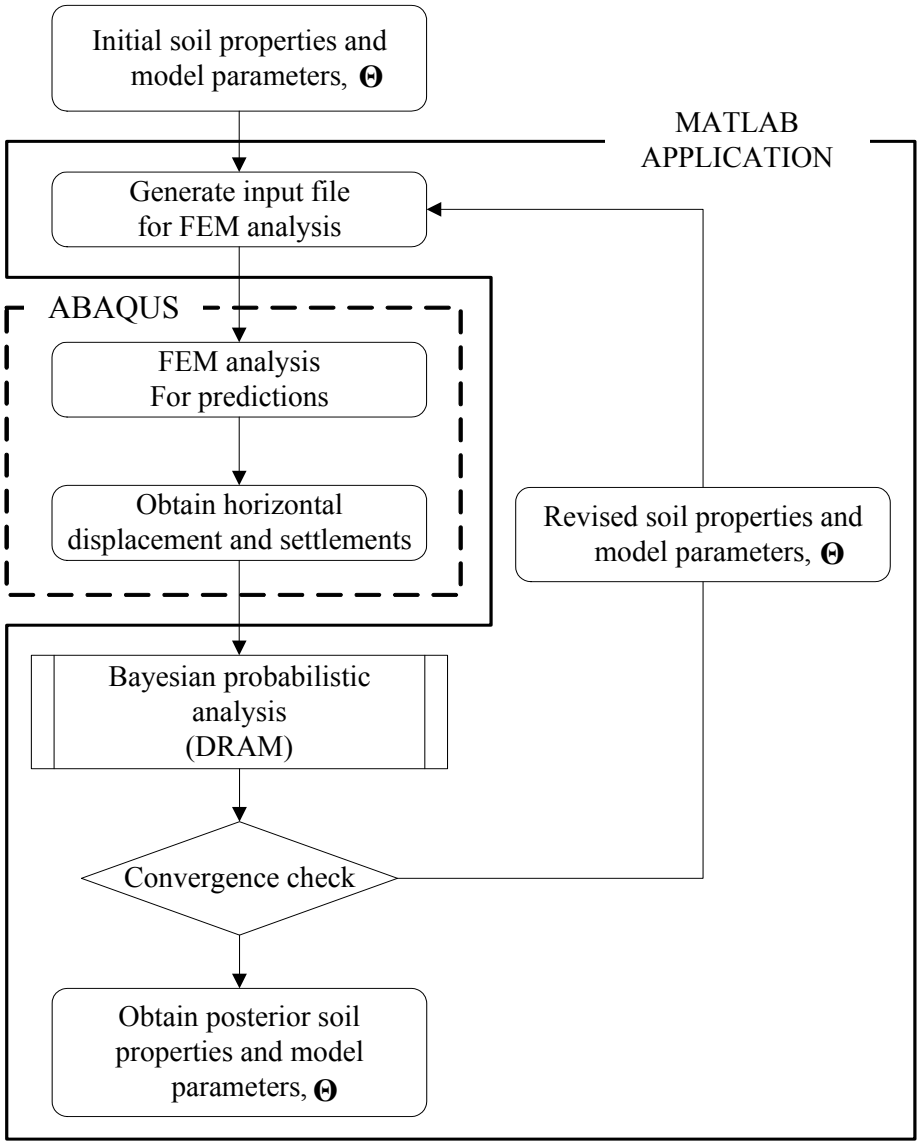

Figure 3.1 Flow diagram for the processes in the MATLAB application

3.2 LURIE Research Center Case History

3.2.1 Project description

The developed probabilistic approach is applied to an actual supported excavation project for the Robert H. Lurie Medical Research Building in Evanston, Illinois (Finno and Roboski 2005). Figure 3.2 shows a plan view of the approximately 80 m by 68 m excavation area. Measurements of both lateral and vertical ground surface settlements were obtained from inclinometers and optical survey. Because of the proximity of the utilities and the use of a relatively flexible excavation support system, extensive monitoring locations were established around the site. The excavation consisted of a 12.8 m deep cut for two basement levels and a flexible retaining system of PZ–27 sheet pile on all sides. Detailed description and ground response of the excavation are provided in Finno and Roboski (2005).

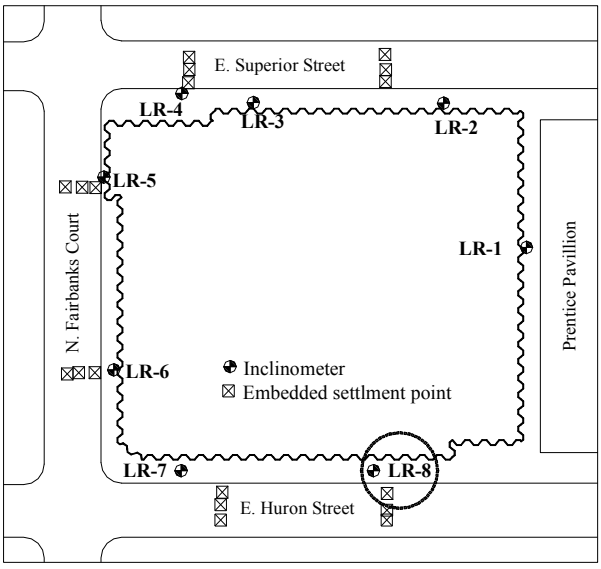

Figure 3.2 Plan view of the Lurie Center excavation (Modified from Finno and Calvello 2005)

3.2.2 Site conditions and measurement data

Beneath the superficial medium dense to dense rubble fill lies a loose to medium dense beach sand as shown in Figure 3.3. The granular soils overlie a sequence of glacial clays of increasing shear strength with depth. Undrained shear strengths based on results of vane shear tests are 29–43 kPa in the soft to stiff clays and 105 kPa in the stiff clay. Excavation of the site and tieback installation took place simultaneously within the site. However, four distinct excavation stages were defined, corresponding to levels immediately below tieback elevations and the final excavated grade as described in Table 3.1.

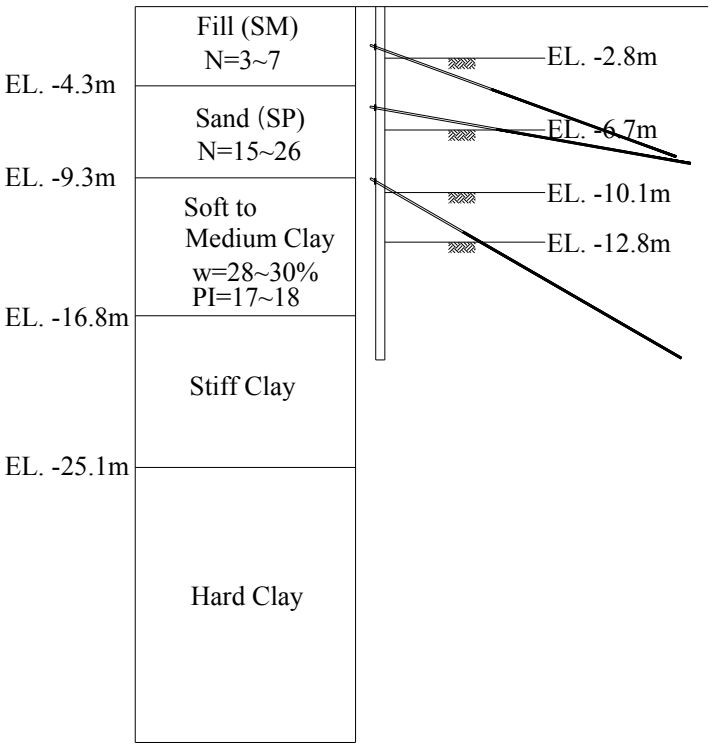

Figure 3.3 Stratigraphy and excavation support system of the Lurie Center excavation (Modified from Finno and Calvello 2005)

Table 3.1 Major construction stages for the Lurie Center case history

Excavation Stage	Activity
0	Potholing and sheet-pile installation
1	Excavate to EL. –2.8 m and install/prestress first level of ground anchors at EL. –2.2 m
2	Excavate to EL. –6.7 m and install/ prestress second level of ground anchors at EL. –5.5 m
3	Excavate to EL. –10.1 m and install/prestress third level of ground anchors at EL. –9.5 m
4	Excavate to EL. –12.8 m

The largest portion of the movements occurred during Stage 3, described in Table 3.1. This is when the excavation reached 0.80 m into the soft to medium clay layer for the installation of the third tieback level. The inclinometer responses indicated that the movements were relatively small while the excavation was proceeding through the fill and sand layers, and jumped from 20 to 60 mm of maximum displacement once the clay layer was reached. Afterwards, very little movement occurred. The inclinometer measurement data from LR–8 in Figure 3.2 are identified as the approximate plane-strain zone based on the observations, so they were used as field measurement data for the calculation (Finno and Roboski 2005).

3.2.3 Choice of constitutive models

The material models used for soft clay vary from very simple ones, such as linear elasticity, to highly sophisticated stress-strain relationships capable of simulating anisotropy and nonlinear stiffness at small strain. Generally, sophisticated material models are able to generate more realistic responses and their predictions are closer to

the actual behavior. However, sophisticated constitutive models need more parameters and require more extensive laboratory investigation and computational effort. For these reasons, it is preferable to use relatively simple models in this application.

Since the input soil properties and model parameters in the probabilistic Bayesian analysis framework are updated continuously as the excavation proceeds, some shortcomings of a simplistic constitutive model can be somewhat counteracted by the newly updated parameters. These parameters are used for the prediction of the next steps. From this point of view, the selection of the soil constitutive model is not as critical as in conventional numerical analyses, as long as the model and its associated parameters work together to give a good prediction. In this sense, the calculated parameters perhaps are not real soil properties in the conventional sense, but the properties which reflect overall effects (heterogeneity, anisotropy, boundary conditions, and stress state etc.) associated with the particular soil model and project.

In terms of material modeling, the soil layers are modeled using the Mohr-Coulomb model and the structural members using a linear-elastic model.

3.2.4 Analysis

Figure 3.4 shows the finite element mesh in relation to soil stratigraphy and excavation steps. The entire mesh is fixed at the bottom and allowed to move vertically and freely at both sides. The mesh behind the sheet pile wall is extended to a distance five times the excavation depth to eliminate the influence of the boundary condition on the model.

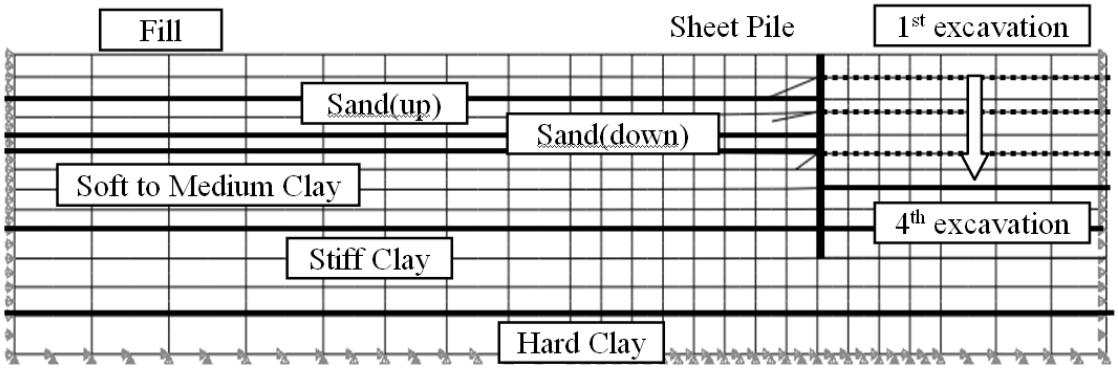

Figure 3.4 Finite element mesh for the Lurie Center case history

Table 3.2 summarizes material properties for each soil layer. In this case, the elastic Young's modulus for each soil layer was assumed to be an unknown parameter. The soils are modeled using 8-node biquadratic elements with reduced integration (CPE8R in ABAQUS (2003)), the sheet pile wall is represented by the 3-node quadratic beam element (B22), and the interfaces between the wall and soils are simulated by the small sliding contact pair. The tiebacks are modeled by 2-D truss elements (T2D2) with axial stiffness.

Table 3.2 Material properties for the Lurie Center case history

Types	γ_t (kN/m^3)	E (MPa)	ν	c (kPa)	ϕ (°)	ψ (°)
Fill	18.8	θ_{E1}	0.20	0	30	2
Sand (up)	19.0	θ_{E2}	0.39	0	35	5
Sand (down)	19.0	θ_{E3}	0.37	0	40	8
Soft to Medium clay	19.1	θ_{E4}	0.49	50	0	-
Stiff clay	20.4	θ_{E5}	0.49	105	0	-
Hard Clay	20.4	θ_{E6}	0.49	383	0	-

In reality, we typically have information about some of the unknown parameters $\boldsymbol{\theta}$, prior to the excavation. To incorporate such information, the Bayesian approach requires that we formulate such prior information in the form of a prior distribution of the unknown parameter. In this study, $\boldsymbol{\theta}$ are assumed to be independent. Therefore, $p(\boldsymbol{\theta})$ is written as the product of the prior marginal distributions, which are assumed to be lognormal based on the range of the each parameter. The prior means are based on previous research (Tu 2007), and the standard deviations are based on an assumed value for the coefficient of variation (COV) of 0.2 as summarized in Table 3.3, which reflects a moderate degree of uncertainty about the actual values of $\boldsymbol{\theta}$. The noninformative prior for $\boldsymbol{\Sigma}$ is formulated following Gardoni et al.(2002).

Table 3.3 Prior distributions for elastic Young modulus in the Lurie Center case history

Parameter ranges	Distribution models	Mean (MPa)	COV
$0 < \theta_{E1} < \infty$	Lognormal	51	0.2
$0 < \theta_{E2} < \infty$	Lognormal	79	0.2
$0 < \theta_{E3} < \infty$	Lognormal	175	0.2
$0 < \theta_{E4} < \infty$	Lognormal	250	0.2
$0 < \theta_{E5} < \infty$	Lognormal	400	0.2
$0 < \theta_{E6} < \infty$	Lognormal	677	0.2

According to the developed Bayesian approach, the posterior estimates represent our updated state of knowledge about the unknown parameters. Table 3.4–3.7 summarize the posterior statistics of $\boldsymbol{\Theta}$ after each excavation step. The updated posterior estimates reflect both the information content of the old and of the new data.

After each subsequent excavation state, the new posterior statistics are estimated by updating the posterior statistics from the previous state with the observations from the current stage. As the excavation steps proceed, the uncertainty in the model parameters decreases. This is because of the additional information content of the new data incorporated in the estimates of the model parameters.

Table 3.4 Posterior statistics of the unknown parameters for the Lurie Center case history using prior information

	θ_{E1}	θ_{E2}	θ_{E3}	θ_{E4}	θ_{E5}	θ_{E6}	σ	ρ_V	ρ_H	ρ_{VH}
Mean	50.38	76.24	168.35	218.61	432.51	689.06	0.0189	0.09	0.15	0.11
Standard deviation	2.43	3.65	8.47	10.21	20.17	31.39	0.0029	0.08	0.07	0.07
Correlation Coefficient										
θ_{E1}	1									
θ_{E2}	0.75	1								
θ_{E3}	0.46	0.34	1							
θ_{E4}	0.10	–0.18	0.56	1						
θ_{E5}	–0.11	–0.16	–0.19	0.33	1					
θ_{E6}	0.12	0.15	0.02	–0.08	–0.79	1				
σ	0.13	0.16	0.26	–0.15	0.13	–0.22	1			
ρ_V	0.22	–0.14	0.19	0.09	0.16	–0.21	–0.02	1		
ρ_H	0.03	0.07	0.04	–0.15	0.04	–0.06	0.03	0.04	1	
ρ_{VH}	0.01	0.08	–0.02	0.17	0.11	–0.10	–0.12	–0.19	0.02	1

Table 3.5 Posterior statistics of the unknown parameters for the Lurie Center case history after 1st stage

	θ_{E1}	θ_{E2}	θ_{E3}	θ_{E4}	θ_{E5}	θ_{E6}	σ	ρ_V	ρ_H	ρ_{VH}
Mean	50.79	77.35	170.38	234.35	382.65	680.35	0.0164	0.10	0.12	0.08
Standard deviation	2.12	3.59	6.78	10.78	18.22	29.60	0.0023	0.07	0.08	0.07
Correlation Coefficient										
θ_{E1}	1									
θ_{E2}	0.69	1								
θ_{E3}	0.43	0.26	1							
θ_{E4}	0.14	–0.12	0.44	1						
θ_{E5}	0.08	0.05	–0.11	0.27	1					
θ_{E6}	0.08	0.10	–0.01	–0.06	–0.63	1				
σ	0.06	0.09	–0.16	–0.07	0.06	–0.19	1			
ρ_V	–0.18	0.08	0.06	–0.07	0.13	–0.18	0.07	1		
ρ_H	0.07	–0.02	0.03	0.05	–0.08	0.15	0.14	0.13	1	
ρ_{VH}	–0.01	0.10	0.07	0.09	0.11	–0.07	0.06	–0.11	0.05	1

Table 3.6 Posterior statistics of the unknown parameters for the Lurie Center case history after 2nd stage

	θ_{E1}	θ_{E2}	θ_{E3}	θ_{E4}	θ_{E5}	θ_{E6}	σ	ρ_V	ρ_H	ρ_{VH}
Mean	51.13	80.35	170.32	238.05	411.57	679.48	0.0132	0.11	0.13	0.08
Standard deviation	2.33	3.58	5.71	9.83	18.16	28.33	0.0021	0.05	0.03	0.03
Correlation Coefficient										
θ_{E1}	1									
θ_{E2}	0.71	1								
θ_{E3}	0.38	0.40	1							
θ_{E4}	–0.09	0.08	0.63	1						
θ_{E5}	0.08	0.13	–0.08	0.25	1					
θ_{E6}	–0.06	0.16	0.08	0.11	0.65	1				
σ	0.04	0.18	0.17	–0.13	0.15	–0.08	1			
ρ_V	0.13	–0.10	0.14	0.07	0.12	–0.16	–0.09	1		
ρ_H	0.04	0.03	–0.07	0.11	0.10	0.09	0.06	0.08	1	
ρ_{VH}	0.03	–0.06	0.08	–0.08	0.03	0.11	–0.14	–0.10	0.02	1

Table 3.7 Posterior statistics of the unknown parameters for the Lurie Center case history after 3rd stage

	θ_{E1}	θ_{E2}	θ_{E3}	θ_{E4}	θ_{E5}	θ_{E6}	σ	ρ_V	ρ_H	ρ_{VH}
Mean	51.08	79.69	176.89	251.38	403.21	677.08	0.0115	0.10	0.08	0.09
Standard deviation	2.15	2.81	4.66	8.17	17.52	28.51	0.0012	0.04	0.03	0.03
Correlation Coefficient										
θ_{E1}	1									
θ_{E2}	0.67	1								
θ_{E3}	0.38	0.26	1							
θ_{E4}	–0.16	0.11	0.56	1						
θ_{E5}	–0.18	–0.10	0.09	0.27	1					
θ_{E6}	0.09	0.08	0.11	–0.13	–0.59	1				
σ	0.11	0.13	0.21	–0.14	–0.13	–0.22	1			
ρ_V	0.22	–0.14	0.19	–0.09	–0.08	–0.10	–0.07	1		
ρ_H	–0.06	0.08	0.10	–0.15	0.04	–0.02	0.08	0.03	1	
ρ_{VH}	0.01	0.04	–0.03	0.07	0.11	–0.10	–0.17	0.09	0.01	1

Figure 3.5 shows the comparisons between the horizontal wall deflections predicted using the proposed probabilistic method using the posterior means and the field measurements from the inclinometer. It also shows the 90% credible interval of the predicted soil movement after each excavation. The width of the credible interval decreases as the excavation proceeds because the additional information helps to reduce uncertainties.

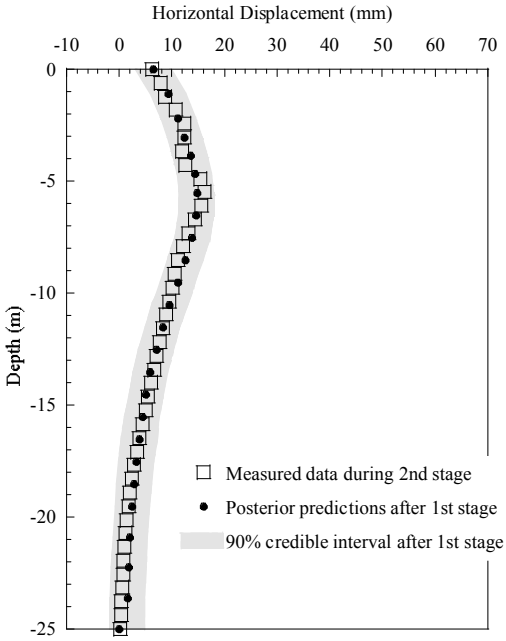

(a) 2nd excavation stage

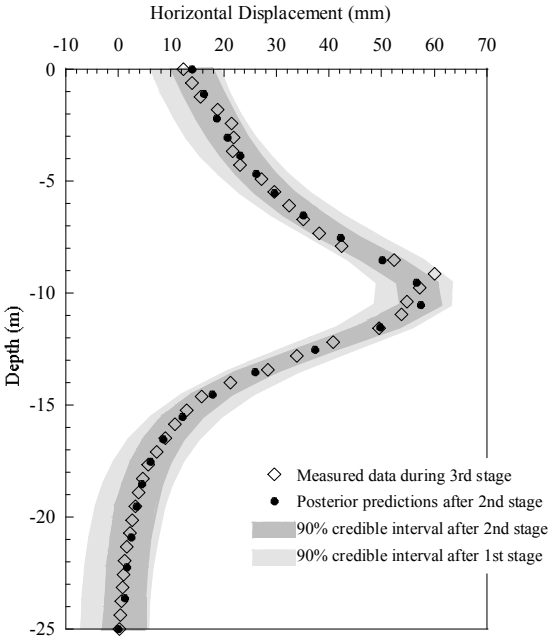

(b) 3rd excavation stage

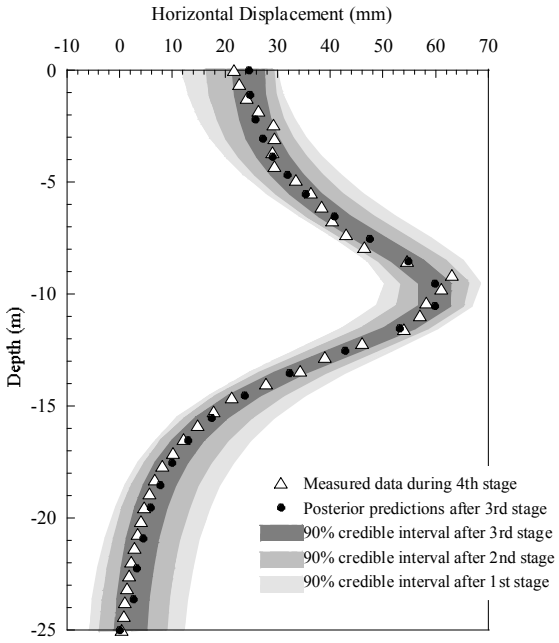

(c) 4th excavation stage

Figure 3.5 Comparison in the range of predicted soil movement after each incremental stage for the Lurie Center case history

Figure 3.6 compares predicted and measured surface settlements after each excavations stage. The predicted values capture accurately the settlement profile and the location of the maximum surface settlement.

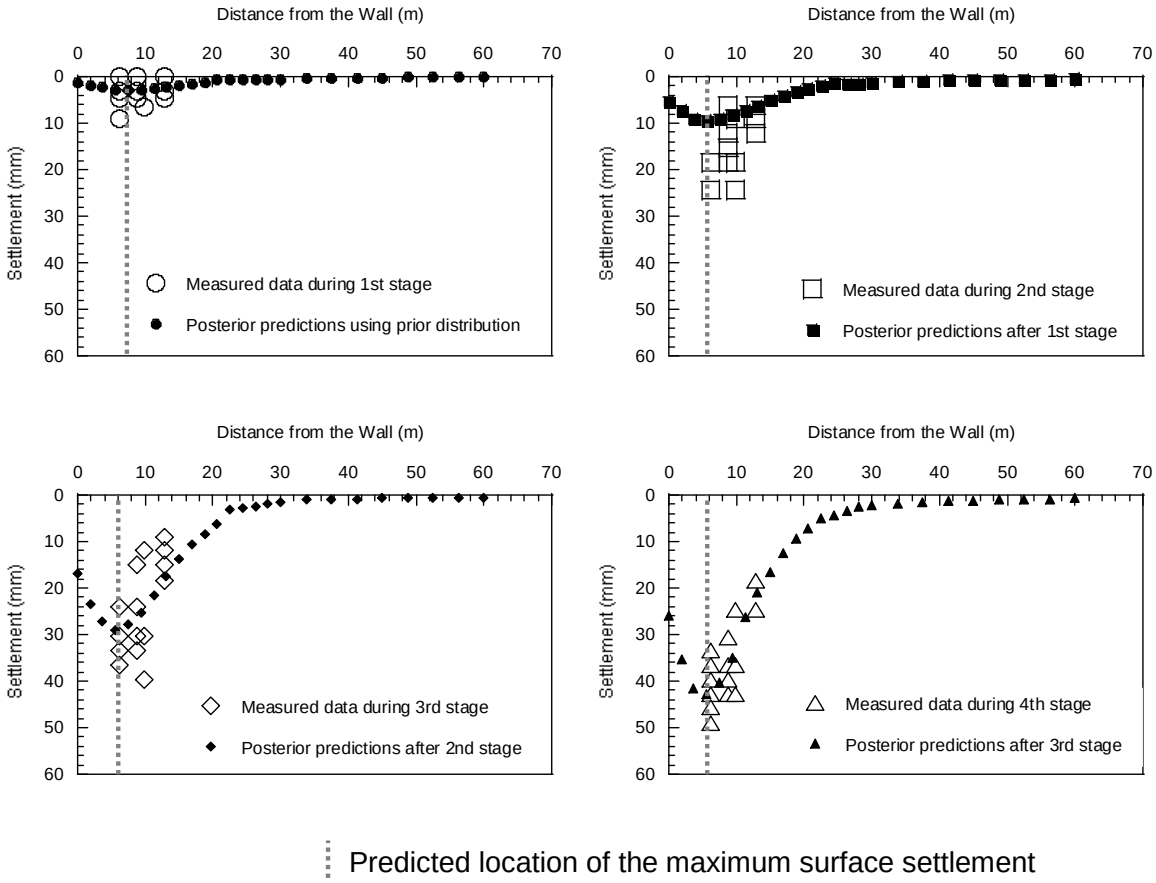

Figure 3.6 Comparison of measured and predicted settlement based on posterior estimates for the Lurie Center case history

The accuracy of the model fit is evaluated using the Mean Absolute Percent Error (*MAPE*) value (Pham 2006). The *MAPE* indicates the average relative error and is an intuitive measure of the accuracy of model predictions. The small values of *MAPE* in Table 3.8 indicate that the proposed probabilistic models become more accurate as the

excavation proceeds. The diagonal terms in Table 3.8 describe the quality of the fit of the proposed probabilistic framework and show smaller values than the lower diagonal terms. As the excavation proceeds, more information is available and the accuracy increase results in a decrease in *MAPE* values. The lower diagonal terms represents how accurate the predictions of deformations in future stages of the excavations are. As expected, the accuracy of the prediction degrades as the model is applied to increasingly more distant excavation steps. As shown by increasing *MAPE* values along each column of Table 3.8.

Table 3.8 *MAPE* values for the Lurie Center case history without measurement errors

%	Stage 1	Stage 2	Stage 3	Stage 4
Stage 1	5.32			
Stage 2	7.49	3.47		
Stage 3	18.24	12.58	3.22	
Stage 4	23.67	19.61	11.53	5.39

3.3 CAOBAO Subway Station Case History

3.3.1 Project description

The excavation for the subway station of Shanghai's first metro line, located off Caobao Road, is the second application of the proposed probabilistic approach. Because of the sensitivity of the project, a very dense instrumentation plan was devised as shown in Figure 3.7. The project was presented in detail by Shao and Macari (2008).

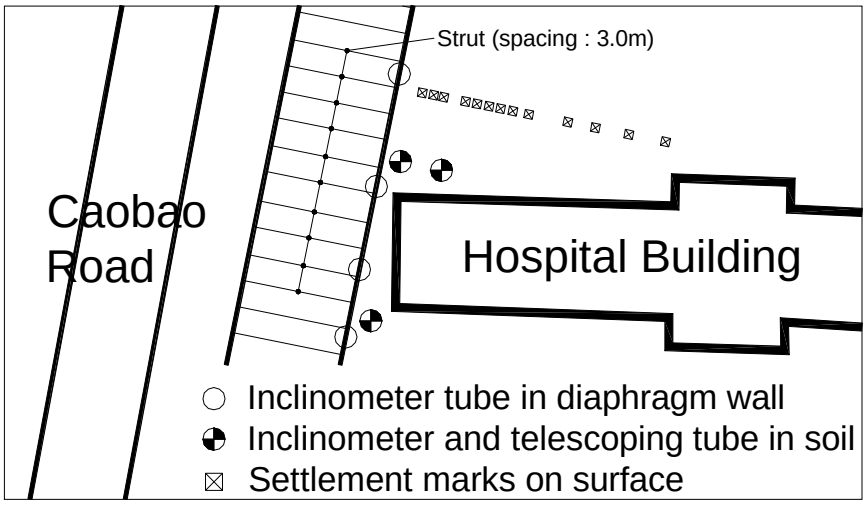

Figure 3.7 Plan view of the Caobao subway station excavation (Modified from Shao and Macari 2008)

Similarly to this study, Shao and Macari (2008) present a procedure integrating field information and a finite element model of the excavation with the goal to improve prediction of deformations during the course of the excavation itself. An optimization scheme was used to minimize the objective function representing the discrepancy between the measured and calculated displacements. The numerical analysis is able to account for unexpected activities or responses by feeding updated field data into the objective function. Therefore, the prediction becomes more realistic as the excavation proceeds. This feedback method, however, does not take into account possible measurement bias or random error. More importantly, the method is purely deterministic and does not capture any underlying uncertainties. The developed Bayesian probabilistic framework accounts for potential measurement errors, incorporates the underlying uncertainty, and is probabilistic providing credible intervals around the deflection predictions.

3.3.2 Site conditions and measurement data

The project site is located in the eastern area of the alluvial plain of the Yangze River Estuary Delta. Clay layers of marine origin are interbedded with sand layers of fluvial origin. The soil within the first 30 m consists primarily of saturated clay and sand. The typical subsurface soil profile and excavation support system are shown in Figure 3.8.

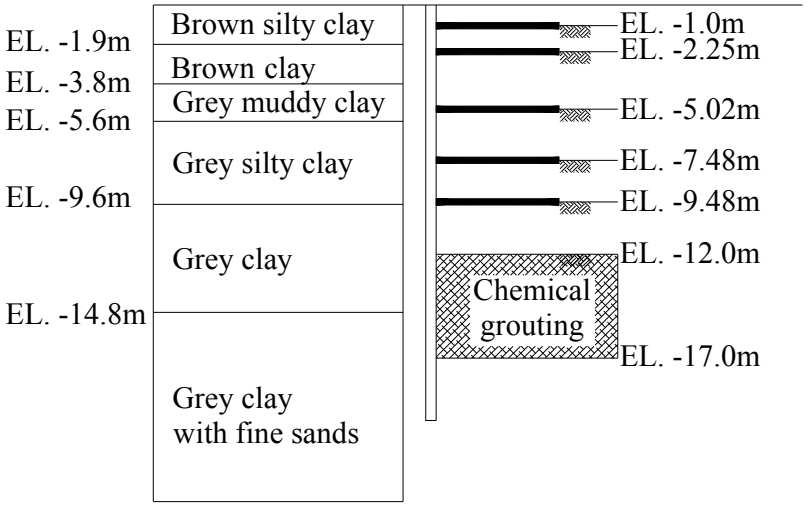

Figure 3.8 Stratigraphy and excavation support system of the Caobao subway excavation (Modified from Shao and Macari 2008)

The excavation is supported by a 0.6 m thick cast-in-place reinforced concrete diaphragm wall extending to a depth of 20 m below the ground surface. Final excavation depth was 12 m. The diaphragm walls were braced internally by four levels of steel pipe struts with 3 m horizontal spacing, as shown in Figure 3.7. Permanent reinforced concrete struts were constructed between the first and the second levels of steel pipe struts to avoid large surface deformation prior to the installation of the temporary steel pipe struts. The soil in the 5 m below the final excavation depth was stabilized by

chemical grouting before excavating to increase stability against bottom heave and to reduce the embedment depth of the diaphragm wall. The detailed construction sequence is described in Table 3.9, and was also used for the numerical simulation.

Table 3.9 Major construction stages in the Caobao subway station case history

Excavation Stage	Activity
0	Potholing and diaphragm wall installation
1	Excavate to EL. –1.0 m without horizontal steel pipe strut
2	Excavate to EL. –2.25 m and install first level horizontal steel pipe strut at EL. –1.0 m
3	Excavate to EL. –5.02 m and cast horizontal reinforced concrete strut at EL. –2.25 m
4	Excavate to EL. –7.48 m and install second level horizontal steel pipe strut at EL. –5.02 m
5	Excavate to EL. –9.48 m and install third level horizontal steel pipe strut at EL. –7.48 m
6	Excavate to EL. –12.0 m and install fourth level horizontal steel pipe strut at EL. –9.48 m

Ground surface settlements were measured by optical survey and the horizontal displacement of the ground and the diaphragm wall were measured using inclinometers installed before the excavation, while the vertical displacements in the ground were measured by a telescoping tube with multilevel steel plates that allows measurement of bottom heave. The detailed location of each measurement is shown in Figure 3.7. The maximum settlement was 57 mm after the completion of Stage 6, and was measured 8–10 m away from the excavation, or more than half of the total excavation depth. The maximum horizontal displacement was about 30 mm after the completion of Stage 6, and did not occur at top of the wall because of the very large stiffness of the concrete and steel pipe struts.

3.3.3 Choice of constitutive models

In terms of material modeling, the soil layers are modeled using the Cam-Clay constitutive law and the structural members using a linear-elastic model with initial input parameters given in Table 3.10 and Table 3.11. Parameters for other materials, such as steel, concrete, and soil–concrete interfaces are assumed constant throughout the entire analysis.

Table 3.10 Material properties for the Caobao subway case history

Types	γ_t (kN/m^3)	e_{ini}	G (kPa)	κ	λ	M	c (kPa)	ϕ (°)	k (m/day)
Soil 1	19.0	1.010	θ_{G1}	$\theta_{\kappa 1}$	$\theta_{\lambda 1}$	θ_{M1}	30.0	14.0	10^{-5}
Soil 2	21.0	0.720	θ_{G2}	$\theta_{\kappa 2}$	$\theta_{\lambda 2}$	θ_{M2}	28.0	18.0	10^{-5}
Soil 3	18.0	1.160	θ_{G3}	$\theta_{\kappa 3}$	$\theta_{\lambda 3}$	θ_{M3}	36.0	13.0	10^{-6}
Soil 4	17.0	1.440	θ_{G4}	$\theta_{\kappa 4}$	$\theta_{\lambda 4}$	θ_{M4}	36.0	22.3	10^{-4}
Soil 5	18.0	1.160	θ_{G5}	$\theta_{\kappa 5}$	$\theta_{\lambda 5}$	θ_{M5}	5.0	22.0	10^{-5}
Soil 6	18.0	1.020	θ_{G6}	$\theta_{\kappa 6}$	$\theta_{\lambda 6}$	θ_{M6}	5.0	32.0	10^{-4}
Soil 7	20.0	0.800	θ_{G7}	$\theta_{\kappa 7}$	$\theta_{\lambda 7}$	θ_{M7}	22.0	34.0	10^{-6}
Diaphragm Wall	Area (m^2/m) = 0.6, Moment of inertia (m^4/m) = 0.018 Young's modulus (kPa) = 2.83E7 Unit weight (kN/m^3) = 25.0 Poisson's ratio = 0.16								
Steel strut	Area (m^2/m) = 0.02 Young's modulus (kPa) = 2.11E8 Effective length (m) = 6.00 Spacing (m) = 3.00 Axial stiffness (kN/m) = 4.22E6								
Concrete strut	Area (m^2/m) = 0.36 Young's modulus (kPa) = 2.43E7 Effective length (m) = 6.00 Spacing (m) = 3.00 Axial stiffness (kN/m) = 8.75E6								

Table 3.11 Prior distributions for soil parameters of the Caobao case history

Parameter ranges	Distribution models	Mean (MPa)	COV
$0< \theta_{G1} <\infty$	Log-Normal	1.900	0.2
$0< \theta_{G2} <\infty$	Log-Normal	4.100	0.2
$0< \theta_{G3} <\infty$	Log-Normal	0.978	0.2
$0< \theta_{G4} <\infty$	Log-Normal	5.860	0.2
$0< \theta_{G5} <\infty$	Log-Normal	8.970	0.2
$0< \theta_{G6} <\infty$	Log-Normal	10.560	0.2
$0< \theta_{G7} <\infty$	Log-Normal	17.600	0.2
$0< \theta_{\kappa 1} <\infty$	Log-Normal	0.038	0.2
$0< \theta_{\kappa 2} <\infty$	Log-Normal	0.022	0.2
$0< \theta_{\kappa 3} <\infty$	Log-Normal	0.040	0.2
$0< \theta_{\kappa 4} <\infty$	Log-Normal	0.045	0.2
$0< \theta_{\kappa 5} <\infty$	Log-Normal	0.032	0.2
$0< \theta_{\kappa 6} <\infty$	Log-Normal	0.026	0.2
$0< \theta_{\kappa 7} <\infty$	Log-Normal	0.015	0.2
$0< \theta_{\lambda 1} <\infty$	Log-Normal	0.184	0.2
$0< \theta_{\lambda 2} <\infty$	Log-Normal	0.165	0.2
$0< \theta_{\lambda 3} <\infty$	Log-Normal	0.193	0.2
$0< \theta_{\lambda 4} <\infty$	Log-Normal	0.190	0.2
$0< \theta_{\lambda 5} <\infty$	Log-Normal	0.184	0.2
$0< \theta_{\lambda 6} <\infty$	Log-Normal	0.171	0.2
$0< \theta_{\lambda 7} <\infty$	Log-Normal	0.150	0.2
$0< \theta_{M1} <\infty$	Log-Normal	0.940	0.2
$0< \theta_{M2} <\infty$	Log-Normal	0.860	0.2
$0< \theta_{M3} <\infty$	Log-Normal	0.890	0.2
$0< \theta_{M4} <\infty$	Log-Normal	1.000	0.2
$0< \theta_{M5} <\infty$	Log-Normal	0.980	0.2
$0< \theta_{M6} <\infty$	Log-Normal	0.940	0.2
$0< \theta_{M7} <\infty$	Log-Normal	1.100	0.2

3.3.4 Analysis

Figure 3.9 shows the finite element mesh in relation to soil stratigraphy and excavation steps. The soils are modeled using 8-node biquadratic pore pressure plane strain elements with reduced integration (CPE8RP in ABAQUS (ABAQUS 2003)), the diaphragm wall is represented by 8-node biquadratic plane strain elements (CPE8R), and the interfaces between the wall and soil are simulated by a small sliding contact pair. The concrete and steel pipe struts are modeled by 2-D truss elements (T2D2) with axial stiffness. In order to minimize the influence of boundaries, the soil beyond a distance where the deformation could be ignored is modeled by infinite elements. The 5-node quadratic one-way infinite elements (CINPE5R), which match the 8-node displacement element, were used.

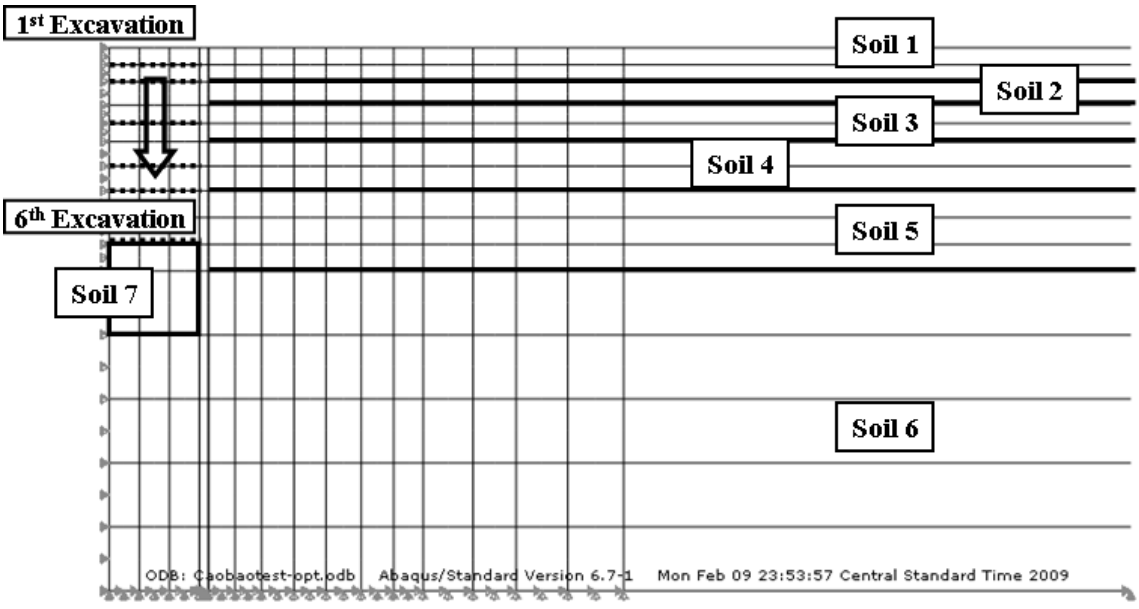

Figure 3.9 Finite element mesh for the Caobao subway excavation

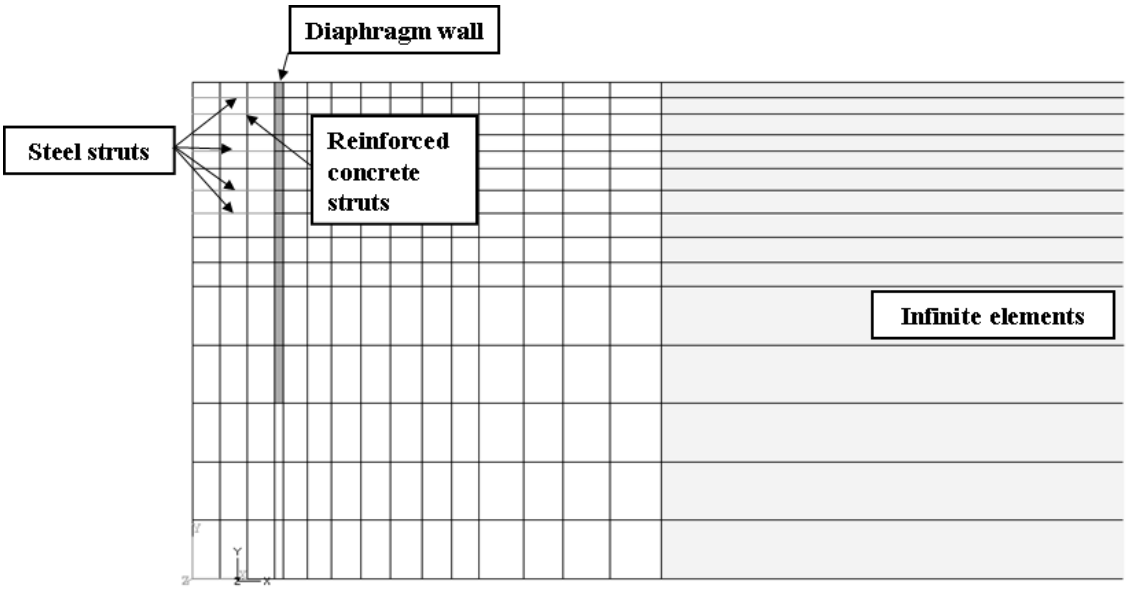

Figure 3.9 Continued

The elastic shear modulus (G), the logarithmic bulk modulus (the slope of unload/reload line, κ), the logarithmic hardening constant (the slope of isotropic compression line, λ), and the slope of the critical state line (M) for each soil layer were assumed to be unknown parameters. In this study, $\boldsymbol{\theta}$ are assumed to be independent. Therefore, $p(\boldsymbol{\theta})$ is written as the product of the prior marginal distributions, which are assumed to be lognormal based on the range of the each parameter. The prior means are based on previous research by Shao and Macari (2008), and the standard deviations are based on an assumed value for the coefficient of variation (COV) of 0.2 as summarized in Table 3.11.

A total of 32 variables, including model parameters (σ, ρ_V, ρ_H, ρ_{VH}), is estimated with the developed Bayesian probabilistic approach. There are no available

data after the first excavation stage. Therefore the Bayesian approach is applied starting from second excavation stage. The posterior statistics of $\boldsymbol{\Theta}$ after each excavation stage are used as the prior information for the subsequent stage. The calculation time to satisfy convergence criteria become exceedingly high for some excavation stages because of the large number of parameters involved, so a two-phase procedure was devised to accelerate convergence for each excavation step. In the first phase, starting values for the parameters in the finite element simulation are determined by minimizing the residual sum of squares (RSS) between the measured and simulated deformations. The results of the first phase are then fed into the second phase, in which the Bayesian probabilistic calculations are carried out as described in Figure 3.1.

After each subsequent excavation stage, the posterior statistics are obtained by updating the posterior statistics from the previous stage with the observations from the current stage. Tables 3.12–3.13 summarize the posterior statistics of the soil properties and model parameters after each excavation step considering measurement errors. As already observed for the previous case study, the uncertainty in the model parameters decreases as the excavation progresses.

Table 3.12 Posterior mean of the unknown soil parameters for the Caobao case history

	Stage	Soil 1	Soil 2	Soil 3	Soil 4	Soil 5	Soil 6	Soil 7
G (MPa)	2	1.900	4.100	0.978	5.860	8.970	10.560	17.600
	3	2.256	8.823	1.173	4.926	8.150	10.784	17.337
	4	2.458	7.581	1.271	4.525	7.968	10.815	17.215
	5	2.768	6.854	1.342	4.120	7.843	11.027	16.437
	6	3.579	5.576	1.348	4.056	6.975	11.486	15.684
κ	2	0.038	0.022	0.040	0.045	0.032	0.026	0.015
	3	0.032	0.024	0.036	0.036	0.030	0.024	0.016
	4	0.032	0.026	0.038	0.041	0.034	0.023	0.017
	5	0.033	0.025	0.039	0.040	0.037	0.022	0.018
	6	0.031	0.027	0.041	0.039	0.036	0.020	0.018
λ	2	0.184	0.165	0.193	0.190	0.184	0.171	0.150
	3	0.172	0.169	0.183	0.201	0.176	0.172	0.157
	4	0.173	0.170	0.182	0.203	0.177	0.176	0.160
	5	0.176	0.171	0.181	0.205	0.179	0.174	0.157
	6	0.178	0.169	0.179	0.204	0.181	0.176	0.158
M	2	0.940	0.860	0.890	1.000	0.980	0.940	1.100
	3	0.925	0.887	0.845	1.083	0.962	0.972	1.151
	4	0.963	0.884	0.866	1.128	0.913	1.018	1.218
	5	0.971	0.913	0.887	1.135	0.937	1.039	1.234
	6	0.984	0.934	0.862	1.169	0.954	1.054	1.266

Table 3.13 Posterior statistics of the unknown model parameters for the Caobao case history

Stage	σ		ρ_V		ρ_H		ρ_{VH}	
	Mean	Standard deviation	Mean	Standard deviation	Mean	Standard deviation	Mean	Standard deviation
2	1.352	2.791	0.092	0.144	0.144	0.161	0.140	0.122
3	3.473	2.151	0.104	0.132	0.113	0.132	0.132	0.162
4	3.304	1.864	0.123	0.164	0.130	0.123	0.123	0.093
5	4.182	1.640	0.112	0.123	0.081	0.091	0.154	0.074
6	4.494	1.563	0.080	0.091	0.120	0.080	0.164	0.091

Table 3.14 and Table 3.15 summarized the *MAPE* values for each excavation stage. The *MAPE* values from the results based on RSS method in Shao and Macari (2008) are also reported in the table for comparison purpose The diagonal terms in the tables describe the quality of the fit of the proposed probabilistic framework for the current stage, while the lower diagonal terms represent the quality of the prediction compared to the measurements in the following stages. The diagonal terms are smaller than the others because the results were derived using also the measurements for the same stage. The *MAPE* values are also affected by the chosen model's ability to fully capture the complexity of the soil profile and soil-structure response to the excavation. This is evident when the *MAPE* values increase or decrease along each column of Table 3.14 or Table 3.15. Each time the excavation enters a new soil layer, which the data have not fully characterized yet, the prediction of future excavation stages becomes less accurate because the model parameters have not been adjusted based on the information specific to that particular soil layer. As the excavation proceeds, more information is

available and the accuracy of the prediction increases and the *MAPE* values decrease. The *MAPE* values continue to decrease from left to right in the table as more data is integrated into the analysis. Finally, when measurement errors are considered, the *MAPE* values increase due to the effect of additional uncertainty in the data.

Table 3.14 *MAPE* values for the Caobao case history without measurement errors

%	Stage 2	Stage 3	Stage 4	Stage 5	Stage 6
Stage 2	24.06 (31.39)[1)]				
Stage 3	33.58 (49.44)	34.86 (30.05)			
Stage 4	32.12 (37.87)	25.44 (28.44)	18.14 (15.61)		
Stage 5	16.18 (31.59)	16.20 (23.55)	11.28 (16.46)	11.54 (15.10)	
Stage 6	20.44 (21.07)	16.53 (16.83)	16.95 (11.22)	9.04 (9.62)	7.74 (8.63)

1) ( ) = Shao and Macari (2008) results

Table 3.15 *MAPE* values for the Caobao case history with measurement errors

%	Stage 2	Stage 3	Stage 4	Stage 5	Stage 6
Stage 2	24.53				
Stage 3	37.04	38.52			
Stage 4	35.47	28.12	23.61		
Stage 5	20.18	19.73	15.67	17.20	
Stage 6	21.77	18.29	19.17	12.58	10.73

Although *MAPE* values obtained with the proposed approach are generally, but not always, lower than those obtained by Shao and Macari (2008), the two methods could be considered roughly equivalent for the prediction of deformation profiles. The

greatest advantage of the proposed method, however, is in its probabilistic framework, which gives predictions of deformations as well as the full probabilistic characterization of the variables. This advantage allows the evaluation of credible intervals for each prediction and sets the stage for a reliability analysis. Eventually, the framework can be used for the development of fragility curves, which can be used to make key decisions in the assessment of the excavation process and for a reliability-based optimal design of the excavation system.

The *MAPE* values describe the quality of the fit in an average sense. At each step, predictions of deformations for subsequent excavation stages calculated after measurements collected at stage 2, 3, 4, and 5, respectively, were considered in the analysis shown in Figures 3.10–3.13. After each excavation stage, the figure is updated because new information is available. The predicted values based on the Bayesian probabilistic framework capture accurately the overall settlement and horizontal displacement profiles, as well as the value and the location of the maximum surface settlement and horizontal displacement, which are closely monitored in excavation projects as indicators of overall performance. These figures also show comparisons among deformations predicted using the proposed probabilistic method, previous research (Shao and Macari 2008), and field measurements.

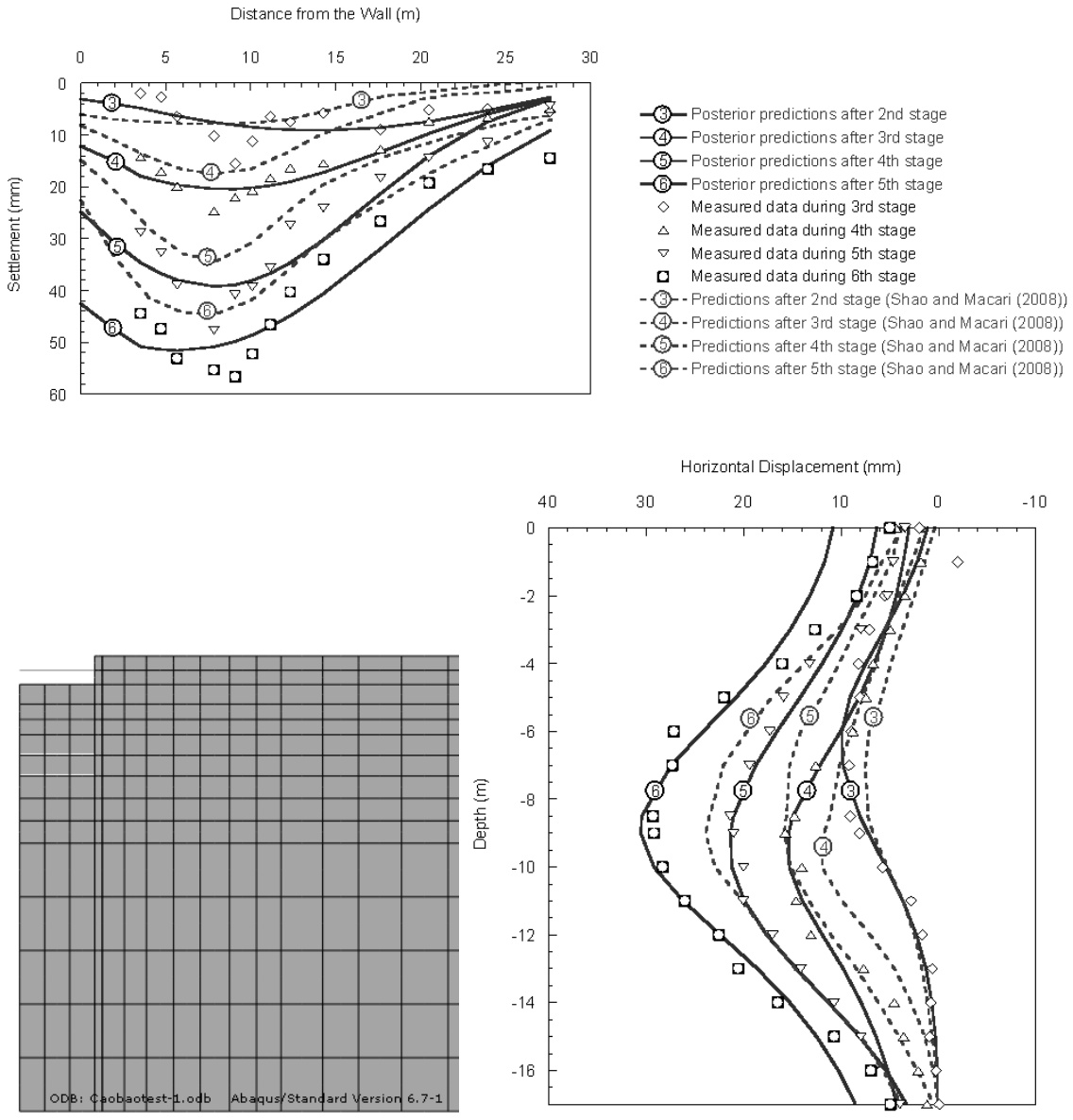

Figure 3.10 Comparison of measured and predicted soil movement based on posterior estimates for the Caobao subway case history after stage 2

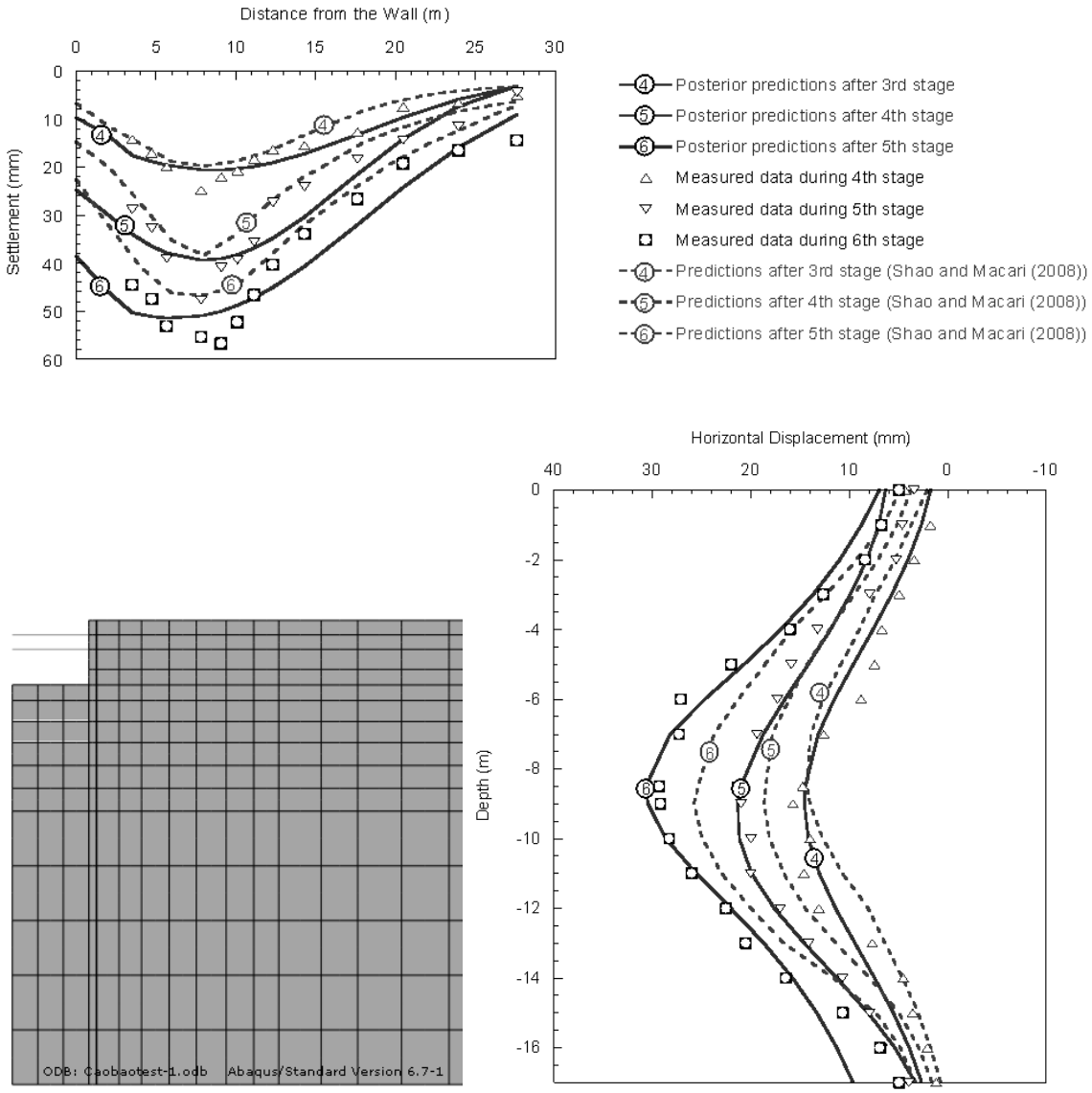

Figure 3.11 Comparison of measured and predicted soil movement based on posterior estimates for the Caobao subway case history after stage 3

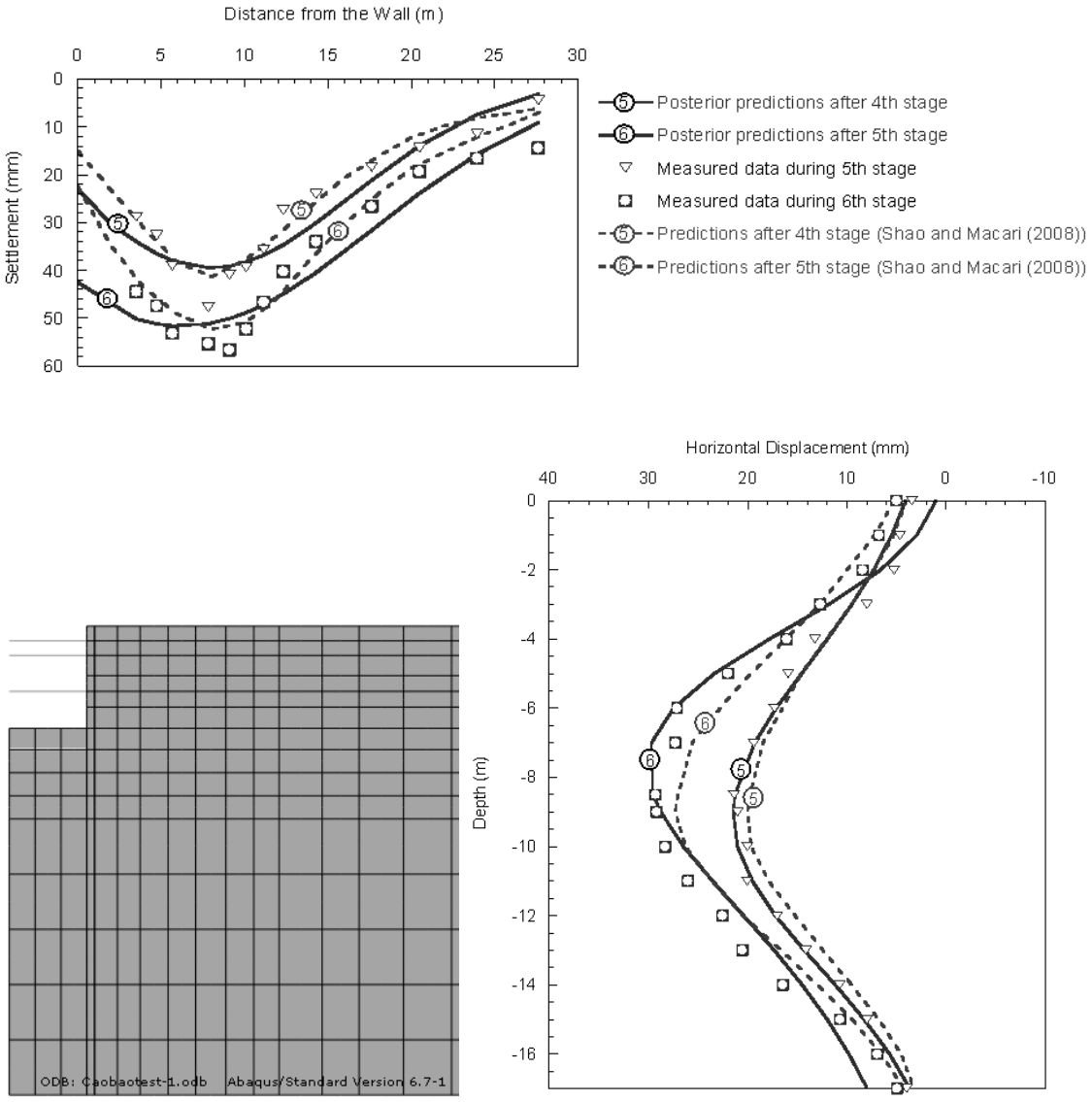

Figure 3.12 Comparison of measured and predicted soil movement based on posterior estimates for the Caobao subway case history after stage 4

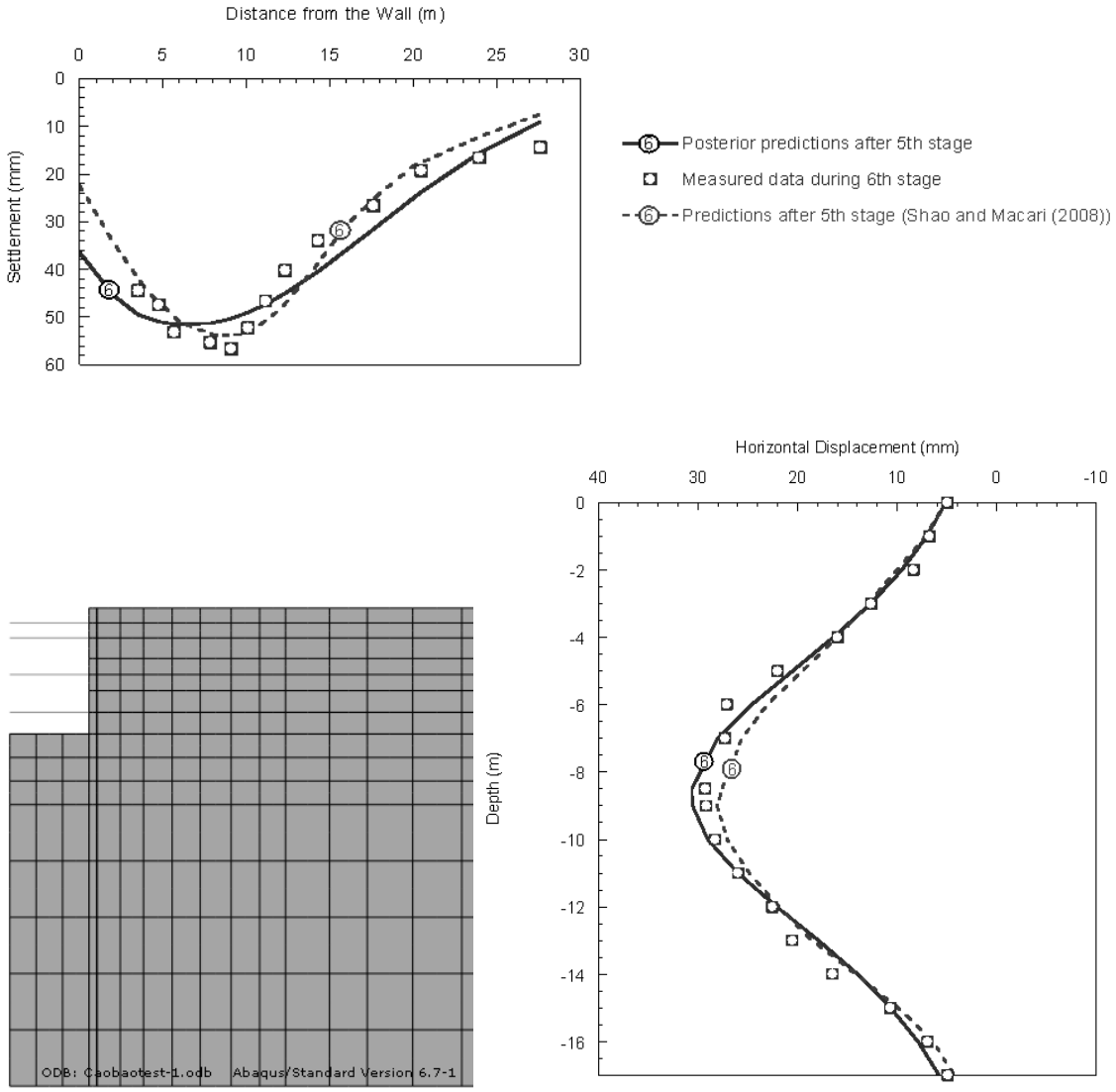

Figure 3.13 Comparison of measured and predicted soil movement based on posterior estimates for the Caobao subway case history after stage 5

Credible intervals can be obtained in addition to the means of the predicted soil movements as shown in Figure 3.14 for the prediction results after each excavation stage. As the excavation proceeds, the width of the credible interval decreases because more available information reduces the uncertainties.

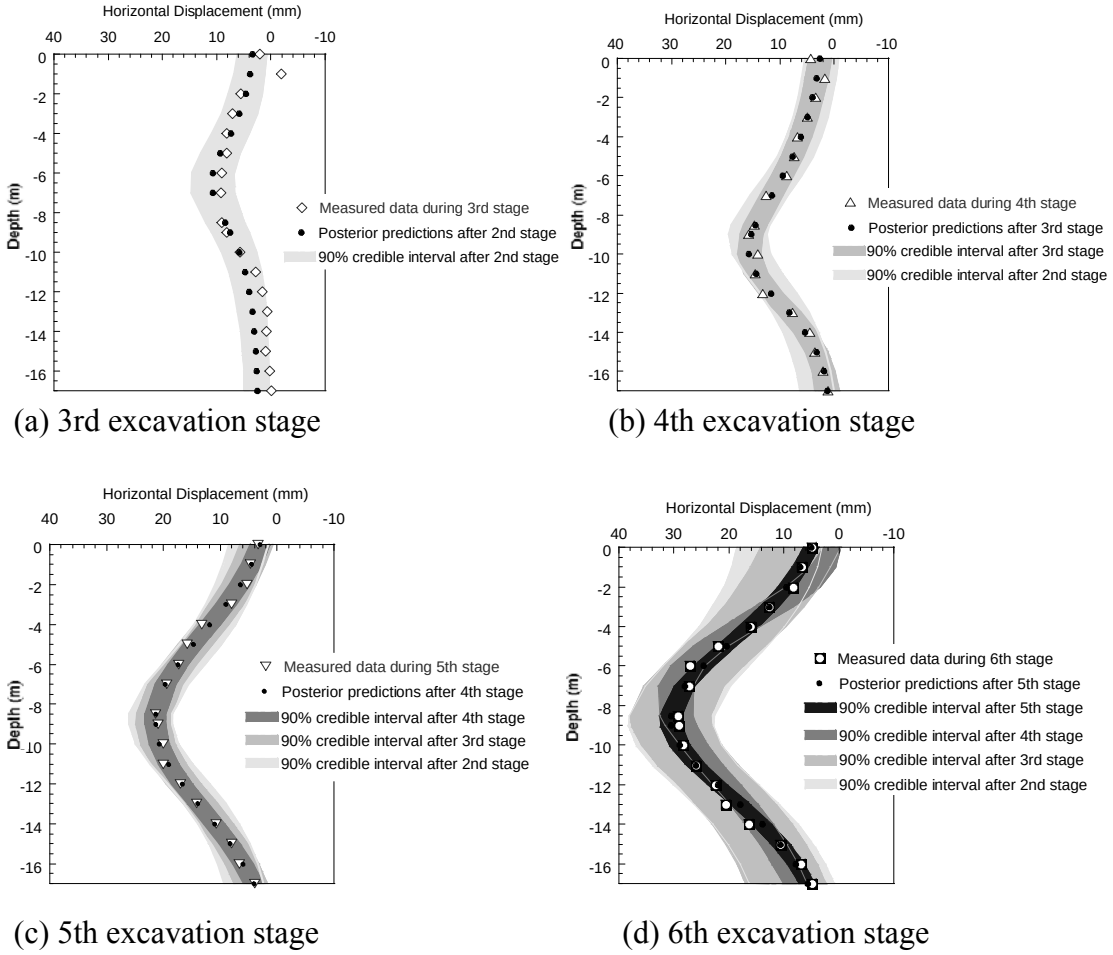

(a) 3rd excavation stage (b) 4th excavation stage

(c) 5th excavation stage (d) 6th excavation stage

Figure 3.14 Comparison in the range of predicted soil movement after each incremental stage for the Caobao subway case history

3.4 Conclusions

This section presents the application of a newly developed Bayesian probabilistic method to estimate the soil properties and predict the deformations in two supported excavation case histories. The two well documented case histories are the Lurie Research Center excavation project in Evanston, Illinois and the Caobao subway excavation project in Shanghai. A MATLAB-based application that can be connected to the general finite element software (i.e., ABAQUS 2003) was developed to automate of

the computer simulations. The two case histories demonstrated the ability of the proposed Bayesian probabilistic method to provide accurate estimates of the deformations in supported excavation problems accounting for all source of information. The estimate of the soil properties and prediction of the deformations in future excavation stages are also updated as new data become available during the excavation process.

It is noted that since the input soil properties and model parameters in the probabilistic Bayesian analysis are updated continuously as the excavation proceeds, some shortcomings of a simplistic constitutive model can be somewhat counteracted by the newly updated parameters. These parameters are used for the prediction of the next steps. From this point of view, the selection of the soil constitutive model is not as critical as in conventional numerical analyses, as long as the model and its associated parameters work together to give a good prediction. In this sense, the calculated parameters perhaps are not real soil properties in the conventional sense, but the properties which reflect overall effects (heterogeneity, anisotropy, boundary conditions, and stress state etc.) associated with the particular soil model and project.

The greatest advantage of the proposed method is in its probabilistic framework, which gives predictions of deformations as well as the full probabilistic characterization of the variables. This advantage allows the evaluation of credible intervals for each prediction and sets the stage for a reliability analysis. Eventually, the framework can be used for the development of fragility curves, which can be used to make key decisions in

the assessment of the excavation process and for a reliability-based optimal design of the excavation system.

4. A BAYESIAN FRAMEWORK TO PREDICT DEFORMATIONS DURING SUPPORTED EXCAVATIONS USING A SEMI-EMPIRICAL APPROACH

Construction of supported excavation systems inevitably causes ground movements including horizontal wall displacement and surface settlement. These ground movements are generally predicted in the design stage by deterministic empirical/semi-empirical methods. These methods, however, do not account for the site-specific conditions, the information that becomes available as the excavation proceeds, and the relevant uncertainties. A Bayesian framework is proposed to predict the ground movements using a semi-empirical approach and to update the predictions in the later stages of excavation based on recorded deformation measurements. The predictions are probabilistic and account for the relevant uncertainties. As an application, the proposed framework is used to predict the three-dimensional deformation shapes at four incremental excavation stages of an actual supported excavation project. The developed approach can be used for the design of optimal revisions of supported excavation systems based on simple calculations rather than complex finite element analysis.

4.1 Introduction

Evaluating the magnitude and distribution of ground movements adjacent to a supported excavation is an important part of the design process, particularly when excavating in an urban environment. The performance of supported excavations is a function of a large

number of interdependent factors such as the ground conditions, type/stiffness of retaining wall, workmanship, construction sequencing, time effects and geometrical boundary conditions. Structural design, empirical/semi-empirical, theoretical limit state soil mechanics methods, and numerical modeling have been used to design safe and cost effective excavation support systems.

Although numerical modeling is a powerful tool, it can be time consuming, requires considerable training for implementation and interpretation of results, and needs values for several input variables for which information is often not available. These issues make numerical analysis impractical for many applications. Furthermore, it does not fully account for all factors involved in the design, construction, and resulting ground response (Moormann 2004; Fuentes and Devriendt 2010). Therefore, empirical/semi-empirical methods are most commonly used to predict the induced ground movements due to a supported excavation. Empirical/semi-empirical methods have five major limitations. First, designs based on empirical/semi-empirical methods can be overly conservative, especially when dealing with layered soil conditions and complex geometries (Long 2001; Finno et al. 2007). Second, much of the current empirical/semi-empirical methods evolved from important empirical observations collected since the 1940's with the construction of the subway systems in Berlin, Chicago, New York, and Oslo (Terzaghi 1943; Peck 1969). Construction materials and support systems have been improved to both enhance safety and reduce ground movements. Third, the empirical/semi-empirical methods do not account for the site-specific characteristics of the soil and loading conditions, and do not incorporate

information from the field measurement data as they become available during the excavation process. Fourth, the empirical/semi-empirical methods do not provide three dimensional deformation profiles but only the magnitude of the maximum deformation with no indication of its location for the horizontal displacement. Fifth, they do not account for the uncertainty in the estimates of the deformations and therefore, they cannot be used to assess the degree of safety of a design or for an optimal reliability-based design.

An adequate representation of model uncertainty is important for reliability analyses based on geotechnical analysis models. A framework for characterizing model uncertainty using observation data has been proposed by several studies (Zhang et al. 2009; Tang et al. 2010). A Bayesian probabilistic framework was proposed to assess soil properties and model uncertainty and to better predict excavation-induced deformations by updating pertinent prior information using field measurement data (Park et al. 2010a). This method calculated the predictions using the general finite element software ABAQUS embedded in a MATLAB®-based application for Bayesian updating of the material parameters and model uncertainty. However, the predictions based on this method require significant computational effort, limiting the appeal of their use.

This study presents a Bayesian framework that addresses these five limitations and the developed framework is used to provide a simple and straightforward formulation that allows updating empirical/semi-empirical charts based on site-specific deformation measurements. The proposed approach continuously updates the model parameters as new measurements become available and provides unbiased predictions of

the three-dimensional deformation shapes during multiple construction stages of supported excavations. The proposed approach can properly account for the relevant uncertainties, so that the actual reliability of the supported excavation system and of the adjacent structures can be assessed. As an application, the proposed framework is used to predict the three-dimensional deformation shapes at four incremental excavation stages of an actual supported excavation project for the Robert H. Lurie Medical Research Building in Evanston, Illinois. The proposed approach can also be used for an adaptive reliability-based optimal design of the excavation system in which the design is modified after each excavation stage to minimize costs and maintain a minimum reliability requirement.

4.2 Excavation-induced Ground Movements by Empirical and Semi-empirical Methods

Several empirical and semi-empirical methods are available to predict the excavation-induced maximum horizontal displacement (Mana and Clough 1981; Wong and Broms 1989; Clough and O'Rourke 1990; Hashash and Whittle 1996; Addenbrooke et al. 2000; Kung et al. 2007) and the surface settlement profile (Caspe 1966; Peck 1969; Mana and Clough 1981; Clough and O'Rourke 1990; Ou et al. 1993; Hashash and Whittle 1996; Hsieh and Ou 1998; Kung et al. 2007). Analysis of excavation-induced ground movements generally consists of the following steps: (1) estimate the maximum horizontal displacement, $\delta_{h,\max}$, (2) estimate the deformation ratio, $\theta_R = \delta_{v,\max} / \delta_{h,\max}$,

where $\delta_{v,\max}$ is the maximum surface settlement, (3) calculate $\delta_{v,\max}$, and (4) estimate the surface settlement profile.

For the estimation of $\delta_{h,\max}$, Mana and Clough (1981) performed parametric finite element (FE) studies comparing 11 published case histories in soft to medium-stiff clays to evaluate the major factors affecting their response. They found that strong correlations could be established between excavation system movement and the safety against basal heave. They proposed nondimensionalized design charts to estimate $\delta_{h,\max}$, $\delta_{v,\max}$, and the surface settlement profile as a function of: (1) the factor of safety against basal heave, (2) soil stiffness, (3) strut stiffness, (4) strut preloads, and (5) excavation width. Wong and Broms (1989) suggested a simple procedure to estimate the horizontal displacement, δ_h, of braced flexible sheet plie walls in clay. They investigated the effects of undrained shear strength, depth and width of the excavation, penetration depth, depth to hard stratum beneath the excavation, and wall stiffness using FE analyses.

Clough and O'Rourke (1990) proposed the normalized semi-empirical chart shown in Figure 4.1 to estimate $\delta_{h,\max}$ for excavations in soft to medium soft clay. This chart provides curves of the normalized horizontal displacement, $\delta_{h,\max} / H_e$, versus the system stiffness, $EI / \gamma_w h_{avg}^4$, where $H_e =$ the excavation depth, $EI =$ the wall stiffness, $\gamma_w =$ the unit weight of water, and $h_{avg} =$ the average support spacing. The curves are parametrized with respect to the load-resistance ratio, L_R, against basal heave given by Terzaghi (1943) as

$$L_R = \frac{5.7\theta_{Sub}B}{(\gamma H_e + q)B - \theta_{Suh}H_e} \tag{4.1}$$

where, θ_{Sub} and θ_{Suh} = the undrained shear strength above and below the excavation, respectively, B = the width of the excavation, γ = the unit weight of the soil, and q = the surcharge load.

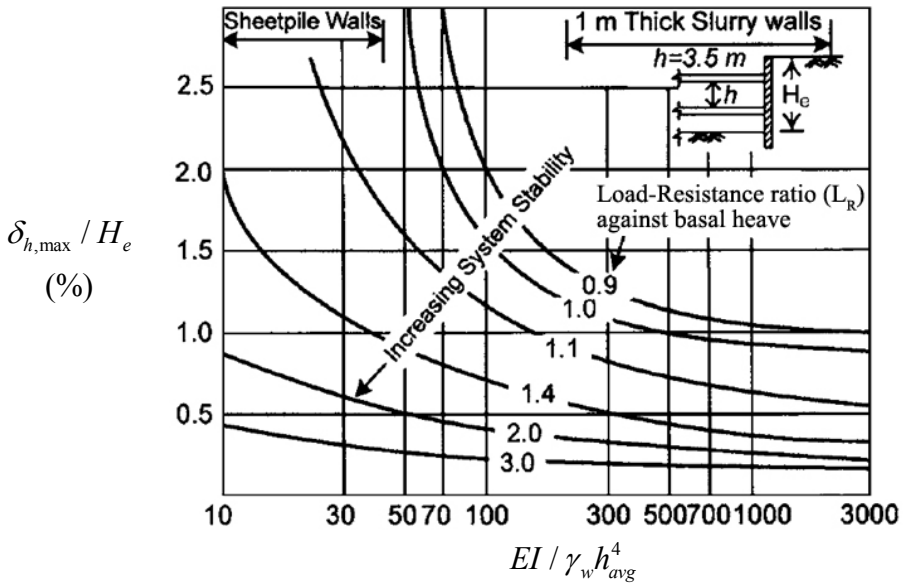

Figure 4.1 Design charts for maximum horizontal displacements (Modified from Clough and O'Rourke 1990)

Hashash and Whittle (1996) investigated the effects of wall embedment depth, support conditions, and stress history profile on the undrained deformations for a braced diaphragm wall in a deep clay deposit. They proposed design charts to estimate $\delta_{h,\max}$, $\delta_{v,\max}$, and the centerline heave as functions of h_{avg}, H_e, and the stress history profile. Addenbrooke et al. (2000) addressed the effects of different initial stress regimes and

various values of prop stiffness for the internal supports to the multipropped support excavation systems in stiff clay. They showed that walls with different support span distances, h_{avg}, and different values of system stiffness could have the same $\delta_{h,\max}$ and the same surface settlement profile if support systems have the same displacement flexibility number, EI / h_{avg}^5. More recently, Kung et al. (2007) developed a semi-empirical equation based on a database of 33 case histories and artificial FE analyses through regression analysis to estimate $\delta_{h,\max}$.

To evaluate the surface settlements and their profiles due to excavations, Caspe (1966) proposed a procedure by which the surface settlements could be estimated provided that the horizontal displacements of the wall, δ_h, were known. He also related the total cross sectional area of the horizontal displacement profile to the total area of the surface settlement profile through Poisson's ratio. Peck (1969) suggested the deformation behaviour was primarily dependent upon the soil type through which an excavation was made. The design chart was developed mostly on monitoring data adjacent to braced steel sheet piles and soldier pile walls with lower system stiffness. He classified soil into three types according to their characteristics: (1) Sand and soft to stiff clay, (2) Very soft to soft clay to a limited depth below the bottom of the excavation, (3) Very soft to soft clay to a significant depth below the bottom of the excavation.

Clough and O'Rourke (1990) proposed dimensionless settlement profiles for estimating surface settlements for the different soil types as shown in Figure 4.2. They found that the $\delta_{v,\max}$ due to the excavation could be conservatively taken to be equal to

$\delta_{h,\max}$. Therefore, they also proposed that Figure 4.1 could be used to predict the maximum surface settlement as well as the maximum horizontal displacement.

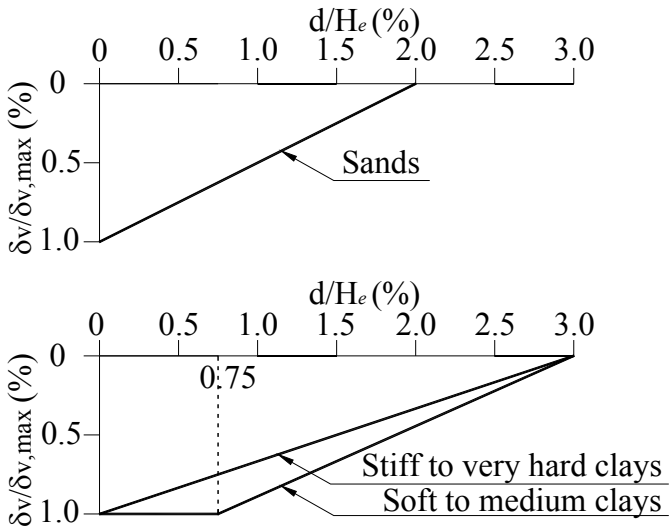

Figure 4.2 Design charts for estimating the profile of surface settlement for different soil types (Modified from Clough and O'Rourke 1990)

Ou et al. (1993) proposed a trilinear line for predicting the spandrel-type surface settlement profile, based on the average value of the observed settlement profiles of 10 excavation histories in Taipei. Hsieh and Ou (1998) proposed a method for estimating the ground surface settlement for both spandrel and concave settlement profiles based on a regression analysis, given the deflection shape of the wall. They suggested that $\delta_{v,\max}$ could be estimated based on the deformation ratio, $\theta_R = \delta_{v,\max} / \delta_{h,\max}$, and also noted that θ_R generally falls in the range of 0.5 to 1.0 for soft to medium clays based on excavation case-history data. More recently, Kung et al. (2007) developed semi-empirical

regression equations to estimate $\delta_{v,\max}$, θ_R, and the surface settlement profile. For the surface settlement profile, they proposed the following expressions

$$\begin{aligned} \delta_v / \delta_{v,\max} &= \left(1.6 \times d / H_e + 0.2\right) && \text{for } 0 \le d / H_e \le 0.5 \\ \delta_v / \delta_{v,\max} &= \left(-0.6 \times d / H_e + 1.3\right) && \text{for } 0.5 \le d / H_e \le 2.0 \\ \delta_v / \delta_{v,\max} &= \left(-0.05 \times d / H_e + 0.2\right) && \text{for } 2.0 \le d / H_e \le 4.0 \end{aligned} \tag{4.2}$$

where, $\delta_v =$ the vertical settlement at a distance, d, from an excavation. In this study, we define the vector of unknown parameters $\boldsymbol{\theta}_{CO} = (\theta_{Sub}, \theta_{Suh}, \theta_R)$ to use Clough and O'Rourke chart for the estimation of $\delta_{h,\max}$ and $\delta_{v,\max}$.

4.3 Analytical Formulation of Semi-empirical Chart

To use the Clough and O'Rourke chart in a Bayesian framework, we need to define analytical expressions for the curves in the chart. A mathematical description of these curves is needed to update the predictions of the ground movements in the later stages of excavation based on the recorded deformation measurements. Since these curves are not defined by analytical relationships, the Box and Cox transformation (1964) is used to formulate the following analytical expression:

$$\left[\frac{\left(\delta_{h,\max} / H_e\right)^{(\theta_1+\theta_2 L_R)} - 1}{\left(\theta_1 + \theta_2 L_R\right)}\right] = \left(\theta_3 + \theta_4 L_R\right) + \left(\theta_5 + \theta_6 L_R\right)\left[\frac{\left(EI / \gamma_w h_{avg}^4\right)^{(\theta_7+\theta_8 L_R)} - 1}{\left(\theta_7 + \theta_8 L_R\right)}\right] \tag{4.3}$$

where, $\boldsymbol{\theta}_{BC} = (\theta_1, \ldots, \theta_8) =$ a set of unknown model parameters first estimated by fitting the model in Eq. (4.3) to the existing curves in the Clough and O'Rourke chart as shown in Figure 4.3, and later updated as deformation measurements become available.

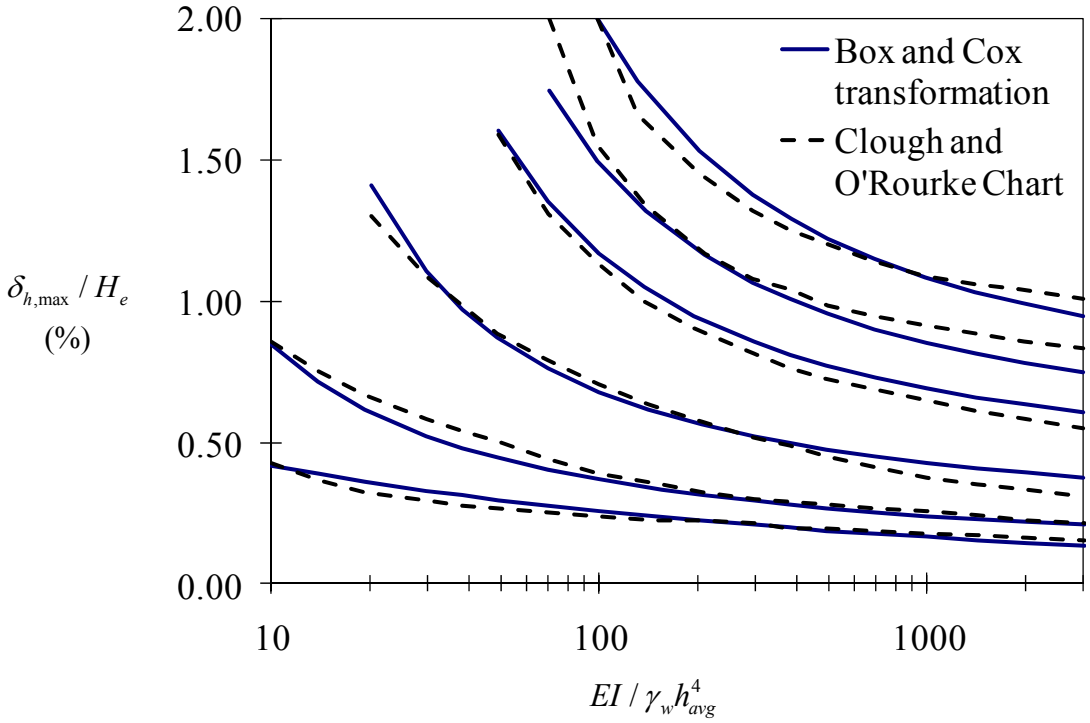

Figure 4.3 Comparison between the original Clough and O'Rourke chart and after applying Box and Cox transformation

4.4 Probabilistic Bayesian Semi-empirical Method

4.4.1 The three-dimensional profile of ground movements

Because Clough and O'Rourke chart does not provide estimate of the locations of $\delta_{h,\max}$ and $\delta_{v,\max}$ and the deformation profile, we develop shape functions for the three

dimensional deformation profiles to compare predicted deformations with the field measurement data that might be available at multiple locations.

This study adopts the shape of the three-dimensional deformation profiles perpendicular and parallel to an excavation as shown in Figure 4.4. These shape functions are established after consideration of numerous alternatives with the objective of capturing the correct deformation shape while maintaining a relatively simple form. The three-dimensional ground movement distribution around an excavated area is predicted using a combination of these shape functions, an assessment of the maximum ground deformation, and knowledge of the geometry of the excavation. After $\delta_{h,\max}$ and $\delta_{v,\max}$ are computed, the following procedure is proposed to predict the three-dimensional ground movements:

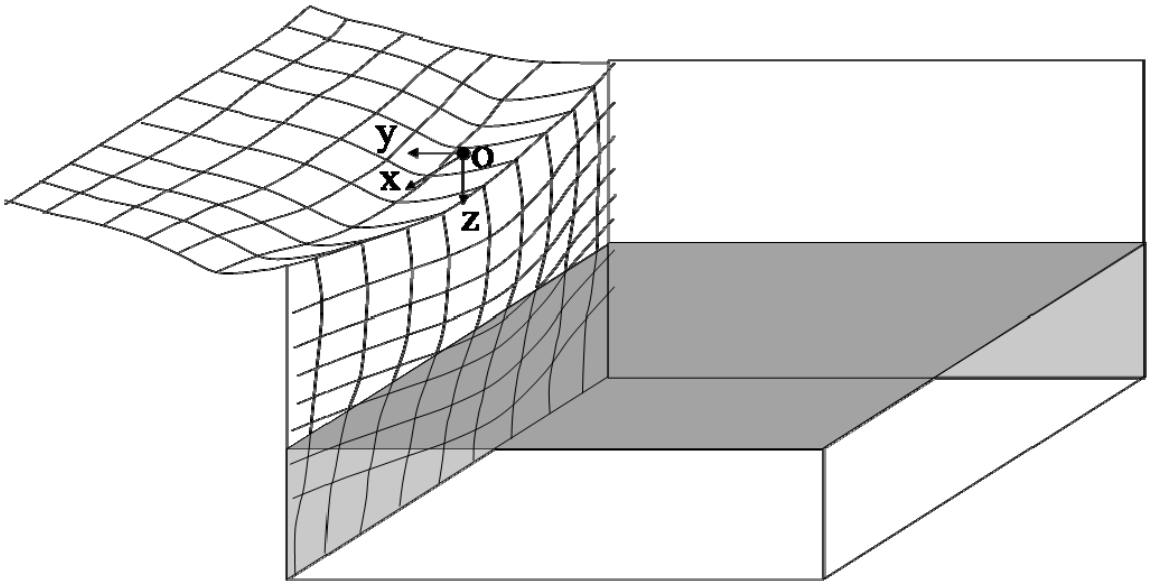

Figure 4.4 Conceptual view of the three-dimensional ground movements around an excavated area

(1) The horizontal displacement profile at depth is determined using the following double S-shape function (Gardoni et al. 2007):

$$f_h(z) = \begin{cases} f_u(z) & z \le \theta_{h,\max} \\ f_l(z) & z > \theta_{h,\max} \end{cases} \tag{4.4}$$

where, $f_u(z)$ and $f_l(z) =$ two S-shape functions defined one above and one below $\theta_{h,\max}$ which is the unknown location of $\delta_{h,\max}$ in the z direction,

$$\begin{aligned} f_u(z) &= \delta_{h,\max}\left[\frac{\theta_{u1}-(z-\theta_{u3})}{\theta_{u1}}\right]^{\theta_{u2}+1} \times\left[\left(\frac{\theta_{u1}-z}{\theta_{u1}}\right)(\theta_{u2}+1)-(\theta_{u2}+2)\right]+\delta_{h,\max}, \\ f_l(z) &= \delta_{h,\max}\left[\frac{\theta_{l1}-(z-\theta_{l3})}{\theta_{l1}}\right]^{\theta_{l2}+1} \times\left[\left(\frac{\theta_{l1}-z}{\theta_{l1}}\right)(\theta_{l2}+1)-(\theta_{l2}+2)\right]+\delta_{h,\max} \end{aligned} \tag{4.5}$$

and θ_{u1}, θ_{u2}, θ_{u3}, θ_{l1}, θ_{l2}, θ_{l3} = unknown model parameters. The location of $\delta_{h,\max}$ is assumed at the center of the excavation in the x direction. The $\theta_{h,\max}$ in the z direction needs to be estimated and updated using the field measurement data. When z approaches $\theta_{h,\max}$, the values of $f_u(z)$ and $f_l(z)$ gradually converge to $\delta_{h,\max}$ under the following conditions,

$$\begin{aligned} \theta_{h,\max} &= \theta_{u1}+\theta_{u3} \text{ or } \theta_{h,\max} = -\theta_{u1}/(1+\theta_{u2}) \\ \theta_{h,\max} &= \theta_{l1}+\theta_{l3} \text{ or } \theta_{h,\max} = -\theta_{l1}/(1+\theta_{l2}) \end{aligned} \tag{4.6}$$

(2) The horizontal displacement parallel to an excavation at depth z is defined by the complementary error function (Finno and Roboski 2005),

$$f_h(x,z) = f_h(z)\left\{1-\frac{1}{2}\text{erfc}\left[\frac{\left(B/2-|x|-\theta_{h1}\right)}{\theta_{h2}}\right]\right\} \tag{4.7}$$

where, θ_{h1} and θ_{h2} = unknown parameters, and $\text{erfc}(x)$ = the complementary error function which is defined as

$$\text{erfc}(x) = \frac{2}{\sqrt{\pi}}\int_x^{\infty} e^{-t^2}\,dt = 1-\text{erf}(x) \tag{4.8}$$

where, $\text{erf}(x)$ = the error function.

(3) The ground surface settlement profile in a direction perpendicular to the excavation at $x = 0$ is estimated using a shifted truncated lognormal distribution,

$$f_v(y) = \frac{1}{\sqrt{2\pi}\theta_{v1}(y-\theta_{v2})}\times\exp\left\{-\frac{1}{2}\left[\frac{\ln(y-\theta_{v2})-\theta_{v3}}{\theta_{v1}}\right]^2\right\}\times\frac{1}{1-F_Y(0)} \tag{4.9}$$

where, θ_{v1}, θ_{v2}, and θ_{v3} = unknown parameters, and

$$F_Y(0) = \frac{1}{2}\left\{1-\text{erf}\left[\frac{\ln(-\theta_{v2})-\theta_{v3}}{\sqrt{2}\theta_{v1}}\right]\right\} \tag{4.10}$$

The location of $\delta_{v,\max}$ is assumed to be at the center of the excavation, and the distance from the excavation, $\theta_{v,\max}$, needs to be estimated and updated from the field measurement data.

(4) The surface settlement parallel to the excavation at distance y is described by the complementary error function

$$f_v(x,y) = f_v(y)\left\{1-\frac{1}{2}\text{erfc}\left[\frac{\left(B/2-|x|-\theta_{v4}\right)}{\theta_{v5}}\right]\right\} \tag{4.11}$$

where, θ_{v4} and θ_{v5} = unknown parameters.

The four shape functions $f_h(z)$, $f_h(x,z)$, $f_v(y)$, and $f_v(x,y)$ which are defined by $\boldsymbol{\theta}_{SF} = (\theta_{u1},\theta_{l1},\theta_{u2},\theta_{l2},\theta_{u3},\theta_{l3},\theta_{h1},\theta_{h2},\theta_{v1},\theta_{v2},\theta_{v3},\theta_{v4},\theta_{v5},\theta_{h,\max},\theta_{v,\max})$ describe the three-dimensional ground movements around the excavated area. The four functions describing the deformation profiles are summarized in Figure 4.5. Note that all the shape functions are mirrored about the centerline of the excavation to give a distribution along the full wall and they are constrained in such a way that when they meet at any locations the deformation value must be the same: $f_h(x=0,z) = f_h(z)$ and $f_v(x=0,y) = f_v(y)$. At the location of $\theta_{h,\max}$ and $\theta_{v,\max}$, the shape functions have maximum deformations and the derivatives should be zero: $f_h(x=0,\ z=\theta_{h,\max}) = \delta_{h,\max}$, $f_v(x=0,\ y=\theta_{v,\max}) = \delta_{v,\max}$, $f_h'(x=0, z=\theta_{h,\max}) = 0$ and $f_v'(x=0, y=\theta_{v,\max}) = 0$. These additional conditions reduce the number of unknown parameters by eliminating 4 unknown parameters from the following equations.

$$
\begin{aligned}
&\theta_{u3} = \theta_{h,\max} - \theta_{u1} \\
&\theta_{v1} = \left(\theta_{v,\max} - \theta_{v2}\right)\left[\theta_{v3} - \ln\left(\theta_{v,\max} - \theta_{v2}\right)\right] \Big/ \theta_{v,\max} \\
&\theta_{h1} \approx B/2 - 2.8\theta_{h2} \\
&\theta_{v4} \approx B/2 - 2.8\theta_{v5}
\end{aligned}
\tag{4.12}
$$

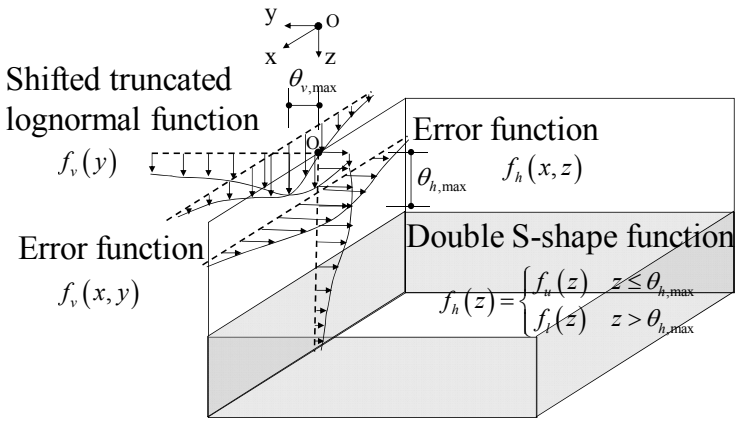

Figure 4.5 Different functions to describe the three-dimensional deformation profiles

4.4.2 Probabilistic models for deformations

A probabilistic model to estimate the deformations for the *k*th excavation stage at the *i*th location, D_{ki}, at a depth/location, z_i, is constructed as follows

$$
D_{ki}\left(z_i\right) = \hat{d}_{ki}\left(\boldsymbol{\theta}; z_i\right) + \sigma\varepsilon_{ki}, \quad k = 1,\ldots,m, \quad i = 1,\ldots,\left(n_V + n_H\right) \tag{4.13}
$$

where $\hat{d}_{ki}$ = the predicted deformation, $\boldsymbol{\theta} = (\boldsymbol{\theta}_{CO}, \boldsymbol{\theta}_{BC}, \boldsymbol{\theta}_{SF})$ = a set of unknown model parameters, $\sigma\varepsilon_{ki}$ = the model error, σ = the unknown standard deviation of the model error, ε_{ki} = a random variable with zero mean and unit variance, n_V = the number of points where the surface settlement is predicted, and n_H = the number of points where the horizontal displacement is predicted. This general formulation also can be applied to

estimate the $\delta_{h,\max}$ or $\delta_{v,\max}$ by using the Clough and O'Rourke chart. In that case, $D_{ki}(z_i) = D_k = \delta_{h,\max}$ or $\delta_{v,\max}$, $\hat{d}_{ki}(\boldsymbol{\theta}; z_i) = \hat{d}_k(\boldsymbol{\theta}_{CO}, \boldsymbol{\theta}_{BC}) =$ the predicted deformation $\delta_{h,\max}$ or $\delta_{v,\max}$ using the Clough and O'Rourke chart. Since the Clough and O'Rourke chart method do not provide the location of maximum deformation, z_i cannot be considered for the model formulation.

The correlation coefficients between ε_{ki} and ε_{kj} of any two horizontal displacements, ρ_H, any two surface settlements, ρ_V, and an horizontal displacement and a surface settlement, ρ_{VH}, all within the same excavation stage k, are additional unknown model parameters. Therefore, the correlation matrix for the kth excavation stage with $(n_V + n_H)$ prediction points can be written as

$$\mathbf{R} = \left(\begin{array}{c|c} \mathbf{R}_V & \mathbf{R}_{VH} \\ \hline \mathbf{R}_{HV} & \mathbf{R}_H \end{array} \right)_{(n_V+n_H)\times(n_V+n_H)} \tag{4.14}$$

where

$$\mathbf{R}_V = \begin{pmatrix} 1 & \cdots & \rho_V & \cdots & \rho_V \\ & \ddots & \vdots & & \vdots \\ & & 1 & \cdots & \rho_V \\ & \text{sym.} & & \ddots & \vdots \\ & & & & 1 \end{pmatrix}_{n_V \times n_V} \qquad \mathbf{R}_H = \begin{pmatrix} 1 & \cdots & \rho_H & \cdots & \rho_H \\ & \ddots & \vdots & & \vdots \\ & & 1 & \cdots & \rho_H \\ & \text{sym.} & & \ddots & \vdots \\ & & & & 1 \end{pmatrix}_{n_H \times n_H}$$

$$\mathbf{R}_{VH} = \begin{pmatrix} \rho_{VH} & \cdots & \rho_{VH} & \cdots & \rho_{VH} \\ & \ddots & \vdots & & \vdots \\ & & \rho_{VH} & \cdots & \rho_{VH} \\ & \text{sym.} & & \ddots & \vdots \\ & & & & \rho_{VH} \end{pmatrix}_{n_V \times n_H} \tag{4.15}$$

The covariance matrix of the model errors, $\boldsymbol{\Sigma}$, can be written as $\boldsymbol{\Sigma} = \mathbf{SRS}$, where $\mathbf{S}$ = the diagonal matrix of standard deviations σ. Finally, $\boldsymbol{\Theta} = (\boldsymbol{\theta}, \boldsymbol{\Sigma}) = (\boldsymbol{\theta}_{CO}, \boldsymbol{\theta}_{BC}, \boldsymbol{\theta}_{SF}, \boldsymbol{\Sigma})$ denotes the set of all unknown parameters in Eq. (4.13). In assessing the probabilistic model, three assumptions are made: (a) the homoskedasticity assumption (the model variance σ^2 is independent of $\boldsymbol{\theta}$), (b) the normality assumption (ε_{ki} follows the normal distribution), and (c) ε_{ki} and ε_{qj} at two different excavation stages ($k \neq q$) are uncorrelated.

The total deformation measurement and deformation estimate using the Clough and O'Rourke chart at the *k*th excavation stage can be written as

$$\begin{aligned} D_k &= \Delta D_1 + \cdots + \Delta D_k = \sum_{m=1}^{k} \Delta D_m \\ \hat{d}_k\left(\boldsymbol{\theta}_{CO}, \boldsymbol{\theta}_{BC}\right) &= \Delta\hat{d}_1\left(\boldsymbol{\theta}_{CO}, \boldsymbol{\theta}_{BC}\right) + \cdots + \Delta\hat{d}_k\left(\boldsymbol{\theta}_{CO}, \boldsymbol{\theta}_{BC}\right) = \sum_{m=1}^{k} \Delta\hat{d}_m\left(\boldsymbol{\theta}_{CO}, \boldsymbol{\theta}_{BC}\right) \end{aligned} \tag{4.16}$$

where $\Delta D_m = D_m - D_{m-1}$ = the incremental deformation at the *m*th excavation stage, $\Delta\hat{d}_m(\boldsymbol{\theta}_{CO}, \boldsymbol{\theta}_{BC}) = \hat{d}_m(\boldsymbol{\theta}_{CO}, \boldsymbol{\theta}_{BC}) - \hat{d}_{m-1}(\boldsymbol{\theta}_{CO}, \boldsymbol{\theta}_{BC})$ = the incremental deformation estimate at the *m*th excavation stage, and $D_0 = \hat{d}_0(\boldsymbol{\theta}_{CO}, \boldsymbol{\theta}_{BC}) = 0$. In our probabilistic model, the model error for each excavation stage is conditionally independent because the total deformation and deformation estimates at the current excavation stage are uncorrelated with those at the future excavation stage. Using Eq. (4.13) we can define the prediction residual as $\mathbf{r}_k(\boldsymbol{\theta}) = [r_{k1}(\boldsymbol{\theta}), \ldots, r_{k(n_V + n_H)}(\boldsymbol{\theta})]$ where $r_{ki}(\boldsymbol{\theta}) = [D_{ki}(z_i) - \hat{d}_{ki}(\boldsymbol{\theta}; z_i)]$. When the Clough and O'Rourke chart is used for the estimation of $\delta_{h,\max}$ and $\delta_{v,\max}$, we can define

the prediction residual as $r_{ki}(\boldsymbol{\theta}) = r_k(\boldsymbol{\theta}_{CO}, \boldsymbol{\theta}_{BC}) = [D_k - \hat{d}_k(\boldsymbol{\theta}_{CO}, \boldsymbol{\theta}_{BC})]$. If the deformation has been recorded at the *j*th stage, the deformation at the *k*th stage where $k > j$ can be obtained by adding the predicted incremental deformation ΔD_{j+1} ,…, ΔD_k to the measured deformation at the *j*th stage. It follows that

$$\begin{aligned} r_k\left(\boldsymbol{\theta}_{CO}, \boldsymbol{\theta}_{BC}\right) &= D_k - \hat{d}_k\left(\boldsymbol{\theta}_{CO}, \boldsymbol{\theta}_{BC}\right) \\ &= \left(\Delta D_{j+1} + \cdots + \Delta D_k\right) - \left[\Delta \hat{d}_{j+1}\left(\boldsymbol{\theta}_{CO}, \boldsymbol{\theta}_{BC}\right) + \cdots + \Delta \hat{d}_k\left(\boldsymbol{\theta}_{CO}, \boldsymbol{\theta}_{BC}\right)\right] \end{aligned} \tag{4.17}$$

In summary, there are 8 unknown parameters, $\boldsymbol{\theta}_{BC}$, in Eq. (4.3), 3 unknown parameters, $\boldsymbol{\theta}_{CO} = (\theta_{Sub}, \theta_{Suh}, \theta_R)$, 11 unknown parameters, $\boldsymbol{\theta}_{SF}$, in Eqs. (4.4)–(4.11), and 4 unknown parameters, $\boldsymbol{\Sigma} = (\rho_H, \rho_V, \rho_{VH}, \sigma)$ for a total of 26 unknown parameters, $\boldsymbol{\Theta} = (\boldsymbol{\theta}, \boldsymbol{\Sigma}) = (\boldsymbol{\theta}_{BC}, \boldsymbol{\theta}_{CO}, \boldsymbol{\theta}_{SF}, \boldsymbol{\Sigma})$ that need to be estimated and updated for each excavation stage.

4.5 Assessment of the Unknown Parameters

4.5.1 Bayesian model updating

The proposed probabilistic approach uses the Bayesian approach to incorporate the field measurements. After each excavation, the Bayesian updating is used to assess the unknown model parameters and also provides a convenient way to update the model as the new set of measurement data becomes available. In the Bayesian updating procedure, the posterior distribution, $p(\boldsymbol{\Theta} | \mathbf{D}_k)$, is estimated using the following rule (Box and Tiao 1992):

$$p\left(\boldsymbol{\Theta}\middle|\mathbf{D}_k\right)=\kappa L\left(\boldsymbol{\Theta}\middle|\mathbf{D}_k\right)p\left(\boldsymbol{\Theta}\right) \tag{4.18}$$

where $\kappa=[\int L(\boldsymbol{\Theta}\,|\,\mathbf{D}_k)\,p(\boldsymbol{\Theta})d\boldsymbol{\Theta}]^{-1}$ = normalizing factor, $L(\boldsymbol{\Theta}\,|\,\mathbf{D}_k)$ = likelihood function representing the objective information on $\boldsymbol{\Theta}$ contained in a set of measurement data $\mathbf{D}_k$, $p(\boldsymbol{\Theta})$ = prior distribution of $\boldsymbol{\Theta}$ defined before the measurement data are available.

Given *n* sets of independent deformation measurements, the posterior distribution can be updated after each new set of measurement data becomes available as

$$p\left(\boldsymbol{\Theta}\middle|\mathbf{D}_1,\ldots,\mathbf{D}_n\right)\propto p\left(\boldsymbol{\Theta}\middle|\mathbf{D}_1,\ldots,\mathbf{D}_{n-1}\right)L\left(\boldsymbol{\Theta}\middle|\mathbf{D}_n\right) \tag{4.19}$$

Because the probabilistic model is nonlinear in the unknown parameter $\boldsymbol{\Theta}$, a closed-form solution is not available and numerical solutions are the only option.

4.5.2 Prior distribution

The $p(\boldsymbol{\Theta})$ should be constructed using the knowledge available before the observations used to construct the likelihood function are made. In reality, we typically have information about the unknown parameters, prior to the excavation. The Bayesian approach requires such prior information in the form of a prior distribution of the unknown parameter.

4.5.3 Likelihood function

The objective information is entered through the likelihood function, $L(\boldsymbol{\Theta}\,|\,\mathbf{D}_k)$. The likelihood function describes the probability of a set of measurement data $\mathbf{D}_k$ for given

values of the model parameters $\boldsymbol{\Theta}$. Following Gardoni et al. (2002), the likelihood function can then be written as

$$L\left(\boldsymbol{\Theta}\middle|\mathbf{D}_k\right) \propto \left\{ \begin{array}{c} \prod\limits_{\text{equality data}} P\left[\sigma\varepsilon_k = r_k\left(\boldsymbol{\theta}_{CO},\boldsymbol{\theta}_{BC}\right)\right] \\ \times \\ \prod\limits_{\text{lower bound data}} P\left[\sigma\varepsilon_k > r_k\left(\boldsymbol{\theta}_{CO},\boldsymbol{\theta}_{BC}\right)\right] \\ \times \\ \prod\limits_{\text{upper bound data}} P\left[\sigma\varepsilon_k < r_k\left(\boldsymbol{\theta}_{CO},\boldsymbol{\theta}_{BC}\right)\right] \end{array} \right\} \times P\left\{ \begin{array}{l} \bigcap\limits_{i=1}^{(n_V+n_H)\ \text{except}\ \delta_{h,\max}\ \text{or}\ \delta_{v,\max}\ \text{location}} \left[\sigma\varepsilon_{ki} = r_{ki}\left(\boldsymbol{\theta}\right)\right] \end{array} \right\} \quad (4.20)$$

Based on the normality and homoskedasticity assumption, and independence at different excavation stages in addition to the transformation rule, we can write the likelihood function for the *k*th excavation stage as (Gardoni et al. 2002)

$$\begin{aligned} L\left(\boldsymbol{\Theta}\middle|\mathbf{D}_k\right) \propto & \left\{ \begin{array}{c} \prod\limits_{\text{equality data}} \left\{\frac{1}{\sigma}\varphi\left[r_k\left(\boldsymbol{\theta}_{CO},\boldsymbol{\theta}_{BC}\right)\right]\right\} \\ \times \\ \prod\limits_{\text{lower bound data}} \left\{\Phi\left[-r_k\left(\boldsymbol{\theta}_{CO},\boldsymbol{\theta}_{BC}\right)\right]\right\} \\ \times \\ \prod\limits_{\text{upper bound data}} \left\{\Phi\left[r_k\left(\boldsymbol{\theta}_{CO},\boldsymbol{\theta}_{BC}\right)\right]\right\} \end{array} \right\} \\ & \times\sigma^{-\left(n_V+n_H\right)}\left(2\pi\right)^{-\left(n_V+n_H\right)/2}\left|\mathbf{R}\right|^{-1/2}\exp\left[-\frac{1}{2\sigma^2}\mathbf{r}_k^T\left(\boldsymbol{\theta}\right)\mathbf{R}^{-1}\mathbf{r}_k\left(\boldsymbol{\theta}\right)\right] \end{aligned} \quad (4.21)$$

where $\varphi(\cdot)$ and $\Phi(\cdot)=$ the standard normal probability density and cumulative distribution functions. Because the Clough and O'Rourke chart only gives values of $\hat{d}_k(\boldsymbol{\theta}_{CO},\boldsymbol{\theta}_{BC})$ for $0.9 \le L_R \le 3.0$, one of three possible outcomes can be realized:

(1) The measured D_k is an equality data if $0.9 \le L_R \le 3.0$. In this case we can write $D_k = \hat{d}_k(\boldsymbol{\theta}_{CO}, \boldsymbol{\theta}_{BC}) + \sigma\varepsilon_k$ or $\sigma\varepsilon_k = r_k(\boldsymbol{\theta}_{CO}, \boldsymbol{\theta}_{BC})$;

(2) The measured D_k is a lower bound to the possible displacement if $L_R < 0.9$. In this case, we have $D_k < \hat{d}_k(\boldsymbol{\theta}_{CO}, \boldsymbol{\theta}_{BC}) + \sigma\varepsilon_k$ or $\sigma\varepsilon_k > r_k(\boldsymbol{\theta}_{CO}, \boldsymbol{\theta}_{BC})$;

(3) The measured D_k is an upper bound to the possible displacement if $L_R > 3.0$. In this case we have $D_k > \hat{d}_k(\boldsymbol{\theta}_{CO}, \boldsymbol{\theta}_{BC}) + \sigma\varepsilon_k$ or $\sigma\varepsilon_k < r_k(\boldsymbol{\theta}_{CO}, \boldsymbol{\theta}_{BC})$.

4.5.4 Posterior estimates

The $p(\boldsymbol{\Theta} | \mathbf{D}_k)$ describes the distribution of $\boldsymbol{\Theta}$ incorporating both the prior information and the objective information from the measurement data. Numerical solutions are the only option to compute the posterior statistics and the normalizing constant because the proposed model is nonlinear in the unknown parameters. In this study, a Markov Chain Monte Carlo (MCMC) algorithm is used for computing the posterior statistics. Markov chains are generated with the likelihood formulation of the probabilistic models based on the initial points and a prior distribution until a convergence criterion is met. We adopt the Geweke's convergence diagnostic to decide when to terminate the MCMC simulations (Geweke 1992). We terminate the simulation when the Geweke's convergence diagnostic is sufficiently large, i.e., larger than 0.95. Additional details

about MCMC can be found in Gilks et al. (1998), Gelman et al. (2004), and Robert and Casella (2004).

4.6 Application of the Proposed Bayesian Framework

The proposed probabilistic framework is applied to an actual supported excavation project for the Robert H. Lurie Medical Research Building in Evanston, Illinois. The excavation consisted of a 12.8 m deep cut and a flexible retaining system of PZ–27 sheet pile on all sides. Detailed description and ground response of the excavation are provided in Finno and Roboski (2005). Figure 4.6 shows a plan view of the approximately 80 by 68 m excavation area. Measurements of both lateral and vertical ground surface settlements were obtained from inclinometers and optical survey. Because of the proximity of the utilities and the use of a relatively flexible excavation support system, extensive monitoring locations were established around the site. To monitor the ground response to excavation activities, 150 surface survey points, 18 embedded settlement points and 30 utility points were installed on three surrounding streets prior to wall installation.

The soil profile consists of granular soils, including fill and sand layers, overlying a sequence of glacial clays of increasing shear strength with depth, as shown in Figure 4.7. Undrained shear strengths based on the results of vane shear tests are 29–43 kPa in the soft to medium clays and 105 kPa in the stiff clay. Figure 4.7 also shows the four distinct excavation stages and their corresponding depth, in addition to the average support spacing. Three levels of tieback anchors provided lateral support on the

south, west, and north walls. Two levels of tieback ground anchors were installed on the east wall due to the presence of the basement of the Prentice Pavilion.

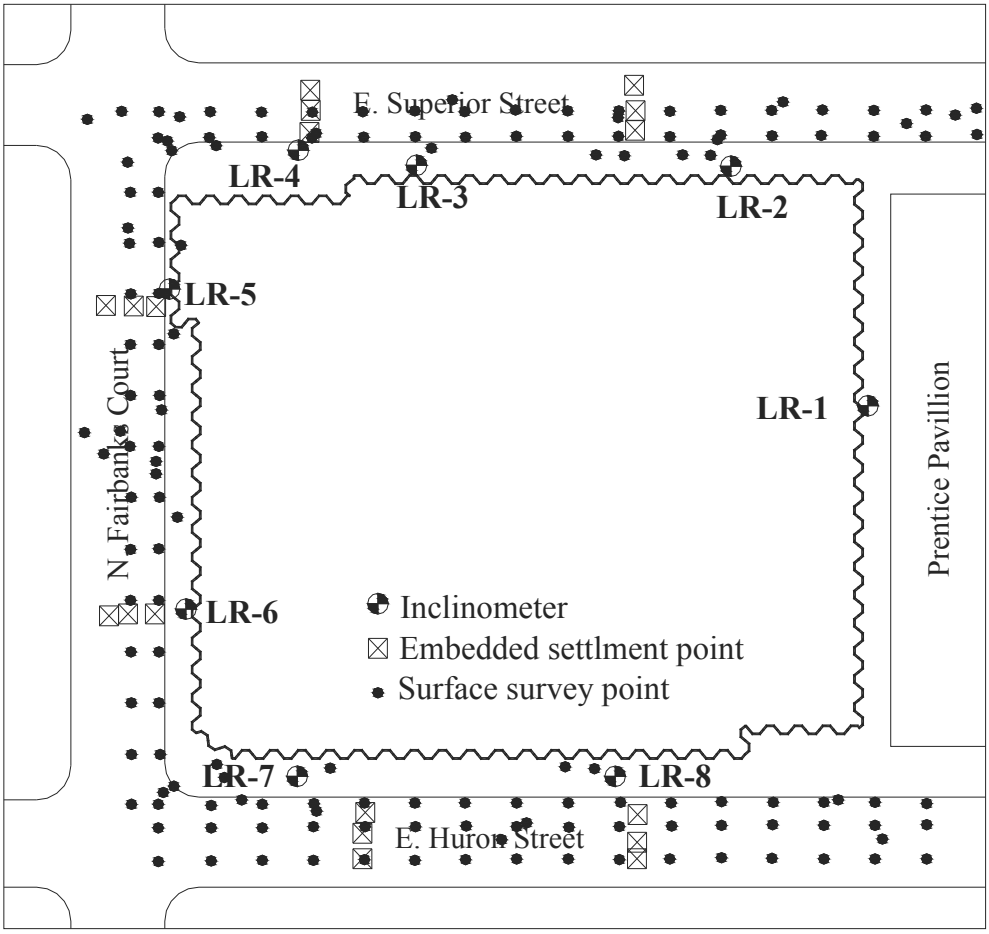

Figure 4.6 General layout of Lurie Center site instrumentation (Modified from Finno and Roboski 2005)

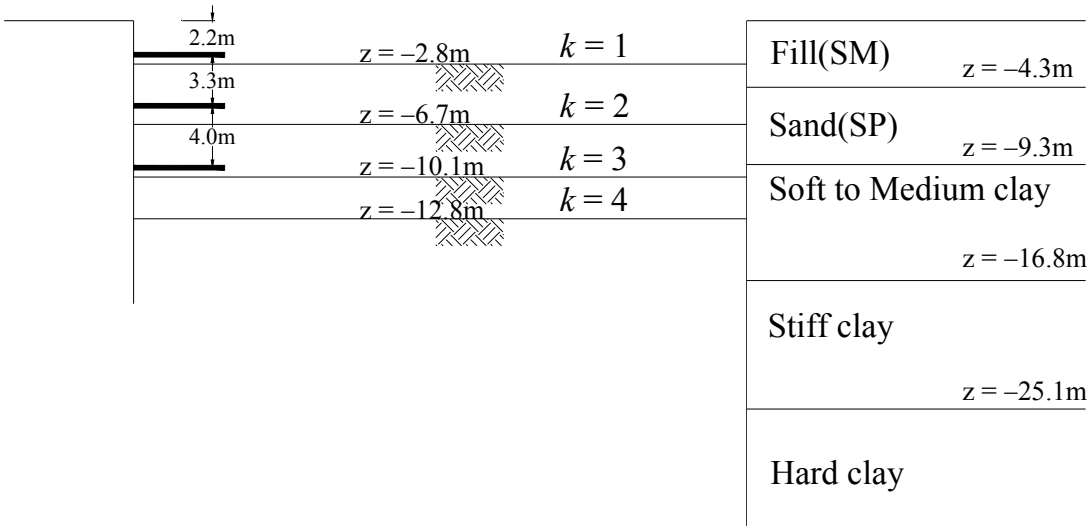

Figure 4.7 Soil stratigraphy and excavation stages at the Lurie Center site

Horizontal displacements measured by LR–2 on the north wall were not obtained because the inclinometer was damaged during the second stage of excavation. There were also site-specific restrictions, which prevented retrieval of complete horizontal displacement measurement data for every excavation stage in some inclinometers (LR–1 and LR–4). The joint prior distribution of $\boldsymbol{\Theta}$ is constructed by assuming that the parameters are statistically independent and that the marginal prior distributions are assumed based on the ranges of the parameters summarized in Table 4.1. The mean values for $\boldsymbol{\theta}_{CO}$ are based on previous research results (Finno and Roboski 2005). The mean values for $\boldsymbol{\theta}_{BC}$ are based on the initial fitting of the original Clough and O'Rourke chart, and the mean values for $\boldsymbol{\theta}_{SF}$ are determined from the previous observations of a nearby excavation site also in Chicago glacial deposits (Tu 2007). The standard deviations are based on an assumed value of 0.2 for the coefficient of variation (COV).

Table 4.1 Prior distributions, means, and standard deviations

Physical meaning	Parameter ranges	Distribution models	Mean	COV
Soil parameters ($\boldsymbol{\theta}_{CO}$)	$0 < \theta_{Sub} < \infty$	Lognormal	50.00	0.20
	$0 < \theta_{Suh} < \infty$	Lognormal	30.00	0.20
	$0 < \theta_{R} < \infty$	Lognormal	0.50	0.20
Shape function parameters ($\boldsymbol{\theta}_{SF}$)	$-\infty < \theta_{u1} < \infty$	Normal	10.00	0.20
	$-\infty < \theta_{l1} < \infty$	Normal	4.00×10^{7}	0.20
	$-\infty < \theta_{u2} < \infty$	Normal	0.10	0.20
	$-\infty < \theta_{l2} < \infty$	Normal	-2.00×10^{7}	0.20
	$-\infty < \theta_{u3} < \infty$	Normal	–5.00	0.20
	$-\infty < \theta_{l3} < \infty$	Normal	–5.00	0.20
	$-\infty < \theta_{h,\max} < \infty$	Normal	10.00	0.20
	$-\infty < \theta_{v,\max} < \infty$	Normal	1.40	0.20
	$-\infty < \theta_{h1} < \infty$	Normal	–0.20	0.20
	$-\infty < \theta_{h2} < \infty$	Normal	10.00	0.20
	$0 < \theta_{v1} < \infty$	Lognormal	0.40	0.20
	$-\infty < \theta_{v2} < \infty$	Normal	–1.00	0.20
	$-\infty < \theta_{v3} < \infty$	Normal	1.50	0.20
	$-\infty < \theta_{v4} < \infty$	Normal	–0.20	0.20
	$-\infty < \theta_{v5} < \infty$	Normal	10.00	0.20
Box and Cox transformation parameters for original Clough and O'Rourke chart ($\boldsymbol{\theta}_{BC}$)	$-\infty < \theta_{1} < \infty$	Normal	–0.52	0.20
	$-\infty < \theta_{2} < \infty$	Normal	–0.18	0.20
	$-\infty < \theta_{3} < \infty$	Normal	5.02	0.20
	$-\infty < \theta_{4} < \infty$	Normal	–1.79	0.20
	$-\infty < \theta_{5} < \infty$	Normal	–1.48	0.20
	$-\infty < \theta_{6} < \infty$	Normal	0.36	0.20
	$-\infty < \theta_{7} < \infty$	Normal	–0.50	0.20
	$-\infty < \theta_{8} < \infty$	Normal	0.22	0.20

Tables 4.2–4.5 summarize the posterior statistics of the unknown model parameters after each stage and for each side of the excavation. The uncertainty in the model parameters decreases as the excavation progresses.

Table 4.2 Posterior mean of the unknown soil parameters, θ_{CO}

Stage		θ_{Sub}	θ_{Suh}	θ_{R}
West side	1	60.18	6.89	5.37
	2	63.51	7.37	1.84
	3	68.39	8.26	0.70
	4	72.16	9.71	0.95
South side	1	65.86	7.68	6.18
	2	66.16	8.75	1.62
	3	70.43	9.08	0.59
	4	75.77	10.85	0.73
North side	1	63.27	7.16	5.89
	2	65.16	8.03	1.37
	3	69.36	8.85	0.67
	4	73.89	10.17	0.75

Table 4.3 Posterior mean of the unknown shape function parameters, $\boldsymbol{\theta}_{SF}$

Stage		θ_{u1}	θ_{l1}	θ_{u2}	θ_{l2}	θ_{u3} *1)	θ_{l3}	$\theta_{h,\max}$	$\theta_{v,\max}$
West side	1	10.00	4.88×10^{7}	0.10	-2.00×10^{7}	–7.56	–5.00	2.44	1.40
	2	53.51	1.17×10^{8}	–2.89	-1.92×10^{7}	–47.41	–4.68	6.10	3.35
	3	40.28	2.60×10^{8}	–3.26	-2.67×10^{7}	–30.53	0.94	9.75	5.05
	4	40.84	2.64×10^{8}	–2.91	-2.71×10^{7}	–31.08	0.28	9.76	6.40
South side	1	10.00	5.08×10^{7}	0.10	-2.00×10^{7}	–7.46	–5.00	2.54	1.40
	2	12.98	1.12×10^{8}	0.95	-1.84×10^{7}	–6.88	–5.33	6.10	3.35
	3	23.57	2.64×10^{8}	–0.42	-2.89×10^{7}	–14.43	1.44	9.14	5.05
	4	28.79	2.76×10^{8}	–2.01	-2.83×10^{7}	–19.04	0.54	9.75	6.40
North side	1	10.00	5.92×10^{7}	0.10	-2.00×10^{7}	–7.04	–5.00	2.96	1.40
	2	25.23	1.27×10^{8}	–1.39	-1.90×10^{7}	–18.52	–5.39	6.71	3.35
	3	26.28	2.29×10^{8}	–1.01	-2.21×10^{7}	–15.92	2.48	10.36	5.05
	4	26.51	1.66×10^{8}	–2.24	-1.51×10^{7}	–15.54	2.44	10.97	6.40

Stage		θ_{h1} *3)	θ_{h2}	θ_{v1} *2)	θ_{v2}	θ_{v3}	θ_{v4} *4)	θ_{v5}
West side	1	11.05	10.34	0.58	–1.24	1.28	11.24	10.27
	2	11.50	10.18	0.37	–3.23	2.07	10.74	10.45
	3	11.24	10.27	0.39	–4.37	2.45	11.50	10.18
	4	10.74	10.45	0.47	–5.54	2.73	11.44	10.20
South side	1	5.22	10.28	0.50	–1.26	1.24	4.49	10.54
	2	4.71	10.46	0.49	–3.01	2.11	4.94	10.38
	3	5.02	10.35	0.49	–4.54	2.52	4.54	10.52
	4	5.58	10.15	0.48	–5.76	2.76	4.66	10.48
North side	1	4.18	10.65	0.30	–1.30	1.15	5.05	10.34
	2	5.10	10.32	0.71	–3.15	2.24	4.68	10.47
	3	5.41	10.21	0.58	–4.59	2.57	4.57	10.51
	4	5.47	10.19	0.53	–5.68	2.77	4.85	10.41

Notes

1) $f_h(x=0,\ z=\theta_{h,\max})=\delta_{h,\max}$,
$\theta_{u3}=\theta_{h,\max}-\theta_{u1}$

2) $f_v(x=0,\ y=\theta_{v,\max})=\delta_{v,\max}$,
$\theta_{v1}=\left(\theta_{v,\max}-\theta_{v2}\right)\left[\theta_{v3}-\ln\left(\theta_{v,\max}-\theta_{v2}\right)\right]\Big/\theta_{v,\mathrm{m}}$

3) $f_h'(x=0, z=\theta_{h,\max})=0$,
$\theta_{h1}\approx B/2-2.8\theta_{h2}$

4) $f_v'(x=0, y=\theta_{v,\max})=0$,
$\theta_{v4}\approx B/2-2.8\theta_{v5}$

5) The H_e and h_{avg} are constant value for each excavation stage and can be found in Figure 4.7.

Table 4.4 Posterior mean of the Box and Cox transformation parameters, θ_{BC}

Stage		θ_1	θ_2	θ_3	θ_4	θ_5	θ_6	θ_7	θ_8
West side	1	–0.61	–0.24	4.98	–1.84	–1.51	0.31	–0.55	0.21
	2	–0.59	–0.25	5.17	–1.87	–1.49	0.40	–0.53	0.23
	3	–0.57	–0.21	5.06	–1.75	–1.52	0.38	–0.51	0.22
	4	–0.56	–0.22	5.07	–1.80	–1.46	0.37	–0.50	0.21
South side	1	–0.95	–0.37	5.02	–2.08	–1.38	0.29	–0.52	0.19
	2	–0.73	–0.48	4.95	–2.14	–1.34	0.28	–0.51	0.23
	3	–0.80	–0.26	5.03	–2.03	–1.46	0.35	–0.48	0.20
	4	–0.63	–0.23	5.42	–1.95	–1.48	0.33	–0.53	0.28
North side	1	–0.86	–0.30	5.13	–1.82	–1.50	0.38	–0.51	0.28
	2	–0.75	–0.34	5.04	–1.76	–1.47	0.41	–0.47	0.19
	3	–0.68	–0.25	5.10	–1.73	–1.48	0.36	–0.50	0.20
	4	–0.66	–0.27	4.96	–1.77	–1.35	0.33	–0.49	0.22

Table 4.5 Posterior statistics of the unknown model parameter

Stage		σ		ρ_V		ρ_H		ρ_{VH}	
		Mean	Standard deviation	Mean	Standard deviation	Mean	Standard deviation	Mean	Standard deviation
West side	1	2.76	2.98	0.13	0.11	0.17	0.09	0.09	0.10
	2	4.88	2.37	0.11	0.12	0.16	0.10	0.12	0.10
	3	5.84	1.64	0.12	0.08	0.13	0.06	0.11	0.07
	4	5.94	1.46	0.10	0.08	0.08	0.07	0.09	0.04
South side	1	2.25	2.85	0.14	0.10	0.15	0.13	0.11	0.14
	2	4.13	2.48	0.12	0.09	0.11	0.12	0.10	0.09
	3	5.32	1.97	0.13	0.09	0.14	0.08	0.10	0.07
	4	5.46	1.38	0.09	0.06	0.08	0.07	0.09	0.05
North side	1	3.45	3.98	0.18	0.12	0.18	0.07	0.11	0.07
	2	5.17	3.85	0.10	0.11	0.15	0.08	0.12	0.07
	3	6.46	2.68	0.11	0.07	0.13	0.04	0.09	0.03
	4	6.78	2.36	0.10	0.05	0.09	0.03	0.07	0.03

Figure 4.8 compares the predicted horizontal displacements after each excavation stage for each side of the Lurie excavation site with the corresponding field measurements. The proposed approach accurately captures the horizontal displacement

profile. Figure 4.8 also compares the proposed method and predictions using a more sophisticated MATLAB®-based application for Bayesian updating using the general finite element software ABAQUS (Park et al. 2010a; Park et al. 2010b). The formulation in Park et al. (2010a) predicts deformations under the assumption of plane strain conditions with a two-dimensional finite element analysis. The case study presented in Park et al. (2010b) is based only on one set of inclinometer measurements (LR–8 at the south wall in Figure 4.6). Away from LR–8 the accuracy of the prediction could deteriorate due to factors such as the spatial variability of the soil stratigraphy and the change in the geometrical boundary conditions, as shown in Figure 4.8. Figure 4.9 shows that predictions for future excavation stages improve if we incorporate the most recent measurements at each excavation stage. This underscores the benefit of incorporating the deformation records as they become available.

The Mean Absolute Percent Error (*MAPE*) is used to quantify the average accuracy of the model fit.

$$MAPE = \frac{1}{n}\left[\sum_{i=1}^{n}\frac{\left|\hat{e}_i - e_i\right|}{e_i}\right]\times 100 \tag{4.22}$$

where $\hat{e}_i$ = the fitted value for displacement e_i, and n = number of observations used to assess the model at each stage. The *MAPE* indicates the average relative error and is an intuitive measure of the accuracy of the model predictions.

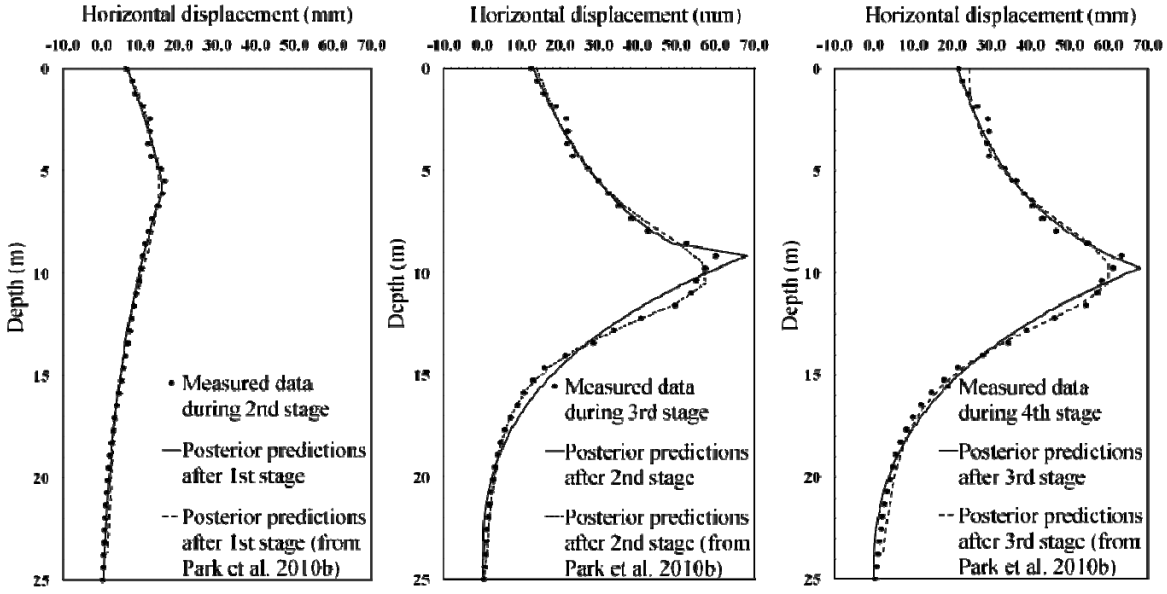

(a) South side

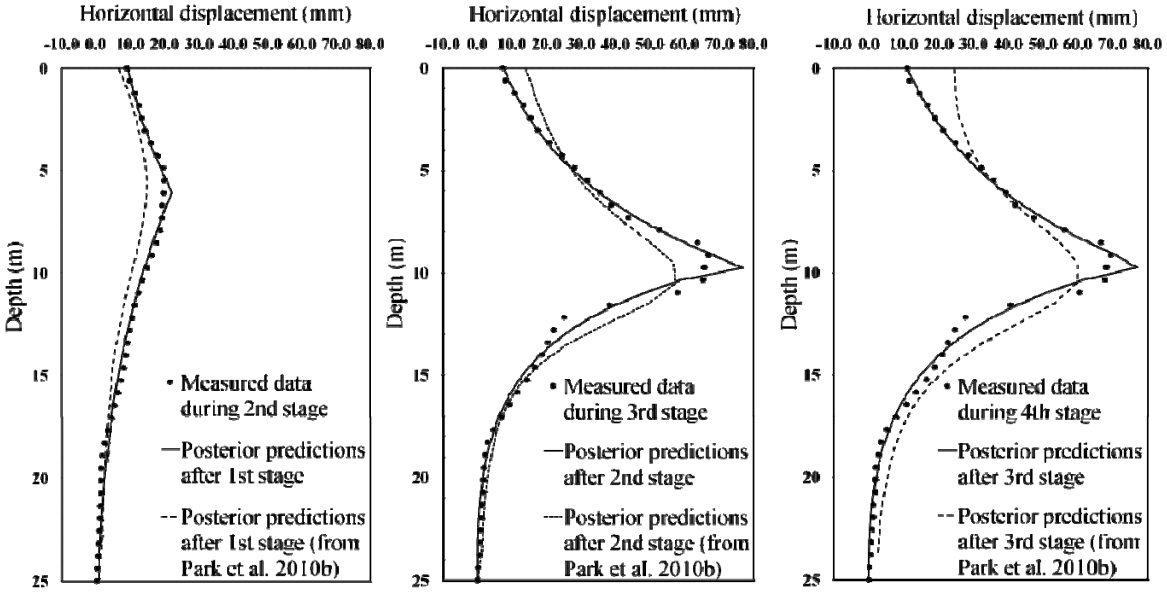

(b) West side

Figure 4.8 Comparison of measured and predicted horizontal displacements

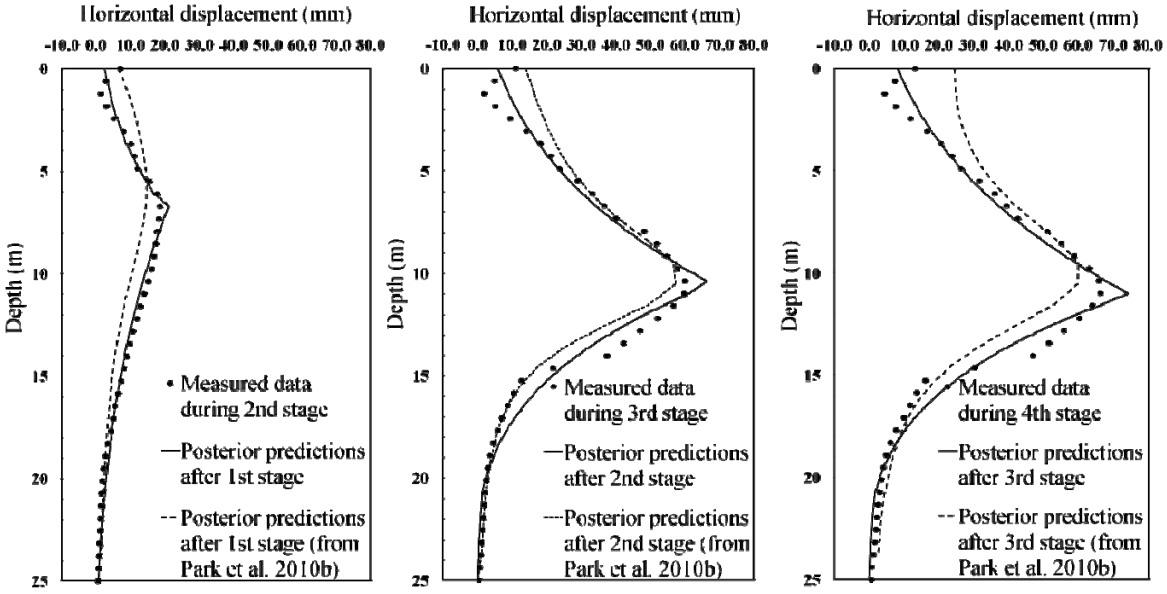

(c) North side

Figure 4.8 Continued

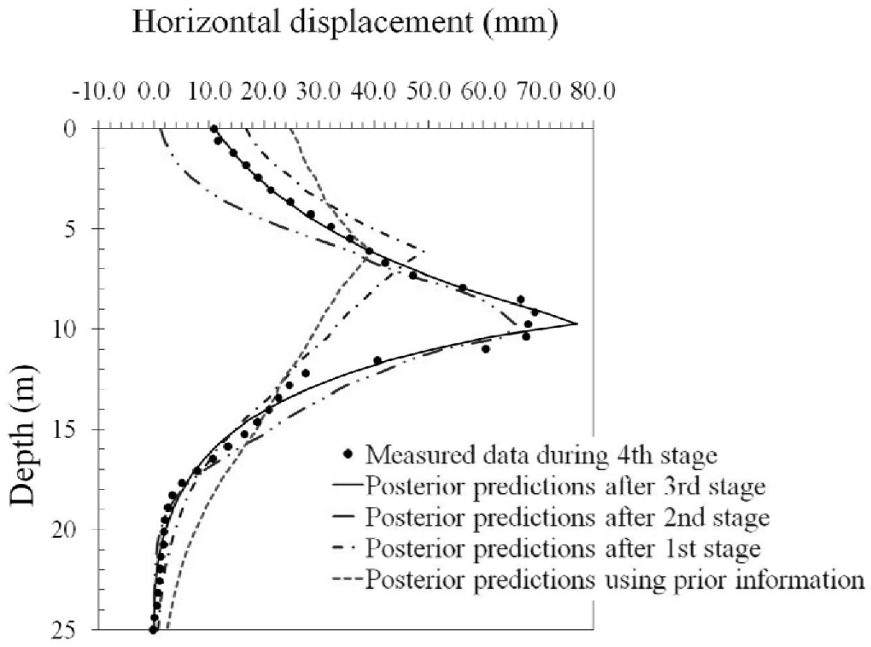

Figure 4.9 Predictions for future excavation stages

Tables 4.6–4.8 lists the values of *MAPE* computed after each excavation stage. The lower diagonal terms in the tables represent the quality of the prediction compared to the measurements in the following stages. The diagonal terms describe the quality of the fit of the proposed framework for the current stage using data for the current stage. Therefore, it is expected, as is observed in Tables 4.6–4.8, that the main diagonal values are smaller than the off-diagonal values, which represent the true predictions. The *MAPE* values continue to decrease from left to right in the table as more data is integrated into the analysis. The more measurements are available, the more accurate the predictions for future excavations are. Although the *MAPE* values in the proposed approach are relatively high compared to the predictions using the finite element analysis (Park et al. 2010b), the results may still be considered reasonable given the ease of the calculation process and the ability of this simplified technique to predict the three-dimensional deformation profiles, which would require considerably larger computational resources and time in finite element simulations.

Table 4.6 *MAPE* values for the example excavation (West Side)

%	Stage 1	Stage 2	Stage 3	Stage 4
Stage 1	33.46 (5.32)			
Stage 2	38.57 (7.49)	32.41 (3.47)		
Stage 3	68.22 (18.24)	38.27 (12.58)	28.29 (3.22)	
Stage 4	78.24 (23.67)	45.54 (19.61)	46.78 (11.53)	29.75 (5.39)

( ) values from Park et al. (2010b)

Table 4.7 *MAPE* values for the example excavation (South Side)

%	Stage 1	Stage 2	Stage 3	Stage 4
Stage 1	38.73 (5.32)			
Stage 2	42.15 (7.49)	32.21 (3.47)		
Stage 3	76.32 (18.24)	54.69 (12.58)	29.30 (3.22)	
Stage 4	89.48 (23.67)	68.59 (19.61)	49.37 (11.53)	31.06 (5.39)

( ) values from Park et al. (2010b)

Table 4.8 *MAPE* values for the example excavation (North Side)

%	Stage 1	Stage 2	Stage 3	Stage 4
Stage 1	48.16 (5.32)			
Stage 2	56.24 (7.49)	42.59 (3.47)		
Stage 3	82.13 (18.24)	58.43 (12.58)	38.24 (3.22)	
Stage 4	93.26 (23.67)	72.36 (19.61)	59.19 (11.53)	33.18 (5.39)

( ) values from Park et al. (2010b)

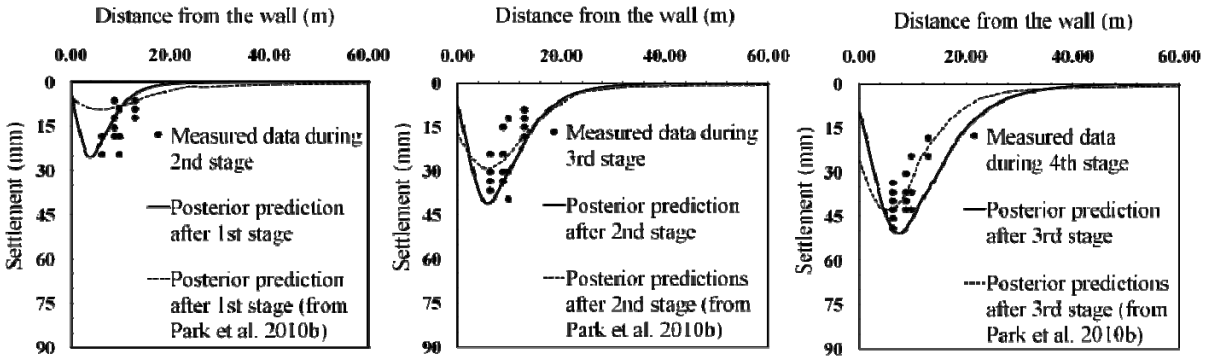

(a) South side

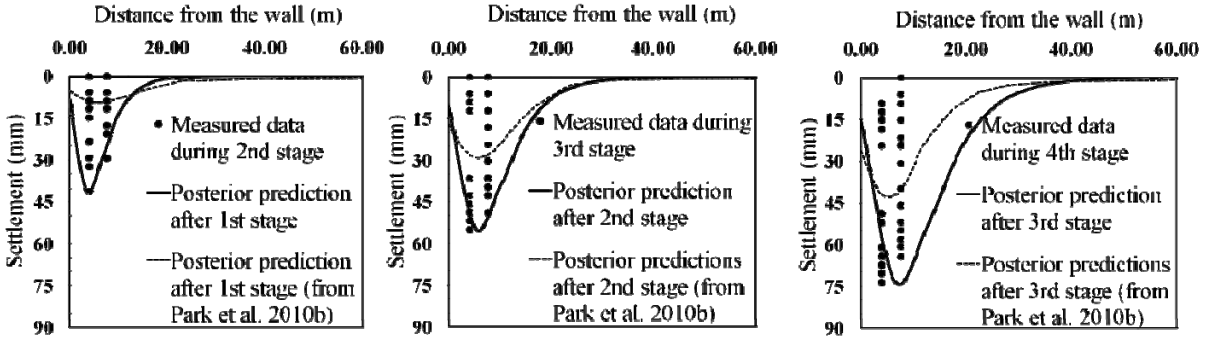

(b) West side

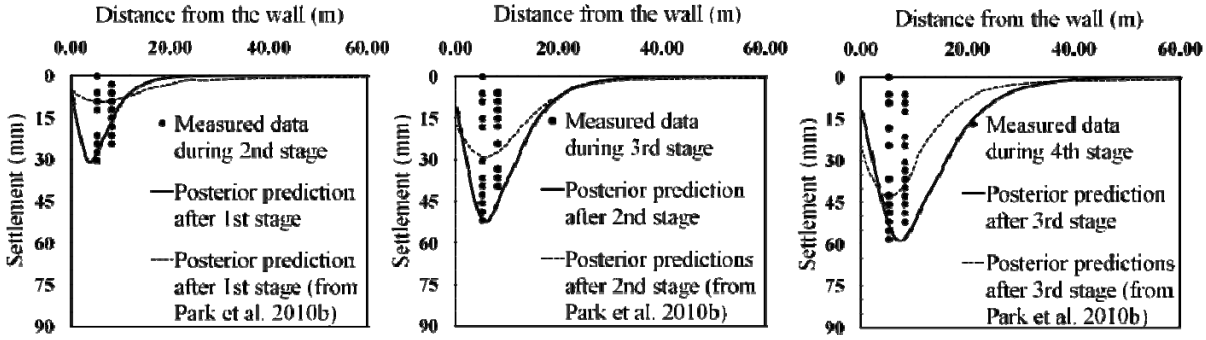

(c) North side

Figure 4.10 Comparison of measured and predicted surface settlements

Similarly, Figure 4.10 compares the surface settlement profiles after each excavation stage. The proposed approach gives good predictions of the maximum settlement and its corresponding location. Due to the limitations mentioned above, the predictions under the assumption of plane strain condition at the south side cannot be extended to a different side of the excavation.

Figures 4.11–4.13 show the complete three-dimensional horizontal deformation profiles and surface settlement profiles after each excavation stage. Due to the site-specific restrictions, only one inclinometer data (LR–3) measuring horizontal displacement was available for the north side. These complete three-dimensional deformation profiles are important to predict the deformation at any locations close to the excavation and to be able to incorporate data collected at different locations. The proposed method can also be used to calculate ground movements at the corners of the excavation. The corner effects due to the increased stiffness of the retaining wall leads to a significant reduction in ground movements. If, however, we have field deformation measurement data that already had the corner effects at the corner location, the ground movements at the corners can be calculated from the combination of both sides of complete three-dimensional deformation profiles.

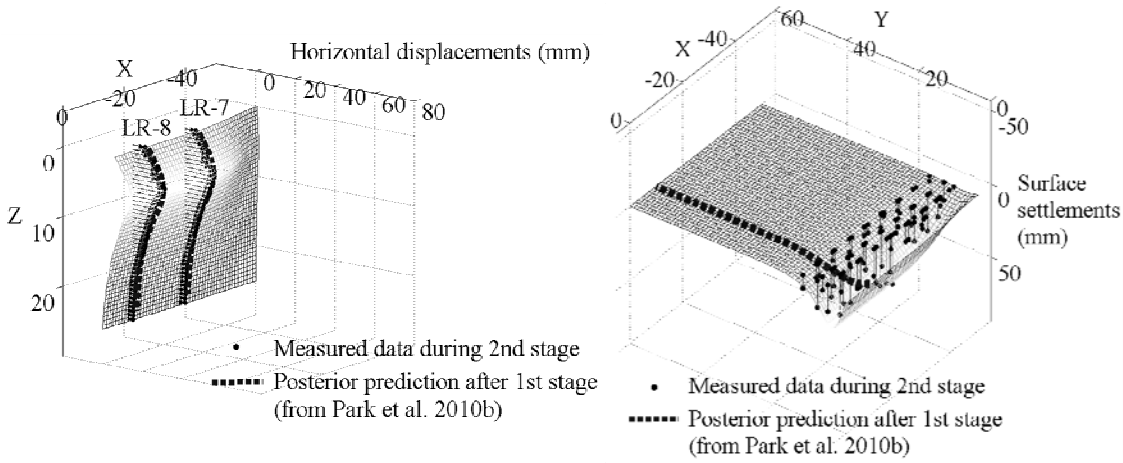

(a) South side

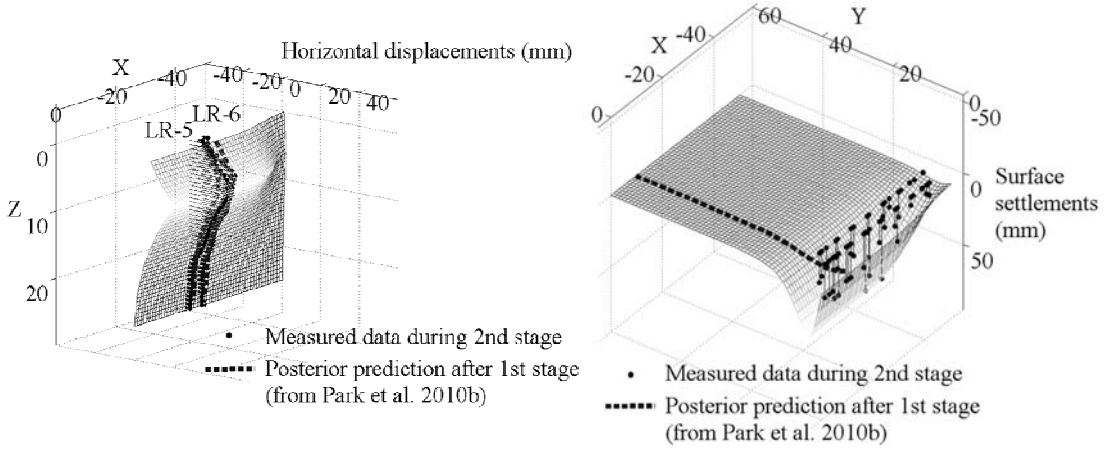

(b) West side

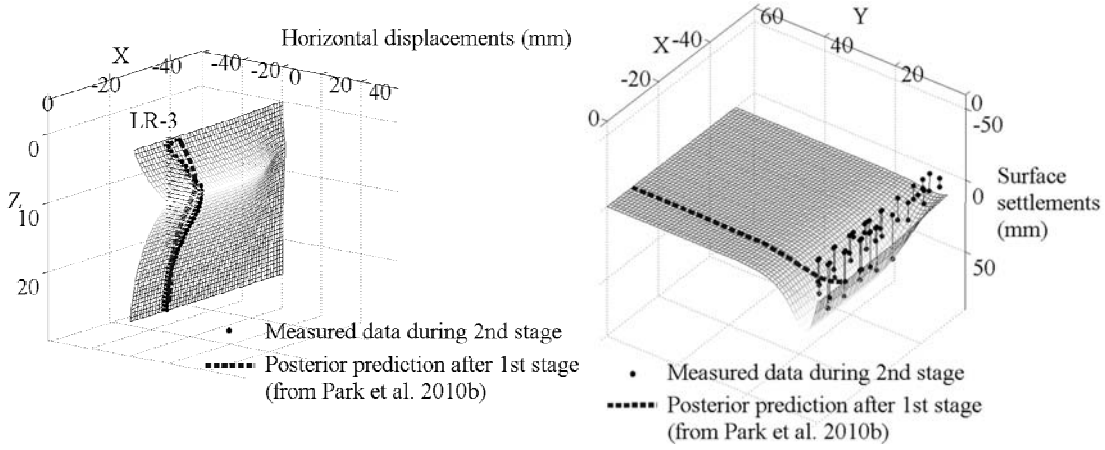

(c) North side

Figure 4.11 Comparison of measured and predicted horizontal displacements and surface settlements based on posterior estimates after stage 1

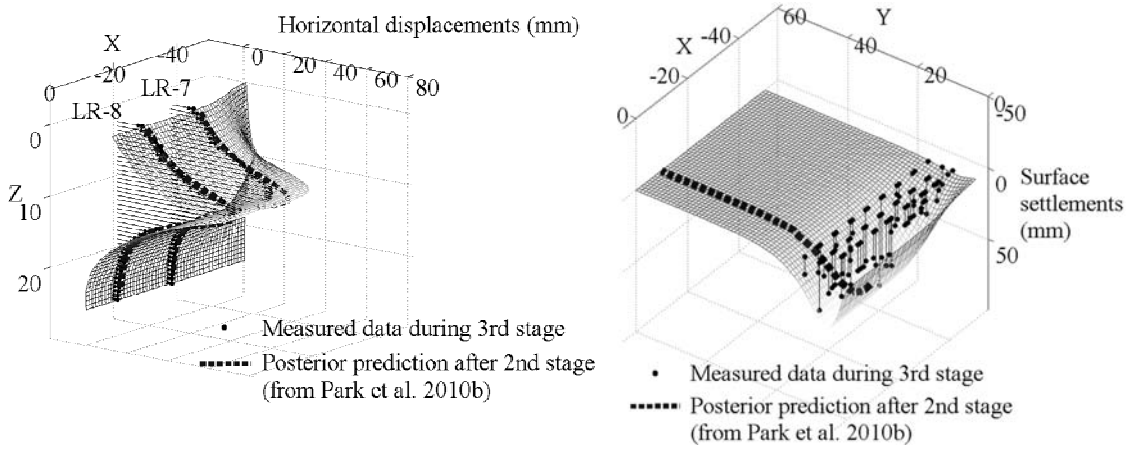

(a) South side

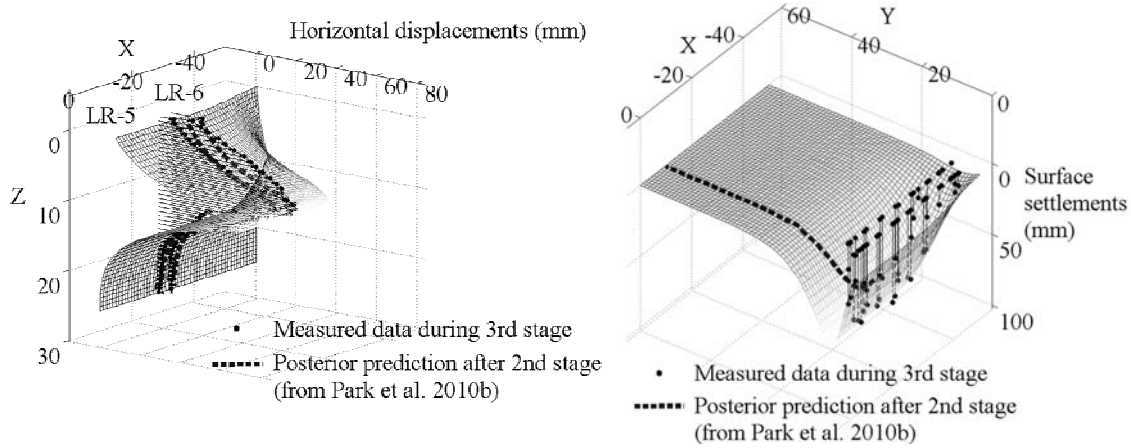

(b) West side

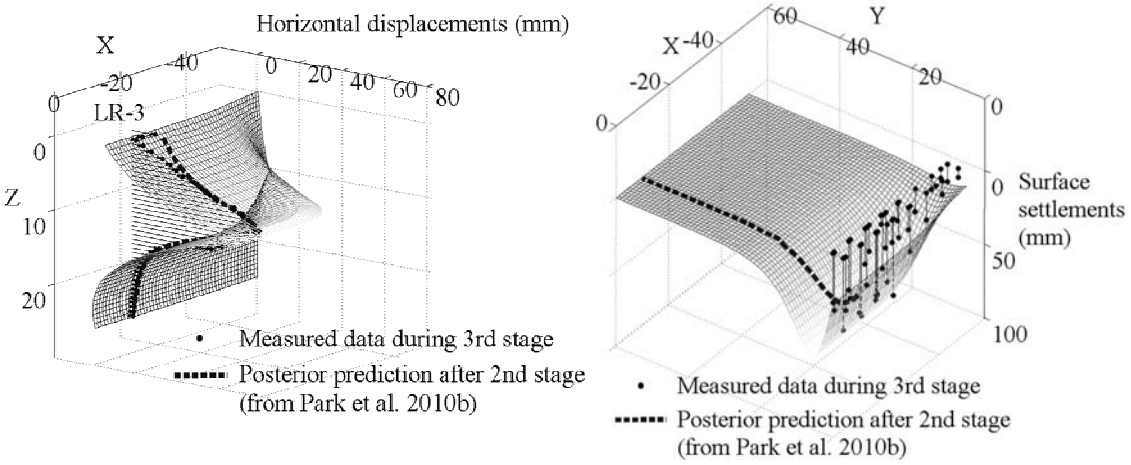

(c) North side

Figure 4.12 Comparison of measured and predicted horizontal displacements and surface settlements based on posterior estimates after stage 2

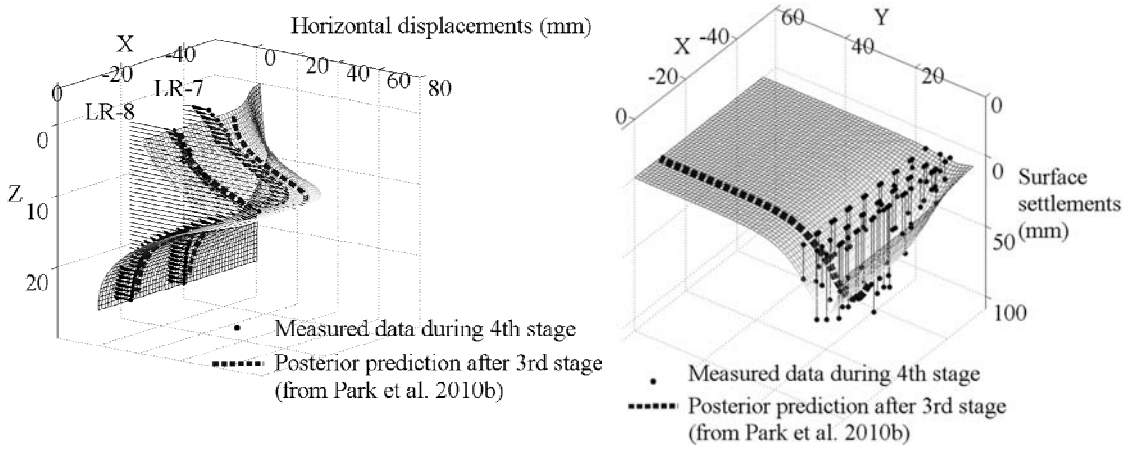

(a) South side

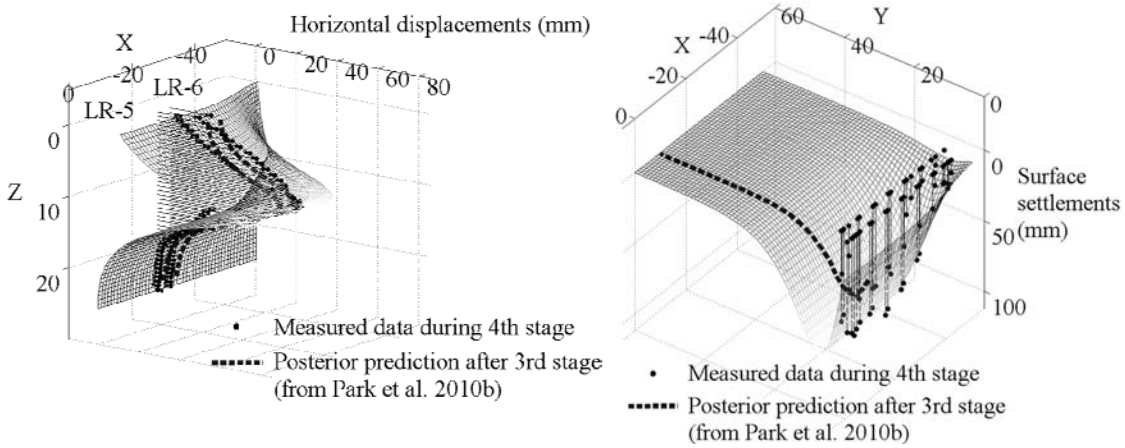

(b) West side

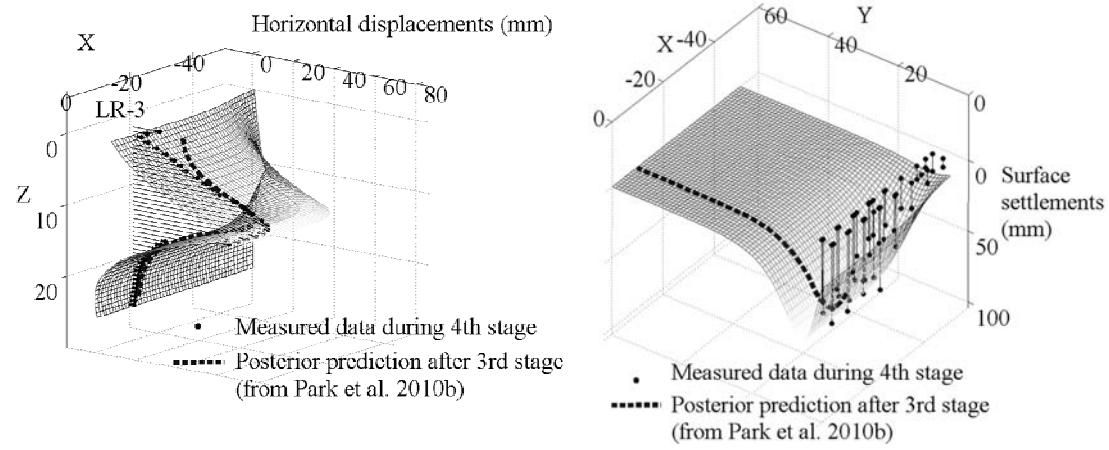

(c) North side

Figure 4.13 Comparison of measured and predicted horizontal displacements and surface settlements based on posterior estimates after stage 3

4.7 Conclusions

A probabilistic framework is proposed to predict three-dimensional deformation profiles due to supported excavations using a semi-empirical approach. A Bayesian formulation is used to assess the unknown model parameters by updating prior information based on site specific field measurements at different locations. The updated model parameters are then used to develop new and more accurate predictions of the deformations in the subsequent stages, until the end of the excavation project. The key advantage of the proposed approach for practicing engineers is that an already common semi-empirical chart can be used together with a few additional simple calculations to better evaluate three-dimensional displacement profiles. This eliminates the need for constitutive laws, complex calculations and finite element models. The developed approach provides a sound basis for making decisions about the design of excavation projects and can be used for optimizing the design of supported excavation systems. The proposed approach can also be used for an adaptive reliability-based optimal design of the excavation system in which the design is modified after each excavation stage to minimize costs and maintain a minimum reliability requirement.

5. RELIABILITY ANALYSIS OF INFRASTRUCTURE ADJACENT TO DEEP EXCAVATIONS

This section provides an approach to conduct a probabilistic assessment of infrastructure damage including buildings, bridges, and utility pipelines due to excavation works in a complex urban area. In current practice, the assessment of excavation-induced damage has mainly focused on a deterministic approach to consider a single failure mode of each component of infrastructure. However, the damage (or failure) of infrastructure is often a complex "system" event that is a function of each "component" event depending on the characteristic of each infrastructure. For reasonable decision-making on excavation designs in the complex urban area, it is essential to accurately estimate the probability of the system failure event based on a probabilistic approach. A Bayesian framework based on a semi-empirical method is used to update the predictions of ground movements in the later stages of excavation based on the field measurements. The system fragility of infrastructure adjacent to excavation works is computed by Monte Carlo Simulation (MCS) employing the component fragility of each infrastructure and the identified correlation coefficients. An example is presented to show how the system reliability for multiple serviceability limit states can be assessed. Sensitivity and importance measures are also computed to identify the key components, unknown parameters and random variables in the model for an optimal design of the excavation works.

5.1 Introduction

In the complex urban environment, ground movements induced by deep excavation works can cause damage on adjacent infrastructure including buildings, bridges, utility pipelines, and other structures. The increasing rate of excavation projects related to urban redevelopment and improvement has contributed to a heightened level of concern regarding the effects of deep excavation on nearby infrastructures.

The infrastructure damage potential due to an excavation is generally influenced by many factors, including the properties of the soil and infrastructure, the type and size of an infrastructure, the relative location between infrastructure and excavation, the magnitude and distribution of load of infrastructure in addition to the self-weight, the excavation induced deformation, and the foundation characteristics of an infrastructure. It is necessary to understand the complex nature of ground deformation characteristic and the extent to which excavation induced deformations are transferred from the ground surface, through the foundation, and to the superstructure to result in architectural or structural damage.

The previous researches have shown that the damage potential (or failure) of each "component" of infrastructure is often governed by serviceability limit state (SLS) rather than ultimate limit state (ULS) (Zhang and Ng 2005; Babu et al. 2006; Park et al. 2007). However, applications of reliability concepts to the excavation design have mainly focused on assessing the stability of the each infrastructure itself, with limited research focusing on the component reliability assessment of the serviceability criterion (Son and Cording 2005; Hsiao et al. 2008; Schuster et al. 2008). Furthermore, the

assessment of excavation-induced infrastructure damage to consider SLS has mainly focused on the component level of infrastructure (Becker 1996a; Becker 1996b; AASHTO 2007). However, the damage (or failure) of infrastructure can be considered as a complex "system" event that is a function of each "component" event depending on the different probabilistic deformation characteristic of each infrastructure due to an excavation work. For example, the bridge can be damaged even though the nearby building is safe under the different definition of limit state of each infrastructure, and which is mainly contingent upon both the relative location and the three-dimensional deformation shape due to the excavation work as shown in Figure 5.1.

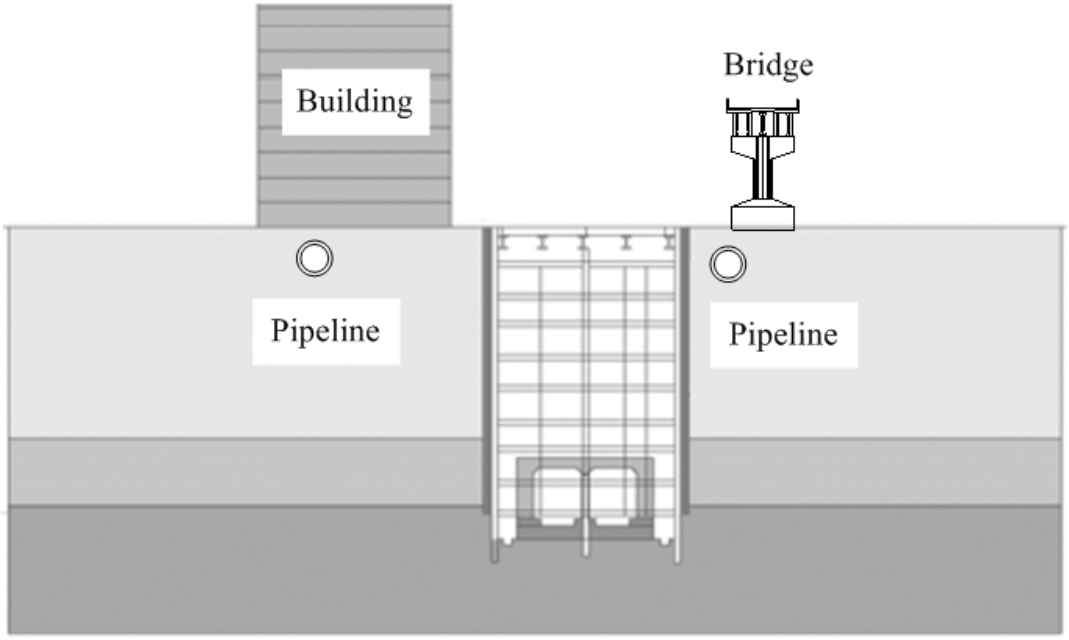

Figure 5.1 Various infrastructures adjacent to deep excavations in urban area

Although an assessment of the damage potential to each infrastructure could be conducted by providing certain ranges of the probability based on component reliability analysis, the system reliability that considers multiple limit state functions of all types of structures nearby an excavation site was not addressed.

This section presents a system reliability analysis framework to assess the conditional probability (fragility) that specified threshold design criteria for multiple serviceability limit states are exceeded. A comprehensive procedure for the analysis of infrastructure damage caused by an excavation involves five main components: (1) determination of the complete three-dimensional ground deformation profiles, (2) selection of major influential factors and corresponding performance functions for each infrastructure to interpret the damage potential effect of excavation works, (3) estimation of the responses of each infrastructure based on the excavation-induced ground movement and infrastructure characteristics, (4) assessment of component fragility of each infrastructure based on different SLS criteria, and (5) assessment of the infrastructure system fragility for multiple SLS criteria to estimate the probability of the infrastructure system failure due to the an excavation.

A previously developed Bayesian framework is used to predict excavation-induced deformations based on the updating semi-empirical design chart using field measurement data (Park et al. 2010c). A Bayesian updating methodology is used to assess the three-dimensional deformation shape including maximum horizontal displacements, surface settlements and ground movement profiles at different locations and for each incremental excavation stage. An example is presented to show how the

system reliability analysis for multiple serviceability limit states can be assessed. The component reliability of each infrastructure based on a single limit function for each excavation step is assessed by the First Order Reliability method (FORM). By considering multiple failure modes and corresponding performance functions of an infrastructure, the system reliability for each excavation step is assessed during the entire excavation process. The system fragility of an infrastructure is computed by Monte Carlo Simulation (MCS) employing the component fragility of each infrastructure and the identified correlation coefficients. Furthermore, sensitivity and importance measures are carried out to identify the key component, the contribution of the parameter(s) or random variable(s) to the reliability of an infrastructure adjacent to the excavation works.

5.2 Damage Descriptions for Various Infrastructures

Allowable serviceability criteria of each infrastructure depend on soil-structure interaction, desired serviceability level, harmful cracking and distortion, restricting the safety or use of the particular structure. In current practice, deformation tolerance specifications are generally prescribed based on minimizing potential damage to adjacent infrastructures. However, analytical solutions for allowable SLS criteria for infrastructures cannot be easily obtained and most criteria for infrastructure damage potential have been developed on the basis of empirical evidence from field observations and damages in existing infrastructures. Because each infrastructure will have different performance characteristic due to the excavation-induced deformation, the existing

serviceability criteria for the various infrastructures in an urban area are reviewed and summarized for this study.

5.2.1 Buildings

Burland and Wroth (1974) proposed a set of definitions based on the displacements of a number of discrete points on a building foundation as shown in Figure 5.2.

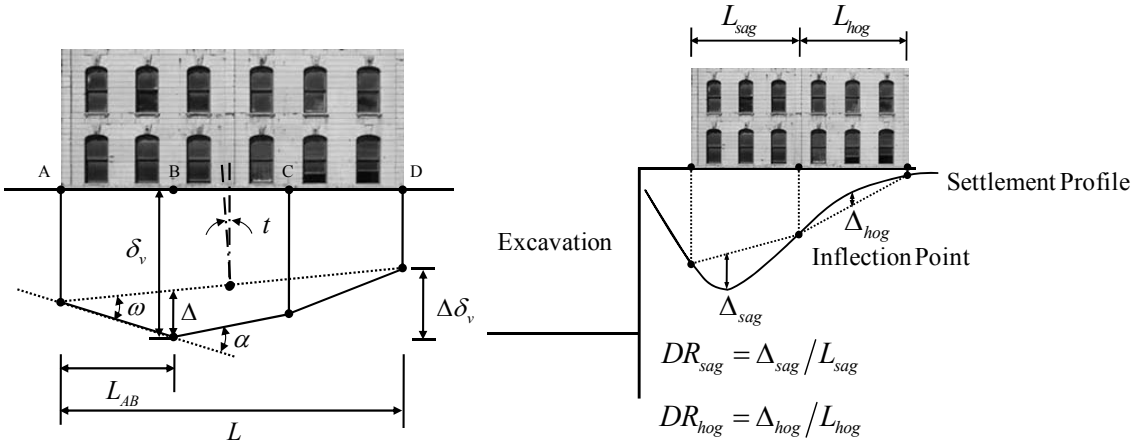

(a) Building distortion parameters (b) Relative deflection and deflection ratio

Figure 5.2 Definitions of building deformation parameters

The followings are used in this study: $\delta_v =$ the total vertical settlement of a given point, $\Delta\delta_v =$ the difference in total vertical settlement between any two points, $\alpha =$ the angular strain which is the gradient between two successive points, $\omega =$ the angular distortion denoted by $\Delta\delta_v / L_{ij}$ is the rotation of the line joining two points relative to the

tilt, L_{ij} = the distance between points i and j, Δ = the relative deflection which is the movement from a straight line joining two reference points, t = the tilt, DR = the deflection ratio denoted by Δ / L where L is the distance between the two reference points defining Δ as shown in Figure 5.2(b). The above definitions only apply to in-plane deformations and no attempt has been made to define three-dimensional behavior. For this study, these definitions are applied to any two dimensional direction in the three-dimensional ground deformation. Furthermore, the same definitions are used for the different type of infrastructure including bridges and utility pipelines.

Recognizing that ground movements are inevitable consequence of excavation, the allowable movements within existing buildings can be considered under the following headings: (1) safety, (2) architectural or aesthetic damage, (3) functional damage, (4) structural damage, (5) prevention or repair. Because of the complexity and difficulty in determining the allowable serviceability criteria for an individual building structure, the limit state of "allowable displacement" is primarily based on field observations of building damage as described before. These criteria vary for the type of building depending on the relative displacement ratios as summarized in Table 5.1. Typical critical values of slope in settlement profile and maximum settlement of building, which have been used for planning and design purposes are summarized in Table 5.2.

Table 5.1 The threshold values of serviceability criteria for buildings

Type of structure	Type of damage/concern	Criterion	Limiting value(s)	Reference
Framed buildings and reinforced load bearing walls	Structural damage	Angular distortion	1/150–1/250	Poulos et al. (2001)
	Cracking in walls and partitions	Angular distortion	1/500 1/1000–1/1400 (end bays)	
	Visual appearance	Tilt	1/300	
	Connection to services	Total settlement	50–75 mm (sands) 75–135 mm (clays)	
Tall buildings and structures with unreinforced load bearing walls	Operation of lifts and elevators	Tilt after lift installation	1/1200–1/2000	
	Cracking by sagging	Deflection ratio	1/1250–1/2500	
	Cracking by hogging	Deflection ratio	1/2500–1/5000	
Isolated foundation	–	Total settlement	25 mm	Eurocode 1 (Gulvanessian and Holický 1996)
Raft foundation	–		50 mm	
Open frames	–		20 mm	
Frames with flexible cladding or finishes	–	Differential settlement between adjacent columns	10 mm	These limiting values apply to foundation on sand. Higher limiting values may be permitted for foundation on clay soil
Frames with rigid cladding or finishes	–		5 mm	
All foundations	–	Angular distortion	1/500	
		Tilt	To be determined by the designer	

Table 5.2 Typical values of maximum building slope and settlement for damage risk assessment (Modified from Rankin 1988)

Risk Category	Maximum slope in the settlement profile of building	Maximum settlement of building (mm)	Description of risk	Description of action required
1 Negligible	1/500 >	10 >	Superficial damage unlikely	No action, except for any buildings identified as particularly sensitive for which an individual assessment should be made.
2 Slight	1/500–1/200	10–50	Possible superficial damage which is unlikely to have structural significance.	Crack survey and schedule of defects, so that any resulting damage can be fairly assessed and compensated. Identify any buildings and pipelines that may be particularly vulnerable to structural damage and assess separately.
3 Moderate	1/200–1/50	50–75	Expected superficial damage and possible structural damage to buildings, possible damage to relatively rigid pipelines	Crack survey, a schedule of defects, and a structural assessment. Predict extent of structural damage, assess safety risk, choose whether to accept damage and repair, take precautions to control damage or, in extreme cases, demolish. Buried pipelines at risk: identify vulnerable services, and decide whether to repair, replace with a type less likely to suffer damage, or divert.
4 High	1/50 <	75 <	Expected structural damage to buildings. Expected damage to rigid pipelines, possible damage to other pipelines.	

5.2.2 Bridges

All bridge abutments and foundations nearby excavation works in urban area are likely to move due to the excavation-induced displacements, and the suggested damage criteria

for different types of bridges are established to maintain the safety, quality of ride and function of the bridge as summarized in Table 5.3. As Moulton et al. (1985) suggested, the tolerable differential settlement and corresponding angular distortion increased with the span length in most previous studies. The general span length of bridges is dependent on the bridge type as summarized in Table 5.4. In this study, the typical prestressed concrete girders of spans in urban areas ranging from 25 to 40m are assumed (Du and Au 2005).

Table 5.3 The threshold values of serviceability criteria for bridges

Bridges	Type of damage/concern	Criterion	Limiting value(s)	Reference
General	Ride quality	Total settlement	100 mm	Poulos et al. (2001)
	Structural distress	Total settlement	63 mm	
	Function	Horizontal movement	38 mm	
Multi span	Structural damage	Angular distortion	1/250	
Single span	Structural damage	Angular distortion	1/200	
Multi span	Structural damage	Angular distortion	1/250	AASHTO LRFD Bridge Design Specifications (2007)
Single span	Structural damage	Angular distortion	1/125	
General	Design and construct	Total settlement	≤ 25mm	WSDOT (2010)
		Differential settlement[a]	≤ 19mm	
	Ensure structure can tolerate settlement	Total settlement	≤ 100mm	
		Differential settlement[a]	≤ 76mm	
	Obtain Approval prior to proceeding with design and construction	Total settlement	≥ 100mm	
		Differential settlement[a]	≥ 76mm	

[a]Differential settlement over 30m within pier or abutment, and differential settlement between piers.

Table 5.4 Types of bridges and applicable span length (After Chen and Lui 2005)

Bridge type	Span range (m)	Leading bridge and span length
Prestressed concrete girder	10–300	Stolmasundet, Norway (301m)
Steel I/box girder	15–376	Sfalassa, Italy (376m)
Steel truss	40–550	Quebec, Canada (549m)
Steel arch	50–550	Shanghai Lupu, China (550m)
Concrete arch	40–425	Wanxian, China (425m)
Cable-stayed	110–1,100	Sutong, China (1,088m)
Suspension	150–2,000	Akasi-Kaikyo, Japan (1,991m)

5.2.3 Utility pipelines

Buried pipelines have applications in water supply, sewerage, and oil/natural gas pipelines in complex urban area. Pipelines parallel to deep excavations undergo deformations due to the displacement of the surrounding soil; thereby impose the risk of damage to adjacent buried pipelines. For most utilities that parallel a large excavation in an urban environment, the pipeline can be assumed to move with the soil according to the previous research results (Nath 1983).

Piping materials are generally placed in one of two classifications: flexible or rigid. Most flexible pipes can tolerate deflections in the range of 2–5% of the diameter of the pipe without developing any structural problem (Moser and Folkman 2008). Materials that do not meet this criterion are usually considered to be rigid. Flexible pipes include steel, ductile iron, thermoplastics such as Polyvinyl Chloride (PVC) and High Density Polyethylene (HDPE), thermosetting plastics such as fiberglass-reinforced

polymer (FRP), bar-wrapped concrete cylinder pipe, and corrugated steel pipes. Rigid pipes include reinforced non-cylinder concrete, reinforced concrete cylinder, prestressed concrete cylinder, vitrified clay, polymer concrete, cast iron, asbestos cement and cast-in-place pipes.

A preliminary assessment of the possible effect of excavation-induced movement could be based on the Table 5.5.

Table 5.5 Preliminary assessment of ground movement on a buried pipeline (After Attewell et al. 1986)

Maximum surface settlement (mm)	Rigid pipe	Flexible pipe
$\delta_{v,\max} \leq 10$	Pipe stress increase is not significant compared with other causes of stress such as installation, traffic load, seasonal movement	
$\delta_{v,\max} > 10$	The effects of movement should be assessed in detail	–
$\delta_{v,\max} > 25$	Significant stress increase virtually certain; possible failure of small-diameter pipes	–
$\delta_{v,\max} > 50$	Possible failure of large-diameter pipes	Significant stress increase likely; the effects of movement should be assessed in detail

The behavior of the pipeline depends on the stiffness of the pipeline sections, the position and behavior of the pipe joints, and the nature of the excavation-induced ground deformations. Each type of pipe has one or more performance limits which must be considered for the detailed assessment of the effect of excavation works depending on the pipe materials. The design of flexible pipes is controlled by either ring deflection or

wall buckling as shown in Figure 5.3. Because flexible pipes deform and derive strength from the supporting backfill and adjacent undisturbed soil, the understanding how the flexible pipe relates to the adjacent soil is a key to successful design.

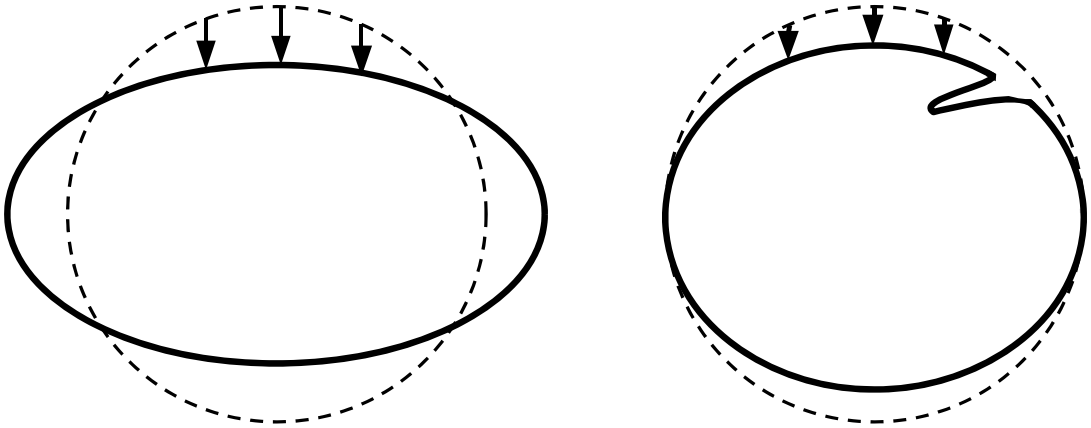

(a) ring deflection (b) wall buckling

Figure 5.3 Possible failure modes of flexible pipes (Modified from Moser and Folkman 2008)

Pipelines are assumed herein to deform along with the ground displacement profiles as rigid links connected by points that are free to rotate as shown in Figure 5.4. The effects of the ground movements on the pipe are concentrated in the joints as relative rotations between adjacent pipe sections. The pipe sections are assumed to have a large flexural rigidity thus preventing any curvature to develop, and the joints are assumed to have no rotational rigidity allowing free rotation. The rotation at the joints is assumed to be longitudinal due to bending of the pipeline. The coordinate system for the joint rotation analyses is shown in Figure 5.5 and the suggested allowable joint rotations of pipelines for different types of joint are summarized in Table 5.6.

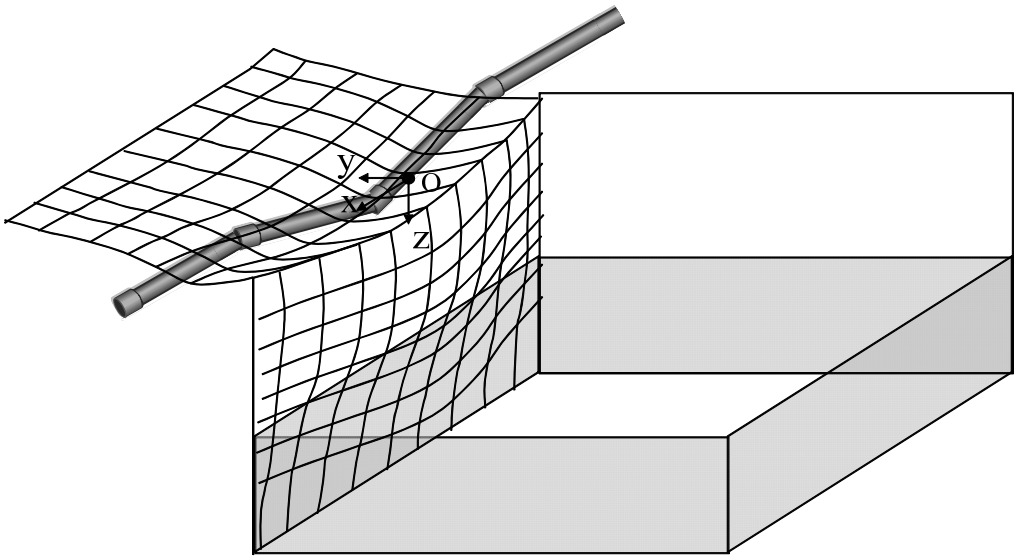

Figure 5.4 Assumed deformation patterns of pipelines

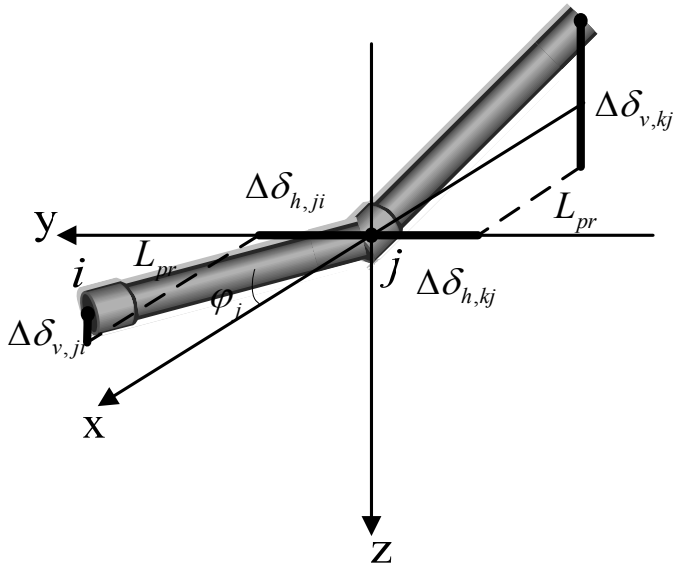

Figure 5.5 Coordinates for joint rotation analyses

Table 5.6 Allowable joint rotations of pipelines due to excavation-induced movements

Pipe material	Joint type	Allowable joint rotation (rad.)	References
Cast Iron	Lead-Caulked	0.09–0.10	Attewell et al. (1986)
	Rubber-Gasket	0.07–0.09	Attewell et al. (1986)
	Mechanical	0.07	Attewell et al. (1986)
Ductile Iron	Rubber-Gasket	0.05–0.09	Bonds (2003)
	Mechanical	0.03–0.14	Bonds (2003)
	Ball and Socket	0.26	Bonds (2003)

5.3 Establishment of Multiple Serviceability Limit State Functions

5.3.1 Buildings

Previous research results have concluded that damage to buildings caused by an excavation is a result of both settlement and horizontal movement of the ground (Bjerrum 1963; Boscardin and Cording 1989; Burland 1995; Son and Cording 2005). In current practice, the excavation-induced maximum surface settlement, $\delta_{v,\max}$, angular distortion, ω, horizontal strain, ε_h, and deflection ratio, DR, are often used as performance indicators for estimating the damage potential of buildings adjacent to an excavation. Son and Cording (2005) developed a phased procedure to estimate the potential for building damage based on ω and ε_h to express the strains induced in a building; and these two parameters can be combined into a single parameter termed as the principal tensile strain in the building. The first limit state function, $g_{11}(\mathbf{X},\boldsymbol{\Theta})$, can be described as

$$g_{11}\left(\mathbf{X},\boldsymbol{\Theta}\right) = \varepsilon_{p,T} - \varepsilon_p\left(\mathbf{X},\boldsymbol{\Theta}\right) \tag{5.1}$$

where, $\mathbf{x}_i = (A_i, S_i, G_i) =$ $\mathbf{x}_i = (A_i, S_i, G_i) =$ the relative location, A_i , size, S_i , and geometry, G_i of adjacent infrastructures to an excavation, which in general are random, $\boldsymbol{\Theta} =$ the unknown model parameters described in Section 4, and $\mathbf{x} = (\mathbf{x}_1, \ldots, \mathbf{x}_r)$ for multiple infrastructures, $\varepsilon_{p,T} =$ a specified principal tensile strain and $1/600$ suggested by Schuster et al. (2008) is used in this study, but it can be changed to different number depending on the importance of the building, $\varepsilon_p(\mathbf{X}, \boldsymbol{\Theta}) =$ the principal tensile strain and can be written as

$$\begin{aligned} \varepsilon_p\left(\mathbf{X}, \boldsymbol{\Theta}\right) &= \omega \sin\alpha_{\max} \cos\alpha_{\max} + \varepsilon_h \left(\cos\alpha_{\max}\right)^2 \\ &= \frac{\Delta\delta_v\left(\mathbf{X}, \boldsymbol{\Theta}\right)}{L} \sin\alpha_{\max} \cos\alpha_{\max} + \frac{\Delta\delta_h\left(\mathbf{X}, \boldsymbol{\Theta}\right)}{L} \left(\cos\alpha_{\max}\right)^2 \end{aligned} \tag{5.2}$$

where $\omega =$ angular distortion as defined in Figure 5.6(a), $\varepsilon_h =$ lateral strain as defined in Figure 5.6(b), $\Delta\delta_v\left(\mathbf{X}, \boldsymbol{\Theta}\right) =$ the difference in the vertical settlement between two points of the adjacent building, $\Delta\delta_h\left(\mathbf{X}, \boldsymbol{\Theta}\right) =$ the difference in the horizontal displacement between two points of the adjacent building, $L =$ the length of adjacent building, and $\alpha_{\max} =$ the angle of the plane on which ε_p acts and direction of crack formation measured from the vertical plane,

$$\alpha_{\max} = 0.5 \tan^{-1}\left(\omega / \varepsilon_h\right) = 0.5 \tan^{-1}\left(\Delta\delta_v\left(\mathbf{X}, \boldsymbol{\Theta}\right) / \Delta\delta_h\left(\mathbf{X}, \boldsymbol{\Theta}\right)\right) \tag{5.3}$$

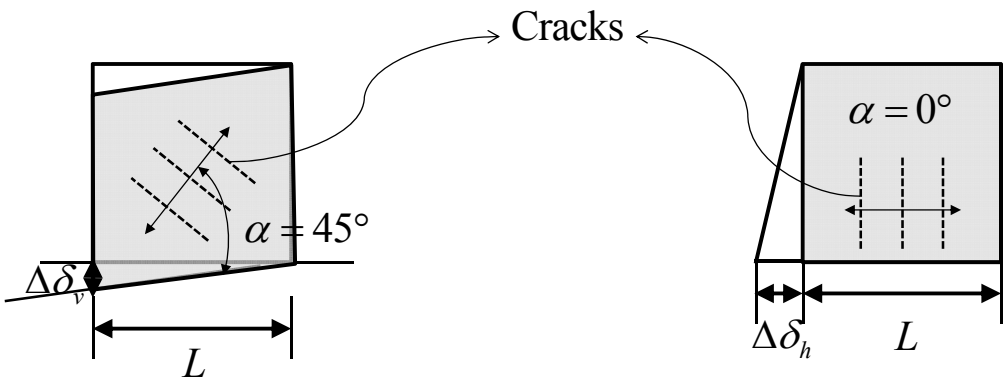

$\omega = \Delta\delta_v / L$ (a) angular distortion

$\varepsilon_h = \Delta\delta_h / L$ (b) lateral strain

Figure 5.6 State of strain at the distorted portion of a building (modified from Son and Cording 2005)

The second limit state function is in terms of a deflection ratio (DR_{sag} or DR_{hog}) proposed by Burland (1995). By assuming no rigid rotation and a single deformation mode, the deflection ratio is equal to the angular distortion of the building and is often employed to assess the potential of damage of adjacent building. An arbitrary ratio of 1/600 is used in this study as the threshold value for the evaluation of this limit state function.

$$g_{12}(\mathbf{X},\boldsymbol{\Theta}) = DR_T - \frac{\Delta\delta_v(\mathbf{X},\boldsymbol{\Theta})}{L} \tag{5.4}$$

where DR_T = the limiting deflection ratio.

The third limit state function can be specified with respect to the maximum surface settlement to assess the excavation-induced building damage potential. Even though more advanced evaluation criteria described above are available, the $\delta_{v,\max}$ has

the advantage of being much easier to measure in the field than ω, ε_h and DR. The tolerable limit of the maximum surface settlement, $\delta_{v\max,T}$, is assumed to be 75mm according to Hsiao et al. (2008). The limit state function can be expressed as:

$$g_{13}\left(\mathbf{X},\boldsymbol{\Theta}\right)=\delta_{v\max,T}-\delta_{v}\left(\mathbf{X},\boldsymbol{\Theta}\right) \tag{5.5}$$

5.3.2 Bridges

From the previous research results as summarized in Table 5.3, we have concluded that damage to bridges is a result of both settlement and horizontal movement of the ground. The performance indicators for estimating the damage potential of bridges adjacent to an excavation can be determined in terms of $\delta_{v,\max}$, $\delta_v(\mathbf{X},\boldsymbol{\Theta})$, ω, $\Delta\delta_v(\mathbf{X},\boldsymbol{\Theta})$.

The first limit state function, $g_{21}(\mathbf{X},\boldsymbol{\Theta})$, employed in this study can be specified with respect to the maximum vertical settlement of the bridge foundations and could be expressed as

$$g_{21}\left(\mathbf{X},\boldsymbol{\Theta}\right)=\delta_{v\max,T}-\delta_{v}\left(\mathbf{X},\boldsymbol{\Theta}\right) \tag{5.6}$$

where $\delta_{v\max,T}$ = the tolerable limit of the maximum surface settlement, $\delta_v(\mathbf{X},\boldsymbol{\Theta})$ = the vertical settlement of each foundation of bridge pier. In this study, the threshold value of the maximum surface settlement is chosen arbitrarily and limited to 25mm.

In most cases, the differential settlement of bridge foundation results in more damage when compared to total settlement. Thus, the second limit state function can be described as following equation

$$g_{22}\left(\mathbf{X},\boldsymbol{\Theta}\right)=\Delta\delta_{v,T}-\Delta\delta_{v}\left(\mathbf{X},\boldsymbol{\Theta}\right) \tag{5.7}$$

where $\Delta\delta_{v,T}$ = the tolerable limit of the differential settlement, $\Delta\delta_{v}(\mathbf{X},\boldsymbol{\Theta})=$ the differential settlement between adjacent bridge piers. In this study, the threshold value of the maximum surface settlement is chosen arbitrarily and limited to 19mm. In a similar way, the third limit state function is a function of the angular distortion of the bridge piers,

$$g_{23}\left(\mathbf{X},\boldsymbol{\Theta}\right)=\omega_{T}-\frac{\Delta\delta_{v}\left(\mathbf{X},\boldsymbol{\Theta}\right)}{L_{s}} \tag{5.8}$$

where, $\omega_{T}=$ the tolerable limit of the angular distortion, $\Delta\delta_{v}(\mathbf{X},\boldsymbol{\Theta})=$ the differential settlement of each foundation of bridge pier, $L_{s}=$ the span length of bridge, and it is assumed 30m in this study. In this study, the threshold value of the angular distortion is chosen arbitrarily and limited to 1/250.

5.3.3 Utility pipelines

The performance indicators for estimating the damage potential of pipelines adjacent to an excavation can be determined in terms of $\delta_{v,\max}$, $\delta_{v}(\mathbf{X},\boldsymbol{\Theta})$, $\Delta\delta_{v}(\mathbf{X},\boldsymbol{\Theta})$, $\Delta\delta_{h}(\mathbf{X},\boldsymbol{\Theta})$. The first limit state function for the buried utility pipeline, $g_{31}(\mathbf{X},\boldsymbol{\Theta})$, employed in this study can be specified with respect to the maximum vertical settlement and could be expressed as

$$g_{31}\left(\mathbf{X},\boldsymbol{\Theta}\right)=\delta_{v\max,T}-\delta_{v}\left(\mathbf{X},\boldsymbol{\Theta}\right) \tag{5.9}$$

where $\delta_{v\max,T}$ = the tolerable limit of the maximum surface settlement, $\delta_v(\mathbf{X},\boldsymbol{\Theta})$ = the vertical settlement of each buried utility pipeline. In this study, the threshold value of the maximum surface settlement is chosen arbitrarily and limited to 10mm for the rigid pipe and 50mm for the flexible pipe.

Finally, we can define the limit state for the large rotation at a joint, possibly leading to excessive leakage or fracture at a joint. The relative rotation between the two adjacent pipe sections needs to be calculated to determine if there is failure at a joint.

$$g_{32}\left(\mathbf{X},\boldsymbol{\Theta}\right) = \varphi_T - \varphi_j\left(\mathbf{X},\boldsymbol{\Theta}\right) \tag{5.10}$$

where φ_T =the tolerable limit of joint rotations depending on the characteristic of pipe material and joint type, φ_j = the joint rotation increase due to an excavation as defined in Figure 5.5. The excavation-induced joint rotation (φ_j) and can be calculated by following equation (Molnar et al. 2003):

$$\varphi_j = \cos^{-1}\left(\frac{\Delta\delta_{h,ji}\Delta\delta_{h,kj} + {L_{pr}}^2 + \Delta\delta_{v,ji}\Delta\delta_{v,kj}}{\sqrt{{\Delta\delta_{h,ji}}^2 + {L_{pr}}^2 + {\Delta\delta_{v,ji}}^2}\sqrt{{\Delta\delta_{h,kj}}^2 + {L_{pr}}^2 + {\Delta\delta_{v,kj}}^2}}\right) \tag{5.11}$$

where L_{pr} = the characteristic length for joint rotation analysis of pipelines, and 6.1m is used as suggested by Molnar et al.(2003).

5.4 Fragility Assessment for Multiple Serviceability Criteria

Fragility is defined as the conditional probability of failure, attaining or exceeding a prescribed limit states, of a component or system for a given set of demand variables.

The failure event for the system is described in terms of unions of componential failure events. In this proposed work, we focused on the estimation of both component and system level fragility assessment of infrastructure. We estimate the fragility of attaining or exceeding specified limiting criteria for the assumed values of each infrastructure including buildings, bridges, and utility pipelines. The limit state function $g_{ij}(\mathbf{X},\mathbf{\Theta}_k)$ is defined such that the event $\{g_{ij}(\mathbf{X},\mathbf{\Theta}_k)\le 0\}$ denotes the attainment or exceedance of the limit state at the *k*th excavation stage. Using the model for three-dimensional profile of ground movement as described before and considering specified thresholds for multiple serviceability criteria, the system fragility can then be formulated as

$$F\left(C_{ij,T},\mathbf{\Theta}_k\right)=\mathrm{P}\left[\bigcup_{i=1,\ldots,3}\bigcup_{j=1,\ldots,3}\left\{g_{ij}\left(\mathbf{X},\mathbf{\Theta}_k\right)\le 0\right\}\middle|C_{ij,T}\right] \tag{5.12}$$

where $\mathrm{P}[A\,|\,\mathbf{s}]=$ the conditional probability of event A for the given values of variables $\mathbf{s}$, $k=$ the excavation stage, $\mathbf{s}=\left[C_{ij,T}\right]=(\varepsilon_{p,T},DR_T,\delta_{v\max,T},\Delta\delta_{v,T},\omega_T,\varphi_T)=$ a specified threshold constant value vector for each limit state function for the various infrastructures, $i, j=$ the indices for each different infrastructure and failure mode. The uncertainty in the event for the given k, $C_{ij,T}$ arises from the inherent randomness in the variables $\mathbf{x}$, the inexact nature of the three-dimensional profile of ground movement model (or its sub-models to estimate $\varepsilon_p(\mathbf{X},\mathbf{\Theta}_k)$, $\delta_v(\mathbf{X},\mathbf{\Theta}_k)$, $\delta_h(\mathbf{X},\mathbf{\Theta}_k)$), and the uncertainty inherent in the model parameters $\mathbf{\Theta}_k$. If we know the detailed characteristics of multiple infrastructures adjacent to excavation works, the $\mathbf{x}$ vector can be treated as a

constant vector. To incorporate the epistemic uncertainties inherent in the unknown model parameters $\boldsymbol{\Theta}_k$, we only consider $\boldsymbol{\Theta}_k$ as random variables. The predictive estimate of system fragility, $\tilde{F}(\mathbf{s})$, is then the expected value of $F(\mathbf{s},\boldsymbol{\Theta}_k)$ over the posterior distribution of $\boldsymbol{\Theta}_k$ (Gardoni et al. 2002), i.e.,

$$\tilde{F}(\mathbf{s}) = \int F(\mathbf{s},\boldsymbol{\Theta}_k) f(\boldsymbol{\Theta}_k) d\boldsymbol{\Theta}_k \tag{5.13}$$

where $f(\boldsymbol{\Theta}_k)$= the posterior probability density function of $\boldsymbol{\Theta}_k$. The First Order Reliability Method (FORM) and the Monte Carlo simulation (MC) are used to estimate the component fragility, and MC is used to estimate the system fragility $\tilde{F}(\mathbf{s})$ in this study, since a closed-form solution of Eq. (5.13) is generally not available.

Figure 5.7 represents a conceptual three dimensional plot that shows the probability of exceedance versus k and $C_{ij,T}$. This figure shows that the probability of exceedance (fragility) decrease as $C_{ij,T}$ increases for a certain excavation stage, and the fragility increase as an excavation proceeds.

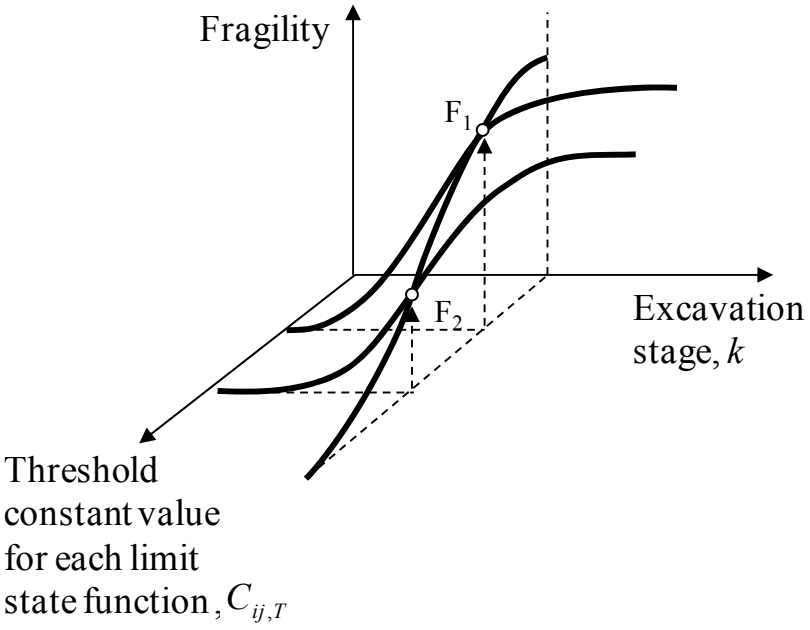

Figure 5.7 Schematic diagram for the fragility of an infrastructure

5.5 Sensitivity and Importance Measures

In this subsection, first we compute the sensitivity measures for the parameters used in the estimate of damage potentials in existing infrastructures caused by excavation works in an urban area. Then, we assess the importance measures for all random variable in the probabilistic model. We note that the sensitivity and importance measures are computed by FORM.

5.5.1 Sensitivity measures

In a reliability analysis, sensitivity measures are used to determine the effects on the reliability of changes in the parameters in the limit state function or in the distribution of the random variables. In particular, we consider the influence on $\beta(\mathbf{s})$ and $F(\mathbf{s})$ of

$\mathrm{E}(\boldsymbol{\Theta}_k)$. The sensitivity measures can be computed following Hohenbichler and Rackwitz (Hohenbichler and Rackwitz 1986). The gradient of the first-order reliability approximation of the fragility is obtained by using the chain rule of the differentiation as

$$\nabla_{[\mathrm{E}(\boldsymbol{\Theta}_k)]} F(\mathbf{s}) = -\varphi(\beta) \nabla_{[\mathrm{E}(\boldsymbol{\Theta}_k)]} \beta(\mathbf{s}) \tag{5.14}$$

where $\varphi(\cdot)$ = the standard normal probability of density function.

Since we are interested in the sensitivities of β with respect to the mean of each random variable, it is convenient to scale $\nabla_{[\mathrm{E}(\boldsymbol{\Theta}_k)]}\beta$ to compare the sensitivity measures of all parameters. On this basis, following Hohenbichler and Rackwitz (1986), we define the vector $\boldsymbol{\delta}$

$$\boldsymbol{\delta} = \mathbf{D} \nabla_{[\mathrm{E}(\boldsymbol{\Theta}_k)]} \beta \tag{5.15}$$

where $\mathbf{D}$ = the diagonal matrix with diagonal elements given by the standard deviation of each random variable. We note that the vector $\boldsymbol{\delta}$ renders the element of these vectors dimensionless and makes the parameter variations proportional to the corresponding standard deviations, which are measures of the underlying uncertainties.

5.5.2 Importance measures

The random variables have different contributions to the variability of the each limit state function for each infrastructure. Following Der Kiureghian and Ke (1995), a vector of importance measures can be defined as

$$\boldsymbol{\gamma}^{\mathrm{T}} = \frac{\hat{\boldsymbol{\alpha}}^{\mathrm{T}} \mathbf{J}_{\mathbf{u}^*,\mathbf{z}^*} \mathbf{D}'}{\left\| \hat{\boldsymbol{\alpha}}^{\mathrm{T}} \mathbf{J}_{\mathbf{u}^*,\mathbf{z}^*} \mathbf{D}' \right\|} \tag{5.16}$$

where $\mathbf{z} = (\boldsymbol{\Theta}, \boldsymbol{\varepsilon})$ = the vector of all random variables, $\boldsymbol{\varepsilon} = (\varepsilon_1, \ldots, \varepsilon_r)$, $\hat{\boldsymbol{\alpha}}$ = a row vector of the negative normalized gradient of the limit state function evaluated at the design point in the standard normal space, $\mathbf{J}_{\mathbf{u}^*,\mathbf{z}^*}$ = the Jacobian of the probability transformation from the original space $\mathbf{z}$ into the standard normal space with respect to the parameters $\mathbf{z}$ and computed at the most likely failure point (design point) $\mathbf{u}^*$, $\mathbf{D}'$ = the diagonal matrix of standard deviations of the equivalent normal variables $\mathbf{z}'$, defined by the linearized inverse transformation $\mathbf{z}' = \mathbf{z}^* + \mathbf{J}_{\mathbf{z}^*,\mathbf{u}^*} \cdot (\mathbf{u} - \mathbf{u}^*)$ at the design point. Each element in $\mathbf{D}'$ is the square root of the corresponding diagonal element of the covariance matrix $\boldsymbol{\Sigma}' = \mathbf{J}_{\mathbf{z}^*,\mathbf{u}^*} \cdot \mathbf{J}^{\mathrm{T}}_{\mathbf{z}^*,\mathbf{u}^*}$ of the variables in $\mathbf{z}'$.

5.6 Application

The proposed reliability analysis approach is applied to an actual supported excavation project for the Robert H. Lurie Medical Research Building in Evanston, Illinois with an imaginary concrete building and bridge as shown in Figure 5.8. The area surrounding the Lurie Center site is heavily populated with underground utilities transmitting water, waste, gas, electric lines, and telecommunication cables. The analyses presented herein focuses on gas mains along the north, west, and south walls of the excavation as summarized in Table 5.7. We note that the building and bridge are imaginary infrastructure but the gas mains are real one. The dimensions of building are assumed to

be 20m (width), 15m (length) and 10m (height). The span length of imaginary bridge is assumed to be 30m as shown in Figure 5.8.

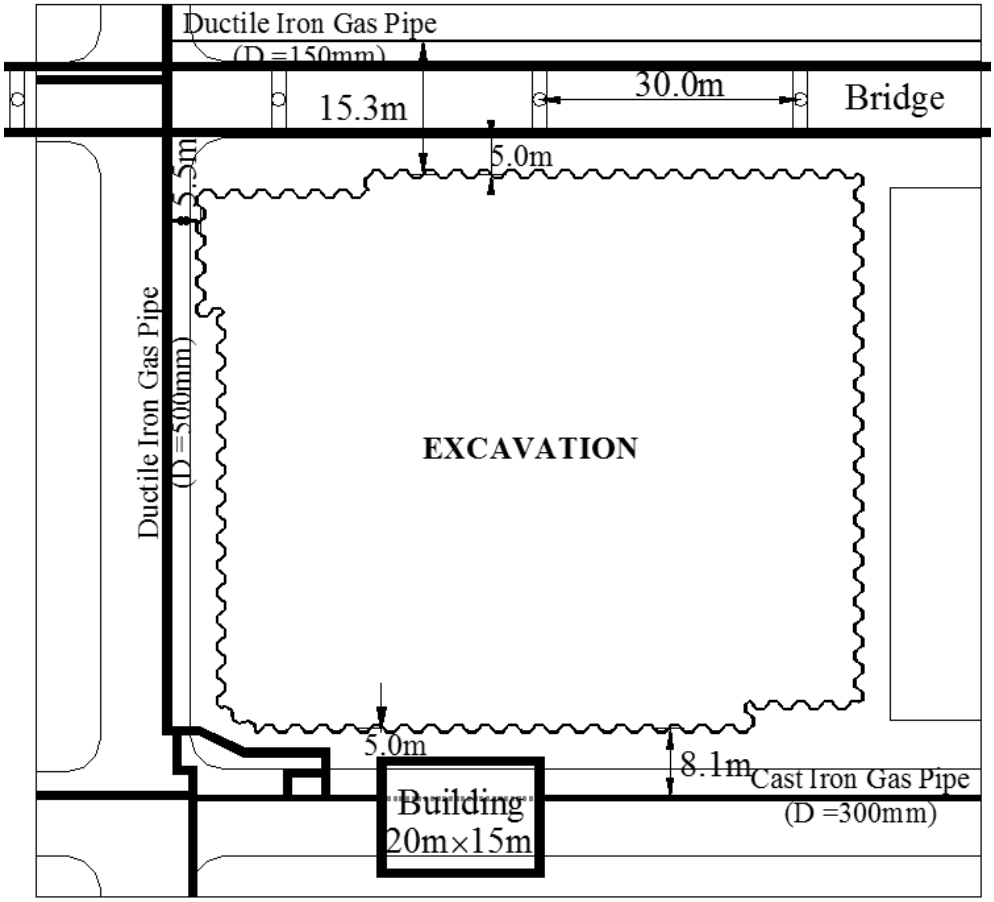

Figure 5.8 General layout of example site including imaginary infrastructures

Table 5.7 Dimensions in utility pipeline adjacent to example site

Pipe material	Direction from excavation	Distance from excavation (m)	Pipe Diameter (mm)
Cast Iron	South	8.1	300
Ductile Iron	North	15.5	150
	West	5.5	500

Figure 5.9 shows a schematic representation of the cross-section with an excavation of 80m (width) and 12.8m (depth). Detailed description and ground response of the excavation are provided in Finno and Roboski (2005). Measurements of both horizontal displacements and vertical ground surface settlements were obtained from inclinometers and optical survey from every side of excavation except the east side as shown in Figure 5.10.

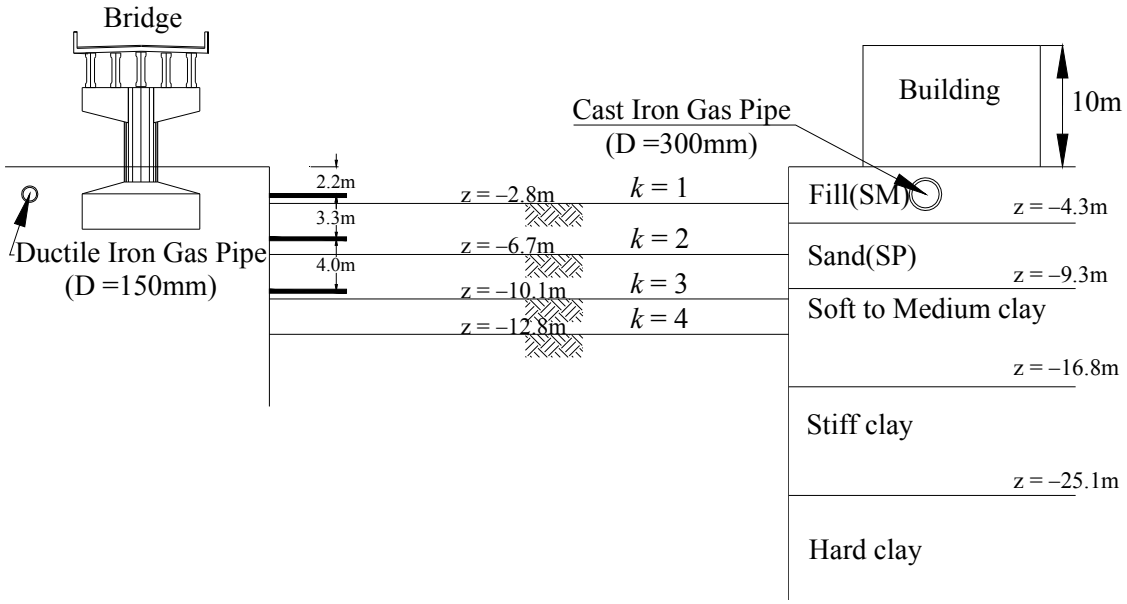

Figure 5.9 Cross-section of example site

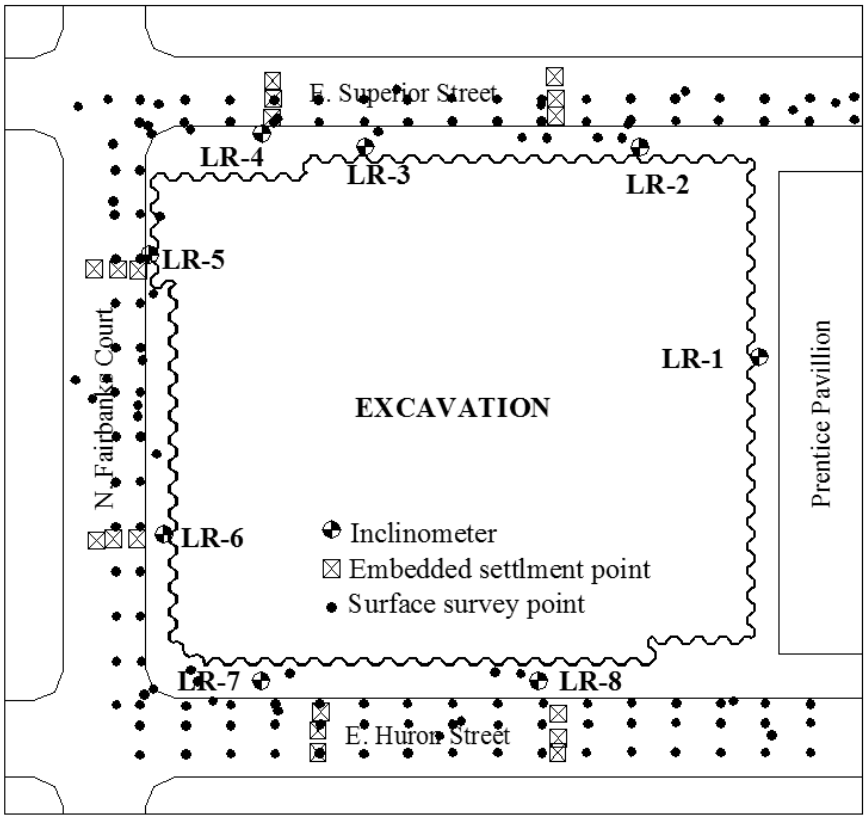

Figure 5.10 General layout of Lurie Center site instrumentation (Modified from Finno and Roboski 2005)

We assume that the infrastructure including buildings, bridges, and utility pipelines adjacent to the excavation site moves with the ground displacement profiles and provides no restraint to the soil. Furthermore, we assume that the initial displacement for the building and bridge after the construction, and initial joint rotations for the gas mains after installation before an excavation are relatively small and negligible when compared with the excavation-induced displacement and joint rotation.

In this example, we can setup the 12 limit state functions to assess the system fragility as followings; 3 for building at the south side, 3 for bridge at the north side, and 2 for gas mains for north, south and west sides.

$$F\left(C_{ij,T},\boldsymbol{\Theta}_k\right)=\mathrm{P}\left[\begin{array}{l}\bigcup\limits_{j=1,2,3}\left\{g_{1j}\left(\mathbf{X},\boldsymbol{\Theta}_k\right)\le 0\right\}\\ \bigcup\limits_{j=1,2,3}\left\{g_{2j}\left(\mathbf{X},\boldsymbol{\Theta}_k\right)\le 0\right\}\\ \bigcup\limits_{j=1,2}\ \bigcup\limits_{q=\mathrm{North,South,West}}\left\{g_{3jq}\left(\mathbf{X},\boldsymbol{\Theta}_k\right)\le 0\right\}\end{array}\middle| C_{ij,T}\right] \tag{5.17}$$

For each *k*th excavation stage, the component reliability analyses are performed for each limit state function criterion. Because the deformation will increase as excavation proceeds, we want to summarize the results for the 4th excavation stage that can be considered as the most dangerous during construction. We also note that the component fragility at the 1st excavation stage is close to zero due to the small excavation-induced deformations.

The component fragility curves for each limit function at the 4th excavation stage are shown in Figure 5.11, and the component fragility decrease as each $C_{ij,T}$ increases as we expected.

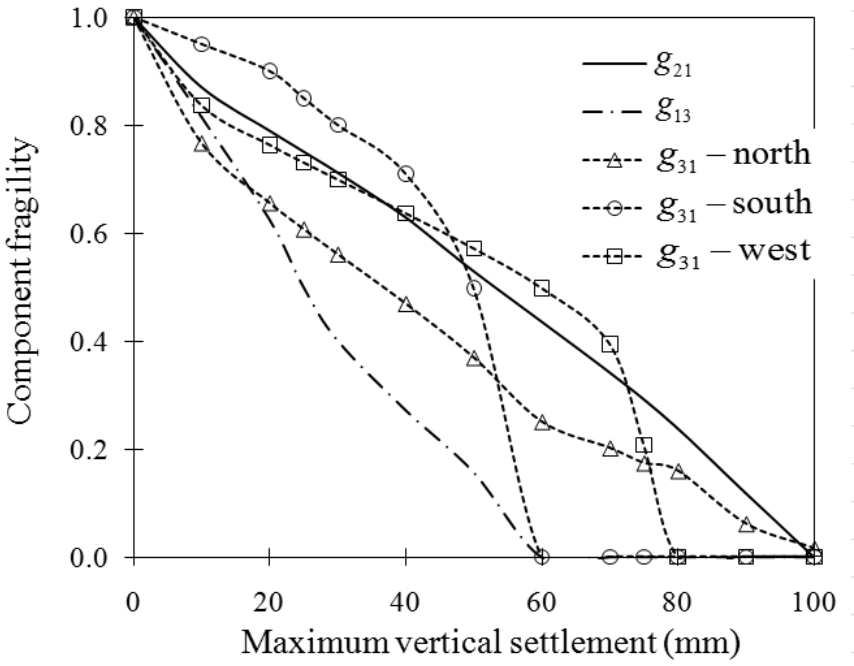

(a) $C_{ij,T} = \delta_{v\max,T}$ case

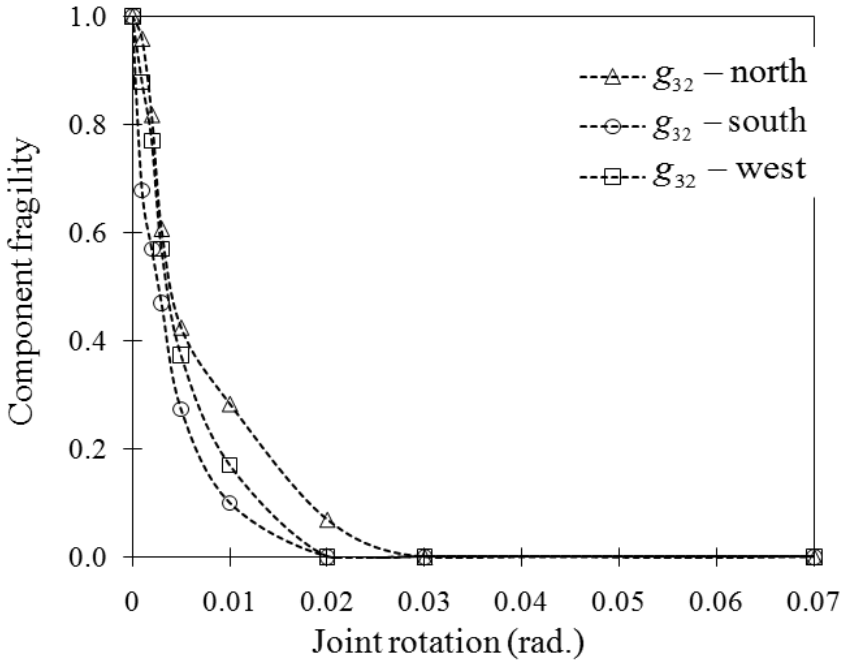

(b) $C_{ij,T} = \varphi_T$ case

Figure 5.11 Component fragility curve of an infrastructure

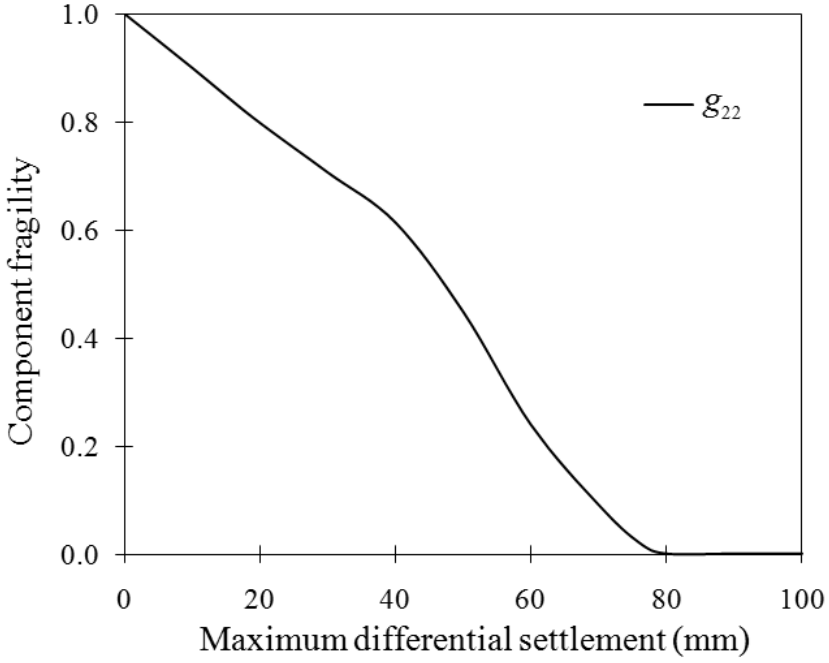

(c) $C_{ij,T} = \Delta\delta_{v,T}$ case

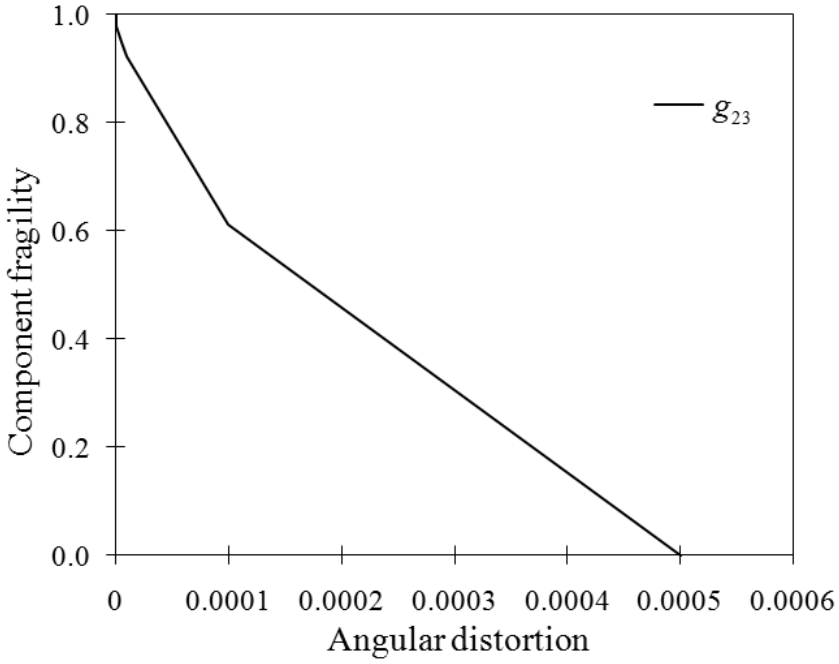

(d) $C_{ij,T} = \omega_T$ case

Figure 5.11 Continued

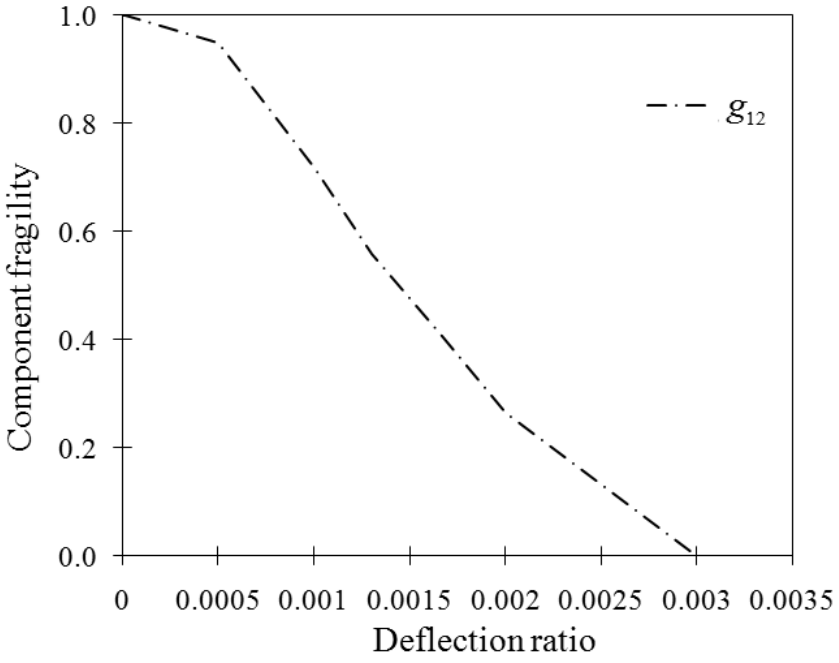

(e) $C_{ij,T} = DR_T$ case

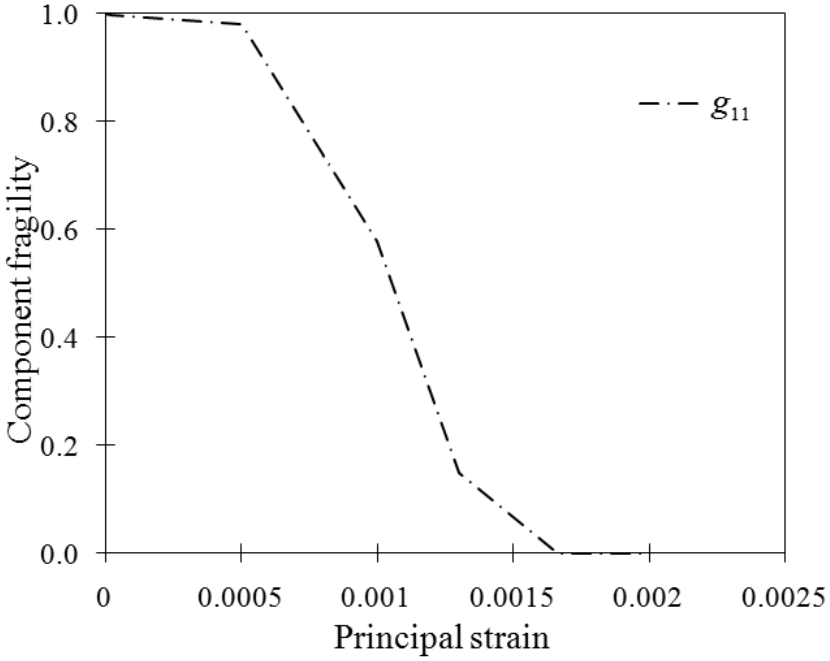

(f) $C_{ij,T} = \varepsilon_{p,T}$ case

Figure 5.11 Continued

The whole excavation is defined as a series system because system failure is defined by a failure of any individual component of different limit state function. The system failure is defined as an event that at least one component exceeds its corresponding limit state. The system fragility curve is computed by Monte Carlo Simulation (MCS) employing component fragility models and the identified correlation coefficients. The correlation coefficients are assumed to be constant over the considered at the same excavation stage. The correlation coefficients matrix for the 4th excavation stage is summarized in Table 5.8. The system fragility curve for the 4th excavation in terms of the maximum vertical settlement is shown in Figure 5.12.

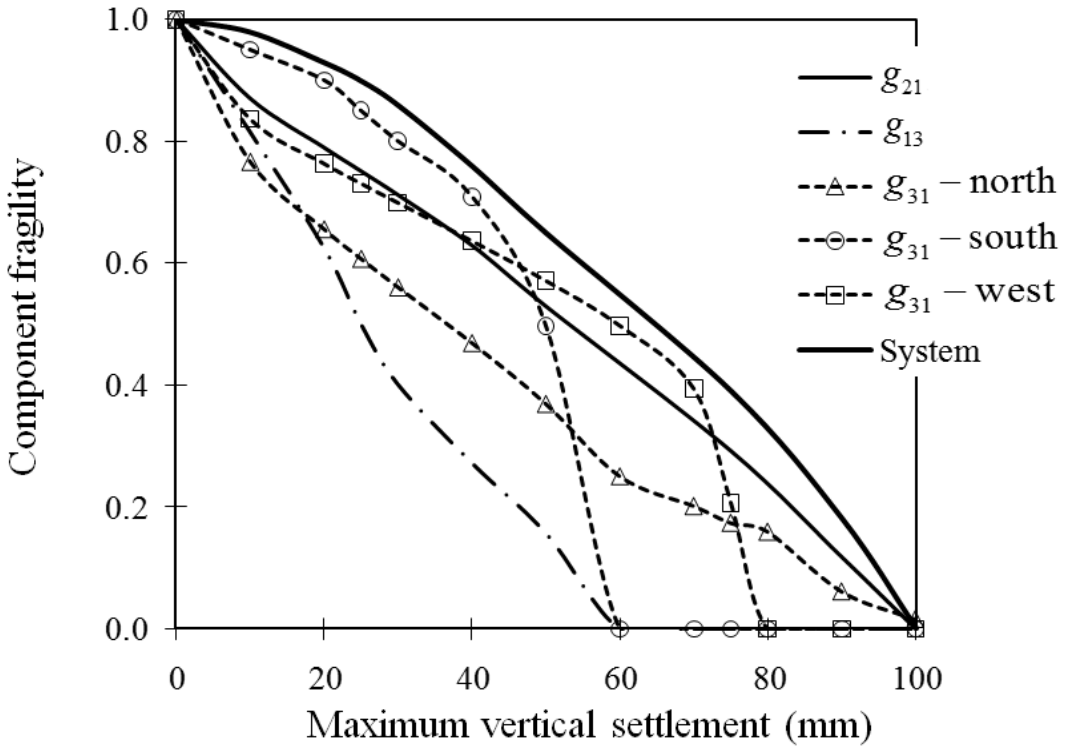

Figure 5.12 System fragility curve of an infrastructure for the 4th excavation stage

Table 5.8 Correlation coefficient matrix for each component at stage 4

			Buildings			Bridges			Pipelines					
									North		South		West	
			g_{11}	g_{12}	g_{13}	g_{21}	g_{22}	g_{23}	g_{31}	g_{32}	g_{31}	g_{32}	g_{31}	g_{32}
Buildings		g_{11}	1											
		g_{12}	0.67	1										
		g_{13}	–0.74	–0.73	1									
Bridges		g_{21}	–0.31	–0.59	0.39	1								
		g_{22}	–0.11	–0.45	0.29	0.89	1							
		g_{23}	–0.06	–0.64	0.95	0.75	0.65	1						
Pipelines	North	g_{31}	–0.01	0.99	0.99	0.98	0.99	0.94	1					
		g_{32}	–0.01	–0.12	0.12	0.12	0.13	0.18	0.13	1				
	South	g_{31}	–0.01	–0.99	0.01	0.99	0.99	0.95	0.99	0.13	1			
		g_{32}	0.99	0.01	0.99	0.01	0.01	0.01	0.01	0.01	–0.01	1		
	West	g_{31}	0.01	0.87	–0.93	–0.91	–0.94	–0.88	–0.97	–0.12	–0.94	0.01	1	
		g_{32}	0.01	–0.11	0.11	0.11	0.11	0.16	0.11	0.04	0.11	0.01	–0.11	1

Figure 5.13 shows the sensitivity measures of all random variables for the component fragility at stage 4. It is observed that the parameters related to the surface settlements including $\mathrm{E}(\theta_{v,\max})$ and $\mathrm{E}(\theta_{v3})$ have larger effects on the component fragility for the settlement related limit state functions $(g_{12}, g_{13}, g_{21}, g_{22}, g_{23}, g_{31})$ for the various infrastructures. Furthermore, the parameters related to the horizontal displacements including $\mathrm{E}(\theta_{u2})$, $\mathrm{E}(\theta_{u3})$ and $\mathrm{E}(\theta_{h2})$ have larger effects on the component fragility for the horizontal deformation related limit state function (g_{11}, g_{32}) for the building and gas mains.

Similarly, Figure 5.14 shows the importance measures of all random variables for the component fragility at stage 4. Observations similar to those made for the sensitivity analysis can be made for the importance measures. We can see that θ_{v3} is the most important variable and $\theta_{v,\max}$ is the second most important variable for the settlement related limit state functions. The positive signs of the importance measures of θ_{v3} and $\theta_{v,\max}$ indicate that these are "load" (demand) variables. The negative sign of the importance measure indicates that this random variable acts as a "resistance" (capacity) variable in the each limit state function.

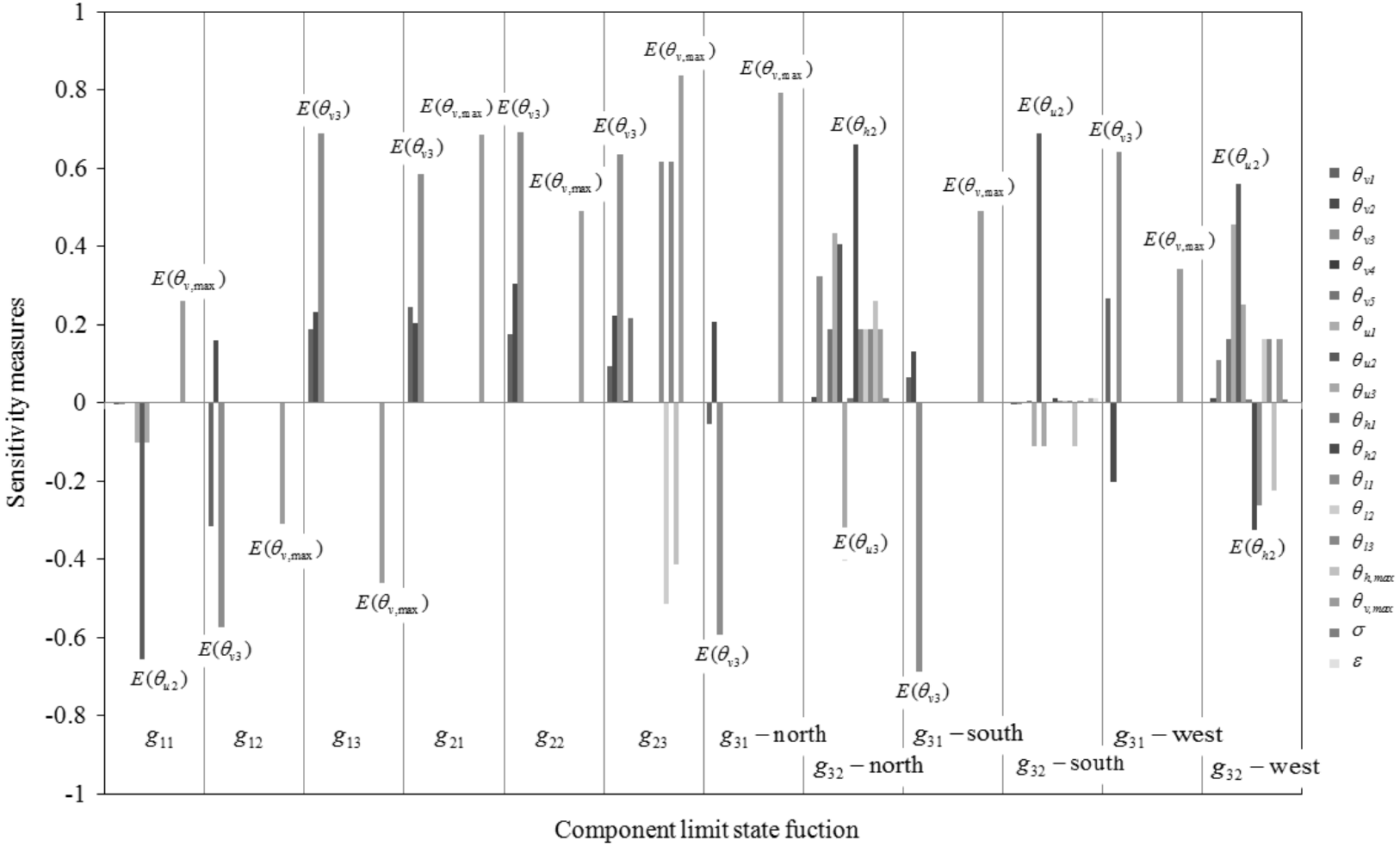

Figure 5.13 Sensitivity measures of all random variables for the system fragility at stage 4

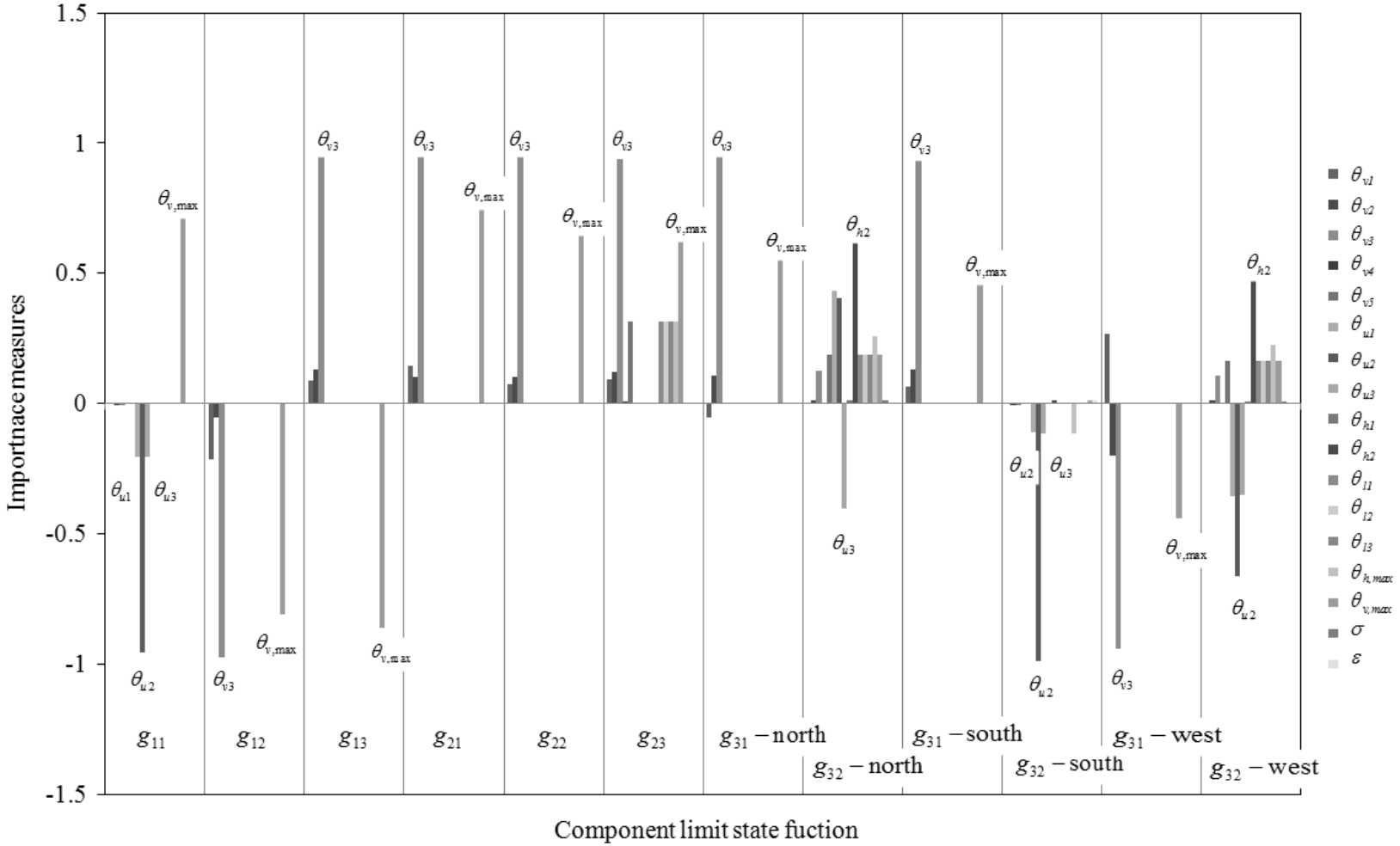

Figure 5.14 Importance measures of all random variables for the component fragility at stage 4

Kang et al. (2008) proposed to use the conditional probability of the component event given the system failure as an importance measure of the component. This conditional probability importance measure (CIM) of the *ij*th component event, E_{ij} , is defined as

$$CIM_{ij} = P\left(E_{ij} \middle| E_{sys}\right) = \frac{P\left(E_{ij}E_{sys}\right)}{P\left(E_{sys}\right)} \tag{5.18}$$

If E_{ij} denotes the event that the $\{g_{ij}(\mathbf{x}, \mathbf{\Theta}_k) \le 0\}$ denotes the attainment or exceedance of the limit state, the system event (E_{sys}) that at least one of the adjacent infrastructure fails is described by

$$\begin{aligned} E_{sys} = {} & E_{11} \cup E_{12} \cup E_{13} \cup E_{21} \cup E_{22} \\ & \cup E_{31-\text{north}} \cup E_{32-\text{north}} \cup E_{31-\text{south}} \cup E_{32-\text{south}} \cup E_{31-\text{west}} \cup E_{32-\text{west}} \end{aligned} \tag{5.19}$$

In order to identify important component events, the CIMs in Eq. (5.18) are computed by the matrix-based system reliability (MSR) method (Song and Kang 2009). Figure 5.15 shows the relative importance of component events at the 4$^{\text{th}}$ excavation stage. We can see that the damage potential for the gas main at the west side $(g_{31} - \text{west})$ is the most important component and the damage potential for the bridge at the north side (g_{22}) is the second most important component for the excavation work.

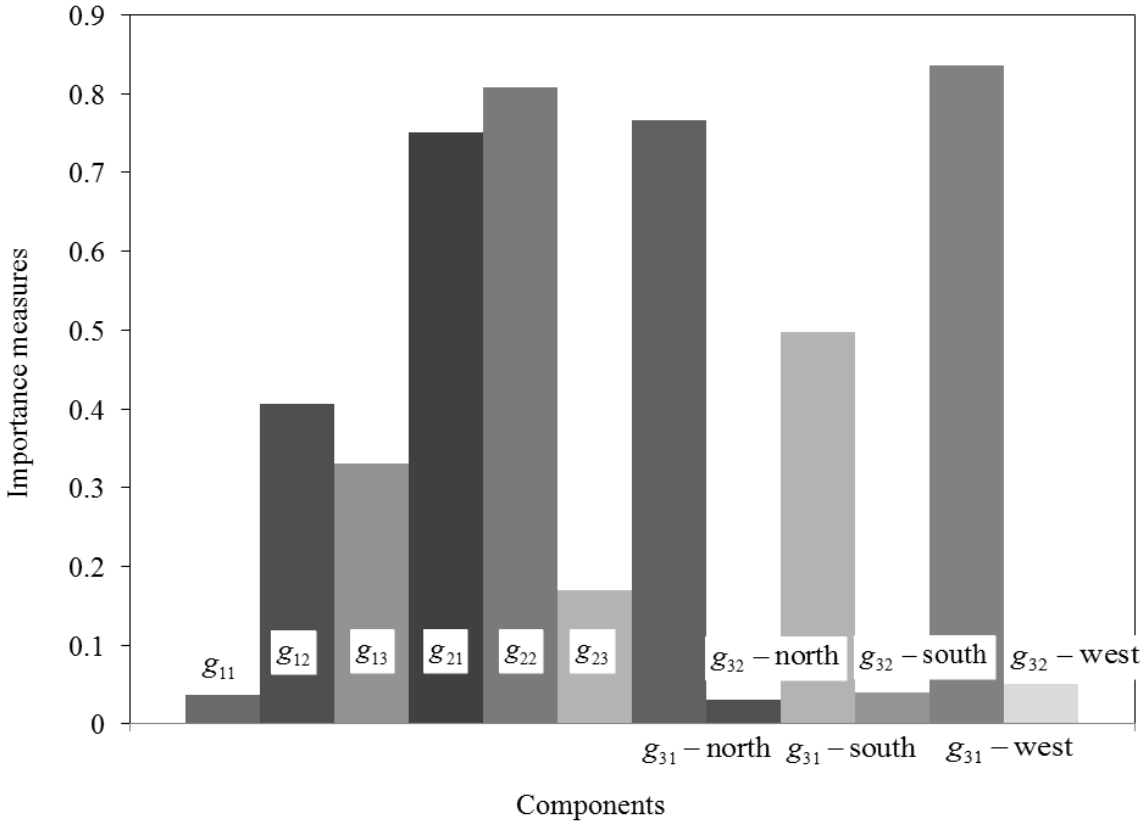

Figure 5.15 Conditional probability importance measures of infrastructure

5.7 Conclusions

A reliability analysis framework is proposed to assess the fragility of excavation-induced infrastructure system damage for multiple serviceability limit states. A Bayesian framework based on a semi-empirical method is used to update the predictions of ground movements in the later stages of excavation based on the field measurements. The component and system fragility estimates for excavation works in an urban area are developed in this study along with sensitivity and importance measures.

Fragility estimates applied to the Lurie excavation site with imaginary infrastructure system including building, bridge and gas mains show that the probability of exceedance decrease as the specified threshold criteria increase.

The sensitivity measures indicates that the parameters related to the surface settlements including $\mathrm{E}(\theta_{v,\max})$ and $\mathrm{E}(\theta_{v3})$ have larger effects on the component fragility than other shape function parameters for the settlement related limit state functions $(g_{12}, g_{13}, g_{21}, g_{22}, g_{23}, g_{31})$ for the various infrastructures. Furthermore, the parameters related to the horizontal displacements including $\mathrm{E}(\theta_{u2})$, $\mathrm{E}(\theta_{u3})$ and $\mathrm{E}(\theta_{h2})$ have larger effects on the component fragility for the horizontal deformation related limit state function (g_{11}, g_{32}) for the building and gas mains.

The importance measures of all random variables for the component fragility at stage 4. The similar trend can be observed for the importance measures. The θ_{v3} is the most important variable and $\theta_{v,\max}$ is the second most important variable for the settlement related limit state functions.

The proposed approach can be used for an adaptive reliability-based optimal design of the excavation system in which the design is modified after each excavation stage to minimize costs and maintain a minimum reliability requirement. This method can also be expanded to any type of excavation projects related to urban redevelopment and infrastructure improvement. For example, additional limit state functions can be added to the system reliability analysis to consider the serviceability of tunnel for a deep excavation within the influence zone of an existing tunnel.

6. RELIABILITY ASSESSMENT OF EXCAVATION SYSTEMS CONSIDERING BOTH STABILITY AND SERVICEABILITY PERFORMANCE

Excavation projects related to urban redevelopment and infrastructure improvement are often governed by serviceability-based design, rather than failure prevention criteria. Deformation tolerance specifications are often prescribed based on minimizing potential damage to adjacent structures. A risk-based approach to serviceability performance that systematically incorporates design parameter uncertainty will allow engineers to address soil uncertainty in performance-based design. This study demonstrates the use of various kinds of reliability methods, such as Response Surface Method (RSM), First Order Reliability Method (FORM), Second Order Reliability Method (SORM), Adaptive Importance Sampling (AIS), Monte Carlo Simulation (MCS), and system reliability, to assess the risk of stability and/or serviceability failure of an entire excavation support system throughout the entire construction process. By considering multiple failure modes (including serviceability criteria) of an excavation, the component and system reliability indices for each excavation step are assessed during the entire excavation process. Sensitivity analyses are conducted for the system reliability calculations, which demonstrate that the adjacent structure damage potential limit state function is the dominant factor for determining excavation system reliability. An example is presented to show how the serviceability performance for braced excavation problems can be assessed based on the system reliability index.

6.1 Introduction

Recent conventional methods for assessing the stability of deep excavation system utilized computational tools such as the Finite Element (FE) method. Various uncertainties, such as the variability of the loadings, geotechnical soil properties, and engineering and geometrical properties of the retaining structure, must be addressed when calculating the stability or serviceability performance of an excavation system.

Much of the early development of reliability analyses in geotechnical engineering focused on slope stability applications, where the reliability index was calculated for one specific failure surface (Tang et al. 1976; Semih Yücemen and Al-Homoud 1990; Chowdhury and Xu 1993; Chowdhury and Xu 1995). For the calculation of reliability index, the deterministic critical failure plane was used (Vanmarcke 1977; Christian et al. 1994); however, the failure plane associate with the minimum reliability index does not always coincide with the deterministic critical failure plane (Li and Lumb 1987). Hence, extensive research has been conducted to find the probabilistic critical failure plane using limit equilibrium methods (Low and Tang 1997; Low et al. 1998; Low 2001; Low 2003). In recent years, FE methods have been increasingly adopted to study slope stability and embankment problems (Smith and Hobbs 1974; Zienkiewicz et al. 1975; Griffiths 1980; Wong 1985; Ugai 1989; Jin-Zhang et al. 1995; Ugai and Leshchinsky 1995; Griffiths and Lane 1999; Smith and Griffiths 2004). Griffiths and Fenton (2004) applied the random FE method toward a reliability analysis of a simple homogeneous slope, in which nonlinear FE analysis was combined with random field theory. However, the application of FE-based probabilistic stability analyses of

embankments or slopes is still very limited because of time and cost restrictions. Recent research has focused on probabilistic approaches to deformation-based design (e.g. Fenton and Griffiths 2002), which can be further extended to additional geotechnical applications with serviceability requirements, such as deep excavations.

For deep-excavations in urban environments, the reliability analyses would be more complex because of uncertainties related to serviceability performance. Phoon and Kulhawy (1999) have defined three primary sources of geotechnical uncertainties: inherent variability, measurement uncertainties, and transformation uncertainty. Because of these uncertainties, the serviceability performance of an excavation system cannot be determined precisely, and the computed lateral wall displacement does not reflect the degree of uncertainty of the underlying random variables (Goh and Kulhawy 2005). In this section, the uncertainties were limited to the coefficient of variation of the geotechnical engineering properties. Spatial correlation uncertainties are not addressed in this study, as site investigation data are often too sparse to conduct spatial correlation analyses in deep excavation design. Although spatial uncertainty is a significant factor in geotechnical engineer design, and, as such, should be included in reliability-based design, it is not within the scope of this research to include spatial correlation analyses. Because usual design stage for deep excavations, we cannot have enough information due to the limited amount of site investigation data.

Several methods can be used to quantify the effect of engineering property uncertainties on the stability and serviceability limit state performance of the whole excavation system. The first direct method would be to carry out Monte Carlo

simulations (MCS), using random variables with specified joint probability distributions to represent these geotechnical uncertainties and to perform a large number of deterministic simulations using a numerical methods (Harr 1987; Melchers 1999; Baecher and Christian 2003; Ang and Tang 2007). A second method could be the use of a stochastic FE method, as described in an earlier section (Griffiths and Lane 1999; Griffiths and Fenton 2004). Another method, which reduces calculation time and resources required for MCS, is the response surface method (RSM). In this approach, the limit state surface is implicitly determined by polynomial regression models through a series of analyses using existing FE codes (Box and Wilson 1954; Bucher and Bourgund 1990; Goh and Kulhawy 2005; Xu and Low 2006). The spreadsheet-based technique (Low and Tang 1997; Low and Tang 2004; Low 2005) could be used to determine the stability and serviceability limit state performance of the excavation system (Goh and Kulhawy 2005).

Recent applications of reliability concepts toward excavation system design have mainly focused on assessing the stability of the structure itself, with limited research focusing on the reliability assessment of serviceability criteria. A Point Estimate Method (PEM) combined with a FE model was used to assess the probability of the horizontal displacement of the top of a cantilever sheet pile wall exceeding an arbitrary threshold value (Schweiger et al. 2001). Also, a comparison of probabilistic, stochastic, fuzzy set and random set methods for reliability analysis of excavation problems was performed (Peschl and Schweiger 2003; Schweiger and Peschl 2005). Although an assessment of the probability of damage to an adjacent building could be conducted by

providing certain ranges of the probability, the system reliability, which considers multiple limit state functions, was not addressed.

The overall objective of this study is to demonstrate the potential of integrating a system reliability analysis technique with the FE method to assess both stability and serviceability performance of braced excavation wall systems in probabilistic terms. By introducing basic structural reliability concepts that reflect the degree of uncertainty of the underlying random variables in the analyses, engineers can address the uncertainties and their effects on the probability of failure as the excavation progresses.

This section will present the fundamental concepts of a reliability analysis, followed by a description of the basic components of the RSM and their incorporation into both component and system reliability analyses. An example is presented to demonstrate the assessment of the system reliability, considering both stability and serviceability performance of a braced excavation.

6.2 Factor of Safety and Reliability Index in Excavation Systems

6.2.1 Factor of safety by strength reduction technique

For complex geotechnical structures, such as deep excavations and tunnels, the definition of a system factor of safety (*FOS*) is not straightforward because many components contribute to the failure mechanism. In the case of a deep excavation, components include: soil strength, water table elevation, the interaction between soil and structural elements, and construction sequencing.

The shear strength reduction technique consists of a successive reduction of the shear strength parameters of the soil until the soil fails or a failure mechanism is developed. The resulting can be obtained by:

$$FOS(\mathbf{X}) = \frac{\tan\phi}{\tan\phi^*} = \frac{c}{c^*} \tag{6.1}$$

where $\mathbf{X}$ is the collection of random input parameters, the shear strength parameters c and ϕ refer to the initial input values, c^* and ϕ^* refer to the reduced values. In this technique, the definition of the *FOS* is the same as that adopted by the conventional limit equilibrium method (e.g. Dawson et al. 1999). It has the advantage that no assumptions need to be made about the location of the failure surface. This technique is a reasonable alternative to limit equilibrium methods (Zienkiewicz et al. 1975; Griffiths 1980; Ugai 1989; Ugai and Leshchinsky 1995; Griffiths and Lane 1999).

When performing strength reduction technique, it must always be determined if the calculation procedures are not terminated by local numerical instability problems. Close examination of failure mechanism, for example, the incremental shear strain distribution of the excavation system, will expose a termination due to numerical instability problems. In this study, it is assumed that the final calculation step of strength reduction for each excavation construction step has resulted in a fully developed failure mechanism. Since the strength of structural element is not influenced by the current strength reduction technique, it is assumed that the final calculation step of strength reduction for each excavation construction step has resulted in a fully developed failure mechanism.

6.2.2 Reliability analysis

Xu and Low (2006) pointed out that the factor of safety calculated from conventional deterministic stability analysis is not a consistent measure of risk. Excavations with factors of safety larger than unity still have some chance of failure, due to the uncertainties involved in characterizing the soil properties, environmental conditions and model errors associated with the analytical technique adopted. Probabilistic stability analysis offers an additional tool to evaluate the stability and serviceability of excavations while accounting for these uncertainties. When a probabilistic stability analysis is conducted, the failure probability for an excavation can be defined as:

$$p_f = P\left[g_k\left(\mathbf{X}\right) \le 0 \right] = \int_{g_k(\mathbf{X})\le 0} f\left(\mathbf{X}\right) d\mathbf{X} \tag{6.2}$$

where $g_k(\mathbf{X})$ are limit state functions, and $f(\mathbf{X})$ is the joint probability density function of the basic variable vectors $\mathbf{X}$. This equation is difficult to evaluate because it is difficult to identify the joint density function and to perform the integration over the entire multidimensional failure domain. A good approximation to Eq. (6.2) is to combine the RSM with the FORM (Xu and Low 2006) as described in section 6.2.4.

6.2.3 Definition of multiple limit state functions

To assess the systematic reliability of an excavation support system considering both stability and serviceability performance, it is suggested that the following three main criteria be considered simultaneously: (1) overall system stability, (2) lateral displacement of the soil and support system, and (3) differential settlement of adjacent

structures. The first limit state function is the ultimate limit-state failure prevention criterion and can be described as following equation:

$$g_1(\mathbf{X}) = C(\mathbf{X}) - D(\mathbf{X}) = FOS(\mathbf{X}) - 1 \tag{6.3}$$

where $C(\mathbf{X})$ is the capacity of excavation, whch will be the factor of safety ($FOS(\mathbf{X})$) obtained from the empirical equation to evaluate bottom heaving or finite element analyses. $D(\mathbf{X})$ is the demand and it will be unity in terms of the factor of safety. However, excavations related to urban redevelopment and infrastructure improvement are mainly governed by serviceability criteria. Because there are often adjacent structures and utilities, as shown in Figure 6.1, predicting deformation is critical for excavation support design.

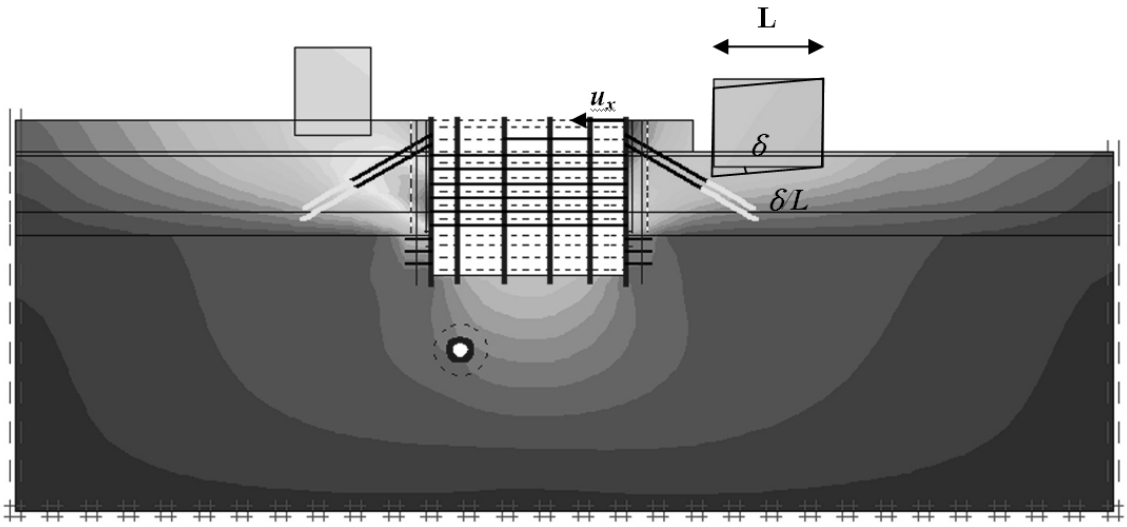

Figure 6.1 Two components of deep excavation design: (1) horizontal wall deflection (u_x) and (2) adjacent building deformation (δ / L)

The second limit state function employed in this analysis can be specified with respect to the maximum displacement of the excavation walls, thus representing a criterion for the serviceability of the support structure. If, for example, the maximum horizontal displacement is limited to 100 mm (chosen arbitrarily in this analysis), the limit state function could be expressed as:

$$g_2(\mathbf{X}) = C(\mathbf{X}) - D(\mathbf{X}) = 100 - u_x(\mathbf{X}) \tag{6.4}$$

where $u_x(\mathbf{X})$ is the maximum displacement obtained from the FE analyses. In a similar way, the third limit state function is a function of the deflection ratio, $\delta(\mathbf{X})/L$, of an adjacent structure (the ratio of the differential settlement between structural elements and the distance between the structural elements, assuming only one deformation mode, i.e. sagging only, and no rigid rotation). By assuming no rigid rotation and a single deformation mode, the deflection ratio is equal to the angular distortion of the building and is often employed to assess the likelihood of damage of adjacent building. For this analysis, the adjacent structure limit state function is defined as:

$$g_3(\mathbf{X}) = C(\mathbf{X}) - D(\mathbf{X}) = 1/600 - \delta(\mathbf{X})/L \tag{6.5}$$

According to Bjerrum (1963), angular distortion is the governing variable in the assessment of permissible deformations of the building (see Table 6.1). An arbitrary ratio of 1/600 is used in this study as the limiting value for the evaluation of this limit state function in order to obtain the reliability in terms of serviceability.

Table 6.1 Damage criteria - limiting angular distortion for various structures (Modified from Bjerrum 1963)

Angular Distortion	Damage Assessment
	Limit where structural damage of general buildings is to be feared.
1/150	Safe limit for flexible brick walls with h/L<0.25. Considerable cracking in panel walls and brick walls.
1/250	Limit where tilting of high, rigid buildings might become visible.
1/300	Limit where difficulties with overhead cranes are to be expected.
1/500	Safe limit for buildings where cracking is not permissible.
1/600	Danger limit for frames with diagonals.
1/750	Limit where difficulties with machinery sensitive to settlements are to be feared.

6.2.4 Response Surface Method (RSM)

The concept of the RSM consists of approximating the unknown implicit limit state function by a simple and explicit function, which is usually an nth order polynomial. When a polynomial function is used to approximate the true limit state function $(g_k(\mathbf{X}))$, experiments or numerical analyses will be performed at various sampling points (x_i) to determine the unknown coefficients in the approximate polynomial limit state function $(g_k'(\mathbf{X}))$. As discussed Xu and Low (2006), the effect of interaction terms on the reliability index will be negligible, such that those terms are ignored. The following second-order polynomial function, without interaction terms, is adopted in this study as suggested by Bucher and Bourgund (1990):

$$g_k'(\mathbf{X}) = l + \sum_{i=1}^{r} m_i x_i + \sum_{i=1}^{r} n_i x_i^2 \tag{6.6}$$

where x_i are random variables and the parameters l, m_i, and n_i are coefficients that need to be determined. By knowing the values of random variables at sampling points

selected for each variable, the value of the function at any point in the design space can be estimated by fitting a second-order polynomial, and only $(2N+1)$ sampling points are required to form the function for problems involving N variables. The procedure for a reliability analysis based upon RSM is also adapted from Xu and Low (2006). This will be discussed in more detail in Section 6.4.

In the first-order reliability method (FORM), an approximation to the probability integral in Eq. (6.2) is obtained by linearizing each limit state function in the standard normal space at an optimal point. Once the approximate polynomial limit state function $(g_k'(\boldsymbol{X}))$ is calculated, the first-order reliability procedures can be used to calculate the reliability index (β_{HL}) (Hasofer and Lind 1974) by following equation:

$$\beta_{HL} = \min_{\mathbf{X}\in\mathbf{F}} \sqrt{\left(\mathbf{X}-\mathbf{M}\right)^T \mathbf{C}^{-1}\left(\mathbf{X}-\mathbf{M}\right)} = \min_{\mathbf{X}\in\mathbf{F}} \sqrt{\left[(x_i-\mu_i)/\sigma_i\right]^T \left(\mathbf{R}\right)^{-1}\left[(x_i-\mu_i)/\sigma_i\right]} \quad (6.7)$$

where $\mathbf{X}$ = vector of random variables, $\mathbf{M}$ = vector of mean values, $\mathbf{C}$ = covariance matrix, $\mathbf{R}$ = correlation matrix, $\mathbf{F}$ = failure region and μ_i, σ_i = mean and standard deviation of random variable x_i, respectively. Eq. (6.7) forms a hyper-ellipsoid in *n*-dimensional space (Low 1996) and β_{HL} could be considered as the shortest distance from the mean value of random variables to the limit state function in standard normal space. This can be calculated, for example, by using the built-in solver optimization tool on Microsoft Excel to minimize β_{HL}, with the constraint that $g_k'\left(\mathbf{X}\right)=0$ (Low and Tang 1997; Low and Tang 2004). The probability of failure can be determined by Eq. (6.8) for Gaussian distributed random variables:

$$p_f \approx \Phi\left(-\beta_{HL}\right) \tag{6.8}$$

where $\Phi(\cdot)$ is the standard normal cumulative distribution function.

6.3 Proposed Method for Reliability Assessment of Excavation Systems

As mentioned in the previous subsection, the three limit state functions will be considered simultaneously for the reliability assessment of an excavation support system. Also, because the reliability index will be influenced by a staged construction process, a reliability index that considers multiple limit state functions should be updated for each excavation step. For each limit state function, the corresponding reliability index (β_{HL}) can be computed by RSM. However, it should be checked with the first-order reliability method (FORM), the second-order reliability method (SORM), Adaptive Importance Sampling (AIS), and Monte Carlo simulations (MCS) because it will become impractical for problems involving a large number of random variables and non-linear limit state functions.

NESSUS (Numerical Evaluation of Stochastic Structures Under Stress), a commercially available software package, was employed to calculate the limit state component reliability indices based on the FORM, SORM, AIS and MCS methods. These reliability indices were compared as verification of the reliability index computed using RSM and to improve the modeling of the limit state surface (Southwest Research Institute 2001; Southwest Research Institute. 2005).

Various methods for the evaluation of reliability index (or probability of failure, p_f) were described in the previous subsection, which were based on individual limit state functions. However, to consider the probability of fulfilling several criteria at the same time, system reliability assessment methods are required. For example, potential damage to adjacent buildings caused by an excavation might exceed the limit state surface even though the $FOS(\mathbf{X}) \geq 1$ limit state is has not been exceeded. Therefore, the excavation problem can be summarized as the assessment of the probability of a series system failure involving multiple limit states due to multiple components and/or multiple failure modes. There are several methods for system reliability calculations. A common approach is to consider reliability bounds for the serial, parallel, and combined systems. However, these methods provide only approximate solutions.

In NESSUS, a system failure is defined using a fault tree, which provides a systematic way to manage multiple failure modes. Through a fault tree, all the failure modes can be defined. A failure mode can involve one or more limit states. By adding all the failure modes, and therefore all the limit states, the system limit surface can be constructed piece by piece. The system reliability can be computed using the AIS method or MCS method in NESSUS. The AIS procedure for system reliability analysis requires the construction of multiple parabolic surfaces. In principle, it is a straightforward extension of the concept for one limit state. The difficult part is to develop a procedure for adding failure regions for additional limit states. This approach is ineffective for cases where system failure is governed by the joint effects from several limit states. In such cases, no limit state can be considered dominant because the most

probable point (MPP) of the individual limit state is not a likely event for a system failure. A more effective computational procedure adds samples progressively based on multiple failure modes.

The probability of failure considering the three failure modes described in section 6.2.3 can be presented in Eq. (6.9) as:

$$p_f = P\left[\left(g_1(\mathbf{X}) \le 0\right) \cup \left(g_2(\mathbf{X}) \le 0\right) \cup \left(g_3(\mathbf{X}) \le 0\right)\right] \tag{6.9}$$

The AIS methods minimize sampling in the safe region by adaptively and automatically adjusting the sampling space from an initial approximation of the failure region. The sampling space is defined using a limit state surface. The performance of AIS depends on the quality of the initial failure region approximation.

The sensitivity factors provide first-order information on the importance of the individual random variables in component reliability analyses. Other sensitivity measures with respect to a distribution parameter (mean or standard deviation) or a limit state function parameter can be estimated based on the sensitivity factors and the distribution transformation (Wu 1994). When a distribution parameter is changed, the sensitivity of p_f with respect to a distribution parameter (θ) can be evaluated using:

$$\frac{\partial p_f}{\partial \theta} = \int_{\Omega} \cdots \int \frac{\partial f(\mathbf{X})}{\partial \theta} dx \tag{6.10}$$

Therefore,

$$\frac{\partial p_f / p}{\partial \theta / \theta} = \int_{\Omega} \cdots \int \frac{\theta}{p} \frac{\partial f(\mathbf{X})}{f(\mathbf{X}) \partial \theta} f(\mathbf{X}) dx = E\left[\frac{\theta \, \partial f(\mathbf{X})}{f(\mathbf{X}) \partial \theta}\right]_{\Omega} \tag{6.11}$$

where the subscript Ω denotes that the expected value is evaluated using the joint PDF in the failure region. In general, numerical differentiation methods can be used to compute the value within $E[\cdot]$. The probabilistic sensitivities can be computed using AIS points within in the failure region. No additional limit state function calculations are required. Based on Eq. (6.11), two types of probabilistic sensitivity coefficients are proposed that are particularly useful for probabilistic design: the standard deviation sensitivity coefficient (S_{σ_i}) and the mean sensitivity coefficient (S_{μ_i}). The two sensitivity coefficients are defined as:

$$S_{\sigma_i} = \frac{\partial \ln p_f}{\partial \ln \sigma} = \frac{\partial p_{f_i} / p}{\partial \sigma_i / \sigma} \tag{6.12}$$

$$S_{\mu_i} = \frac{\partial \ln p_f}{\partial \mu / \sigma} = \frac{\partial p_{f_i} / p}{\partial \mu_i / \sigma_i} \tag{6.13}$$

where μ_i and σ_i are the mean and the standard deviation, respectively, of the random variable $(\mathbf{X})$. In Eq. (6.13), the use of the standard deviation as a scale factor implies that the allowable design range of a mean value is limited to a local region characterized by the random variable variability. When one or more σ_i values are very small (e.g., approaching zero) relative to their allowable μ_i design ranges, it may be more appropriate to replace σ_i with the allowable design ranges in Eq. (6.13). The above coefficients are dimensionless and can take positive, negative, or zero values. If desired, they can be normalized such that the sum of the normalized coefficients becomes one. When an S_{σ_i} is zero or relatively small, it implies that the random variable $(\mathbf{X})$ can be

varied over a wide range without significantly changing p_f. This, in turn, implies that S_{μ_i} will be negligible. On the other hand, when an S_{μ_i} is relatively large, the corresponding S_{μ_i} will also tend to be significant. These trends suggest that S_{σ_i} and S_{μ_i} are strongly related and both can be used to identify key contributing random variables.

6.4 Applications

This subsection presents an example in which the procedures described previously are used to evaluate the reliability index (or p_f) for braced excavations in soft clays. Goh and Kulhawy (2005) pointed out that the accuracy of the wall movement predictions through FE analyses is heavily dependent on the constitutive soil model used, and how accurately the parameters (derived from laboratory and in-situ tests) for the soil model reflect the actual ground conditions. In this example, the constitutive soil behavior was modeled with the Mohr–Coulomb elastic perfectly plastic model. A more complex constitutive soil model is more preferable for clays, therefore this approach could be expanded to another type of constitutive soil model such as modified Cam-Clay model. Only four random variables of the upper soft marine clay were considered to simplify the computations in this research. It is assumed that a first-story building is located adjacent to the site where excavation work takes place, located 4.5 m away from the sheet pile wall. The dimensions of building are assumed to be 10m (width) and 4m (height). The distribution pressure caused by imaginary concrete building was assumed

to be 40kN/m^2. Figure 6.2 shows a schematic representation of the cross-section with an excavation of 27m (width) and 7.4m (depth).

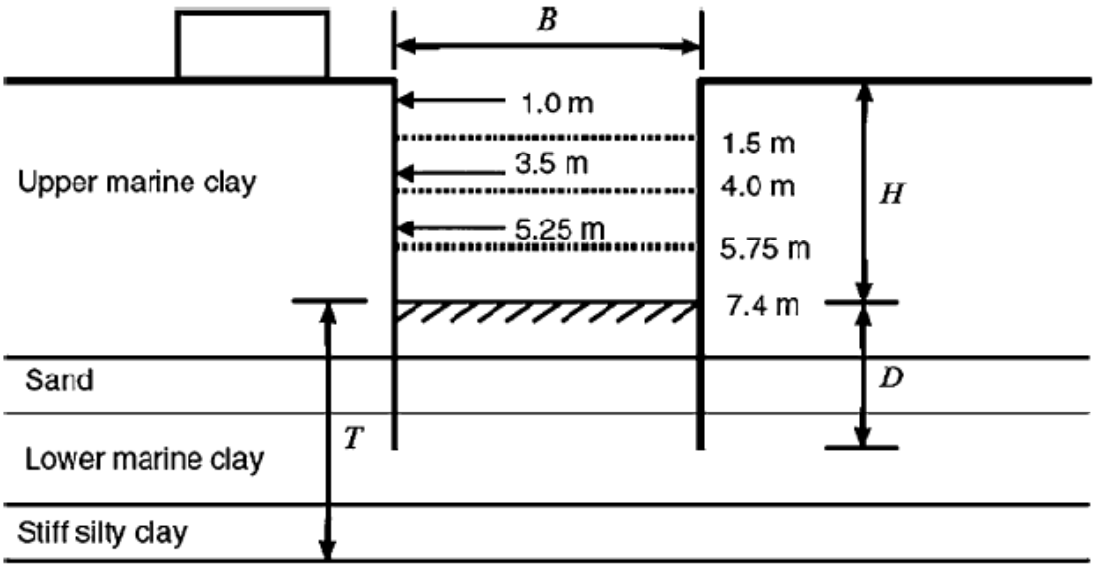

Figure 6.2 Cross-section of braced excavation and soil stratigraphy (Modified from Goh and Kulhawy 2005, not to scale)

Table 6.2 The engineering properties of each soil layer (modified from Goh and Kulhawy 2005)

Depth(m)	γ (kN/m^3)	υ	Eu (kPa)	E′ (kPa)	Su (kPa)	Ø	Ko
0-24.5	16	0.49	9000	-	30	0	1.0
24.5-27.0	18	0.30	-	30000	2	35	0.43
27.0-35.0	17	0.49	20000	-	50	0	1.0
35.0-40.0	19	0.49	48000	-	80	0	1.0

Table 6.3 Summary of wall and strut properties (modified from Goh and Kulhawy 2005)

Type	E(kN/m^3)	Moment of Inertia (m^4/m)	Cross-sectional Area (m^4/m)
Sheet Pile Wall	2.04×10^{8}	2.28×10^{-4}	1.86×10^{-2}
Strut (at 1.00m)	2.04×10^{8}	6.80×10^{-4}	2.96×10^{-3}
Strut (at 3.50m)	2.04×10^{8}	6.80×10^{-4}	2.96×10^{-3}
Strut (at 5.25m)	2.04×10^{8}	1.13×10^{-3}	3.72×10^{-3}

The soil profile and soil properties are summarized in Table 6.2. The wall and strut properties are shown in Table 6.3 and the sheet pile wall was driven to a depth of 22.6m. A plane-strain FE analysis was conducted, using the commercial FE software suite PLAXIS. The soil is modeled by 15-node triangular elements. Linear elastic beam elements were used to model the sheet pile wall. A plot of the mesh and major excavation steps are shown in Figure 6.3.

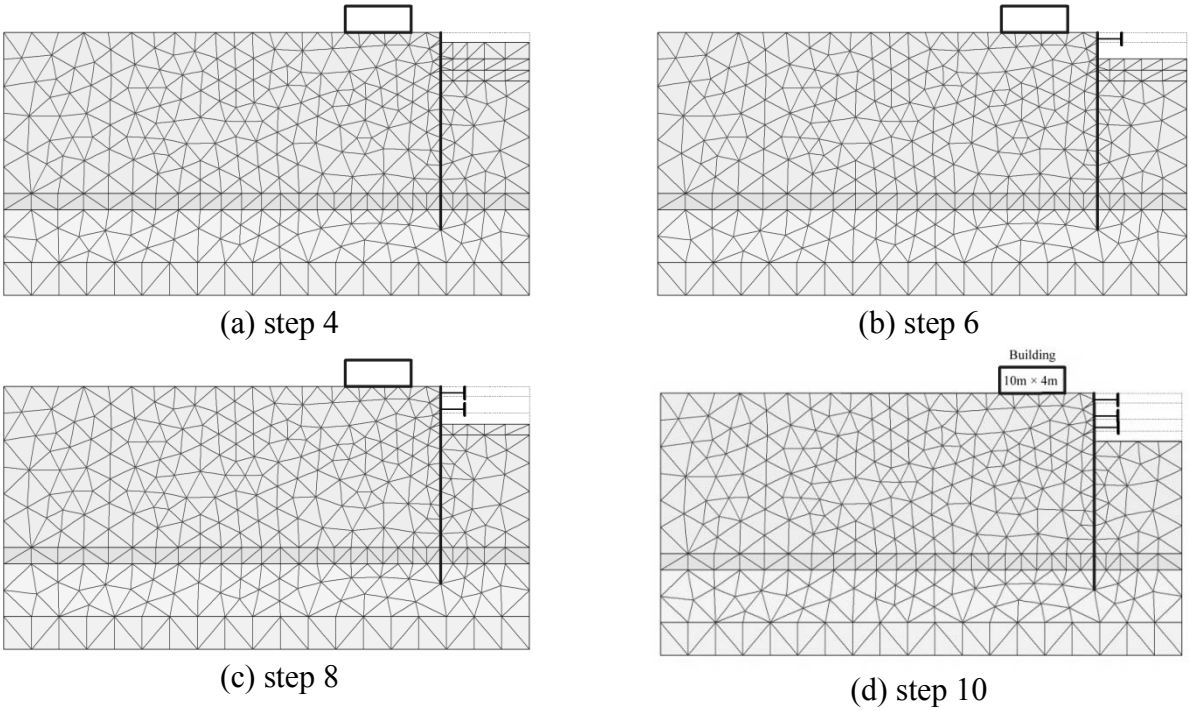

(a) step 4 (b) step 6

(c) step 8 (d) step 10

Figure 6.3 Finite element mesh and major excavation steps

In this example, structural elements such as walls and foundation slabs have been also modeled as linear elastic materials, as shown in Table 6.4.

Table 6.4 Parameters for building structure

Structural element	Type	Axial stiffness (EA) (kN/m)	Flexural stiffness (EI) ($kN/m^2/m$)
Foundation slab	Elastic	2.2×10^7	1.173×10^6
Walls	Elastic	2.2×10^7	1.173×10^6

Only half of the excavation was modeled, assuming symmetric conditions. To simplify the computations, only four random variables were used in the analyses. The variables were the undrained shear strength (S_u), undrained elastic modulus (E_u), soil unit weight (γ), and coefficient of earth pressure at rest (K_0) of the upper soft marine clay. The means, standard deviations $(\mu_i,\ \sigma_i)$ and coefficients of variations (COV) of the parameters are summarized in Table 6.5. As discussed in Goh and Kulhawy (2005), the typical geotechnical characteristics of the Singapore upper marine clay were used to simplify the computations. Even though the undrained shear strength generally shows much more variability than unit weight, they indicated that the COV values in Table 6.5 are typical of the Singapore marine clay. In this study, we adapted their data to show how one can introduce a system reliability concept to assess excavation systems. However, the proposed approach can also be extended to account for the spatial correlation by use of a geostatistical approach or random field method.

Table 6.5 Summary of random variables and statistical data (modified from Goh and Kulhawy 2005)

Variables	Mean (μ_i)	Standard deviation (σ_i)	Coefficient of variation (COV)
S_u (kPa)	30	4.5	0.15
E_u (kPa)	9000	1800	0.20
γ (kN/m^3)	16	2.1	0.13
K_0	1	0.15	0.15

For simplicity, the random variables are assumed to be independent and normally distributed. It is assumed that the other parameters in the problem are known deterministically. It is also assumed that consolidation effects do not play a significant role for the excavation-induced movements. Therefore, series of undrained analyses were performed and the computational steps have been defined as follows:

1. Initial in-situ stresses.
2. Activation of buildings, reset displacements after this step.
3. Install the sheet pile wall.
4. Excavate to a depth of 1.5m (Figure 6.3(a)).
5. Install struts at 1.0m.
6. Excavate to a depth of 4.0m (Figure 6.3(b)).
7. Install struts at 3.5m.
8. Excavate to a depth of 5.75m (Figure 6.3(c)).
9. Install struts at 5.25m.
10. Excavate to a depth of 7.4m (Figure 6.3(d)).

11. Execute shear strength reduction (SSR) technique in order to obtain factor of safety for each excavation steps (Figure 6.4(a) for step 4, Figure 6.4(b) for step 6, Figure 6.4(c) for step 8, Figure 6.4(d) for step 10).

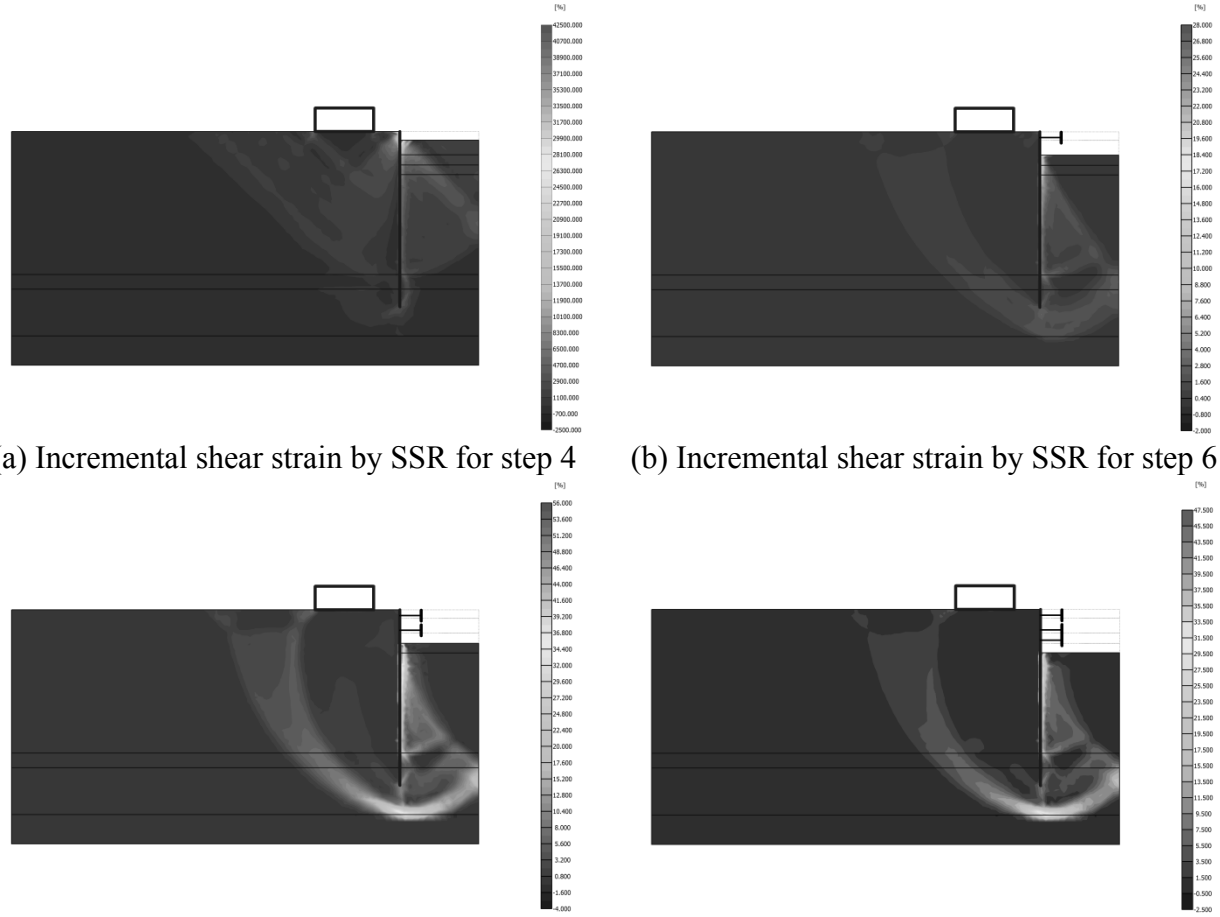

(a) Incremental shear strain by SSR for step 4 (b) Incremental shear strain by SSR for step 6

(c) Incremental shear strain by SSR for step 8 (d) Incremental shear strain by SSR for step 10

Figure 6.4 SSR results during construction process

6.4.1 Conventional deterministic approach

When a braced excavation is located in a soft clay stratum, the clay may flow beneath the wall and into excavation, producing basal heave. Anticipated bottom heave in

braced excavations in clay soils can be estimated by simple limit equilibrium method as discussed in (Terzaghi 1943). Terzaghi's method as presented in Eq. (6.14) is used for shallow or wide excavations where H / B, as illustrated in Figure 6.2, is less than one.

$$FOS = \frac{N_c S_u}{H\left(\gamma - \frac{S_u}{0.7B}\right)} \tag{6.14}$$

where, N_c is a bearing capacity factor which is a function of geometry, B is the excavation width and H is the depth of excavation. The calculation result for each excavation step is summarized in the last row of Table 6.6.

Table 6.6 Input sampling points for approximation of limit state function based on FEM

Calculation Number	Su (kPa)	Eu (kPa)	Ko	γ (kN/m^3)	FOS			
					Step 4	Step 6	Step 8	Step 10
1	34.5	9000.0	1.0	16.0	7.832	5.881	4.961	4.236
2	25.5	9000.0	1.0	16.0	6.530	5.352	4.522	3.765
3	30.0	10800.0	1.0	16.0	7.387	5.595	4.719	3.834
4	30.0	7200.0	1.0	16.0	7.404	5.617	4.845	4.087
5	30.0	9000.0	1.15	16.0	7.403	5.637	4.792	4.030
6	30.0	9000.0	0.85	16.0	7.429	5.628	4.729	4.019
7	30.0	9000.0	1.0	18.1	6.706	5.286	4.430	3.685
8	30.0	9000.0	1.0	13.9	7.995	6.015	5.241	4.416
9	30.0	9000.0	1.0	16.0	7.393	5.627	4.794	3.940
Deterministic Analysis Results	30.0	9000.0	1.0	16.0	7.910	2.966	1.977	1.582

To simplify the calculation, the characteristics of upper soft clay were used. Even though there have been numerous modified approach to assess the stability against heaving, for example, Bjerrum and Eide (1956) and NAVFAC (1982), the effects caused

by both the stiffness of the wall and the embedment depth (denoted D in Figure 6.2) could not be considered in the conventional limit analysis approach. Also, it cannot consider the complex stratified geometry of soil layers.

6.4.2 Component reliability assessments by RSM

When applying the RSM into the excavation problem, the serviceability limit state surface cannot be solved explicitly through one or more equations. Instead, numerical procedures are employed to obtain an implicit solution. Therefore, the failure domain only can be understood through repeated point-by-point numerical analyses with different input values. A closed form limit state surface then is constructed artificially using response surface models. Once the approximate limit state has been obtained, the first order reliability procedures can be used to calculate the reliability index. For excavation stages 4, 6, 8, and 10 (as defined in the previous subsection), the component reliability analyses were performed for each approximate polynomial limit state function criterion (factor of safety, $g_1'(\mathbf{X})$, maximum displacement of the wall, $g_2'(\mathbf{X})$, and angular distortion of a building, $g_3'(\mathbf{X})$). Based on the procedures described earlier, the sampling points and the resulting factors of safety are summarized in Table 6.6. Also, the approximate limit state function (calculated by RSM) for each excavation step is summarized in Table 6.7.

Table 6.7 The calculated approximate limit state function by response surface method

Excavation	The approximate limit state function $(g_1'(\mathbf{X}))$
Step 4	$g_1'(c_u, E_u, K_0, \gamma) = FOS(\mathbf{X}) - 1$ $= \left[1, c_u, E_u, K_0, \gamma, {c_u}^2, {E_u}^2, {K_0}^2, \gamma^2\right] \begin{bmatrix} -2.80\text{E}+00 \\ 7.74\text{E}-01 \\ -1.56\text{E}-05 \\ -2.07\text{E}+00 \\ 5.43\text{E}-03 \\ -1.05\text{E}-02 \\ 6.02\text{E}-10 \\ 9.91\text{E}-01 \\ -9.76\text{E}-03 \end{bmatrix} - 1$
Step 6	$g_1'(c_u, E_u, K_0, \gamma) = FOS(\mathbf{X}) - 1$ $= \left[1, c_u, E_u, K_0, \gamma, {c_u}^2, {E_u}^2, {K_0}^2, \gamma^2\right] \begin{bmatrix} 7.20\text{E}+00 \\ 9.09\text{E}-02 \\ 1.13\text{E}-04 \\ -4.21\text{E}-01 \\ -3.39\text{E}-01 \\ -5.36\text{E}-04 \\ -6.62\text{E}-09 \\ 2.24\text{E}-01 \\ 5.17\text{E}-03 \end{bmatrix} - 1$
Step 8	$g_1'(c_u, E_u, K_0, \gamma) = FOS(\mathbf{X}) - 1$ $= \left[1, c_u, E_u, K_0, \gamma, {c_u}^2, {E_u}^2, {K_0}^2, \gamma^2\right] \begin{bmatrix} 4.77\text{E}+00 \\ 2.04\text{E}-01 \\ 3.32\text{E}-05 \\ 3.20\text{E}+00 \\ -4.91\text{E}-01 \\ -2.59\text{E}-03 \\ -3.80\text{E}-09 \\ -1.50\text{E}+00 \\ 9.31\text{E}-03 \end{bmatrix} - 1$
Step 10	$g_1'(c_u, E_u, K_0, \gamma) = FOS(\mathbf{X}) - 1$ $= \left[1, c_u, E_u, K_0, \gamma, {c_u}^2, {E_u}^2, {K_0}^2, \gamma^2\right] \begin{bmatrix} 1.91\text{E}+01 \\ -1.26\text{E}-01 \\ -1.83\text{E}-04 \\ -7.51\text{E}+00 \\ -9.77\text{E}-01 \\ 2.98\text{E}-03 \\ 6.28\text{E}-09 \\ 3.77\text{E}+00 \\ 2.51\text{E}-02 \end{bmatrix} - 1$

Table 6.7 The calculated approximate limit state function by response surface method (continued)

Excavation	The approximate limit state function $(g_2'(\mathbf{X}))$
Step 4	$g_2'(c_u, E_u, K_0, \gamma) = 100 - u_X(\mathbf{X})$ $= 100 - \left[1, c_u, E_u, K_0, \gamma, {c_u}^2, {E_u}^2, {K_0}^2, \gamma^2\right] \begin{bmatrix} 2.70\text{E}+01 \\ -1.59\text{E}-02 \\ -4.63\text{E}-03 \\ 4.00\text{E}-01 \\ 8.57\text{E}-01 \\ 2.47\text{E}-04 \\ 1.71\text{E}-07 \\ 0.00\text{E}+00 \\ -4.44\text{E}-16 \end{bmatrix}$
Step 6	$g_2'(c_u, E_u, K_0, \gamma) = 100 - u_X(\mathbf{X})$ $= 100 - \left[1, c_u, E_u, K_0, \gamma, {c_u}^2, {E_u}^2, {K_0}^2, \gamma^2\right] \begin{bmatrix} 1.89\text{E}+02 \\ -2.52\text{E}-01 \\ -1.21\text{E}-02 \\ -2.44\text{E}+02 \\ 2.00\text{E}+00 \\ 3.46\text{E}-03 \\ 4.49\text{E}-07 \\ 1.33\text{E}+02 \\ 1.02\text{E}-02 \end{bmatrix}$
Step 8	$g_2'(c_u, E_u, K_0, \gamma) = 100 - u_X(\mathbf{X})$ $= 100 - \left[1, c_u, E_u, K_0, \gamma, {c_u}^2, {E_u}^2, {K_0}^2, \gamma^2\right] \begin{bmatrix} 6.88\text{E}+02 \\ -2.95\text{E}+00 \\ -1.67\text{E}-02 \\ -1.12\text{E}+03 \\ -4.25\text{E}-01 \\ 4.42\text{E}-02 \\ 6.16\text{E}-07 \\ 6.08\text{E}+02 \\ 1.27\text{E}-01 \end{bmatrix}$
Step 10	$g_2'(c_u, E_u, K_0, \gamma) = 100 - u_X(\mathbf{X})$ $= 100 - \left[1, c_u, E_u, K_0, \gamma, {c_u}^2, {E_u}^2, {K_0}^2, \gamma^2\right] \begin{bmatrix} 1.16\text{E}+03 \\ -1.07\text{E}+01 \\ -1.99\text{E}-02 \\ -1.69\text{E}+03 \\ -9.73\text{E}+00 \\ 1.51\text{E}-01 \\ 7.27\text{E}-07 \\ 9.29\text{E}+02 \\ 5.26\text{E}-01 \end{bmatrix}$

Table 6.7 The calculated approximate limit state function by response surface method (continued)

Excavation	The approximate limit state function $(g_3'(\mathbf{X}))$
Step 4	$g_3'(c_u, E_u, K_0, \gamma) = 1/600 - \delta(\mathbf{X})/L$ $= 1/600 - \left[1, c_u, E_u, K_0, \gamma, {c_u}^2, {E_u}^2, {K_0}^2, \gamma^2\right] \begin{bmatrix} -1.92\text{E}-04 \\ 6.85\text{E}+01 \\ -2.50\text{E}-08 \\ 1.31\text{E}-05 \\ 2.37\text{E}-05 \\ -1.23\text{E}-08 \\ 1.05\text{E}-12 \\ -8.89\text{E}-06 \\ -5.67\text{E}-08 \end{bmatrix}$
Step 6	$g_3'(c_u, E_u, K_0, \gamma) = 1/600 - \delta(\mathbf{X})/L$ $= 1/600 - \left[1, c_u, E_u, K_0, \gamma, {c_u}^2, {E_u}^2, {K_0}^2, \gamma^2\right] \begin{bmatrix} 2.65\text{E}-03 \\ 1.30\text{E}-05 \\ -1.24\text{E}-07 \\ -5.39\text{E}-03 \\ 7.64\text{E}-05 \\ -1.78\text{E}-07 \\ 4.54\text{E}-12 \\ 2.86\text{E}-03 \\ -6.35\text{E}-07 \end{bmatrix}$
Step 8	$g_3'(c_u, E_u, K_0, \gamma) = 1/600 - \delta(\mathbf{X})/L$ $= 1/600 - \left[1, c_u, E_u, K_0, \gamma, {c_u}^2, {E_u}^2, {K_0}^2, \gamma^2\right] \begin{bmatrix} 1.24\text{E}-02 \\ 1.99\text{E}-05 \\ -2.41\text{E}-07 \\ -2.40\text{E}-02 \\ 3.52\text{E}-05 \\ -2.72\text{E}-07 \\ 8.81\text{E}-12 \\ 1.29\text{E}-02 \\ 1.46\text{E}-06 \end{bmatrix}$
Step 10	$g_3'(c_u, E_u, K_0, \gamma) = 1/600 - \delta(\mathbf{X})/L$ $= 1/600 - \left[1, c_u, E_u, K_0, \gamma, {c_u}^2, {E_u}^2, {K_0}^2, \gamma^2\right] \begin{bmatrix} 2.82\text{E}-02 \\ -2.28\text{E}-04 \\ -3.47\text{E}-07 \\ -3.89\text{E}-02 \\ -4.95\text{E}-04 \\ 3.54\text{E}-06 \\ 1.27\text{E}-11 \\ 2.11\text{E}-02 \\ 1.94\text{E}-05 \end{bmatrix}$

For the case where the FE method is used, the approximate limit state function becomes a second-order polynomial function without interaction terms as described in section 6.2.4. The reliability index is calculated using the ellipsoid method by (Low and Tang 1997; Low and Tang 2004), as summarized in Table 6.8. From the above results, it can be concluded that the soil strength parameters of soil are large enough to prevent failure for all construction stages.

Table 6.8 Results of the reliability analyses, with respect to $g_1'(\mathbf{X})$, for excavation steps 4,6,8, and 10

Excavation	Reliability index (β_{HL})	Probability of failure (p_f) (%)
Step 4	24.079	0.00
Step 6	20.240	0.00
Step 8	15.515	0.00
Step 10	12.839	0.00

The same procedure is also applied to calculate the reliability index for the serviceability limit state functions, i.e. maximum horizontal displacement of the wall, $g_2'(\mathbf{X})$, and angular distortion of building structure, $g_3'(\mathbf{X})$. The results of both serviceability limit state function analyses are summarized in Table 6.9. As shown in Table 6.9, the probability of failure caused by maximum horizontal displacement abruptly increases from step 6 to step 10. The probability of failure would decrease with an increase in support system stiffness. The continuous assessment of reliability index during the excavation sequence allows engineers to determine the depths at which the maximum probability of failure will occur.

Table 6.9 Results of the reliability analyses, with respect to $g_2'(\mathbf{X})$, for excavation steps 4,6,8, and 10

Excavation	$g_2'(\mathbf{X})$		$g_3'(\mathbf{X})$	
	Reliability index (β_{HL})	Probability of failure (p_f) (%)	Reliability index (β_{HL})	Probability of failure (p_f) (%)
Step 4	10.173	0.00	22.427	0.00
Step 6	3.828	0.01	3.469	0.03
Step 8	1.416	7.84	0.875	19.07
Step 10	0.712	23.82	0.064	47.47

The variation of the reliability index with excavation depth is roughly concave as shown in Figure 6.5(a), which in turn means a progressive increase of probability of failure with an increase in excavation depth. For example, the probability of failure for an excavation depth of 1.5m ($p_f = 0.00(\%)$) is increased to for an excavation depth of 7.4m ($p_f = 23.82(\%)$) as shown in Figure 6.5(b).

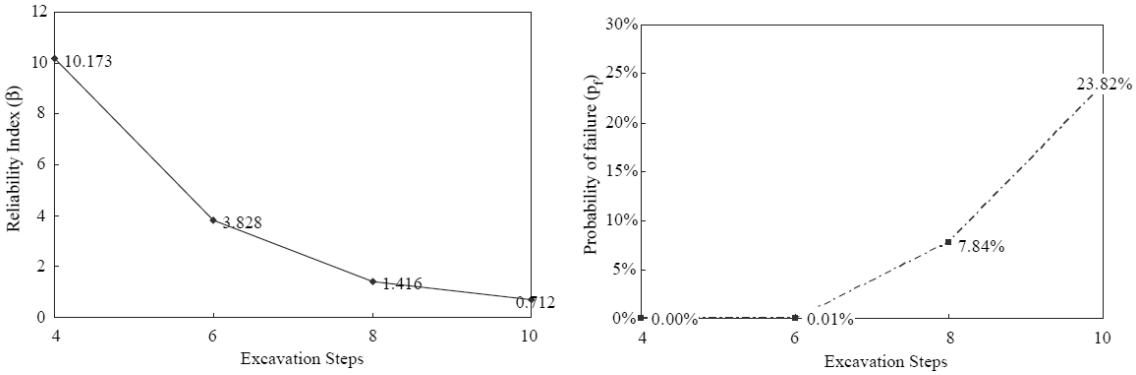

Figure 6.5 Plot of reliability index and probability of failure for each excavation step

Reliability indices corresponding to different values of u_X can be obtained by repeatedly evaluating β_{HL} at closely spaced increments of u_X. The plot of β_{HL} versus u_X for this example is shown in Figure 6.6. It is also possible to establish the relationship between β_{HL} and p_f and to plot the results in the form shown in Figure 6.6. This plot allows the designer to evaluate the probability of exceeding u_X. For example, if the maximum horizontal displacement is limited to 100 mm, the limit state function could be expressed as $g_2(\mathbf{X}) = 100 - u_X(\mathbf{X})$, then Figure 6.6 shows that the probability of the maximum horizontal displacement exceeding 100mm is around 23.82%. If the limit state function was changed to $g_2(\mathbf{X}) = 200 - u_X(\mathbf{X})$, then the probability of the maximum horizontal displacement exceeding 200mm is around 2.63%.

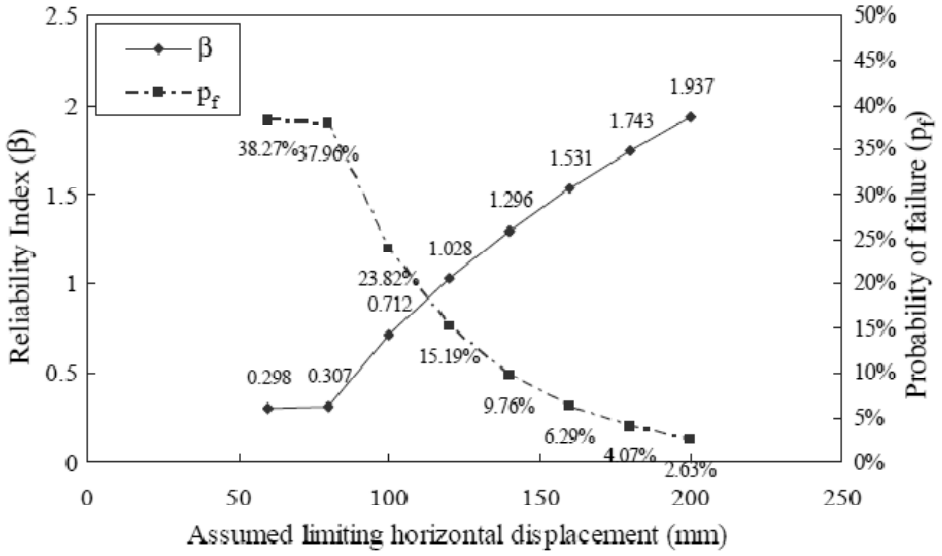

Figure 6.6 Reliability index versus assumed limiting horizontal wall displacement for excavation step 10

Finally, the component reliability index that considers potential damage to adjacent structures of excavation is summarized. As shown in Table 6.9, the probability of failure defined as excessive deflection of an adjacent structure, also abruptly increases from step 6 to step 10. Moreover, the amount of increase in the probability of failure as the excavation depth increases is much higher than that of $g_2'(\mathbf{X})$.

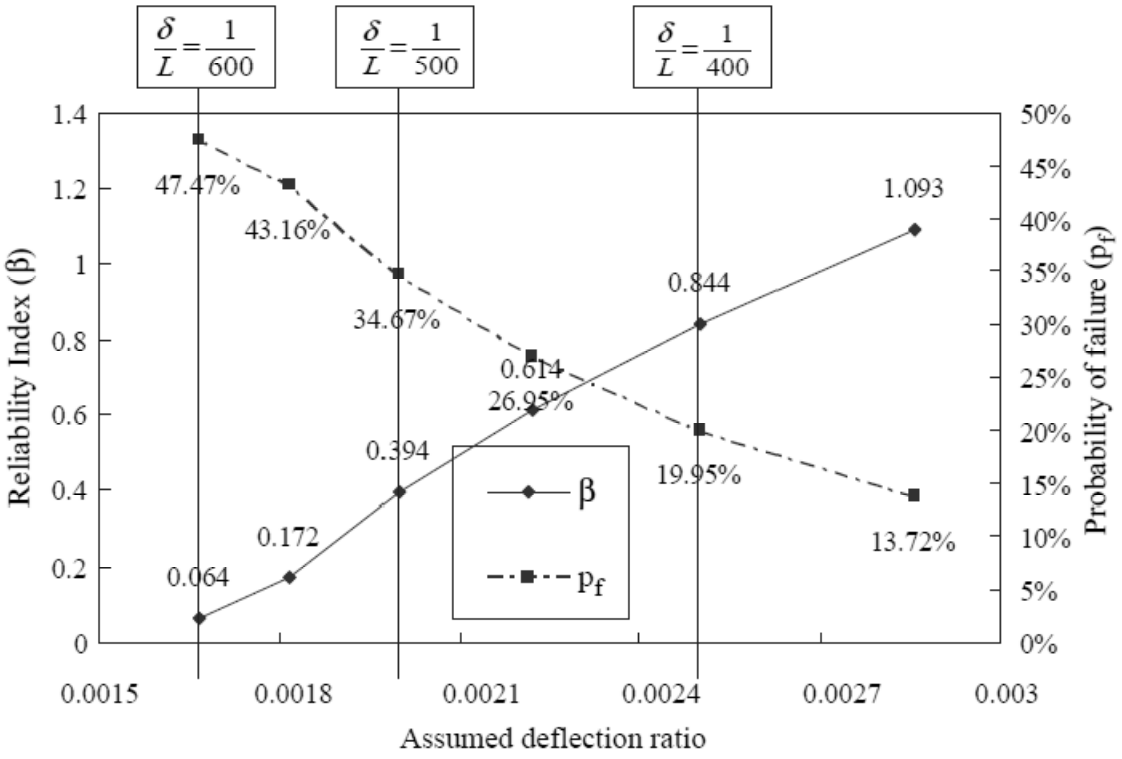

Figure 6.7 Reliability index versus assumed deflection ratio for excavation step 10

Reliability indices corresponding to different values of δ / L can be obtained by repeatedly evaluating β_{HL} at closely spaced increments of δ / L. It is also possible to

establish the relationship between δ / L and the probability of failure p_f and to plot the results in the form shown in Figure 6.7. This type of plot allows the designer to evaluate the probability of not exceeding δ / L.

However, the solutions by RSM, which are described in this subsection, become computationally impractical for problems involving many random variables and non-linear performance functions, particularly when mixed or statistically dependent random variables are involved. Bauer and Pula (2000) have also found that the response surface method can sometimes lead to false design points. Therefore, one needs to compare RSM solutions with solutions by other reliability methods for validation.

6.4.3 Component reliability assessments by FORM, SORM, AIS and MCS

Generally, there are time limitations for identifying and addressing design problems during construction. One-thousand PLAXIS simulations were performed to obtain the probabilistic characteristic of each limit state function. The probability density function (PDF) and the cumulative distribution function (CDF) for each limit state function and for each excavation stage were calculated. Figure 6.8 shows one example the PDF and CDF for excavation step 10. All limit state function parameters (factor of safety, maximum horizontal displacements, and deflection ratio) were well fitted to a normal distribution function type, as shown in the Figure 6.8. Therefore, the distribution of each limit state function can be modeled in following Eq. (6.15):

$$
\begin{aligned}
g_1(\mathbf{X}) &= FOS(\mathbf{X}) - 1 = [\mu_{FOS}(\mathbf{X}) + \sigma_{FOS}(\mathbf{X})\varepsilon_{FOS}] - 1 \\
g_2(\mathbf{X}) &= 100 - u_X(\mathbf{X}) = 100 - [\mu_{u_X}(\mathbf{X}) + \sigma_{u_X}(\mathbf{X})\varepsilon_{u_X}] \\
g_3(\mathbf{X}) &= 1/600 - \delta(\mathbf{X})/L = 1/600 - [\mu_{\delta/L}(\mathbf{X}) + \sigma_{\delta/L}(\mathbf{X})\varepsilon_{\delta/L}]
\end{aligned}
\tag{6.15}
$$

where μ_i, σ_i are constants and $\varepsilon_j \sim N(0,1)$ is a normally distributed random disturbance (error term). The number of simulation was determined by following relative error convergence criterion:

$$
\frac{|\rho_i - \rho_{i-1}|}{\rho_{i-1}} \le \varepsilon_r \tag{6.16}
$$

where ρ_i, ρ_{i-1} are correlation coefficient of i th and $(i-1)$ th simulation and ε_r is tolerance of 5%. As the number of simulation increases, the relative error of correlation coefficient converges to zero for all excavation stages as shown in Figure 6.9. The minimum number of calculations to obtain the probabilistic characteristic of each limit state function was determined based on this criterion. After 1,000 simulations, the final correlation coefficient of each limit state function parameter was also calculated for all excavation steps. The calculated correlation coefficient for excavation step 10 is presented in Table 6.10.

Table 6.10 The correlation coefficient of each limit state function for excavation step 10

	$g_1(\mathbf{X})$	$g_2(\mathbf{X})$	$g_3(\mathbf{X})$
$g_1(\mathbf{X})$	1	0.048	0.050
$g_2(\mathbf{X})$	0.048	1	0.015
$g_3(\mathbf{X})$	0.050	0.015	1

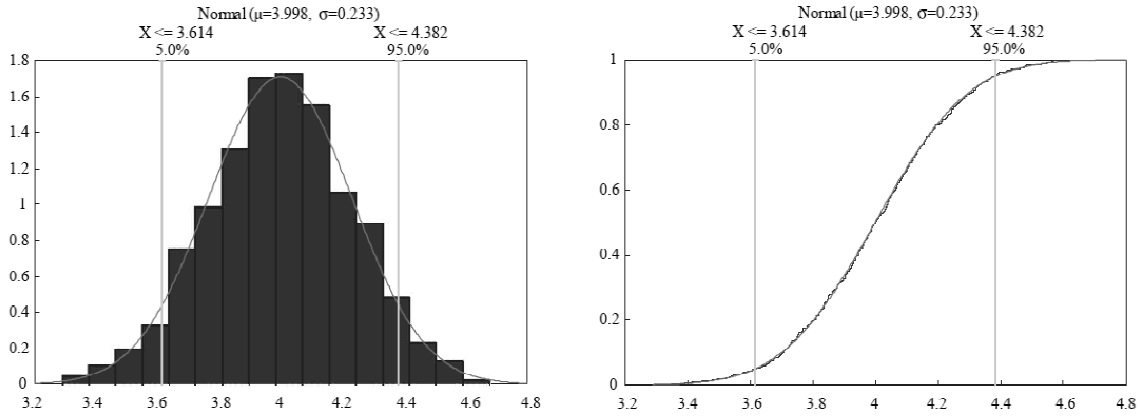

(a) Factor of safety

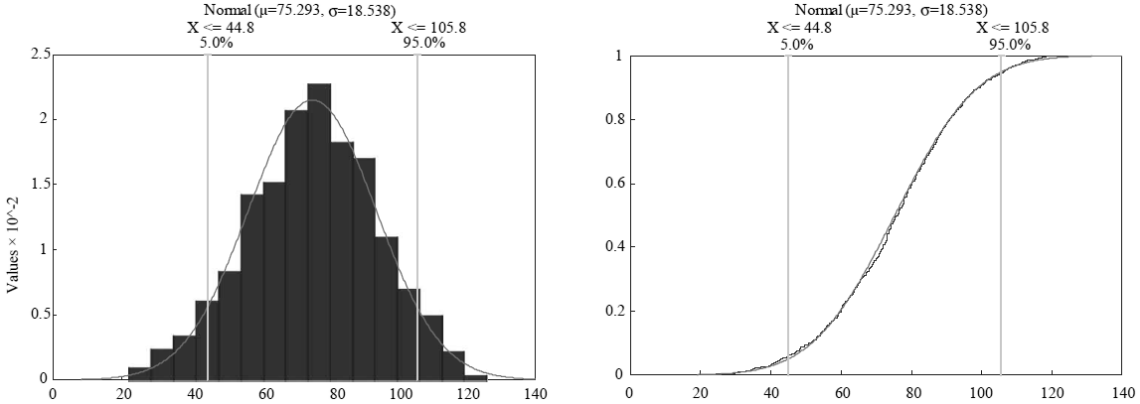

(b) Maximum horizontal displacement

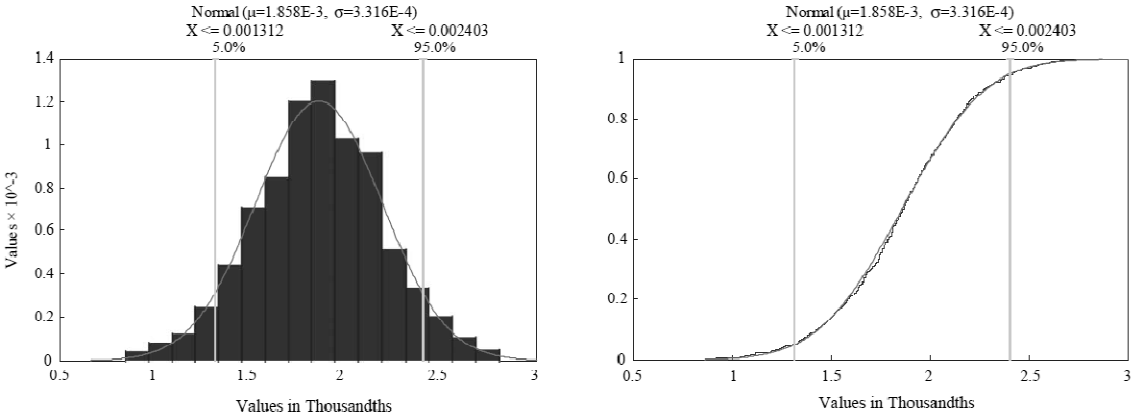

(c) Deflection ratio

Figure 6.8 The relative error of correlation coefficient

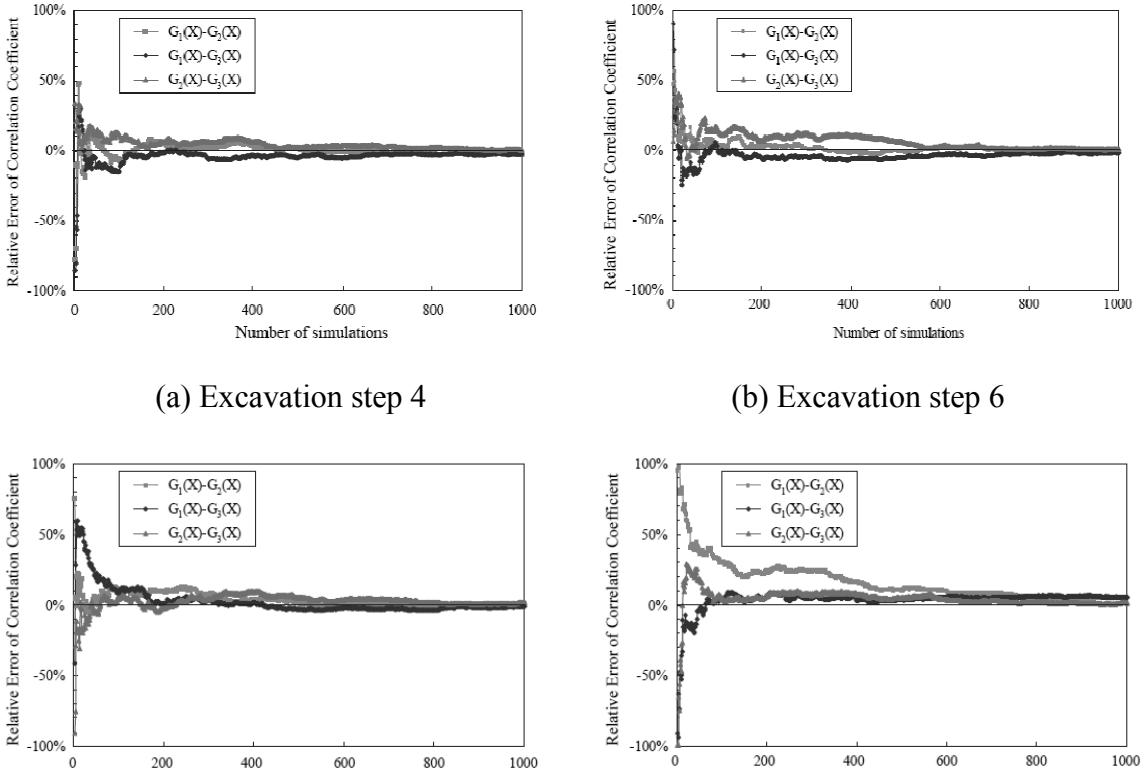

(a) Excavation step 4

(b) Excavation step 6

(c) Excavation step 8

(d) Excavation step 10

Figure 6.9 The PDF and CDF for excavation step 10 by 1,000 PLAXIS simulations

Based on information in Section 6.3, the FORM, SORM, MCS (1,000,000 simulations), and AIS techniques were applied to calculate the reliability index or the probability of failure. The results are summarized in Table 6.11, Table 6.12, and Table 6.13. Because the all limit state functions are expressed by linear equations, the plane-based AIS technique was applied. Also, due to the same reason, the FORM and SORM results were equal. However, if one defines a nonlinear limit state function for each failure mode, one would obtain different results between the FORM and SORM. The trend of the probability of failure is very similar to the results obtained using response

surface methods; however, the magnitudes of the reliability index (or the probability of failure) were quite different. In this example, the probability of failure calculated by RSM gives higher value than other component reliability methods. For example, the difference in the probability of failure for excavation step 10 for $g_2(\mathbf{X})$ is about 15%, by comparison between the Table 6.9 and Table 6.12. Moreover, the difference in the probability of failure for excavation step 10 for $g_3(\mathbf{X})$ is about 19%, by comparison between the Table 6.9 and Table 6.13. These results might be caused by: the correlated effects of each random variable, the error in finding the optimal β_{HL}, or the shortage of the sampling range of response surface method. It can be concluded that caution is required when adapting RSM for the purpose of a simplified calculation of the probability of failure.

Table 6.11 Reliability analyses results for $g_1(\mathbf{X})$

Excavation	FORM		SORM		MCS	AIS
	β	$p_f(\%)$	β	$p_f(\%)$	$p_f(\%)$	$p_f(\%)$
Step 4	24.03	0.00	24.03	0.00	0.00	0.00
Step 6	20.24	0.00	20.24	0.00	0.00	0.00
Step 8	15.51	0.00	15.51	0.00	0.00	0.00
Step 10	12.84	0.00	12.84	0.00	0.00	0.00

Table 6.12 Reliability analyses results for $g_2(\mathbf{X})$

Excavation	FORM		SORM		MCS	AIS
	β	$p_f(\%)$	β	$p_f(\%)$	$p_f(\%)$	$p_f(\%)$
Step 4	55.26	0.00	55.26	0.00	0.00	0.00
Step 6	13.20	0.00	13.20	0.00	0.00	0.00
Step 8	3.98	0.00	3.98	0.00	0.00	0.00
Step 10	1.33	9.13	1.33	9.13	9.11	9.13

Table 6.13 Reliability analyses results for $g_3(\mathbf{X})$

Excavation	FORM		SORM		MCS	AIS
	β	$p_f(\%)$	β	$p_f(\%)$	$p_f(\%)$	$p_f(\%)$
Step 4	67.06	0.00	67.06	0.00	0.00	0.00
Step 6	12.67	0.00	12.67	0.00	0.00	0.00
Step 8	1.89	2.94	1.89	2.94	2.93	2.94
Step 10	0.58	28.22	0.58	28.22	28.19	28.22

Because most of sampling points in MCS are selected close to the failure region of each limit state function in NESSUS, the reliability index by MCS shows somewhat smaller value rather than FORM and SORM. However, when using AIS method, which minimizes sampling in the safe region by adaptively and automatically adjusting the sampling space from an initial approximation of failure region, gives the almost same results with FORM and SORM.

6.4.4 System reliability assessment

The whole excavation system is defined as a series system because failure is defined by a failure of any individual component. The probability of failure of a series system is the union of the probabilities of failure for three different failure modes, as described in Eq.

(6.9). Using NESSUS, the MCS, AIS method could be used for the calculation of system reliability problem. The AIS method resulted in somewhat smaller probability of failure than that of MCS, as summarized in Table 6.14. In excavation step 10, a drastic increase (about 46%) of the probability of system failure was calculated, which is greater than the probability of failure calculated from each component reliability analysis as shown in Table 6.12 and Table 6.13. For example, even if the excavation system is in the safe region of $g_2(\mathbf{X})$ (i.e. the maximum horizontal displacement will not exceed 100mm), the failure point can be located in failure region of $g_3(\mathbf{X})$ (i.e. the angular distortion of a building could exceed 1/600).

Table 6.14 The probability of failure by NESSUS for system reliability

Excavation	Monte Carlo Simulation	Adaptive Importance Sampling
	p_f(%)	p_f(%)
Step 4	0.00	0.00
Step 6	0.00	0.00
Step 8	2.94	2.94
Step 10	74.23	69.63

6.4.5 Sensitivity analysis

System reliability sensitivity analyses are more complex than single limit state sensitivity analyses because there are multiple 'most probable' points. The sensitivity factors derived from the individual limit state function cannot be used to derive the system reliability sensitivities because the contribution from the individual limit function cannot be quantified easily. For the system reliability calculation, the sensitivity should

be checked to judge which limit state function most influences the probability of failure of the whole system. The result of this sensitivity analysis is summarized in Table 6.15. For both MCS and AIS methods, the limit state function $g_3(\mathbf{X})$ has a predominant effect on the behaviour of whole system. However, the role of the limit state function $g_2(\mathbf{X})$ was greatly increased in the AIS method, as summarized in Table 6.15.

Table 6.15 Sensitivity levels by MCS and AIS

Limit state function	MCS		AIS	
	S_σ	S_μ	S_σ	S_μ
$g_1(\mathbf{X})$	19.78	-403.68	0.07	-0.001
$g_2(\mathbf{X})$	4.10	-15.80	0.19	0.23
$g_3(\mathbf{X})$	2370.67	-1.24E7	1.20	-0.69

6.4.6 Comparisons of various reliability assessment methods

Figure 6.10 summarizes a comparison of the probabilities of failure computed using various methods described in the previous subsection. In some cases, such as Figure 6.10 (a), the probability of failure based on RSM will give larger values than system reliability approaches. Although RSM has advantages due to simple calculation procedures, the proper sampling range for finding the failure point is critical. Also, the correlated effects of each random variable should be checked. From Figure 6.10(b), (c), and (d), the system reliability approach always gives higher probability of failure than any other component reliability approach, which is caused by combination effects of all failure modes, as explained in Section 6.4.3.

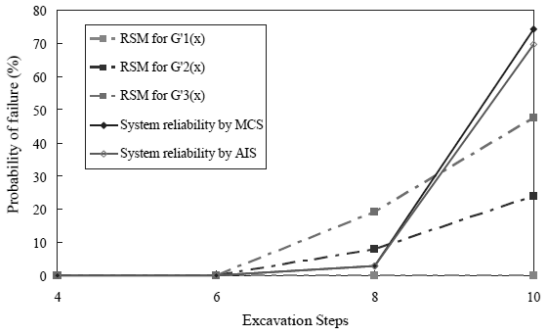

(a) RSM vs. System reliability analysis

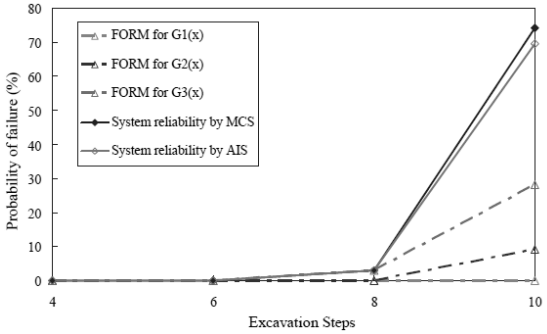

(b) FORM vs. System reliability analysis

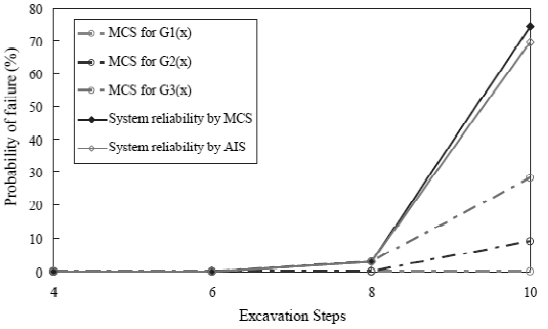

(c) MCS vs. System reliability analysis

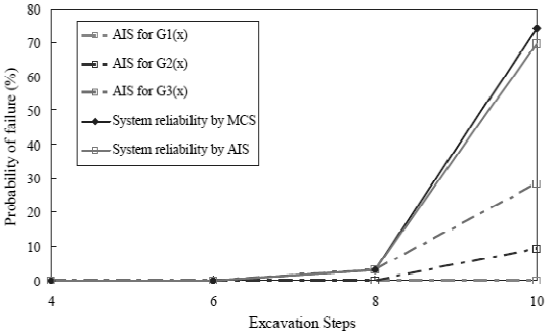

(d) AIS vs. System reliability analysis

Figure 6.10 Comparison between system probability of failure and component probability of failure

6.5 Conclusions

The serviceability performance of excavation systems is critically important in the design of many deep excavation projects because of liability for damage to existing adjacent infrastructure or buildings. Because of uncertainties associated with most geotechnical material properties, the serviceability limit state performance of the wall and adjacent structure cannot be determined precisely, and the computed displacement does not reflect the degree of uncertainty of the underlying random variables.

This section presents a serviceability limit state function (i.e., $g_3(\mathbf{X})$ for damage potential of building) that considers the angular distortion of an adjacent structure. In this study, the 1/600 criteria was arbitrarily selected for simple illustrative purposes because it is often selected as design criteria for limiting differential settlement (e.g. Burland 1977; Boscardin and Cording 1989). However, the reliability index for another criteria, such as 1/500 for different type of structure, can be easily calculated by just changing the limit state function in the following equation as $g_3(\mathbf{X}) = 1/500 - \delta(\mathbf{X})/L$. By adapting FEM analyses, the differential deformation of a structure can be considered in probabilistic terms using basic structural reliability concepts. This section demonstrates that the reliability index can be assessed by using FORM and by incorporating RSM, using a numerical procedure such as the FE method. An example was presented to demonstrate the feasibility and efficiency of this approach. Also, system reliability can be calculated to assess the reliability of a staged excavation system by employing the probabilistic analysis program NESSUS. The work presented herein consists of a new general method for assessing the probability of exceeding any excavation system design criteria. The proposed approach accounts for both safety and serviceability limit states at the component and system level. This method can be further developed into a design framework that will allow engineers to estimate the safety of excavation systems in terms of probability of fulfilling their criteria and might also be used as a decision tool on determining the support system properties during design and between construction stages. In addition, a sensitivity analysis of the system reliability allows users to determine how reliabilities are influenced by different sources of limit

state functions. In the excavation example, it was demonstrated that the damage potential limit state function ($g_3(\mathbf{X})$) should be assessed to insure the stability of whole excavation system.

7. RELIABILITY ANALYSIS OF TUNNEL FACE STABILITY CONSIDERING SEEPAGE AND STRENGTH INCREASE WITH DEPTH

The settlement profiles in shallow tunnel construction in an urban area are mainly affected by the face stability. Face stability analyses provides the most probable failure mechanisms and the understanding about parameters that need to be considered for the evaluation of ground movements caused by tunneling. The limiting tunnel collapse pressure in a Mohr-Coulomb (c', ϕ') soil is derived from the upper bound method (UBM) of limit analysis theory to maintain face stability. The derived UBM solution can consider the effect of seepage into the tunnel face and strength increase with depth.

The influence of seepage forces and depth-dependent effective cohesion is investigated for a dual-cone failure mechanism using the UBM implemented by numerical analysis. The upper bound analytical derivation for depth-dependent effective cohesion and corresponding numerical results are presented and compared to those presented by previous authors. In addition, the numerical analysis demonstrated the influence of tunnel diameter on required face supporting pressure.

After the derived UBM solution is verified with the numerical experiments, the probabilistic model is proposed to calculate the unbiased limiting tunnel collapse pressure. A reliability analysis of a shallow circular tunnel driven by a pressurized shield in a frictional and cohesive soil is presented to consider the inherent uncertainty in the input parameters and the proposed model. The ultimate limit state (ULS) for the face

stability is considered in the analysis. The probability of failure that exceeding a specified applied pressure at the tunnel face is estimated. Sensitivity and importance measures are computed to identify the key parameters and random variables in the model.

7.1 Introduction

Face stability analyses are required to determine the proper pressure to be used for pressurized shield construction of shallow circular tunnels. Analytical, limit based methods have been developed (Atkinson and Potts 1977; Davis et al. 1980) to calculate the optimum supporting pressure, which avoids face collapse (active failure) and surface 'blow-out' (passive failure).

Active failure of the tunnel face is caused by surcharge and self weight exceeding the frictional resistance and tunnel face pressure. Under passive conditions, the roles are reversed and the face pressure causes blow-out with resistance being provided by the surcharge, frictional resistance, and self-weight. Three failure mechanisms which involve the movement of solid conical blocks with circular cross sections, proposed by Leca and Dormieux (1990), are shown in Figure 7.1. MI and MII failure mechanisms are single-cone and dual-cone systems, respectively; where the cones move into the excavation. An MIII failure mechanism is a single-cone, passive mechanism, where the cone moves outward to the surface.

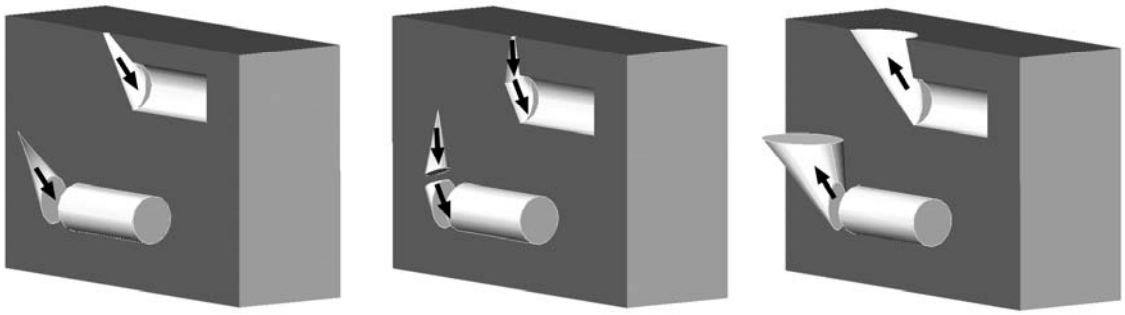

(a) MI **(b) MII** **(c) MIII**

Figure 7.1 Failure mechanisms

In this section, the MII collapse failure mechanism, which is most common failure pattern in shield tunneling (Chambon and Corte 1994), is investigated by the upper-bound theorem. Lee and Nam (2001) proposed that the seepage forces acting on the tunnel face under steady-state flow conditions should be considered if the tunnel is located under the groundwater table. However, general solutions for the limiting tunnel collapse pressure in a Mohr-Coulomb (c', ϕ') soil which combine the depth-dependence of effective cohesion (c') of NC clays and the influence of seepage have not been reported.

The stability analysis of tunnels and the computation of soil displacements due to tunnelling were commonly performed using deterministic approaches (Jardine et al. 1986; Yoo 2002; Mroueh and Shahrour 2003; Wong et al. 2006; Eclaircy-Caudron et al. 2007). A reliability-based approach for the analysis of tunnels is more rational since it enables one to consider the inherent uncertainty in the input parameters and the models. In this study, a reliability-based analysis of a shallow circular tunnel driven by a

pressurized shield in a Mohr-Coulomb (c', ϕ') soil is presented. After the derived UBM solution is verified with the numerical experiments using FLAC^{3D}, the probabilistic model that accurately predicts the limiting tunnel collapse pressure and account for all the prevailing uncertainties is proposed.

As an application, a reliability analysis of a shallow circular tunnel driven by a pressurized shield is presented to consider the inherent uncertainty in the input parameters and the proposed model. The developed probabilistic model is used to assess the conditional probability (fragility) of exceeding a specified applied pressure at the tunnel face threshold. Sensitivity and importance measures are carried out to identify the contribution of the random variable(s) to the reliability of the tunnel face stability.

7.2 Kinematic Approach to Face Stability Analysis Based on Upper Bound Theorem

7.2.1 Failure mechanism geometry

The MII active failure state can be idealized by considering a circular rigid tunnel of diameter (D) driven under a depth of cover (C) in soil with an effective cohesion (c') increasing at rate (ρ) with depth. A surcharge (σ_S) is applied at the ground surface and a constant retaining pressure ($\hat{\sigma}_T$) is applied to the tunnel face.

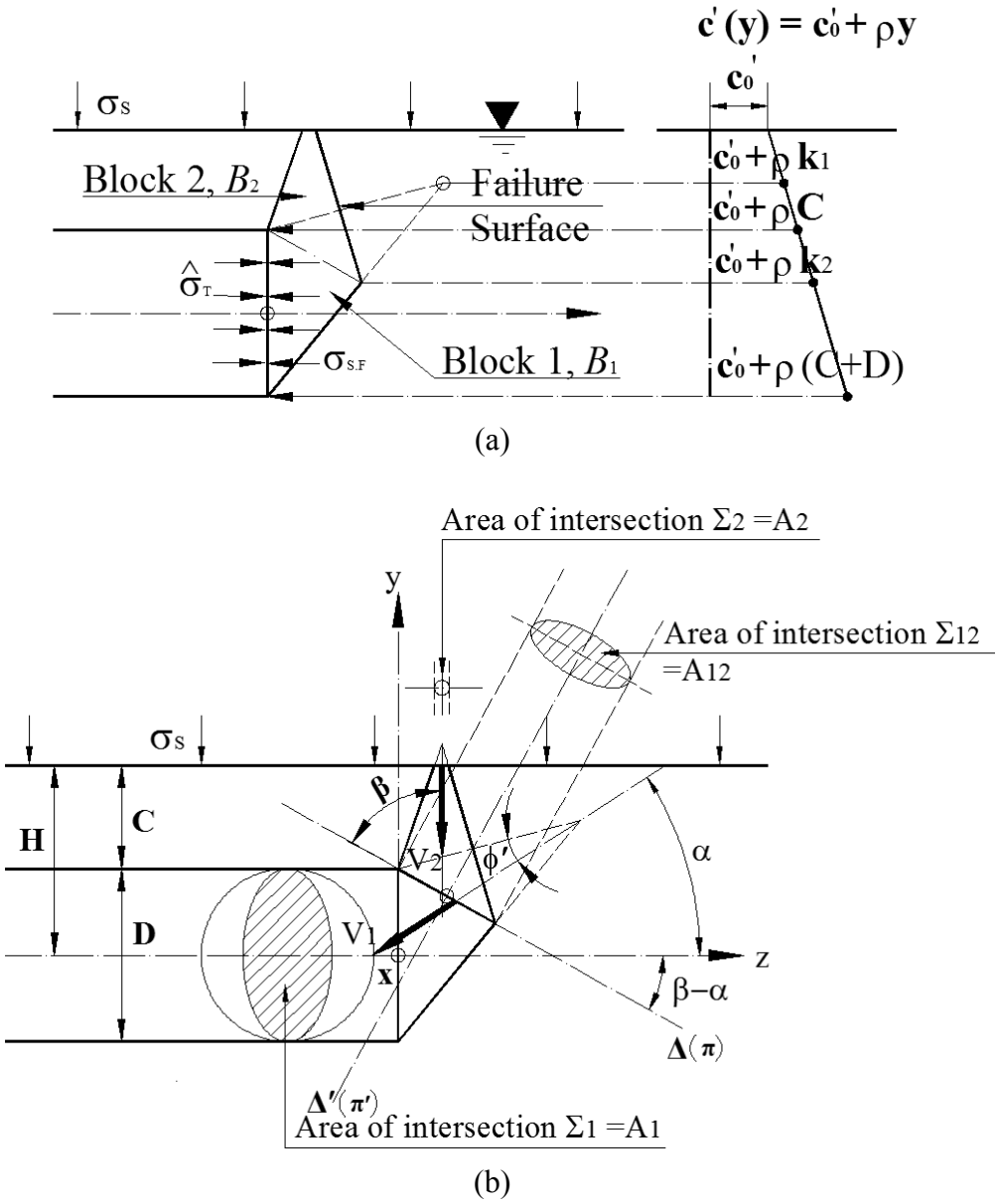

Figure 7.2 Collapse mechanism of tunnel face by the two conical blocks

Figure 7.2(a) shows a schematic cross-section of the MII failure mechanism geometry. Kinematically admissible failure mechanisms must be considered to obtain upper-bound solutions, initially developed by Leca and Dormieux (1990). An MII

failure occurs as two conical blocks move vertically and into the tunnel face, as shown in Figure 7.2 (b). The two conical blocks consist of: (1) B_1, a cone truncated by plane π, which is perpendicular to the page and represented as line $\Delta(\pi)$ in Figure 7.2 (b), (2) B_2, a cone corresponding to the removed, upper section of the cone B_1, mirrored about a plane π', such that the axis of B_2 is vertical. The mirror plane, π', is also perpendicular to the page and passes through the center of the ellipse created by the intersection between B_1 and B_2.

As such, the orientation of initial plane, π, is defined by the requirement that the axis of B_2 be oriented vertically and that π' pass through the center of the ellipse formed by the intersection of B_1 and B_2. Therefore, the MII failure mechanism geometry can be characterized by the angle of the axis of B_1 from horizontal, α, as shown in Figure 7.2(b).

For all three failure mechanisms, the intersection of the tunnel face and the adjacent block forms an ellipse, Σ_1, with a major axis length equal to $D/2$. For the MII failure mechanism, the intersection between blocks B_1 and B_2 is an ellipse, Σ_{12}, in plane π.

7.2.2 Derivation of upper bound solutions

This subsection summarizes the kinematic upper bound solutions to the MII failure mechanism, as originally reported by Leca and Dormieux (1990) and modified by Lee

and Nam (2001). However, a new solution is derived to account for an increasing shear strength with depth for normally consolidated (NC) clays .

The upper bound limit analysis solution is found by comparing the power of external applied loads, P_E , to the dissipation power caused by system movement, P_V . When the external power exceeds the dissipation power, an upper bound state exists. The following subsections describe the derivations of the upper bound solution, as introduced by Leca and Dormieux (1990), along with the modifications for increasing soil strength. The reader is referred to Leca and Dormieux (1990) for additional geometric derivations.

7.2.2.1 Dissipation power

The dissipation power associated with the MII failure is calculated from the integration of plastic energy dissipation per unit area along block interfaces,

$$P_V = P_{1V} + P_{2V} + P_{12V} \tag{7.1}$$

where P_{1V} is the contribution of the surface between B_1 and the surrounding soil, P_{2V} is the contribution of the surface between B_2 and surrounding soil and P_{12V} is the contribution of the interface between B_1 and B_2, represented as Σ_{12}. The dissipation is a function of the resistance along the interface surface and the block velocity, therefore the dissipation power of the three interfaces are given as:

$$P_{1V} = \left[c_0' + (\rho y)_{y=k_1}^{y=C+D} \right] \cdot V_1 \cos\phi' \cdot S_{B1} \tag{7.2}$$

$$P_{2V} = \left[c_0' + (\rho y)_{y=0}^{y=k_2} \right] \cdot V_2 \cos\phi' \cdot S_{B2} \tag{7.3}$$

$$P_{12V} = \left[c_0' + (\rho y)_{y=c}^{y=k_2} \right] \cdot V_{12} \cos\phi' \cdot A_{12} \tag{7.4}$$

where S_{B1} and S_{B2} are the perimeter surface areas of B_1 and B_2, respectively, A_{12} is the area of Σ_{12}, V_1 and V_2 are the velocities of B_1 and B_2, and V_{12} is the relative velocity between B_1 and B_2. Leca and Dormieux (1990) derives the geometry of the surface areas and the velocity fields with the following equations:

$$S_{B1} = \frac{\pi D^2}{4} \left[R_A \frac{\cos\alpha}{\sin\phi'} - R_C R_D \cos(\alpha + \phi') \right] \tag{7.5}$$

$$S_{B2} = \frac{\pi D^2}{4} \left[R_C R_D \cos(\alpha + \phi') - \frac{\sin\phi'}{\cos^2\phi'} \left(\frac{\cos^2\phi'}{\sin\phi'} \frac{{R_C}^2}{\cos(\alpha + \phi')} - \frac{2C}{D} \right)^2 \right] \tag{7.6}$$

$$A_{12} = \frac{\pi D^2}{4} \frac{\cos^2(\alpha + \phi')}{\cos\phi'} \frac{\sqrt{\sin(\beta - \phi')}}{\left[\sin(\beta + \phi') \right]^{3/2}} \tag{7.7}$$

$$V_1 = \frac{\sin(\beta + \phi')}{\sin(\beta - \phi')} V_2 \tag{7.8}$$

$$V_{12} = \frac{\cos\alpha}{\sin(\beta - \phi')} V_2 \tag{7.9}$$

where R_A, R_C, and R_D are simplified geometric coefficients, introduced by Leca and Dormieux (1990):

$$R_A = \frac{\left[\cos(\alpha - \phi')\cos(\alpha + \phi')\right]^{1/2}}{\cos\phi'} \tag{7.10}$$

$$R_C = \frac{\cos(\alpha + \phi')}{\cos\phi'}\left[\frac{\sin(\beta - \phi')}{\sin(\beta + \phi')}\right]^{1/2} \tag{7.11}$$

$$R_D = \frac{\sin\beta}{\sin\phi'\sin(\beta + \phi')} \tag{7.12}$$

β is the angle between the intersection of B_1 and B_2 and vertical, and can be shown as:

$$\beta = 45° + \frac{\alpha}{2} \tag{7.13}$$

7.2.2.2 Power of external loads

The power of the external loads, P_E, can be calculated as

$$P_E = P_T + P_S + P_\gamma + P_{S.F.} \tag{7.14}$$

where,

$$P_T = -\hat{\sigma}_T V_1 \cos\alpha A_1 \tag{7.15}$$

$$P_S = \sigma_S V_2 A_2 \tag{7.16}$$

$$P_\gamma = \gamma V_1 \sin\alpha V_{B1} + \gamma V_2 V_{B2} \tag{7.17}$$

$$P_{S.F.} = \sigma_{S.F.}\frac{\pi D^2}{4}\frac{R_A}{R_C{}^2}\frac{\cos\alpha\cos^2(\alpha + \phi')}{\cos^2\phi'} \tag{7.18}$$

P_T is the power of the tunnel face pressure (σ_T), P_S is the power of the surcharge (σ_S), P_γ is the power of the soil unit weight (γ), and $P_{S.F.}$ is the power of seepage pressure $(\sigma_{S.F.})$. The contact areas A_1 and A_2 correspond to the surface Σ_1 and the area of the intersection between the B_2 and the ground surface, respectively. The areas are defined as:

$$A_1 = \frac{\pi D^2}{4} \frac{\sqrt{\cos(\alpha - \phi')\cos(\alpha + \phi')}}{\cos\phi'} \tag{7.19}$$

$$A_2 = \frac{\pi D^2}{4} \left[\frac{\sin\beta\cos\alpha}{\sin\phi'\sin(\beta + \phi')} - \left(\frac{2C}{D} + 1 \right) \right]^2 \tan^2\phi' \tag{7.20}$$

The soil unit weight component of the external power depends on the volume of the failure blocks, V_{B1} and V_{B2}, which are given as:

$$V_{B1} = \frac{\pi D^3}{12} \left(R_A R_B - R_C{}^3 \frac{\cos\phi'}{2\sin\phi'} \right) \tag{7.21}$$

$$V_{B2} = \frac{\pi D^3}{12} \left\{ R_C{}^3 \frac{\cos\phi'}{2\sin\phi'} - \frac{\sin^2\phi'}{2\cos^2\phi'} \left[\frac{\cos^2\phi'}{\sin\phi'} \frac{R_C{}^2}{\cos(\alpha + \phi')} - \frac{2C}{D} \right]^3 \right\} \tag{7.22}$$

where R_A and R_C are given in equations (7.10) and (7.11) and R_B is defined as:

$$R_B = \frac{\cos(\alpha - \phi')\cos(\alpha + \phi')}{\sin(2\phi')} \tag{7.23}$$

7.2.2.3 Upper bound theorem

Using the upper bound theorem, an MII failure mechanism will be avoided if the external power is below the dissipative power, shown as:

$$P_E \leq P_V \tag{7.24}$$

Substitution of equations (7.1) through (7.23) into equation (7.24) will give an upper bound solution in the following form:

$$N_S Q_S + N_\gamma Q_\gamma \leq Q_T + \frac{\sin\phi'}{\cos\alpha}\frac{R_F \cdot R_c^2}{R_A} \tag{7.25}$$

The three loading parameters (Q_S, Q_γ, Q_T) and the coefficients (N_S, N_γ) are given in equations (7.26) − (7.30) as defined by Leca and Dormieux (1990) and Lee and Nam (2001). A new parameter (R_F) is introduced which accounts for the increase in soil effective cohesion, and is given in Eq. (7.32):

$$Q_S = \left(K_p - 1\right)\frac{\sigma_S}{\sigma_C} + 1 \tag{7.26}$$

$$Q_T = \left(K_p - 1\right)\frac{\hat{\sigma}_T - \sigma_{S.F.}}{\sigma_C} + 1 \tag{7.27}$$

$$Q_\gamma = \left(K_p - 1\right)\frac{\gamma D}{\sigma_C} \tag{7.28}$$

$$N_S = \frac{1}{\cos\alpha\cos^2\phi'}\frac{\sin\left(\beta - \phi'\right)}{\sin\left(\beta + \phi'\right)}\frac{{R_E}^2}{R_A} \tag{7.29}$$

$$N_\gamma = \frac{1}{3}\left[\begin{array}{l} \tan\alpha R_B + \dfrac{\cos\phi'\cos(\beta+\phi')}{2\sin\phi'\sin(\beta+\phi')}\dfrac{{R_C}^3}{R_A} - \\ \dfrac{1}{2\sin\phi'\cos\alpha\cos^2\phi'}\dfrac{\sin(\beta-\phi')}{\sin(\beta+\phi')}\dfrac{{R_E}^3}{R_A} \end{array}\right] \tag{7.30}$$

$$R_E = \frac{\cos^2\phi'}{\cos(\alpha+\phi')}{R_C}^2 - \frac{2C}{D}\sin\phi' \tag{7.31}$$

$$R_F = \cos\phi' \cdot \left\{\begin{array}{l} \left[\dfrac{\cos\alpha}{\sin\phi'}\dfrac{R_A}{{R_C}^2} - \cos(\alpha+\phi')\dfrac{R_D}{R_C}\right]\rho(C+D-k_1) + \\ \left[\dfrac{\cos^2\phi' R_C R_D}{\cos(\alpha+\phi')} - \dfrac{{R_E}^2}{\sin\phi'\cos^2(\alpha+\phi')}\right]\rho(k_2) + \\ \left[\dfrac{2\cos\beta\sin 2\phi'\cos(\alpha+\phi')}{\sin\beta}\cdot\dfrac{{R_D}^2}{R_C}\right]\rho(k_2-C) \end{array}\right\} \tag{7.32}$$

where, σ_C is the unconfined compression strength, K_p is the Rankine passive earth pressure coefficient, $\sigma_{S.F.}$ is the seepage pressure acting on the tunnel face, γ is the unit weight of the soil, D is the tunnel diameter, k_1 is the apex of block 1 (B_1), and k_2 is the lowest point of the intersection between B_1 and B_2. Relation (7.32) provides the best upper bound associated with an MII failure mechanism when N_S and N_γ are maximized by optimizing α.

The parameters Q_S and Q_γ are imposed geometric and loading conditions, and the supporting pressure $\hat{\sigma}_T$ should be chosen such that failure of the tunnel during construction is prevented. The selection of supporting pressure corresponds to:

$$Q_T = N_S Q_S + N_\gamma Q_\gamma - \frac{\sin\phi'}{\cos\alpha}\frac{R_F \cdot R_c^2}{R_A} \tag{7.33}$$

which can be rewritten, after substitution, as:

$$\left[\left(K_p - 1\right)\frac{\hat{\sigma}_T - \sigma_{S.F.}}{\sigma_C}\right] = N_S Q_S + N_\gamma Q_\gamma - \frac{\sin\phi'}{\cos\alpha}\frac{R_F {R_C}^2}{R_A} - 1 \tag{7.34}$$

$$\hat{\sigma}_T = \frac{\left[N_S Q_S + N_\gamma Q_\gamma - \frac{\sin\phi'}{\cos\alpha}\frac{R_F {R_C}^2}{R_A} - 1\right]\sigma_C + \sigma_{S.F.}}{\left(K_P - 1\right)} \tag{7.35}$$

The parameters in equations (7.33)−(7.35) correspond to geometry and Mohr-Coulomb soil properties except for the seepage pressure acting on the tunnel face. To calculate the seepage pressures acting on the tunnel face, the failure surface must be pre-determined from the limit analysis. Given this failure surface, seepage pressures acting on the tunnel face can be obtained from the difference of total head between the tunnel face and the failure surface. The average predicted seepage pressure is calculated using numerical analyses by FLAC^{3D}.

7.3 Numerical Analysis of Face Stability using FLAC^{3D}

7.3.1 FLAC^{3D} numerical modeling

In order to investigate the behaviour of the tunnel face and to verify the newly developed UBM solutions, numerical analyses with the commercially available finite-difference code FLAC^{3D} (FLAC3D 2009) are carried out. In the numerical model, only one half is included due to symmetry condition. The model is sufficiently large to allow for any

possible failure mechanism to develop and to avoid any influence from the boundary effects as shown in Figure 7.3.

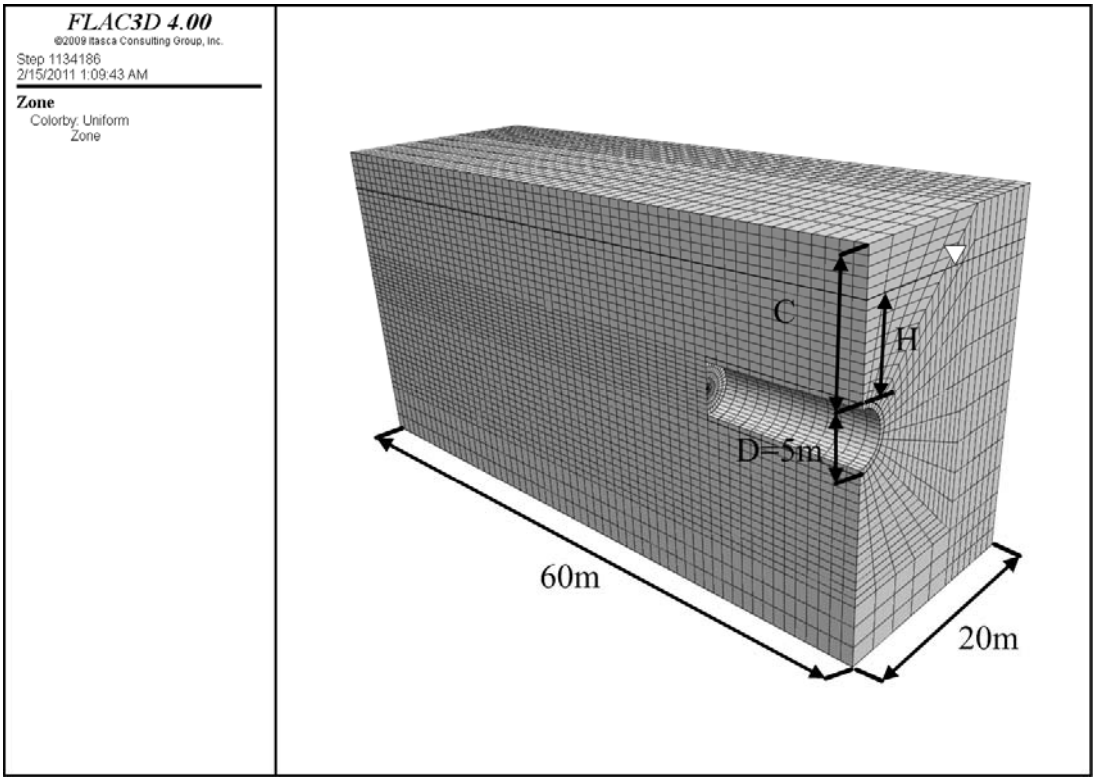

Figure 7.3 Numerical mesh for the tunnel face stability in FLAC^{3D}

The water table is assumed to be varied above the tunnel crown depending on the diameter of tunnel. In order to focus the analysis on the face failure in front of the shield machine, the excavation process was simulated using a simplified single-step excavation scheme, assuming that the tunnel is excavated 13 m (the general length of the shield machine) instantaneously. A uniform retaining pressure is applied to the tunnel face to simulate tunneling under compressed air. The highest pressure applied to the tunnel face

for which soil collapse would occur is computed. This collapse pressure is the one for which the soil in front of the tunnel face undergoes downward movement. It is called the tunnel active pressure.

A circular tunnel of diameter $D = 5$ m and various cover depth C is driven in a c$-\phi'$ soil is considered as shown in Figure 7.3. The size of the numerical model is 20 m in the X direction, 60 m in the Z direction, and 40 m in the Y direction. These dimensions are chosen so as not to affect the value of the tunnel collapse pressure. A three-dimensional nonuniform mesh is used. The tunnel face region is subdivided into 100 separate zones since very high stress gradients are developed in that region. The bottom boundary is assumed to be fixed and the vertical boundaries are constrained in motion in the normal direction. A conventional elastic perfectly plastic model based on the Mohr-Coulomb failure criterion is adopted to represent the soil. The soil elastic properties employed are Young's modulus, $E = 240$ MPa and Poisson's ratio, $\nu = 0.3$. The value of the angle of internal friction and cohesion of the soil used in the analysis are $c_0' = 0 \sim 3$ kN/m^2, $\phi' = 35^\circ$, $\rho = 0.1$ kN/m^2/m and $c_0' =$ variable, respectively. The soil unit weight is taken equal to 15.2 kN/m^3. We have to note that the soil elastic properties have a negligible effect on the collapse pressure. A concrete lining of 0.4m thickness is used in the analysis. The lining is simulated by a shell of linear elastic behavior. Its elastic properties are Young's modulus $E = 15$GPa and Poisson's ratio $\nu =$ 0.2. The lining is connected to the soil via interface elements that follow Coulomb's law. The interface is assumed to have a friction angle equal to two-thirds of the soil angle of internal friction and cohesion equal to zero. Normal stiffness, $K_n = 10^{11}$ Pa/m

and shear stiffness, $K_s = 10^{11}$ Pa/m are assumed to this interface. These parameters are a function of the neighboring elements rigidity and do not have a major influence on the collapse pressure. In terms of the fluid property, the porosity and permeability are assumed constant as 0.3 and $10^{-12}\,\mathrm{m}^2\cdot\mathrm{sec/Pa}$, respectively The fluid density is $9.8\,\mathrm{kN/m}^3$ and fluid bulk modulus assumed to be 2.0GPa. For the computation of a tunnel collapse pressure using FLAC^{3D}, we use a stress control method (Mollon et al. 2009). Figure 7.4 shows the collapse velocity field given by FLAC^{3D}, and Figure 7.5 shows the corresponding collapse displacement field at the time of failure. Stability against tunnel face collapse is ensured as long as the applied pressure ($\sigma_{applied}$) is greater than the tunnel collapse pressure (σ_T).

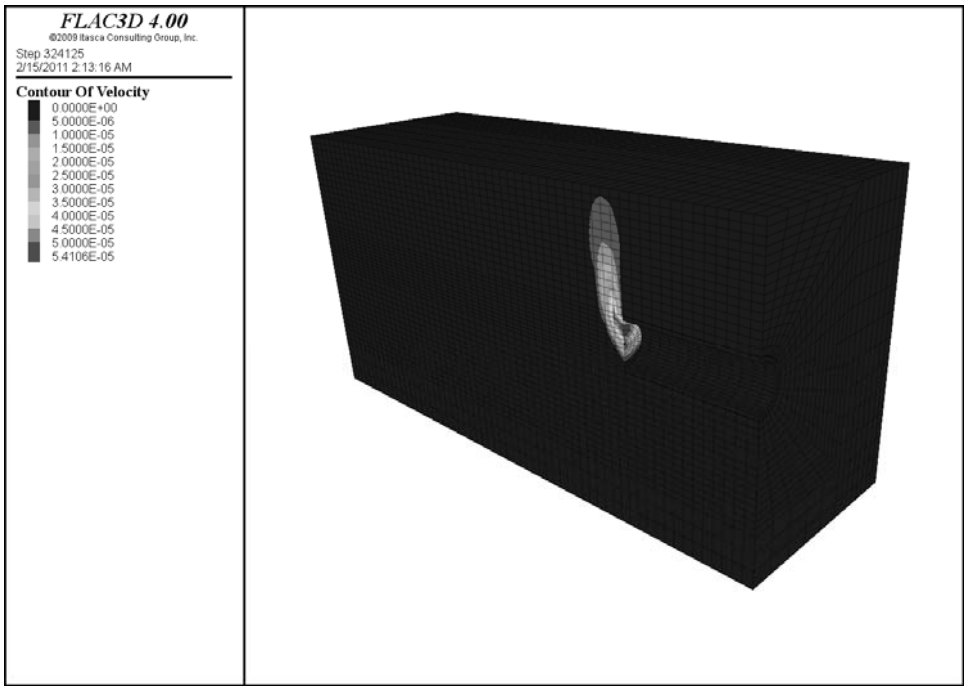

Figure 7.4 Contour of velocity (without seepage)

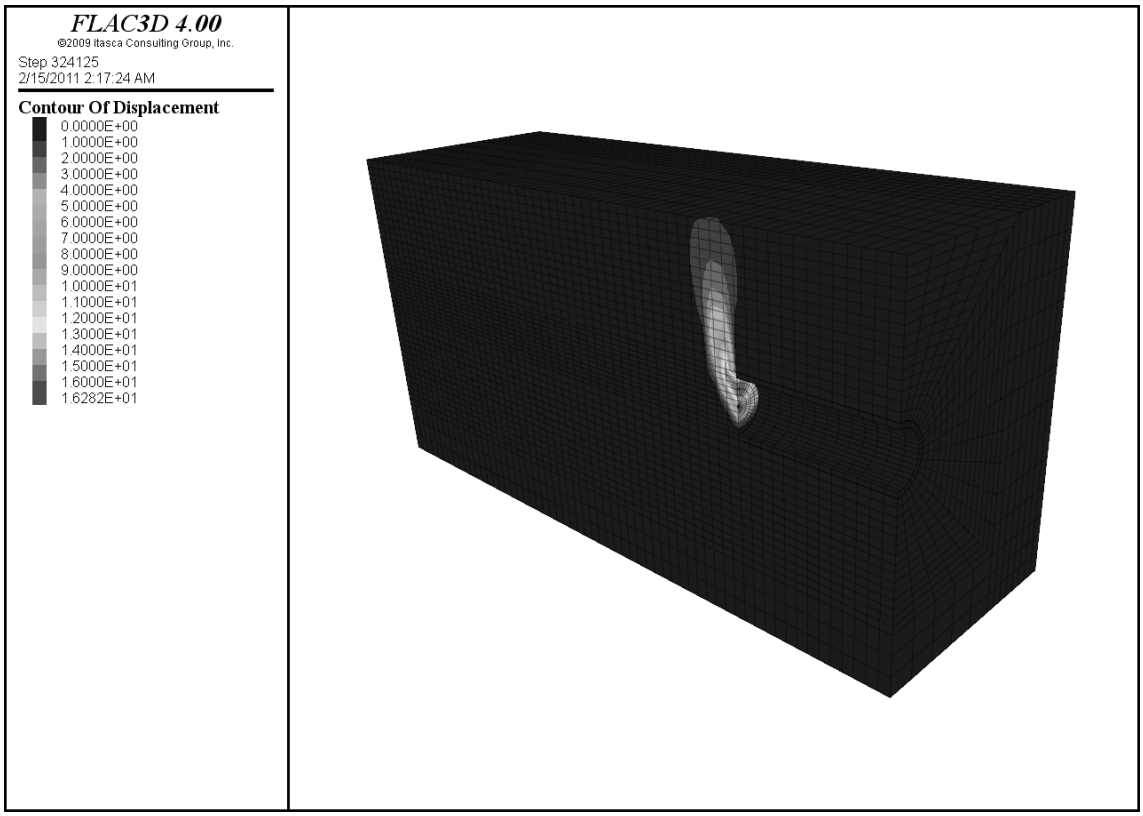

Figure 7.5 Contour of displacement (without seepage)

7.3.2 Seepage into the tunnel

Steady-state flow occurs when at any point in a flow field the magnitude and direction of the flow velocity are constant with time. Transient flow occurs when at any point in a flow field the magnitude or direction of the flow velocity changes with time. The steady-state approach is valid as long as the water table is not drawn down by the existence of the tunnel. Steady-state groundwater flow condition is assumed in the analysis. There are two different types of the drainage condition during a tunnel construction such as the drainage type and the water-proof type. In the drainage type, ground water is drained through the tunnel wall as well as the tunnel face, while in the

water-proof type drainage is allowed only through the tunnel face. After applying the hydrostatic heads to the domain as an initial condition, the pressure heads at the wall and the face of the tunnel are taken to be zero in the drainage type while only those of the face are taken to be zero in the water-proof type. During tunnel construction below groundwater level, flow of groundwater into the tunnel leads to total head loss around tunnel, and causes the seepage pressure around the tunnel.

Figure 7.6 and Figure 7.7 show the comparison in the pore pressure distribution between before and after tunnel excavation. Figure 7.8 and Figure 7.9 show the collapse velocity field with seepage pressure and the corresponding displacement vector at the time of failure. We can see that the location of a failure plane in front of the tunnel face is somewhat changed after the consideration of seepage effect.

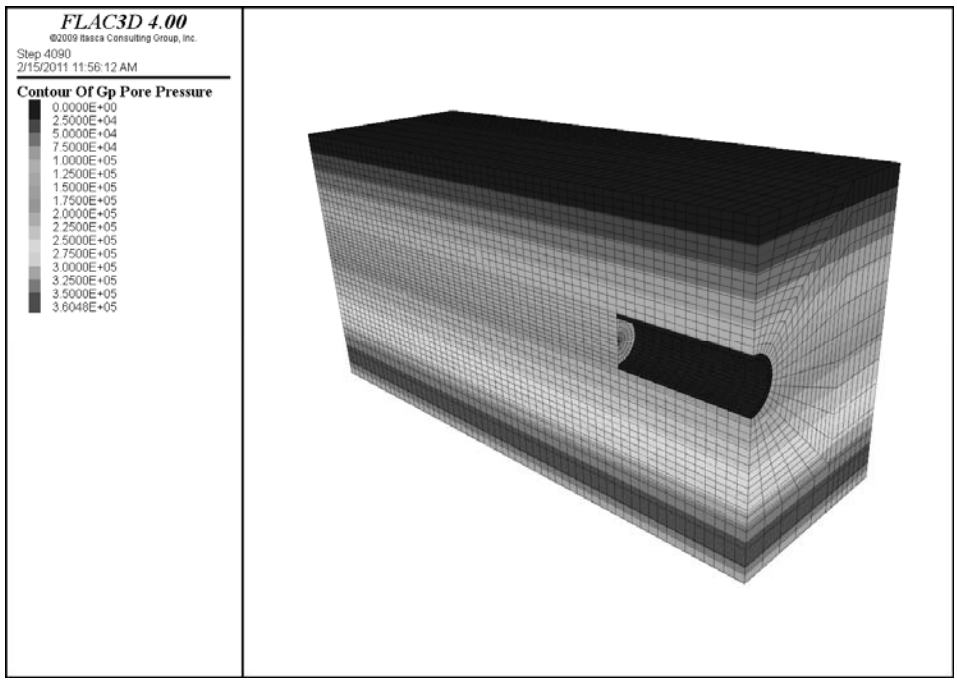

Figure 7.6 Pore pressure distribution before tunnel excavation

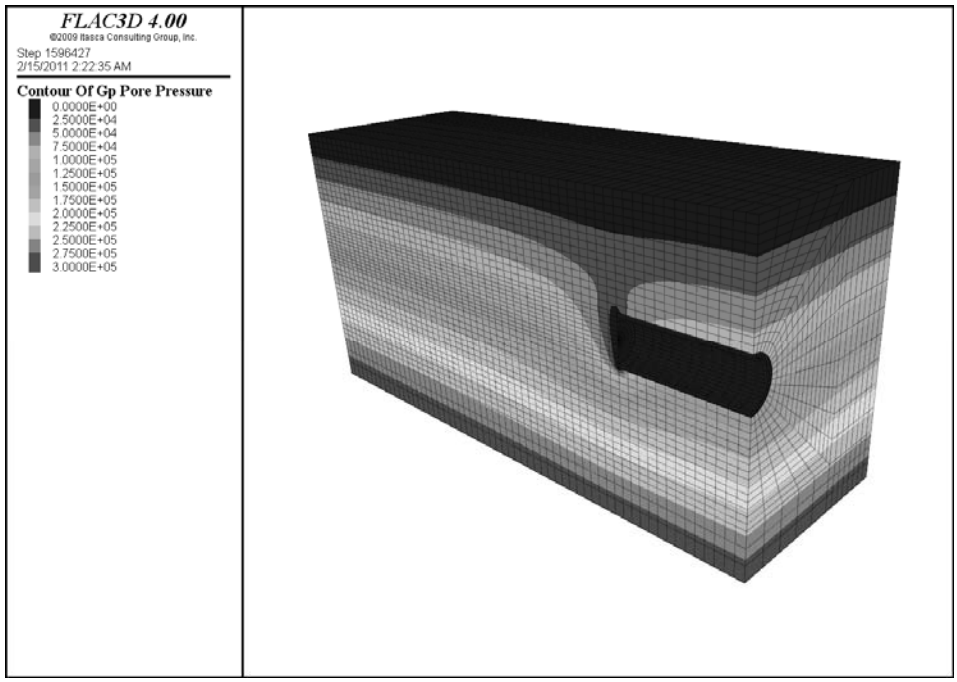

Figure 7.7 Pore pressure distribution after tunnel excavation

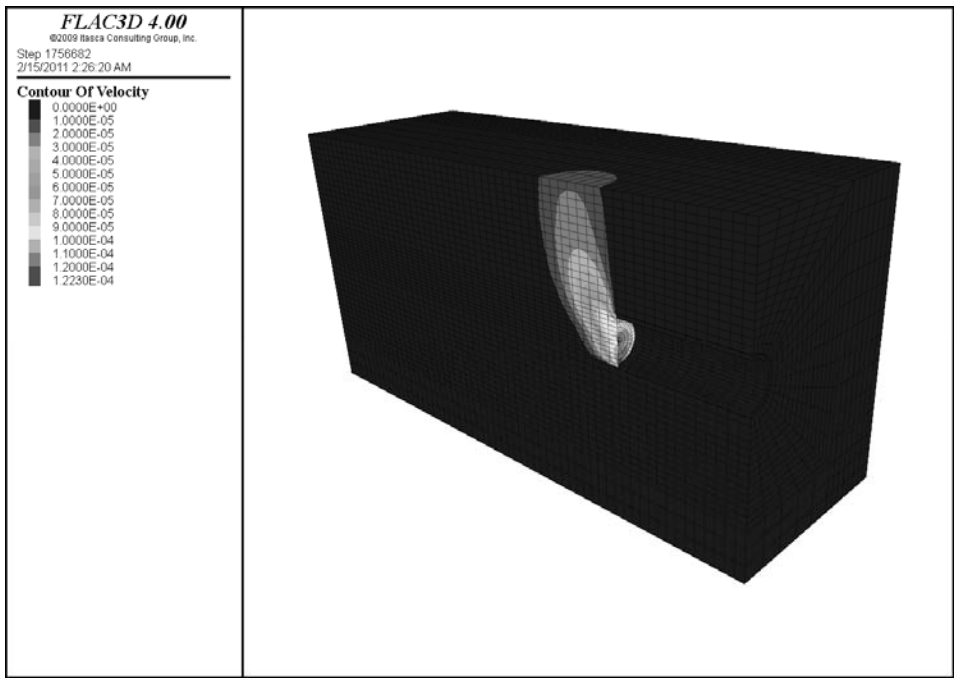

Figure 7.8 Contour of velocity (with seepage)

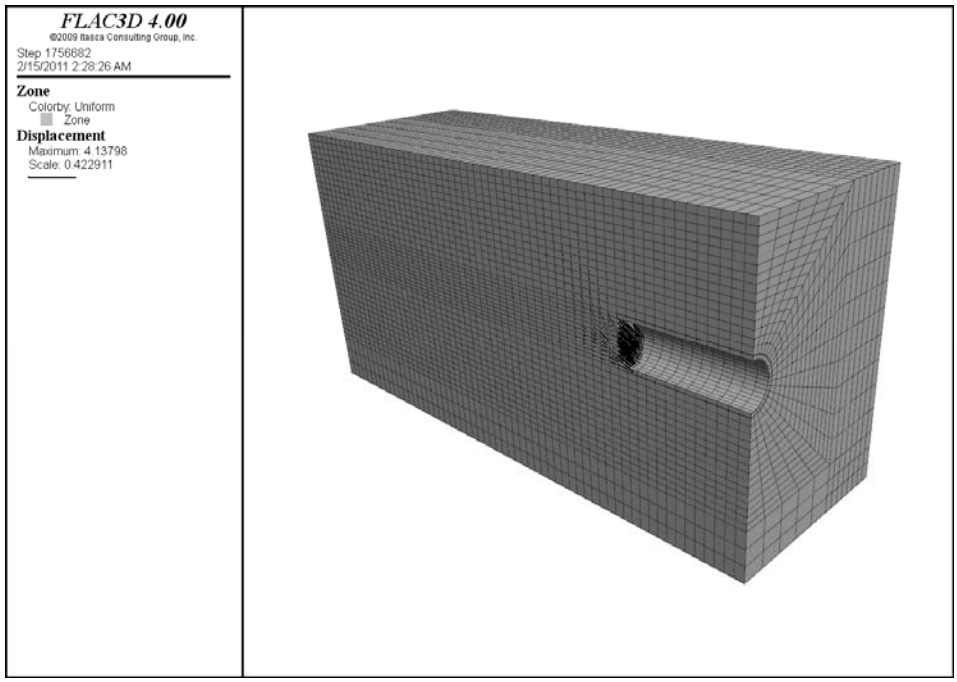

Figure 7.9 Displacement vector (with seepage)

7.3.3 Numerical analysis cases

The analyses are conducted for 40 cases of ground conditions as summarized in Table 7.1. Each case involves analyses with both the drainage and the water-proof type for the seepage analysis.

Table 7.1 Cases of analysis for the calculation of the limiting collapse pressure

		c_0'									
		0	0.25	0.50	0.75	1.00	1.25	1.50	2.00	2.50	3.00
ρ	0	Case M01	Case M02	Case M03	Case M04	Case M05	Case M06	Case M07	Case M08	Case M09	Case M10
	1.00	Case M11	Case M12	Case M13	Case M14	Case M15	Case M16	Case M17	Case M18	Case M19	Case M20
	1.50	Case M21	Case M22	Case M23	Case M24	Case M25	Case M26	Case M27	Case M28	Case M29	Case M30
	2.00	Case M31	Case M32	Case M33	Case M34	Case M35	Case M36	Case M37	Case M38	Case M39	Case M40

7.3.4 Comparison with UBM solution

The analyses cases are designed to understand the effect of strength increase with depth. The parameter ranges are chosen after considering the acceptable field condition. The limiting collapse pressures by UBM for various cases are calculated as summarized in Table 7.2 and Table 7.3. When the depth-dependent rate of change (represented as ρ) of effective cohesion increases, the required face supporting pressure decreases. The negative limiting collapse pressure values in both tables indicate that additional face supporting pressure is unnecessary to ensure the stability of the tunnel face.

Table 7.2 The calculation of the limiting collapse pressure by UBM ($C = 5$m, $D =$ 5m, $H = 5$m, i.e., $C/D = 1$, $H/D = 1$)

		c_0'									
		0	0.25	0.50	0.75	1.00	1.25	1.5	2.00	2.50	3.00
ρ	0	14.15	13.80	13.44	13.08	12.73	12.37	12.01	11.30	10.58	9.87
	1.00	14.15	11.85	9.54	7.23	4.93	2.62	0.31	−4.30	−8.92	−13.53
	1.50	14.14	10.87	7.59	4.31	1.03	−2.26	−5.54	−12.10	−18.67	−25.23
	2.00	14.14	9.90	5.64	1.38	−2.87	−7.13	−11.39	−19.90	−28.42	−36.93

Table 7.3 The calculation of the limiting collapse pressure by UBM ($C = 10$m, $D =$ 5m, $H = 10$m, i.e., $C/D = 2$, $H/D = 2$)

		c_0'									
		0	0.25	0.50	0.75	1.00	1.25	1.50	2.0	2.50	3.00
ρ	0	17.29	16.93	16.58	16.22	15.86	15.51	15.15	14.43	13.72	13.01
	1.00	17.28	13.77	10.25	6.73	3.21	−0.30	−3.82	−10.86	−17.90	−24.94
	1.50	17.27	12.19	7.09	1.99	−3.11	−8.21	−13.31	−23.51	−33.71	−43.91
	2.00	17.26	10.61	3.93	−2.75	−9.43	−16.11	−22.79	−36.16	−49.52	−62.88

7.4 Probabilistic Model Formulation

A probabilistic model to predict the limiting collapse pressure of tunnel face can be written as

$$\sigma_T(\mathbf{X}) = \hat{\sigma}_T(\mathbf{X}) + \gamma(\mathbf{X}) + s\varepsilon \tag{7.36}$$

where, σ_T = the limiting collapse pressure by the FLAC^{3D} , $\hat{\sigma}_T$ = the limiting collapse pressure by the upper bound theorem is defined in Eq. (7.35), $\mathbf{X} = (\alpha, \beta, k_1, k_2, c_0', \phi', \rho, \gamma, C, D, \sigma_S, \sigma_{S.F.})$ = the random variables, $\gamma(\mathbf{X})$ = the correction term for the bias inherent in the deterministic model that is expressed as a function of the variables $\mathbf{X}$, $s\varepsilon$ = the model error, s = the unknown standard deviation of the model error, ε = a random variable with zero mean and unit variance of standard normal distribution. In assessing the probabilistic model, the following assumptions are made: (a) the model variance σ^2 is independent of $\mathbf{X}$ (homoskedasticity assumption), and (b) ε follows the normal distribution (normality assumption). These assumptions are verified by using diagnostic plots of the data or the residuals versus the model predictions. After reviewing the diagnostic plot of the residuals as shown in Figure 7.10, we introduce the constant correction term that is independent of the random variables, $\gamma(\mathbf{X}) = 0.075$, to remove potential bias in the model. The normality assumption is also checked in the Q-Q normal plot of the residuals as shown in Figure 7.11. Figure 7.12 shows the comparison in the limiting collapse pressure between by UBM solutions and FLAC^{3D} numerical models.

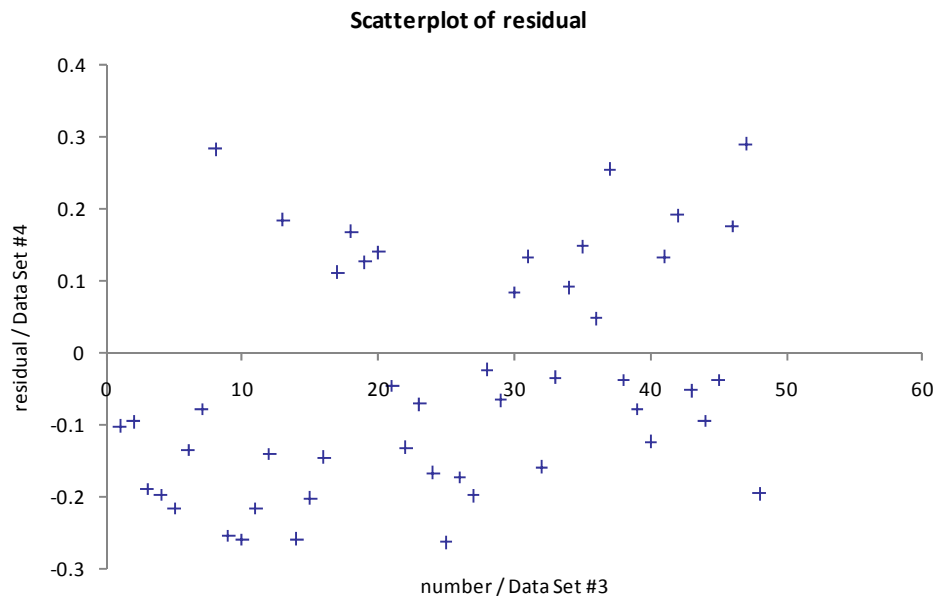

Figure 7.10 Diagnostic plot of the residuals

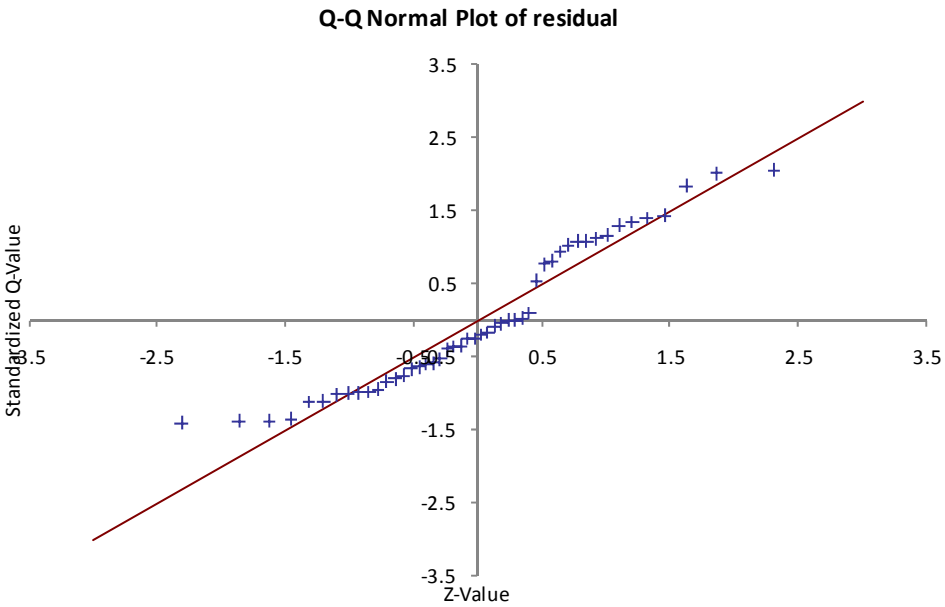

Figure 7.11 Q-Q normal plot of the residuals

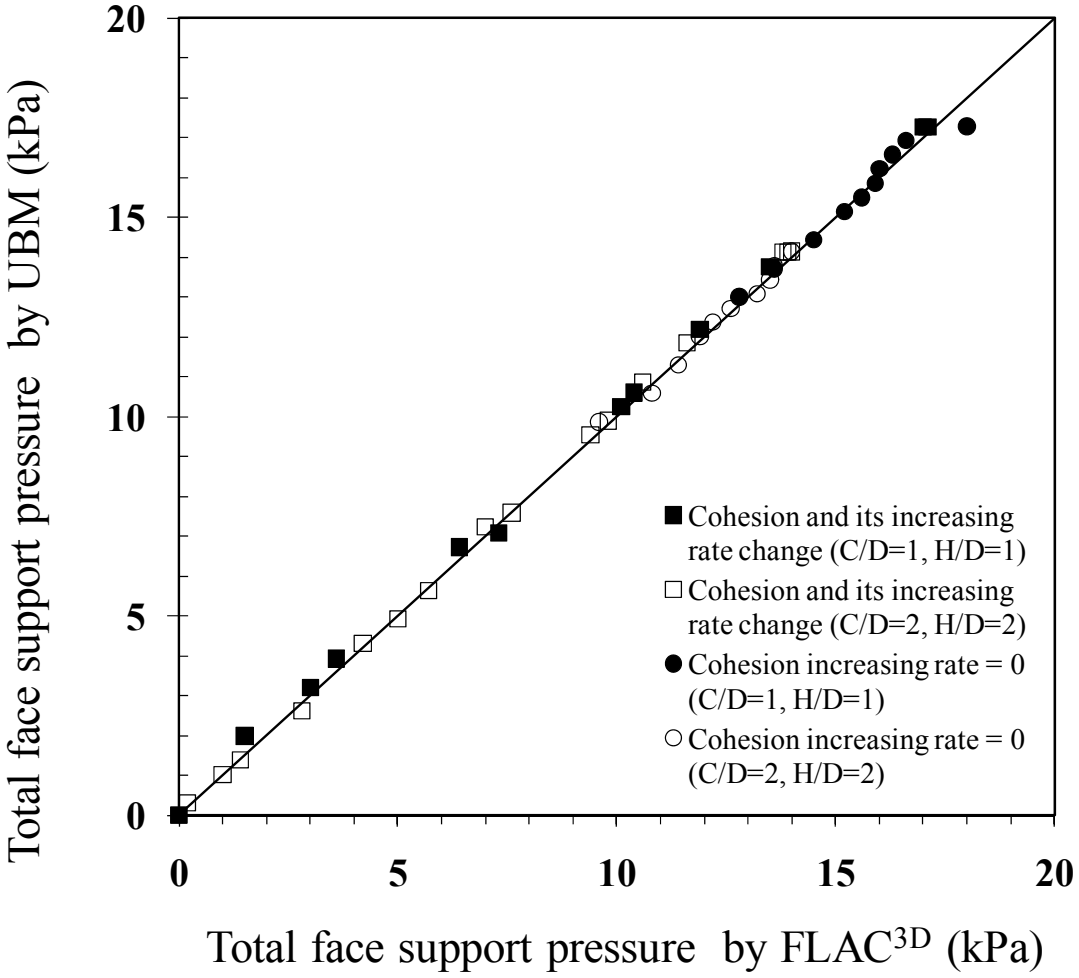

Figure 7.12 Comparison in the limiting collapse pressure between UBM and FLAC^{3D} numerical models

7.5 Application

7.5.1 Tunnel face stability by UBM solution

The upper bound solution that accounted for the influence of seepage force and the depth-dependence of effective cohesion of NC clays for the limiting face collapse pressure is calculated using a spread sheet program created for this research. As shown in Figure 7.13 in case of ϕ'=35°, $\gamma = 15.2(\text{kN/m}^3)$, $C = 10\text{m}$, $D = 5\text{m}$, the water level,

$H = 5$m, when the depth-dependent rate of change (ρ) of effective cohesion increases, the required face supporting pressure decreases. A value of ρ =0 corresponds to a homogenous soil, with constant cohesion. In Figure 7.13 in case of ϕ' =35°, γ = 15.2(kN/m^3), ρ =0.1(kN/m^2/m) and c_0' =1 (kN/m^2), the negative supporting pressure values indicate that additional face supporting pressure is unnecessary to ensure the stability of the tunnel face. In this case, the surcharge (σ_S) will have very little influence on face collapse because the tunnel is deep enough (C / D =2). This is because the results of failure shape and support pressure have the same values when the depth ratio (C / D) is greater than 0.2 as shown in Figure 7.14. Figure 7.15 shows the required face supporting pressure as a function of tunnel diameter and effective cohesion. As the tunnel diameter increases, the required face supporting pressure will also increase. Even if the failure happens in the very shallow depth when depth ratio is larger than 0.2, the effect of surcharge is very small compared to the changes in the required supporting pressure by other parameters such as tunnel diameter, cover depth, effective cohesion as previously shown in Figure 7.14.

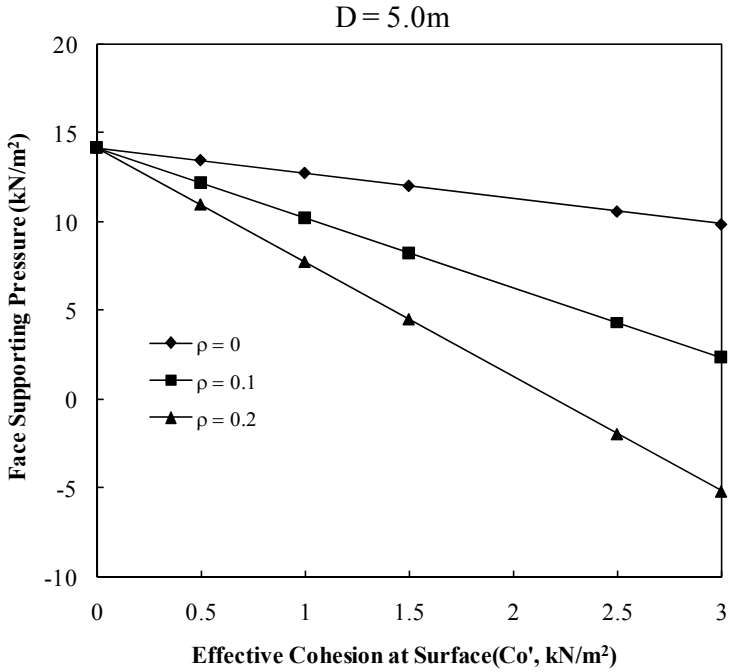

Figure 7.13 Change of support pressure with variation of the rate of change of effective cohesion with depth

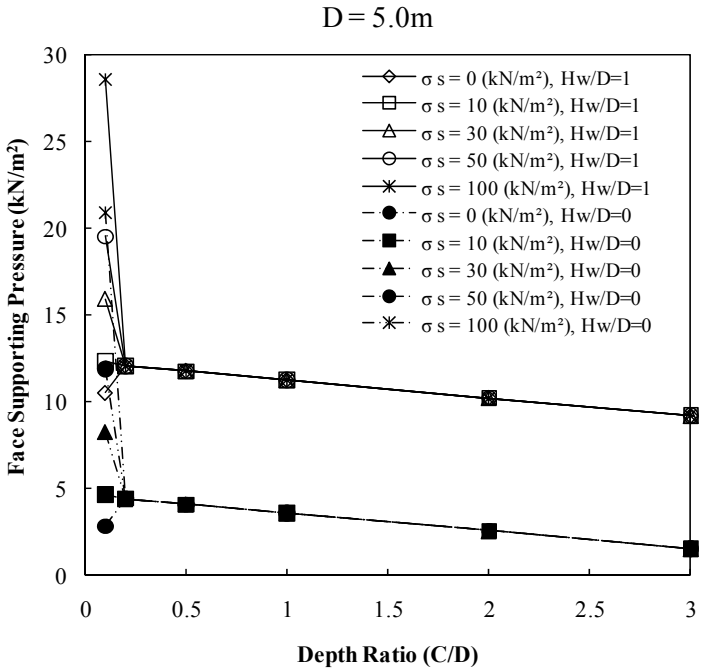

Figure 7.14 Change of support pressure with variation of surcharge and depth ratio

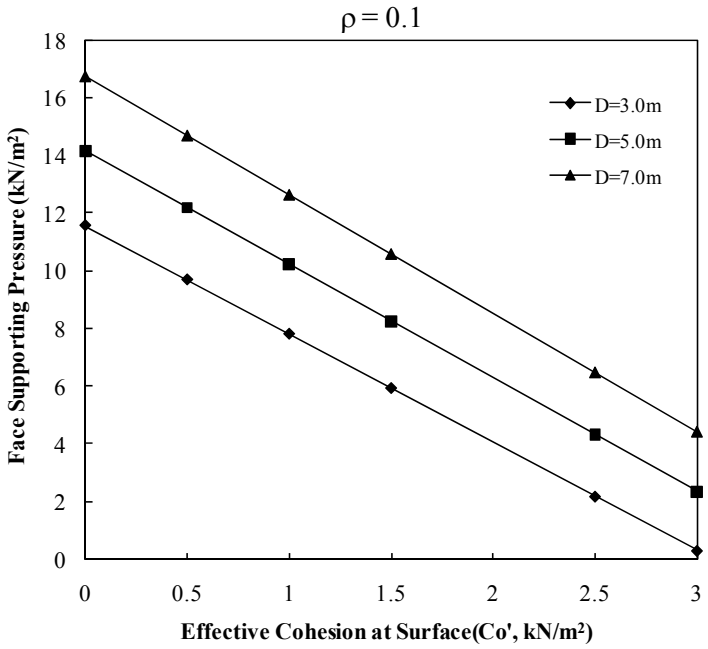

Figure 7.15 Change of support pressure with variation of tunnel diameter (D)

The relationship between groundwater depth, tunnel depth, tunnel diameter, and required tunnel support pressure for a sand and an NC clay material is shown in Figure 7.16. The cohesionless sand results are those reported by Lee et al. (2003) (ϕ'=35º, c' =0). The cohesive material results were computed using the spreadsheet, based on the derivation described herein (c_0'=10 kN/m^2, ϕ'=35, ρ = 0.5 kN/m^2/m). Figure 7.16 illustrates the large influence of ground-water conditions on required tunnel face supporting pressure for both soil types and for drained and waterproof tunnel construction methods. Although, the influence of seepage pressure on the upper bound required supporting pressure is less for an NC clay material, this effect must be considered for this material type.

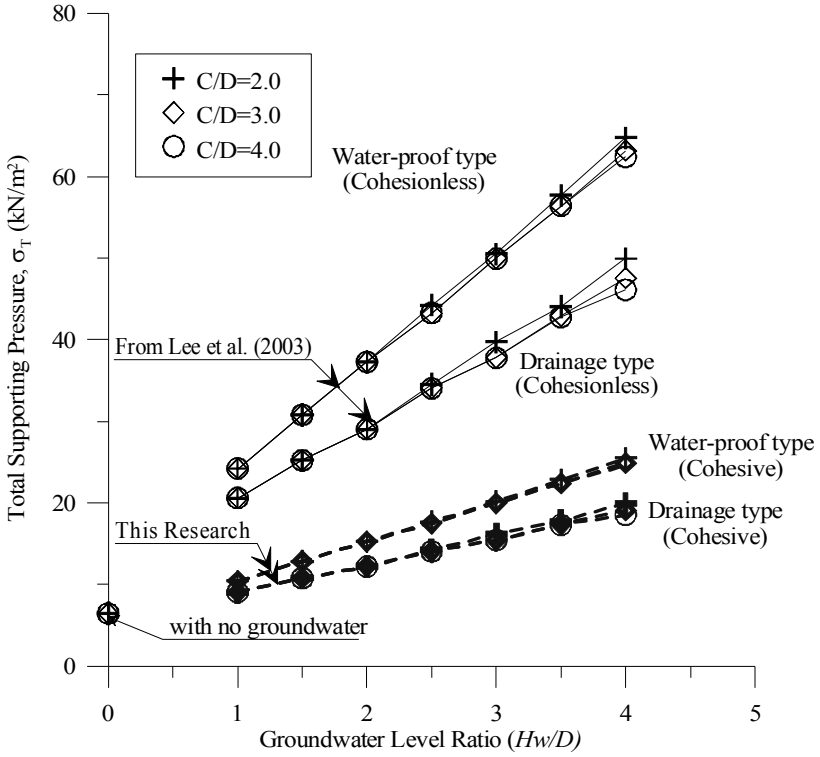

Figure 7.16 Change of support pressure with variation of the H/D

7.5.2 Reliability analysis

The limit state function, $g(\mathbf{X})$, with respect to the collapse of tunnel face in the ULS can be described as

$$g(\mathbf{X}) = \sigma_{applied} - \sigma_T(\mathbf{X}) \tag{7.37}$$

where, $\sigma_{applied}$ = the applied pressure on the tunnel face and $\sigma_T(\mathbf{X})$ = the limiting collapse pressure calculated by the FLAC^{3D} as described in the previous subsection.

When a probabilistic stability analysis is conducted, the failure probability for the tunnel face collapse can be defined as:

$$p_f = P\left[g(\mathbf{X}) \le 0\right] = \int_{g(\mathbf{X})\le 0} f(\mathbf{X}) d\mathbf{X} \tag{7.38}$$

where $f(\mathbf{X})$ is the joint probability density function of the basic variable vectors $\mathbf{X} = (\alpha,\ \beta,\ k_1,\ k_2,\ c_0',\ \phi',\ \rho,\ \gamma,\ C,\ D,\ \sigma_S,\ \sigma_{S.F.})$. The reliability analyses using first-order reliability method (FORM), the second-order reliability method (SORM), and Monte Carlo simulations (MCS) are performed based on the parameters summarized in Table 7.4. In this case, some of the parameters (C, D, σ_S, $\sigma_{S.F.}$) are assumed to be constant values.

Table 7.4 Parameters for the reliability analysis

Parameter ranges	Distribution models	Mean	COV
$0 < c_0' < \infty$	Lognormal	1.00	0.20
$0 < \phi' < \infty$	Lognormal	35.0	0.20
$0 < \rho < \infty$	Lognormal	0.50	0.20
$0 < \gamma < \infty$	Lognormal	15.2	0.20

C=10.0m, D=5.0m, σ_S=10kN/m^2, $\sigma_{S.F.}$=34.9kN/m^2

The reliability index for the different applied pressure values can be obtained as shown in Figure 7.17. As the applied pressure on the tunnel face increase, the reliability index also increases and it also means that the probability of failure will decrease.

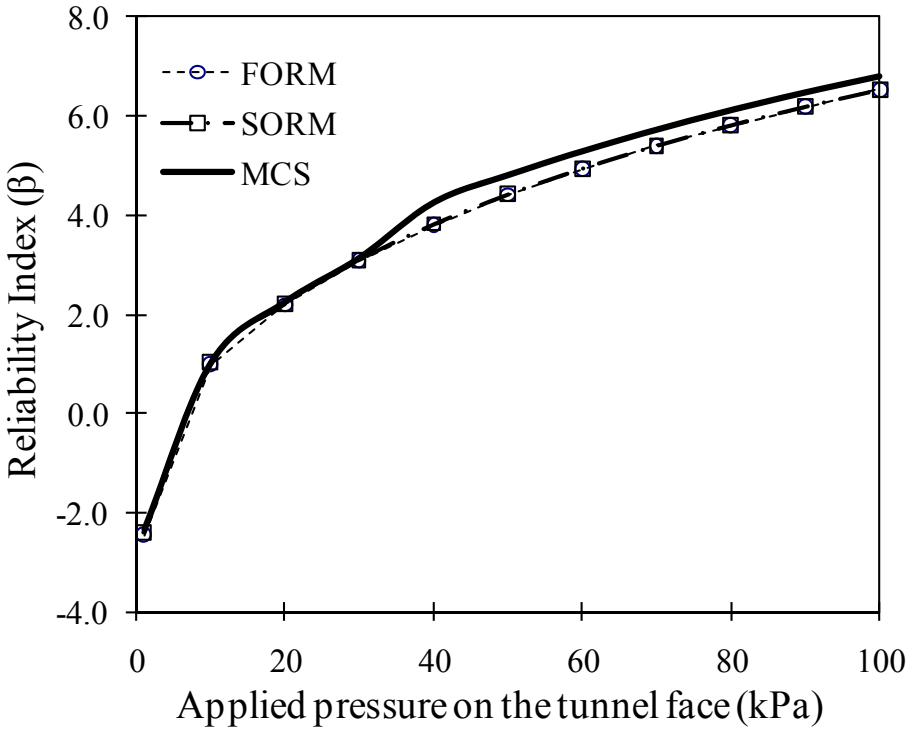

Figure 7.17 Reliability index for the different applied pressure values

7.5.3 Sensitivity and importance measures

In a reliability analysis, sensitivity measures are used to determine the effects on the reliability of changes in the parameters in the limit state function or in the distribution of the random variables.

Figure 7.18 shows the sensitivity measures as a function of the applied pressure on the tunnel face. It is observed that ϕ' have larger effects on the reliability. As the applied pressure increases, the tunnel face stability is most sensitive to ϕ'.

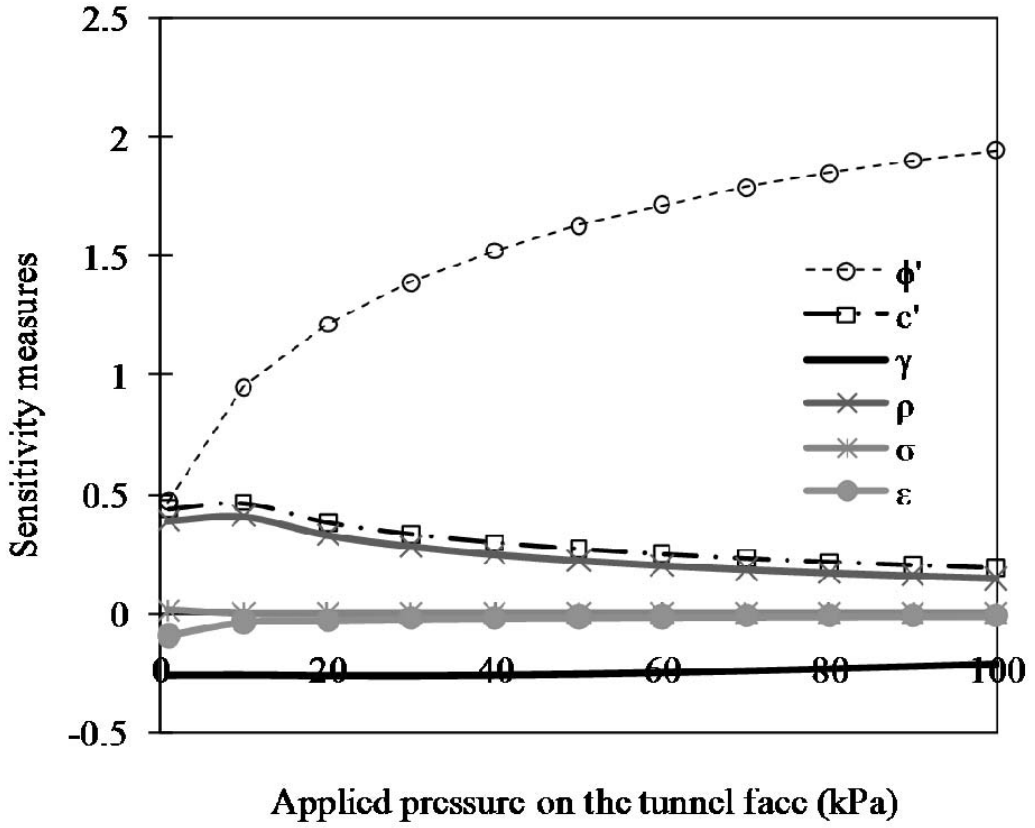

Figure 7.18 Sensitivity measures for the random variables

Figure 7.19 shows the importance measures of all random variables for the tunnel face stability. Observations similar to those made for the sensitivity analysis can be made for the importance measures. We can see that ϕ' is the most important variable and γ is the second most important variable.

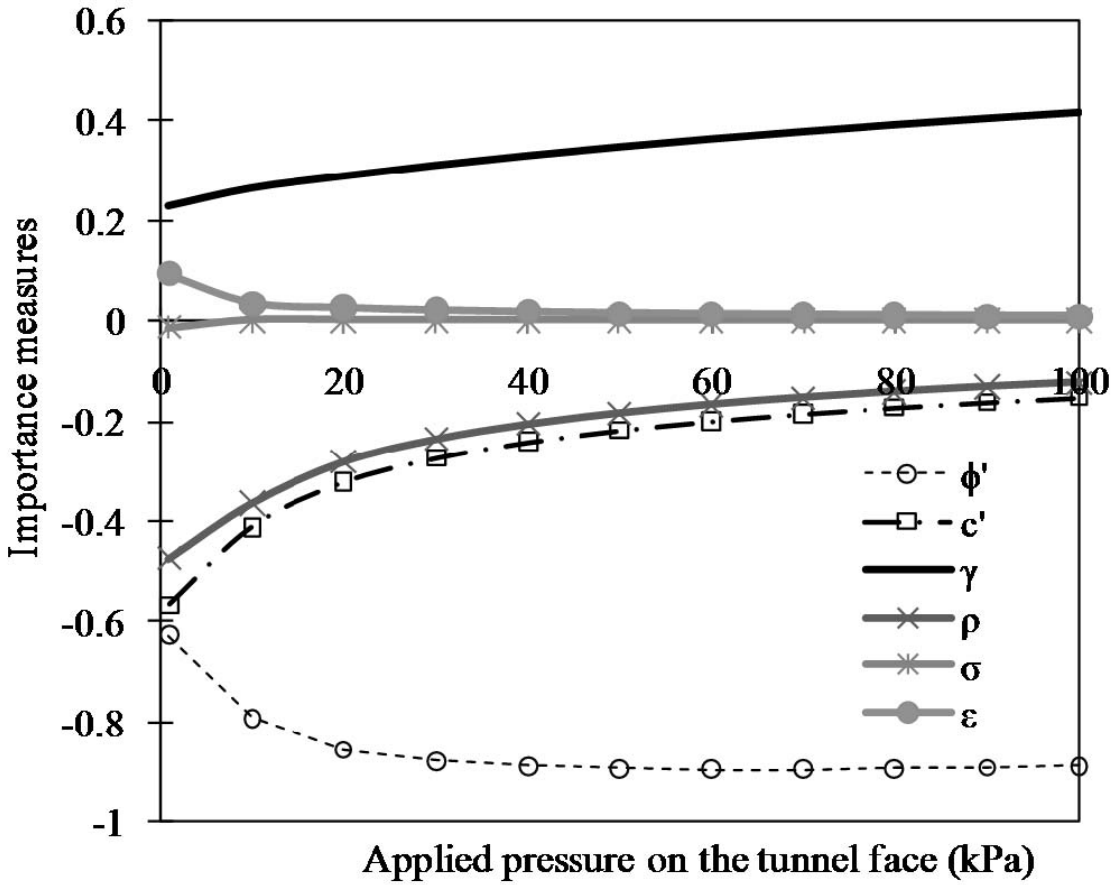

Figure 7.19 Importance measures for the random variables

7.6 Conclusions

The limiting tunnel collapse pressure in a Mohr-Coulomb (c', ϕ') soil is derived from the upper bound method (UBM) of limit analysis theory to maintain face stability. The derived UBM solution can consider the effect of seepage into the tunnel face and strength increase with depth. The influence of seepage forces and depth-dependent effective cohesion is investigated for a dual-cone failure mechanism using the UBM implemented by numerical analysis. The upper bound analytical derivation for depth-

dependent effective cohesion and corresponding numerical results are presented and compared to those presented by previous authors. In addition, the numerical analysis demonstrated the influence of tunnel diameter on required face supporting pressure.

After the derived UBM solution is verified with the numerical experiments, the probabilistic model is proposed to calculate the unbiased limiting tunnel collapse pressure. A reliability analysis of a shallow circular tunnel driven by a pressurized shield in a frictional and cohesive soil is presented to consider the inherent uncertainty in the input parameters and the proposed model. The ultimate limit state (ULS) for the face stability is considered in the analysis. The probability of failure that exceeding a specified applied pressure at the tunnel face is estimated. Sensitivity and importance measures are computed to identify the key parameters and random variables in the model.

8. CONCLUSIONS AND RECOMMENDATIONS

The main goal of this research is to investigate and develop analytical methods for addressing uncertainty during observation-based, adaptive design of deep excavation and tunneling projects. In order to fulfill the objective, computational procedures based on a Bayesian probabilistic framework are developed for comparative analysis between observed and predicted soil and structure response during construction phases.

8.1 Estimating Soil Properties and Deformations During Staged Excavations — I. A Bayesian Approach

A probabilistic methodology is developed to estimate soil properties and model uncertainty to better predict deformations during supported excavations. A Bayesian approach is used to assess the unknown soil properties by updating pertinent prior information based on field measurement data. The proposed method provides up-to-date predictions that reflect all sources of available information, and properly account for of the underlying uncertainty. In the example, the soils properties and the model parameters are updated after each excavation stage. The updated parameters are then used to develop new and more accurate predictions of the deformations in the subsequent excavation stages. This approach can be used for the design of optimal revisions for supported excavation systems. By applying the proposed Bayesian approach to the reliability-based design of geotechnical engineering projects, engineers

can combine the advantages of the observational method with the advantages of probabilistic methods.

8.2 Estimating Soil Properties and Deformations During Staged Excavations — II. Application To Case Histories

The two well documented case histories are the Lurie Research Center excavation project in Evanston, Illinois and the Caobao subway excavation project in Shanghai. A MATLAB-based application that can be connected to the general finite element software (i.e., ABAQUS 2003) is developed to automate of the computer simulations. The two case histories demonstrated the ability of the proposed Bayesian probabilistic method to provide accurate estimates of the deformations in supported excavation problems accounting for all source of information.

The estimate of the soil properties and prediction of the deformations in future excavation stages are also updated as new data become available during the excavation process. The greatest advantage of the proposed method is in its probabilistic framework, which gives predictions of deformations as well as the full probabilistic characterization of the variables. This advantage allows the evaluation of credible intervals for each prediction and sets the stage for a reliability analysis. Eventually, the framework can be used for the development of fragility curves, which can be used to make key decisions in the assessment of the excavation process and for a reliability-based optimal design of the excavation system.

8.3 A Bayesian Framework to Predict Deformations During Supported Excavations Using A Semi-Empirical Approach

A probabilistic framework is proposed to predict three-dimensional deformation profiles due to supported excavations using a semi-empirical approach. A Bayesian formulation is used to assess the unknown model parameters by updating prior information based on site specific field measurements at different locations. The updated model parameters are then used to develop new and more accurate predictions of the deformations in the subsequent stages, until the end of the excavation project.

The key advantage of the proposed approach for practicing engineers is that an already common semi-empirical chart can be used together with a few additional simple calculations to better evaluate three-dimensional displacement profiles. This eliminates the need for constitutive laws, complex calculations and finite element models. The developed approach provides a sound basis for making decisions about the design of excavation projects and can be used for optimizing the design of supported excavation systems. The proposed approach can also be used for an adaptive reliability-based optimal design of the excavation system in which the design is modified after each excavation stage to minimize costs and maintain a minimum reliability requirement.

8.4 Reliability Analysis of Infrastructure Adjacent to Deep Excavations

A reliability analysis framework is proposed to assess the fragility of excavation-induced infrastructure system damage for multiple serviceability limit states. A Bayesian framework based on a semi-empirical method is used to update the predictions of ground

movements in the later stages of excavation based on the field measurements. The component and system fragility estimates for excavation works in an urban area are developed in this study along with sensitivity and importance measures. The proposed approach can be used for an adaptive reliability-based optimal design of the excavation system in which the design is modified after each excavation stage to minimize costs and maintain a minimum reliability requirement. This method can also be expanded to any type of excavation projects related to urban redevelopment and infrastructure improvement. For example, additional limit state functions can be added to the system reliability analysis to consider the serviceability of tunnel for a deep excavation within the influence zone of an existing tunnel.

8.5 Reliability Assessment of Excavation Systems Considering Both Stability and Serviceability Performance

The serviceability performance of excavation systems is critically important in the design of many deep excavation projects because of liability for damage to existing adjacent infrastructure or buildings. This section presents a serviceability limit state function that considers the angular distortion of an adjacent structure. By adapting FEM analyses, the differential deformation of a structure can be considered in probabilistic terms using basic structural reliability concepts. This section demonstrates that the reliability index can be assessed by using FORM and by incorporating RSM, using a numerical procedure such as the FE method. An example was presented to demonstrate the feasibility and efficiency of this approach. Also, system reliability can be calculated

to assess the reliability of a staged excavation system by employing the probabilistic analysis program NESSUS. The work presented herein consists of a new general method for assessing the probability of exceeding any excavation system design criteria. The proposed approach accounts for both safety and serviceability limit states at the component and system level. This method can be further developed into a design framework that will allow engineers to estimate the safety of excavation systems in terms of probability of fulfilling their criteria and might also be used as a decision tool on determining the support system properties during design and between construction stages. In addition, a sensitivity analysis of the system reliability allows users to determine how reliabilities are influenced by different sources of limit state functions.

8.6 Reliability Analysis of Tunnel Face Stability Considering Seepage and Strength Increase with Depth

The limiting tunnel collapse pressure in a Mohr-Coulomb (c', ϕ') soil is derived from the upper bound method (UBM) of limit analysis theory to maintain face stability. The derived UBM solution can consider the effect of seepage into the tunnel face and strength increase with depth. The influence of seepage forces and depth-dependent effective cohesion is investigated for a dual-cone failure mechanism using the UBM implemented by numerical analysis. The upper bound analytical derivation for depth-dependent effective cohesion and corresponding numerical results are presented and compared to those presented by previous authors. In addition, the numerical analysis demonstrated the influence of tunnel diameter on required face supporting pressure.

After the derived UBM solution is verified with the numerical experiments, the probabilistic model is proposed to calculate the unbiased limiting tunnel collapse pressure. A reliability analysis of a shallow circular tunnel driven by a pressurized shield in a frictional and cohesive soil is presented to consider the inherent uncertainty in the input parameters and the proposed model. The ultimate limit state (ULS) for the face stability is considered in the analysis. The probability of failure that exceeding a specified applied pressure at the tunnel face is estimated. Sensitivity and importance measures are computed to identify the key parameters and random variables in the model.

8.7 Future Research Areas

Although the objectives of this research have been achieved, there are some limitations and valuable extensions that merit further study in the future.

In this study, we did not consider the spatial correlation in the probabilistic Bayesian analysis to estimate the soil properties and predict the deformations, in a system reliability approach to assess excavation systems, and in a reliability analysis of a shallow circular tunnel to assess the tunnel collapse pressure. However, the proposed approach can also be extended to account for the spatial correlation by use of a geostatistical approach or random field method.

The proposed approach can be easily expanded to a system reliability approach for complex excavation projects related to urban redevelopment and infrastructure improvement. For example, for a deep excavation within the influence zone of an existing tunnel, additional limit state functions can be added to the system reliability

analysis (for example, the allowable crown / sidewall displacement of tunnel or the allowable stress for secondary lining) to consider the stability and/or serviceability of tunnel.

Also, this research is mainly focused on the most dangerous steps during the excavation. It is expected that the reliability indices after the installation of struts for each excavation step will somewhat increase. However, the whole construction procedure, considering the time schedule of support installation, should be involved to assess the reliability of excavation.

For the reliability analysis of the tunnel face stability, the ultimate limit state (ULS) is only considered in this study. However, additional serviceability limit state (SLS) functions can be added to the system reliability analysis (for example, the settlement profiles due to an applied face support pressure) to assess the face pressure-induced soil displacements for the infrastructure located tunnel excavation area.

REFERENCES

AASHTO. (2007). "AASHTO LRFD bridge design specifications." American Association of State Highway and Transportation Officials, Washington, D.C.

ABAQUS. (2003). *ABAQUS version 6.5 documentation*. ABAQUS, Inc., Providence, R.I.

Addenbrooke, T. I., Potts, D. M., and Dabee, B. (2000). "Displacement flexibility number for multipropped retaining wall design." *Journal of Geotechnical and Geoenvironmental Engineering*, 126(8), 718-726.

Ang, A. H.-S., and Tang, W. H. (2007). *Probability Concepts in Engineering : Emphasis on Applications in Civil & Environmental Engineering*, John Wiley & Sons, New York.

Atkinson, J. H., and Potts, D. M. (1977). "Stability of a shallow circular tunnel in cohesionless soil." *Géotechnique*, 27(2), 203-215.

Attewell, P. B., Yeates, J., and Selby, A. R. (1986). *Soil Movements Induced by Tunnelling and Their Effects on Pipelines and Structures*, Chapman & Hall, New York.

Babu, G. L. S., Murthy, B. R. S., and Rao, R. S. (2006). "Reliability analysis of deflection of buried flexible pipes." *Journal of Transportation Engineering*, 132(10), 829-836.

Baecher, G. B., and Christian, J. T. (2003). *Reliability and Statistics in Geotechnical Engineering*, Wiley, Hoboken, NJ.

Bauer, J., and Pula, W. (2000). "Reliability with respect to settlement limit-states of shallow foundations on linearly-deformable subsoil." *Computers and Geotechnics*, 26(3-4), 281-308.

Becker, D. E. (1996a). "Eighteenth Canadian geotechnical colloquium: Limit states design for foundations. Part I. An overview of the foundation design process." *Canadian Geotechnical Journal*, 33(6), 956-983.

Becker, D. E. (1996b). "Eighteenth Canadian geotechnical colloquium: Limit states design for foundations. Part II. Development for the national building code of Canada." *Canadian Geotechnical Journal*, 33(6), 984-1007.

Bjerrum, L. (1963). "Allowable settlement of structures." *Proc., the 3rd European Conference on Soil Mechanics and Foundation Engineering*, Weisbaden, Germany, 135-137.

Bjerrum, L., and Eide, O. (1956). "Stability of strutted excavations in clay." *Géotechnique*, 6(1), 32-47.

Bonds, R. W. (2003). "Ductile iron pipe joints and their uses." Ductile Iron Pipe Research Association, Birmingham, AL.

Boscardin, M. D., and Cording, E. J. (1989). "Building response to excavation-induced settlement." *Journal of Geotechnical Engineering*, 115(1), 1-21.

Box, G. E. P., and Cox, D. R. (1964). "An analysis of transformations." *Journal of the Royal Statistical Society. Series B (Methodological)*, 26(2), 211-252.

Box, G. E. P., and Tiao, G. C. (1992). *Bayesian Inference in Statistical Analysis*, Wiley-Interscience, New York.

Box, G. E. P., and Wilson, K. B. (1954). "The exploration and exploitation of response surfaces: some general considerations and examples." *Biometrics*, 10(1), 16-60.

Bucher, C. G., and Bourgund, U. (1990). "A fast and efficient response surface approach for structural reliability problems." *Structural Safety*, 7(1), 57-66.

Burland, J. B. (1995). "Settlement of buildings and associated damage." *Proc. of IS-Tokyo '95 the First International Conference on Earthquake Geotechnical Engineering*, Tokyo, Japan, 1189-1201.

Burland, J. B., Broms, B.B. and DeMello, V.F. "Behavior of foundations and structures." *Proc. of the Ninth International Conference on Soil Mechanics and Foundation Engineering*, Tokyo, 495-546.

Burland, J. B., and Wroth, C. P. (1974). "Settlement of buildings and associated damage." *Proc. of Conference on Settlement of Structures*, Pentech Press, London, Cambridge, UK, 611-654.

Calvello, M., and Finno, R. J. (2004). "Selecting parameters to optimize in model calibration by inverse analysis." *Computers and Geotechnics*, 31(5), 411-425.

Caspe, M. S. (1966). "Surface settlement adjacent to braced open cuts." *Journal of the Soil Mechanics and Foundations Division*, 92(4), 51-59.

Chambon, P., and Corte, J.-F. (1994). "Shallow tunnels in cohesionless soil: Stability of tunnel face." *Journal of Geotechnical Engineering*, 120(7), 1148-1165.

Chen, W.-F., and Lui, E. M. (2005). *Handbook of Structural Engineering*, CRC Press, Boca Raton, FL.

Chowdhury, R. N., and Xu, D. W. (1993). "Rational polynomial technique in slope-reliability analysis." *Journal of Geotechnical Engineering*, 119(12), 1910-1928.

Chowdhury, R. N., and Xu, D. W. (1995). "Geotechnical system reliability of slopes." *Reliability Engineering & System Safety*, 47(3), 141-151.

Christian, J. T., Ladd, C. C., and Baecher, G. B. (1994). "Reliability applied to slope stability analysis." *Journal of Geotechnical Engineering*, 120(12), 2180-2207.

Chua, C. G., and Goh, A. T. C. (2005). "Estimating wall deflections in deep excavations using Bayesian neural networks." *Tunnelling and Underground Space Technology*, 20(4), 400-409.

Clough, G. W., and O'Rourke, T. D. (1990). "Construction induced movements of insitu walls." *Design and Performance of Earth Retaining Structures*, P. Lambe and L. A. Hansen, eds., ASCE, Ithaca, NY., 439-470.

Cording, E. J. "Evaluation and control of ground movements around tunnels and excavations in soil." *Proceedings of the Twelfth International Conference on Soil Mechanics and Foundation Engineering*, Rio de Janeiro, Brazil, 106-131.

Davis, E. H., Gunn, M. J., Mair, R. J., and Seneviratne, H. N. (1980). "The stability of shallow tunnels and underground openings in cohesive material." *Géotechnique*, 30(4), 397-416.

Dawson, E. M., Roth, W. H., and Drescher, A. (1999). "Slope stability analysis by strength reduction." *Géotechnique*, 49(6), 835-840.

Du, J. S., and Au, F. T. K. (2005). "Deterministic and reliability analysis of prestressed concrete bridge girders: comparison of the Chinese, Hong Kong and AASHTO LRFD Codes." *Structural Safety*, 27(3), 230-245.

Dunnicliff, J. (1988). *Geotechnical Instrumentation for Monitoring Field Performance*, Wiley, New York.

Eclaircy-Caudron, S., Dias, D., and Kastner, R. (2007). "Assessment of soil parameters met during a tunnel excavation: Use of inverse analysis on in situ measurements---Case of Bois de Peu (France)." Advances in Measurement and Modeling of Soil Behavior (GSP 173), ASCE, Denver, CO, 1-10.

Fenton, G. A., and Griffiths, D. V. (2002). "Probabilistic foundation settlement on spatially random soil." *Journal of Geotechnical and Geoenvironmental Engineering*, 128(5), 381-390.

Finno, R. J. (2007). "Use of monitoring data to update performance predictions of supported excavations." *Proc. of the 7th International Symposium on Field Measurements in Geomechanics*, J. DiMaggio and P. Osborn, eds., ASCE, Boston, MA, 1-30.

Finno, R. J., Blackburn, J. T., and Roboski, J. F. (2007). "Three-dimensional effects for supported excavations in clay." *Journal of Geotechnical and Geoenvironmental Engineering*, 133(1), 30-36.

Finno, R. J., and Calvello, M. (2005). "Supported excavations: Observational method and inverse modeling." *Journal of Geotechnical and Geoenvironmental Engineering*, 131(7), 826-836.

Finno, R. J., and Roboski, J. F. (2005). "Three-dimensional responses of a tied-back excavation through clay." *Journal of Geotechnical and Geoenvironmental Engineering*, 131(3), 273-282.

FLAC3D. (2009). *Fast Lagrangian Analysis of Continua in 3 Dimensions.* ITASCA Consulting Group, Inc., Minneapolis, Minnesota.

Fuentes, R., and Devriendt, M. (2010). "Ground movements around corners of excavations: Empirical calculation method." *Journal of Geotechnical and Geoenvironmental Engineering*, 136(10), 1414-1424.

Gardoni, P., Der Kiureghian, A., and Mosalam, K. M. (2002). "Probabilistic capacity models and fragility estimates for reinforced concrete columns based on experimental observations." *Journal of Engineering Mechanics*, 128(10), 1024-1038.

Gardoni, P., Reinschmidt, K. F., and Kumar, R. (2007). "A probabilistic framework for Bayesian adaptive forecasting of project progress." *Computer-Aided Civil and Infrastructure Engineering*, 22(3), 182-196.

Gelman, A., Carlin, J. B., Stern, H. S., and Rubin, D. B. (2004). *Bayesian Data Analysis*, Chapman & Hall/CRC, Boca Raton, FL.

Geweke, J. (1992). "Evaluating the accuracy of sampling-based approaches to the calculation of posterior moments." *Bayesian Statistics 4* J. M. Bernardo, J. Berger, A. P. Dawid, and A. F. M. Smith, eds., Oxford University Press, Oxford, UK, 169-193.

Gilks, W. R., Richardson, S., and Spiegelhalter, D. J. (1998). *Markov Chain Monte Carlo in Practice*, Chapman & Hall, Boca Raton, Fla.

Goh, A. T. C., and Kulhawy, F. H. (2005). "Reliability assessment of serviceability performance of braced retaining walls using a neural network approach." *International Journal for Numerical and Analytical Methods in Geomechanics*, 29(6), 627-642.

Goh, A. T. C., Kulhawy, F. H., and Wong, K. S. (2008). "Reliability assessment of basal-heave stability for braced excavations in clay." *Journal of Geotechnical and Geoenvironmental Engineering*, 134(2), 145-153.

Green, G. E., and Mikkelsen, P. E. (1988). "Deformation measurements with inclinometers." *Transportation Research Record*, 1169(1169), 1-15.

Griffiths, D. V. "Finite element analyses of walls, footings and slopes." *Proc. of Symposium on Computer Applications to Geotechnical Problems in Highway Engineering*, Cambridge, UK, 122–146.

Griffiths, D. V., and Fenton, G. A. (2004). "Probabilistic slope stability analysis by finite elements." *Journal of Geotechnical and Geoenvironmental Engineering*, 130(5), 507-518.

Griffiths, D. V., and Lane, P. A. (1999). "Slope stability analysis by finite elements." *Géotechnique*, 49(3), 387-403.

Gulvanessian, H., and Holický, M. (1996). *Designers' Handbook to Eurocode 1: Basis of Design*, Thomas Telford, London, UK.

Harr, M. E. (1987). *Reliability-Based Design in Civil Engineering*, McGraw-Hill, New York.

Hashash, Y. M. A., and Finno, R. J. (2008). "Development of new integrated tools for predicting, monitoring, and controlling ground movements due to excavations." *Practice Periodical on Structural Design and Construction*, 13(1), 4-10.

Hashash, Y. M. A., Marulanda, C., Ghaboussi, J., and Jung, S. (2003). "Systematic update of a deep excavation model using field performance data." *Computers and Geotechnics*, 30(6), 477-488.

Hashash, Y. M. A., and Whittle, A. J. (1996). "Ground movement prediction for deep excavations in soft clay." *Journal of Geotechnical and Geoenvironmental Engineering*, 122(6), 474-486.

Hasofer, A. M., and Lind, N. C. (1974). "Exact and invariant second-moment code format." *ASCE J Eng Mech Div*, 100(EM1), 111-121.

Hohenbichler, M., and Rackwitz, R. (1986). "Sensitivity and importance measures in structural reliability." *Civil Engineering Systems*, 3(4), 203-209.

Hsiao, E. L., Schuster, M., Juang, C. H., and Kung, G. C. (2008). "Reliability analysis and updating of excavation-induced ground settlement for building serviceability assessment." *Journal of Geotechnical and Geoenvironmental Engineering*, 134(10), 1448-1458.

Hsieh, P. G., and Ou, C. Y. (1998). "Shape of ground surface settlement profiles caused by excavation." *Canadian Geotechnical Journal*, 35(6), 1004-1017.

Jardine, R. J., Potts, D. M., Fourie, A. B., and Burland, J. B. (1986). "Studies of the influence of non-linear stress strain characteristics in soil-structure interaction." *Géotechnique*, 36(3), 377-396.

Jeffreys, H. (1961). *Theory of Probability*, Clarendon Press, Oxford, UK.

Jin-Zhang, Z., Williams, D. J., and Wen-Lin, X. (1995). "Search for critical slip surfaces based on finite element method." *Canadian Geotechnical Journal*, 32(2), 233-246.

Kang, W.-H., Song, J., and Gardoni, P. (2008). "Matrix-based system reliability method and applications to bridge networks." *Reliability Engineering & System Safety*, 93(11), 1584-1593.

Kung, G. C., Juang, C. H., Hsiao, E. L., and Hashash, Y. A. (2007). "Simplified model for wall deflection and ground-surface settlement caused by braced excavation in clays." *Journal of Geotechnical and Geoenvironmental Engineering*, 133(6), 731-747.

Leca, E., and Dormieux, L. (1990). "Upper and lower bound solutions for the face stability of shallow circular tunnels in frictional material." *Géotechnique*, 40(4), 581-606.

Lee, I.-M., and Nam, S.-W. (2001). "The study of seepage forces acting on the tunnel lining and tunnel face in shallow tunnels." *Tunnelling and Underground Space Technology*, 16(1), 31-40.

Li, K. S., and Lumb, P. (1987). "Probabilistic design of slopes." *Canadian Geotechnical Journal*, 24(4), 520-535.

Long, M. (2001). "Database for retaining wall and ground movements due to deep excavations." *Journal of Geotechnical and Geoenvironmental Engineering*, 127(3), 203-224.

Low, B. K. (1996). "Practical probabilistic approach using spreadsheet." *Geotechnical Special Publication*, ASCE, Madison, WI, 1284-1302.

Low, B. K. (2001). "Probabilistic slope analysis involving generalized slip surface in stochastic soil medium." *Proc. of the 14th Southeast Asian Geotechnical Conference*, A.A.Balkema Publishers, Hong Kong, 825-830.

Low, B. K. (2003). "Practical probabilistic slope stability analysis." *Proc., 12th Panamerican Conf. on Soil Mechanics and Geotechnical Engineering and 39th U. S. Rock Mechanics Symp.*, M.I.T., Cambridge, MA, 2777-2784.

Low, B. K. (2005). "Reliability-based design applied to retaining walls." *Géotechnique*, 55(1), 63-75.

Low, B. K., Gilbert, R. B., and Wright, S. G. (1998). "Slope reliability analysis using generalized method of slices." *Journal of Geotechnical and Geoenvironmental Engineering*, 124(4), 350-362.

Low, B. K., and Tang, W. H. (1997). "Efficient reliability evaluation using spreadsheet." *Journal of Engineering Mechanics*, 123(7), 749-752.

Low, B. K., and Tang, W. H. (2004). "Reliability analysis using object-oriented constrained optimization." *Structural Safety*, 26(1), 69-89.

Mana, A. I., and Clough, G. W. (1981). "Prediction of movements for braced cuts in clay." *Journal of the Geotechnical Engineering Division*, 107(6), 759-777.

Melchers, R. E. (1999). *Structural Reliability Analysis and Prediction*, John Wiley, New York.

Mikkelsen, P. E. (2003). "Advances in inclinometer data analysis." *Field Measurements in Geomechanics: Proc. of the Sixth International Symposium on Field Measurements in Geomechanics*, F. Myrvoll, ed., Taylor & Francis, Oslo, Norway, 555-568.

Mollon, G., Dias, D., and Soubra, A.-H. (2009). "Probabilistic analysis of circular tunnels in homogeneous soil using response surface methodology." *Journal of Geotechnical and Geoenvironmental Engineering*, 135(9), 1314-1325.

Molnar, K. M., Finno, R. J., and Rossow, E. C. (2003). "Analysis of effects of deep braced excavations on adjacent buried utilities." School of Civil and Environmental Engineering, Northwestern University, Evanston, IL.

Moormann, C. (2004). "Analysis of wall and ground movements due to deep excavations in soft soil based an a new worldwide database." *Soils and Foundations*, 44(1), 87-98.

Moser, A. P., and Folkman, S. (2008). *Buried Pipe Design*, McGraw-Hill, New York.

Moulton, L. K., GangaRao, H. V. S., and Halvorsen, G. T. (1985). *Tolerable Movement Criteria for Highway Bridges*. Federal Highway Administration, U.S. Department of Transportation, Washington, D.C.

Mroueh, H., and Shahrour, I. (2003). "A full 3-D finite element analysis of tunneling-adjacent structures interaction." *Computers and Geotechnics*, 30(3), 245-253.

Nath, P. (1983). "Trench excavation effects on adjacent buried pipes - finite-element study." *Journal of Geotechnical Engineering*, 109(11), 1399-1415.

NAVFAC (United States Naval Facilities Engineering Command). (1982). *Foundations and Earth Structures (NAVFAC DM-7.2.)*, Dept. of the Navy, Alexandria, VA.

Ou, C. Y., Hsieh, P. G., and Chiou, D. C. (1993). "Characteristics of ground surface settlement during excavation." *Canadian Geotechnical Journal*, 30(5), 758-767.

Park, J. K., Blackburn, J. T., and Gardoni, P. (2007). "Reliability assessment of excavation systems considering both stability and serviceability performance." *Georisk: Assessment & Management of Risk for Engineered Systems & Geohazards*, 1(3), 123-141.

Park, J. K., Gardoni, P., and Biscontin, G. (2010a). "Estimating soil properties and deformations during staged excavations − I. A Bayesian approach." *Computers and Geotechnics*, submitted.

Park, J. K., Gardoni, P., and Biscontin, G. (2010b). "Estimating soil properties and deformations during staged excavations − II. Application to case histories." *Computers and Geotechnics*, submitted.

Park, J. K., Gardoni, P., and Biscontin, G. (2010c). "A Bayesian framework to predict deformations during supported excavations based on a semi-empirical method." The 11th International Conference on Applications of Statistics and Probability in Civil Engineering, Zürich, Switzerland, submitted.

Peck, R. B. (1969). "Deep excavations and tunneling in soft ground." *Proc. of the Seventh International Conference on Soil Mechanics and Foundation Engineering*, Mexico City, 225-290.

Peschl, G. M., and Schweiger, H. F. (2003). "Reliability analysis in geotechnics with finite elements - comparison of probabilistic, stochastic and fuzzy set methods." *Proc. of the 3rd International Symposium on Imprecise Probabilities and their Applications* (ISIPTA'03), 437-451.

Pham, H. (2006). *Springer Handbook of Engineering Statistics*, Springer, London.

Phoon, K. K., and Kulhawy, F. H. (1999). "Characterization of geotechnical variability." *Canadian Geotechnical Journal*, 36(4), 612-624.

Poulos, H. G., Carter, J. P., and Small, J. C. (2001). "Foundations and retaining structures - research and practice." *Proc. of the 15th International Conference on Soil Mechanics and Geotechnical Engineering*, Istanbul, Turkey, 2527-2606.

Rankin, W. J. (1988). "Ground movements resulting from urban tunnelling: Predictions and effects." Geological Society, London, *Engineering Geology Special Publications*, 5(1), 79-92.

Rao, C. R., and Toutenburg, H. (1999). *Linear Models Least Squares and Alternatives*, Springer, New York.

Robert, C. P., and Casella, G. (2004). *Monte Carlo Statistical Methods*, Springer, New York.

Rubin, D. B. (1987). "The calculation of posterior distributions by data augmentation: Comment: A noniterative sampling/importance resampling alternative to the data

augmentation algorithm for creating a few imputations when fractions of missing information are modest: The SIR algorithm." *Journal of the American Statistical Association*, 82(398), 543-546.

Schuster, M. J., Juang, C. H., Roth, M. J. S., and Rosowsky, D. V. (2008). "Reliability analysis of building serviceability problems caused by excavation." *Géotechnique*, 58(9), 743-749.

Schweiger, H. F., and Peschl, G. M. (2005). "Reliability analysis in geotechnics with the random set finite element method." *Computers and Geotechnics*, 32(6), 422-435.

Schweiger, H. F., Thurner, R., and Pottler, R. (2001). "Reliability analysis in geotechnics with deterministic finite elements - Theoretical concepts and practical application." *International Journal of Geomechanics*, 1(4), 389-413.

Semih Yücemen, M., and Al-Homoud, A. S. (1990). "Probabilistic three-dimensional stability analysis of slopes." *Structural Safety*, 9(1), 1-20.

Shao, Y., and Macari, E. J. (2008). "Information feedback analysis in deep excavations." *International Journal of Geomechanics*, 8(1), 91-103.

Smith, I. M., and Griffiths, D. V. (2004). *Programming the Finite Element Method*, John Wiley & Sons, Hoboken, N.J.

Smith, I. M., and Hobbs, R. (1974). "Finite element analysis of centrifuged and built-up slopes." *Géotechnique*, 24(4), 531-559.

Son, M., and Cording, E. J. (2005). "Estimation of building damage due to excavation-induced ground movements." *Journal of Geotechnical and Geoenvironmental Engineering*, 131(2), 162-177.

Song, J., and Kang, W.-H. (2009). "System reliability and sensitivity under statistical dependence by matrix-based system reliability method." *Structural Safety*, 31(2), 148-156.

Southwest Research Institute. (2001). *NESSUS Theoretical Manual.* Southwest Research Institute, San Antonio, TX.

Southwest Research Institute. (2005). *NESSUS Getting Started Manual.* Southwest Research Institute, San Antonio, TX.

Tang, W. H., Yucemen, M. S., and Ang, A. H. S. (1976). "Probability-based short term design of soil slopes." *Canadian Geotechnical Journal*, 13(3), 201-215.

Tang, W. H., Zhang, J., and Zhang, L. M. (2010). "Characterizing geotechnical model uncertainty." *Proc. of the 10th International Conference on Structural Safety and Reliability*, H. Furuta, D.M. Frangopol & M. Shinozuka ed., Taylor & Francis Group, London, 114-123.

Terzaghi, K. (1943). *Theoretical Soil Mechanics*, John Wiley & Sons, New York.

Tu, X. (2007). "An Incrementally Non-linear Model for Clays with Directional Stiffness and a Small Strain Emphasis," Ph.D. dissertation, Northwestern University, Evanston, IL.,.

Ugai, K. (1989). "A method of calculation of global safety factor of slopes by elasto-plastic FEM." *Soils and Foundations*, 29(2), 190-195.

Ugai, K., and Leshchinsky, D. (1995). "Three-dimensional limit equilibrium and finite element analyses: A comparison of results." *Soils and Foundations*, 35(4), 1-7.

Vanmarcke, E. H. (1977). "Reliability of earth slopes." *ASCE J Geotech Eng Div*, 103(11), 1247-1265.

Wong, F. S. (1985). "Slope reliability and response surface method." *Journal of Geotechnical Engineering*, 111(1), 32-53.

Wong, H., Subrin, D., and Dias, D. (2006). "Convergence-confinement analysis of a bolt-supported tunnel using the homogenization method." *Canadian Geotechnical Journal*, 43(5), 462-483.

Wong, K. S., and Broms, B. B. (1989). "Lateral wall deflections of braced excavations in clay." *Journal of Geotechnical Engineering*, 115(6), 853-870.

WSDOT. (2010). *Geotechnical Design Manual.* Washington State Department of Transportation, Administrative and Engineering Publications, Olympia, WA.

Wu, Y. T. (1994). "Computational methods for efficient structural reliability and reliability sensitivity analysis." *AIAA journal*, 32(8), 1717-1723.

Xu, B., and Low, B. K. (2006). "Probabilistic stability analyses of embankments based on finite-element method." *Journal of Geotechnical and Geoenvironmental Engineering*, 132(11), 1444-1454.

Yoo, C. (2002). "Finite-element analysis of tunnel face reinforced by longitudinal pipes." *Computers and Geotechnics*, 29(1), 73-94.

Zhang, J., Zhang, L. M., and Tang, W. H. (2009). "Bayesian framework for characterizing geotechnical model uncertainty." *Journal of Geotechnical and Geoenvironmental Engineering*, 135(7), 932-940.

Zhang, L. M., and Ng, A. M. Y. (2005). "Probabilistic limiting tolerable displacements for serviceability limit state design of foundations." *Géotechnique*, 55(2), 151-161.

Zienkiewicz, O. C., Humpheson, C., and Lewis, R. W. (1975). "Associated and non-associated visco-plasticity and plasticity in soil mechanics." *Géotechnique*, 25(4), 671-689.

VITA

Jun Kyung Park received his B.S. (1997) degree and M.S. (1999) degree in the Department of Civil Engineering both from Korea University, Seoul, Korea. In August 2005, he came to Texas A&M University to pursue a Ph.D. in geotechnical engineering at the Zachry Department of Civil Engineering and received his Ph.D. in August 2011. Prior to coming to Texas A&M University, he was a senior engineer at the Sambo Engineering Co., Ltd., Korea and Dodam Enginnering & Construction Co., Ltd., Korea for six and half years. During his Ph.D. studies, Dr. Park received the Academic Excellence Award during 2008 – 2009 and his research ability was recognized at the U.S. Department of Transportation, Federal Highway Administration in 2007, as he was awarded the Eisenhower Graduate Fellowship. He also served as a Graduate Research/Teaching Assistant for Drs. Giovanna Biscontin and Paolo Gardoni developing adaptive reliability analysis framework in excavation problems, performing finite element analysis of double-wall impact protection levee design and developing state-of-the-art interdisciplinary graduate course in engineering ethics.

His research interests are foundation engineering, risk and reliability analysis for geotechnical/tunneling problems, inverse analysis based on Bayesian and extended logic, uncertainty identification/characterization/propagation, geostatistics for probabilistic site characterization, stochastic geo/rock mechanics.

Dr. Park may be reached at 3136 TAMU, College Station, TX 77843-3136. His email address is jkpark0215@hotmail.com.